Title
Wireless channel characterization at 2.4 GHz for multiple antenna systems

Permalink
https://escholarship.org/uc/item/4zt6j1n8

Author
Wood, Leslie Caroline

Publication Date
2008

UNIVERSITY OF CALIFORNIA, SAN DIEGO

Wireless Channel Characterization at 2.4 GHz for Multiple Antenna Systems

A Dissertation submitted in partial satisfaction of the requirements for the degree
Doctor of Philosophy

in

Electrical Engineering (Signal and Image Processing)

by

Leslie Caroline Wood

Committee in charge:

Professor William Hodgkiss, Chair
Professor William Coles, Co-Chair
Professor William Kuperman
Professor Laurence Milstein
Professor Paul Siegel

2008

The Dissertation of Leslie Caroline Wood is approved, and it is acceptable in quality and form for publication on microfilm and electronically:

Co-Chair

Chair

University of California, San Diego

2008

To my parents

TABLE OF CONTENTS

LIST OF SYMBOLS

$\mathbf{A}^{\mathbf{T}}$	Transpose of matrix A
$\mathbf{A}^{\mathbf{H}}$	Complex transpose of matrix A
$\mathbf{A}^{\mathbf{1/2}}$	Matrix square root of A
$\widetilde{\mathbf{A}}$	Element-wise square root of matrix A
$\mathbf{A} \circ \mathbf{B}$	Element-wise multiplication of matrices A and B
$\mathbf{A} \otimes \mathbf{B}$	Kronecker tensor product of matrixes A and B
det(A)	Determinant of matrix A
tr(A)	Trace of matrix A
$\lVert\mathbf{A}\rVert_2$	2-norm of matrix A
$\lVert\mathbf{A}\rVert_F$	Frobenius norm of matrix A
$\mathbf{A}^{\mathbf{-1}}$	Inverse of matrix A
C_{UT}	Uninformed transmitter capacity
$\mathbf{H}$	Channel matrix
$\mathbf{H}_{\mathbf{weich}}$	Channel matrix formed by Weichselberger model
$\mathbf{H}_{\mathbf{kron}}$	Channel matrix formed by Kronecker model
$\mathbf{R}_{\mathbf{Tx}}$	Correlation matrix at the transmitter link end
$\mathbf{R}_{\mathbf{Rx}}$	Correlation matrix at the receiver link end
$\mathbf{\Omega}$	Power coupling matrix in the Weichselberger model

LIST OF FIGURES

LIST OF TABLES

ACKNOWLEDGEMENTS

I am deeply grateful to many people for their support over the years. First and foremost, I would like to thank my advisor, Professor William Hodgkiss, for his guidance, constant support, and encouragement throughout my graduate studies. His insight and experience with the challenges of experimental data made this dissertation possible. I would also like to thank my committee members, Dr. William Coles, Dr. William Kuperman, Dr. Laurence Milstein, and Dr. Paul Siegel for their valuable time and interest in my work.

I owe special thanks to Michael Jensen and the researchers at the Brigham Young University Wireless Research Laboratory for the measured data used in the MIMO portions of this work.

I would like to recognize friends and colleagues for their support. In particular, I'd like to thank Tasha Vanesian for her assistance with MATLAB and her patience in reviewing publications, Adam Anderson for his enthusiastic discussions on MIMO, and Christine Libbey for her support with SIMO data collection.

I would also like to express my sincere gratitude to my family for their support and unwavering encouragement. Finally, I'd like to express my deep appreciation to Ryan Drogo for his love, patience and understanding throughout these years of study.

Chapter 2, in part, is a reprint of the material as it appears in "Indoor Spatial Correlation Measurements at 2.4 GHz," L. C. Wood and W. S. Hodgkiss, *Conference Record of the Thirty-Ninth Asilomar Conference on Signals, Systems and Computers, 2005*, pp.1588-1592 and "A Comparison of Indoor and Outdoor Spatial Correlation Measurements at 2.4 GHz," *Fortieth Asilomar Conference on Signals, Systems and*

Computers, 2006. ACSSC '06, pp.463-467. The dissertation author was the primary author of these papers.

Chapter 4, in part, is a reprint of the material as it appears in "MIMO Channel Models and Performance Metrics," L. C. Wood and W. S. Hodgkiss, *Global Telecommunications Conference, 2007. GLOBECOM '07. IEEE* , vol., no., pp.3740-3744, 26-30 Nov. 2007 and "Understanding the Weichselberger Model: A Detailed Investigation," L. C. Wood and W. S. Hodgkiss, submitted to MILCOM 2008. The dissertation author was the primary author of these papers.

Chapter 5, in part, is a reprint of the material as it appears in "Impact of Analytical Channel Models on Geometrical Channel Correlation Structures," L. C. Wood and W. S. Hodgkiss, VTC. Fall 2008, In press. The dissertation author was the primary author of this paper.

Chapter 6, in part, is a reprint of the material as it appears in "Impact of Channel Models on Adaptive M-QAM Modulation for MIMO Systems," L. C. Wood and W. S. Hodgkiss, *Wireless Communications and Networking Conference, 2008. WCNC 2008. IEEE* , vol., no., pp.1316-1321, March 31 2008-April 3 2008 and "A Reduced-Rank Eigenbasis MIMO Channel Model," L. C. Wood and W. S. Hodgkiss, *Proceedings of IEEE Wireless Telecommunications Symposium*, WTS 2008, pp.78-83, 24-26 April 2008. The dissertation author was the primary author of these papers.

Chapter 8, in part, is a reprint of the material as it appears in “Performance of MIMO Channel Models with Channel State Information at the Transmitter,” L. C. Wood and W. S. Hodgkiss, Globecom 2008, In Press. The dissertation author was the primary author of this paper.

VITA

2002	Bachelor of Science in Electrical Engineering University of California, San Diego
2003-2008	Research Assistant Department of Electrical and Computer Engineering University of California, San Diego
2004	Masters of Science in Electrical Engineering University of California, San Diego
2008	Doctor of Philosophy in Electrical Engineering University of California, San Diego

PUBLICATIONS

L. C. Wood and W. S. Hodgkiss, "Understanding the Weichselberger Model: A Detailed Investigation," MILCOM 2008, Submitted.

L. C. Wood and W. S. Hodgkiss, "Performance of MIMO Channel Models with Channel State Information at the Transmitter," Globecom 2008, In press.

L. C. Wood and W. S. Hodgkiss, "On the Performance of Analytical Channel Models in Capturing Channel Correlation Structure," Proceedings of VTC, Fall 2008, In Press.

L. C. Wood and W. S. Hodgkiss, "A Reduced-Rank Eigenbasis MIMO Channel Model," *Proceedings of IEEE Wireless Telecommunications Symposium*, WTS 2008, 24-26 April 2008.

L. C. Wood and W. S. Hodgkiss, "Impact of Channel Models on Adaptive M-QAM Modulation for MIMO Systems," *Wireless Communications and Networking Conference, 2008. WCNC 2008. IEEE* , pp.1316-1321, March 31 2008-April 3 2008.

L. C. Wood and W. S. Hodgkiss, "MIMO Channel Models and Performance Metrics," *Global Telecommunications Conference, 2007. GLOBECOM '07. IEEE*, pp.3740-3744, 26-30 Nov. 2007.

L. C. Wood and W. S. Hodgkiss, "A Comparison of Indoor and Outdoor Spatial Correlation Measurements at 2.4 GHz," *Fortieth Asilomar Conference on Signals, Systems and Computers, 2006. ACSSC '06.* pp.463-467, Oct.-Nov. 2006.

L. C. Wood and W. S. Hodgkiss, "Indoor Spatial Correlation Measurements at 2.4 GHz," *Conference Record of the Thirty-Ninth Asilomar Conference on Signals, Systems and Computers, 2005*, vol., no., pp.1588-1592, Oct. 28 2005-Nov. 1 2005.

FIELDS OF STUDY

Major Field: Electrical Engineering
    Signal and Image Processing
    Professor William Hodgkiss

ABSTRACT OF THE DISSERTATION

Wireless Channel Characterization at 2.4 GHz for Multiple Antenna Systems

by

Leslie Caroline Wood

Doctor of Philosophy in Electrical Engineering

(Signal and Image Processing)

University of California, San Diego, 2008

Professor William Hodgkiss, Chair

Professor William Coles, Co-Chair

The use of multiple antennas at one or both ends of a communication link can improve both the capacity and reliability of the system in a fading environment. However, the performance of the system depends heavily on the inherent structure of the channel itself. In this dissertation we focus our attention on the characterization of the wireless channel, modeling the channel, and the practical implications of the channel knowledge on the transmission strategy.

The first part of this dissertation considers single-input multiple-output (SIMO) transmission systems. For these systems, receiver diversity is available to improve the reliability of the communication link. The improvement available is governed by spatial correlation. This portion outlines the construction of a dual channel measurement system and channel measurements. Modeling is used to further understand the environment and the received power patterns.

The second part of this dissertation focuses on multiple-input multiple-output (MIMO) transmission systems. MIMO channel models are introduced, along with a framework for comparing the predictive performances of the models. Two analytical models, the Kronecker model and the structured eigenbasis model, are examined in detail. The differences in how the underlying physics in the channel are captured by the models are discussed, highlighting the performance impact. Geometrical models are used to investigate the model representations of the correlation matrix and the impact of system parameters on the model structure.

The final portion of this work focuses on practical transmission system considerations. The ability of analytical models to accurately predict the performance of two systems using M-QAM modulation is investigated. The performances of the two analytical models, the Kronecker and Weichselberger models, are compared against the predicted performance using measured data. Reduced rank modeling, and other strategies to reduce feedback overhead are discussed. Additionally, the issue of how to best use the channel, showing when spatial multiplexing is preferred for correlated channels, is explored. Finally, the time sensitivity of feedback on a system is discussed.

The effect of delay is investigated and the predictive performance of the analytical models is explored.

1 Introduction

1.1 Background

Wireless communications have become an integral part of everyday life. In order to meet the needs of consumers with increasing system reliability, higher transmission rates for faster data throughput, and increased mobility, the communications industry has looked to multiple antenna systems.

Multiple antenna systems employ multiple antennas at the transmitter, receiver, or both. By using the antennas in a smart fashion, it may be possible to achieve array gain or diversity gain when multiple antennas are located at either the transmitter or receiver link ends. When multiple antennas are present at both link ends, however, the achievable data rate can potentially be increased linearly proportional to the minimum of the number of antennas at the link ends [1-3]. The increase in channel capacity arises from a technique known as spatial multiplexing. To achieve the linear increase in throughput shown in [1], the channel is assumed to be Gaussian, with uncorrelated Rayleigh fading.

Generally, the performance achievable using multiple antennas depends on the nature of the channel [4-7]. Typically, the signal strength at a receive antenna varies greatly with small changes in its position [5-7]. This occurs when the received signal is a composite of many signals arriving from many different directions. Through propagation mechanisms such as reflection, diffraction, and scattering, objects in the channel, or scatterers, create multiple paths from the transmitter to the receiver. The paths traveled are of different lengths. Thus the signals arrive at the receiver with different amplitudes and phases. This concept is illustrated in Figure 1.1. When the phases of multiple signals align, constructive interference occurs, and the signal power is strengthened.

However, when the phases of the arriving signals are opposing, destructive interference occurs. The degradation caused by this destructive interference can be highly detrimental to receiver performance. This phenomenon is referred to as multipath interference.

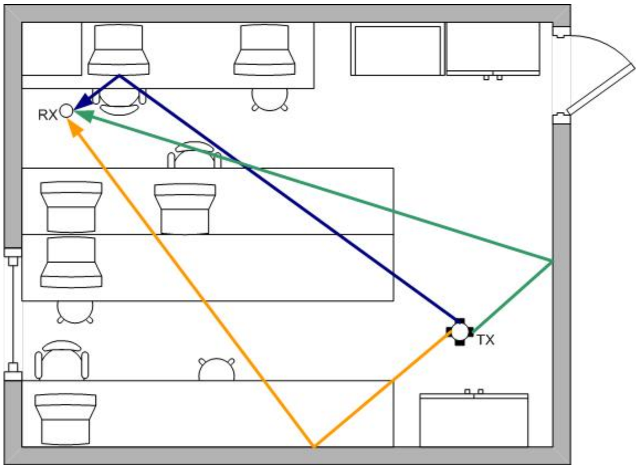

Figure 1.1: Example multipath scenario in an indoor environment.

Diversity systems are typically used to combat the issues arising from multipath interference. An overview of diversity systems can be found in [5, 8-9] and the references therein. Alternatively, the different paths of the channel can be exploited to transmit unique data streams. By resolving different paths, the throughput can be increased without increasing the system bandwidth. This transmission strategy is known as spatial multiplexing. This concept was introduced by Winters in [10], but was not developed into a practical transmission strategy until the later work of Foschini in [2-3]. The tradeoff between exploiting the spatial dimension of the channel for diversity or increased throughput is a fundamental problem that must be addressed by MIMO system designers [11-15].

An aspect of the channel that significantly impacts the usefulness of a particular transmission strategy is spatial correlation. For Gaussian channels in which a line of sight does not exist between transmitter and receiver, the second order statistics completely describe the channel, governing the throughput possible. The throughput of multi-antenna Gaussian channels was explored by Teletar in [1]. The linear increase in the throughput, or alternatively, in the capacity, of the channel for MIMO versus SISO was computed using the assumption that individual paths in the MIMO channel are independent of each other, and thus uncorrelated for Gaussian channels. However, through experimental measurement campaigns, it has been found that this assumption is not valid for most measured channels. In fact, depending on the environment, the capacity of a measured channel often falls short of the limit given by Foschini [6, 16-18]. To approach the MIMO capacity bound, space-time algorithms rely heavily on the multipath characteristics of the channel, and hence, knowledge of the spatial correlation. The overall performance of a signaling scheme is highly dependent on the environment. Thus, there is need to accurately model the MIMO channel in order to properly evaluate the performance gains of MIMO versus diversity or single antenna systems.

To test algorithms and design optimal architectures, several models for multiple antenna systems have been created, with varying capabilities in accurately representing the channel and spatial correlation. Most channel models fit into one of three categories: physical, geometric-statistical, and analytical. A good overview of channel models can be found in [6, 19-21] and the references therein. In order to characterize the behavior of real channels and compare model performances, measurements are necessary in multiple environments. From these measurements, model parameters can be estimated, allowing channel models to be realistically synthesized. In this case, the model is used as a channel simulator. However, the model may be able to be used at a more fundamental level in system design. If the model captures the underlying physics of the channel, it may offer insight into the tradeoff in system resources. In this case, the model can be exploited for use in system design.

1.2 Notations

The following notations are used in this work: $\mathbf{A}^{\mathbf{H}}$ and $\mathbf{A}^{\mathbf{T}}$ indicate the conjugate transpose and the transpose of matrix **A**, respectively. $\mathbf{I}_{\mathbf{n}}$ is the n x n identity matrix. Logarithms, log( ), are base-2 unless otherwise noted. The use of tr(**A**) and det(**A**) indicates the trace and determinant of matrix **A**, respectively. Bold-typeface is used to denote matrix or vector quantities.

1.3 Basic Communication Models

Consider a single-input single-output (SISO) communication link, and assume the physical channel is linear. We can then describe the channel from a signal processing perspective as a linear filter. If the channel is additionally assumed to be time-invariant and causal, the input-output relationship of the channel is determined by the convolution of the input x(t) and the channel's impulse response h(t),

$$y(t) = x(t)*h(t) \tag{1.1}$$

where * denotes convolution. Via the Fourier transform, the equivalent representation in the frequency domain is:

$$Y(f) = X(f)H(f) \tag{1.2}$$

In this form, H(f) operates as a transfer function, describing how the channel modifies the spectrum of the input signal. For this reason, the channel description is often referred to as the channel transfer matrix.

In general, the channel may be time dispersive. That is, given an input at any time instance, the resulting output from the channel is spread out over time. In the frequency domain, the time dispersive nature means $H(f)$ is not constant with respect to frequency. Channels that treat frequencies differently are said to be frequency selective.

In practical transmission scenarios, noise is also a factor. Typically, noise is modeled as an additive random process, with the distribution usually selected to be white, complex Gaussian distributed. This leads to the additive white Gaussian noise channel model description:

$$y(t) = h(t)*x(t) + n(t) \tag{1.3}$$

Commonly, modeled channels in the literature are assumed to be non-time dispersive. This assumption leads to a simplification of the channel, which makes it attractive for use in theoretical frameworks due to its simplicity. If the impulse response of the channel is not time-dispersive, then it can be reduced to a single complex constant between the transmitter and receiver. In this case, we can express the communication system as:

$$y(t) = hx(t) + n(t) \tag{1.4}$$

where h is referred to as the complex gain of the channel. For compactness, the explicit reference to the time varying nature of the channel shown in (1.4) is typically suppressed, giving the traditional time-domain SISO narrowband communication model equation,

$$y = hx+n \tag{1.5}$$

When multiple antennas, n_r, are available at the receiver, the channel becomes a vector channel,

$$\mathbf{y} = \mathbf{h}x+ \mathbf{n} \tag{1.6}$$

where **y**, **h**, and **n** are n_r x 1 vectors. Such a system, in which a single transmit antenna feeds information to multiple receive antennas is called a single-input multiple-output (SIMO) system.

If we now consider the SISO description of a non-time dispersive, causal, time invariant channel in the framework of multiple-input multiple output (MIMO) systems, we arrive at the typical narrowband MIMO channel model, in which the input output relationship is described as

$$\mathbf{y} = \mathbf{H}\mathbf{x} + \mathbf{n} \tag{1.7}$$

where **x** is the n_t dimensional transmit vector, **y** is the n_r dimensional receive vector, **H** is the n_r x n_t matrix of channel gains, and the n_r components of the noise vector **n** are assumed to be i.i.d. complex circularly symmetric Gaussian distributed random entries with zero mean and variance σ_n^2

1.4 Outline of Dissertation

The rest of this dissertation is outlined below.

In Chapter 2, spatial correlation in the context of SIMO systems will be explored. Spatial diversity techniques and the impact of spatial correlation on system performance will be discussed. An overview of a dual channel SIMO measurement system will be presented, with additional details to be found in the Appendix. This system was used to probe the channel, collecting channel data in a variety of environments. From this measured data, the correlation coefficient between receive antennas was estimated for both indoor and outdoor transmission scenarios. The effects of correlation are explored as a function of frequency and of receive antenna interelement spacing. To better understand the underlying physics of the transmission scenarios, basic ray tracing techniques are used to generate similar received power fields. Additionally, the impact of mutual coupling on the measurements will also be analyzed.

Chapter 3 shifts the focus from SIMO systems to MIMO communications. This chapter presents an overview of different correlation models in the literature, concentrating on correlation-based analytical channel models. A framework for comparing the capabilities of the models will be introduced, including a discussion on channel metrics and beamforming techniques. Real-world channel data measurements will be used to determine how well the models represent different environments. Geometrical-based models will also be introduced and used as a vehicle to enhance the understanding of the fundamental differences between the analytical correlation-based models.

Chapter 4 introduces the measurement environments, transmission scenarios, and measurement hardware. Estimation of model parameters from measured data and channel model synthesis will be discussed. The performance of two correlation-based analytical models in predicting system performance will be compared using the channel metrics defined in Chapter 3. Furthermore, a detailed analysis of the structured eigenbasis model will illuminate how the underlying physics in the channel are captured, highlighting the model aspects that drive the performance differences.

Chapter 5 uses geometrical models to investigate the analytical model representations of the correlation matrix and the impact of system parameters on the model structure. This chapter shows that the structured eigenbasis model proposed by Weichselberger in [22] can be used to capture the unique characteristics of a variety of geometrical environments with reasonable accuracy. Additionally, the impact of the models on the correlation matrix is explored. The differences in the correlation matrix representation are discussed from the perspective of system performance. Using the geometrical models, the effects of system and environmental configurations on model parameters, such as the number of scattering clusters and the separation between transmit and receive arrays, are investigated.

In Chapter 6, the focus turns to practical transmission systems, where M-QAM open loop and closed loop architectures are investigated. The performances of the two analytical models, the Kronecker and Weichselberger models, are compared against the predicted performance using measured data. Reduced rank modeling, and other strategies to reduce feedback overhead are discussed.

Chapter 7 focuses on how to best use the channel, showing when spatial multiplexing is preferred for correlated channels. This analysis is carried out by comparing the minimum constellation distances required to support spatial diversity and spatial multiplexing. This analysis is related back to the coupling matrix of the structured eigenbasis model, allowing spatial multiplexing preferred channels to be predicted from the power coupling matrix of the model.

Chapter 8 deals with an additional practical system aspect: the latency sensitivity of feedback. This chapter examines the impact of delayed channel state information at the transmitter, as well as the impact of delayed channel distribution information. The ability of the channel models to predict the effects of the delay is investigated. Additionally, the issue of both the transmitter and receiver having delayed channel information is explored for a variety of measured environments.

In Chapter 9, key points are summarized and potential future research directions are discussed.

1.5 References

[1] I. E. Telatar, "Capacity of multi-antenna Gaussian channels," Eur. Trans.Telecomm., ETT, vol. 10, pp. 585-595, Nov./Dec. 1999.

[2] G. J. Foschini and M. J. Gans, "On Limits of Wireless Communications in a Fading Environment when UsingMultiple Antennas." *Wirel. Pers. Commun.* vol. 6, 3, Mar. 1998, pp. 311-335.

[3] G. J. Foschini, "Layered Space-Time Architecture for Wireless Communications in a Fading Environment When using Multiple Antennas," Bell Labs Technical Journal, vol. 1, pp. 41-59, Autumn 1996.

[4] Goldsmith, S. A. Jafar, N. Jindal, and S. Vishwanath, "Capacity limits of MIMO channels," *IEEE Journal on Selected Areas in Communications,* vol.21, no.5, pp. 684-702, June 2003.

[5] W. C. Jakes, "Mobile Communications," New York: John Wiley & Sons, 1974.

[6] C. Oestges and B. Clerckx. *MIMO Wireless Communications*, Elsevier Ltd, London, 2007.

[7] H. Van Trees, *Optimum Array Processing*. New York, Wiley-Interscience, 2002.

[8] S. M. Alamouti, "A simple transmit diversity technique for wireless communications," *IEEE J. Sel. Areas Commun.*, vol. 16, no. 8, pp. 1451–1458, Oct. 1998.

[9] A. F. Molisch and M. Z. Win, "MIMO systems with antenna selection," *Microwave Magazine, IEEE* , vol.5, no.1, pp. 46-56, Mar 2004.

[10] J. H. Winters, "Smart antennas for wireless systems," IEEE Personal Commun. Mag., vol. 5, pp. 23-27, Feb. 1998.

[11] D. N. C. Tse, P. Viswanath, and L. Zheng, "Diversity-multiplexing tradeoff in multiple-access channels," IEEE Trans. Information Theory, vol. 50, pp. 1859-1873, Sept. 2004.

[12] A. Goldsmith, Wireless Communications. New York, NY.: Cambridge University Press, 2005.

[13] S. Loyka and G. Levin, “On Finite-SNR Diversity-Multiplexing Tradeoff," *2007 IEEE Global Telecommunications Conference*, vol., no., pp.1456-1461, 26-30 Nov. 2007.

[14] W.-Y. Shin, S.-Y. Chung, and Y. H. Lee, “Diversity–Multiplexing Tradeoff and Outage Performance for Rician MIMO Channels,” *IEEE Trans. on Information Theory,* vol.54, no.3, pp.1186-1196, March 2008.

[15] K. Azarian, K.; H. El Gamal, “The Throughput–Reliability Tradeoff in Block-Fading MIMO Channels,” *IEEE Trans. on Information Theory,* vol.53, no.2, pp.488-501, Feb. 2007.

[16] M. J. Gans, N. Amitay, Y. S. Yeh, H. Xu, R. A. Valenzuela, T. Sizer, R. Storz, D.Taylor, W. M. MacDonald, C. Tran, and A. Adamiecki, "BLAST system capacity measurements at 2.44 GHz in suburban outdoor environments," in Proc. IEEE VTC 2001, 2001, pp. 288-292.

[17] D. Chizhik, J. Ling, P. Wolniansky, R. A. Valenzuela, N. Costa, and K. Huber, "Multiple-Input, Multiple-Output Measurements and Modeling in Manhattan," IEEE JSAC, vol. 21, April 2003.

[18] J. W. Wallace and M. A. Jensen, “Experimental analysis of the time-varying MIMO channel,” *Antennas and Propagation Society International Symposium 2006*, IEEE, 9-14 July 2006, pp. 321- 324.

[19] D. Gesbert, M. Shafi, D-S Shiu; P.J. Smith, and A. Naguib, "From theory to practice: an overview of MIMO space-time coded wireless systems," *IEEE Journal on Selected Areas in Communications,* vol.21, no.3, pp. 281-302, Apr 2003.

[20] A.J. Paulraj, D.A. Gore, R.U. Nabar, H. Bolcskei, "An overview of MIMO communications - a key to gigabit wireless," *Proceedings of the IEEE* , vol.92, no.2, pp. 198-218, Feb 2004.

[21] M. A. Jensen and J. W. Wallace, "A review of antennas and propagation for MIMO wireless communications," *IEEE Transactions on Antennas and Propagation*, vol.52, no.11, pp. 2810-2824, Nov. 2004.

[22] W. Weichselberger, M. Herdin, H. Özcelik, and E. Bonek, “A Stochastic MIMO Channel Model with Joint Correlation at Both Link Ends,” *IEEE Trans Wireless Communications*, vol 5, no. 1. Jan 2006, pp. 90-100.

2 SIMO Systems

2.1 Introduction

With the crowding of the Industrial, Scientific, and Medical (ISM) band at 2.4 GHz, further measurements are needed to better characterize and accurately model the wireless channel in a variety of user environments. This chapter begins with an introduction to Single-Input Multiple-Output (SIMO) communication systems. The concept of spatial diversity is explained and spatial correlation is defined. Overviews of the experimental test bed and the measurement environments are given. The effects of spatial correlation are explored in several indoor and outdoor environments as a function of antenna interelement spacing. Additionally, spatial correlation is also examined at different frequencies in the ISM band. This is unlike most SIMO measurement campaigns presented in literature, which have focused on investigating wireless channel characteristics from a narrowband perspective by using only single frequency channel sounding techniques. Basic ray tracing models are applied to further the understanding of the channel. The effects of mutual coupling on spatial correlation are also considered.

2.2 Multipath and SIMO Communications

To combat the effects of multipath environments, many devices implement some form of diversity, such as frequency, time, code, or spatial. This chapter focuses on the latter, in which multiple antenna branches are used to try to achieve better system performance. In this study, multiple antennas will be located at the receiver link end.

In recent studies, attention has been given to characterizing the improvements possible through spatial diversity in indoor environments. These studies have shown that diversity combining techniques would be useful for interelement spacings that are a fraction of a wavelength [1-6]. In [1], a dual antenna receiver system was used to explore cross polarization diversity at 1.8 GHz. In [2], a comparison of gains possible from spatial, polarization, and pattern diversity was presented for a 2.05 GHz system. Similar measurements for dual antenna handsets were made in [3]. The system employed in [4] was a switched antenna system, taking measurements consecutively rather than simultaneously. Antenna orientation, K-factor, and delay spread were explored at 1.9 GHz. Additionally, several SISO measurement systems have characterized path loss [5-8]. Spatial correlation effects in hallways are investigated from both transmitter and receiver perspective in [9]. Work performed at 1.95 GHz explores correlation in indoor environments for Multiple Input Multiple Output (MIMO) systems [10]. Only recently have researchers begun characterizing the wireless channel using systems with a more broadband perspective [11-14].

2.3 Spatial Correlation

The correlation coefficient is defined in multiple ways in the literature, each providing a measure of the similarity between signals [15]. One definition is for the envelope correlation coefficient:

$$\rho_{env} = \frac{E[r_1 r_2] - E[r_1]E[r_2]}{\sigma_{r_1}\sigma_{r_2}} \tag{2.1}$$

where r_1 and r_2 are the samples of the envelope received on each channel, and σ_1 and σ_2 the corresponding standard deviations, which normalize the correlation value to a maximum value of unity. For a SIMO system, r_1 and r_2 are obtained from different receiver antennas.

Similarly, the power correlation of r_1 and r_2 is defined as:

$$\rho_{pwr} = \frac{E\left[r_1^{\ 2} r_2^{\ 2}\right] - E\left[r_1^{\ 2}\right]E\left[r_2^{\ 2}\right]}{\sigma_{r_1^{\ 2}} \sigma_{r_2^{\ 2}}} \tag{2.2}$$

where $\sigma_{r_x^{\ 2}}$ refers to the corresponding standard deviation from antenna r_x.

Under certain channel conditions, it has been demonstrated that these two correlation coefficients are related, such that $\rho_{env} \approx \rho_{pwr}$ [16].

2.4 Spatial Diversity Techniques

Spatial diversity techniques are inherently dependent on the amount of spatial correlation present. Consider a dual antenna receiver communications system. If both antennas are located close together, they will receive essentially the same signal. Data streams from either antenna could be used to determine what was transmitted with equivalent performance. In this case, the streams are highly correlated. While strong correlation is not an issue if both antennas are receiving strong signals, problems arise if fading occurs. Since the antennas are highly correlated, if the signal on one antenna fades, the other antenna will likely fade as well, potentially breaking the communication link. However, if the antennas are placed farther apart, they are more likely to be subjected to slightly different received signals. In this scenario, the antennas are less correlated. If one antenna fades, the other is less likely to do so.

As an example of one diversity technique, switching can occur between antennas, allowing the receiver to process only the data stream on the antenna with the highest signal to noise ratio (SNR). An alternate method is to combine the signals from both antennas in a smart fashion to increase the receiver's overall knowledge and reliability of the transmitted information. One such combining scheme, called maximal ratio combining, combines signal knowledge together according to the SNR on each received channel. The joint probability density function (pdf) for dual channel maximal ratio combining is given as [17]:

$$f_{\gamma_1,\gamma_2}(\gamma_1,\gamma_2)=\frac{1}{\bar{\gamma}_1\bar{\gamma}_2(1-\rho)}\exp\left(-\frac{1}{1-\rho}\left[\frac{\gamma_1}{\bar{\gamma}_1}+\frac{\gamma_2}{\bar{\gamma}_2}\right]\right)I_0\left(\frac{2\sqrt{\rho\gamma_1\gamma_2}}{(1-\rho)\sqrt{\bar{\gamma}_1\bar{\gamma}_2}}\right)\quad \gamma_1,\gamma_2\geq 0 \quad (2.3)$$

where γ_1, γ_2 are the SNRs on each received branch, $\bar{\gamma}_1$, $\bar{\gamma}_2$ are the average branch SNRs, and ρ is the power correlation coefficient between the two branches.

This pdf can be integrated to find the probability that the SNR drops below some threshold. The cumulative distribution function is given as [18]:

$$F_{\gamma_{MRC}}(\gamma)=\frac{\bar{\gamma}_A-\bar{\gamma}_A e^{-\frac{\gamma}{\bar{\gamma}_A}}-\bar{\gamma}_B+\bar{\gamma}_B e^{-\frac{\gamma}{\bar{\gamma}_B}}}{\sqrt{(\bar{\gamma}_1+\bar{\gamma}_2)^2+4\bar{\gamma}_1\bar{\gamma}_2\rho}}\quad \gamma\geq 0 \quad (2.4)$$

where the parameters $\bar{\gamma}_A$ and $\bar{\gamma}_B$ are defined, respectively, as:

$$\bar{\gamma}_A=\frac{2\bar{\gamma}_1\bar{\gamma}_2(1-\rho)}{(\bar{\gamma}_1+\bar{\gamma}_2)+\sqrt{(\bar{\gamma}_1+\bar{\gamma}_2)^2+4\bar{\gamma}_1\bar{\gamma}_2\rho}}, \quad (2.5)$$

$$\bar{\gamma}_B=\frac{2\bar{\gamma}_1\bar{\gamma}_2(1-\rho)}{(\bar{\gamma}_1+\bar{\gamma}_2)-\sqrt{(\bar{\gamma}_1+\bar{\gamma}_2)^2+4\bar{\gamma}_1\bar{\gamma}_2\rho}} \quad (2.6)$$

Using (2.4), the probability of link outage, defined as the probability the combiner output SNR falls below a threshold SNR, was computed. For these computations, the average branch SNR on channel 1 is assumed to be the same as the average branch SNR on channel 2. This assumption is indicative of a propagation environment where the signals received on the dual channels experience similar average fading attenuations. By computing the cumulative distribution function for different values of ρ, the impact of spatial correlation on the total system SNR using MRC reception can be observed. Note that for an MRC system, the total system SNR is the sum of the individual branch SNRs. The effect of spatial correlation on the total system SNR using MRC reception is shown in Figure 2.1 as a function of the threshold SNR, γ. Sizeable diversity performance gain is achieved when the correlation coefficient between branches drops from 0.999 to 0.9, with most of the diversity gain extracted for correlations below 0.5.

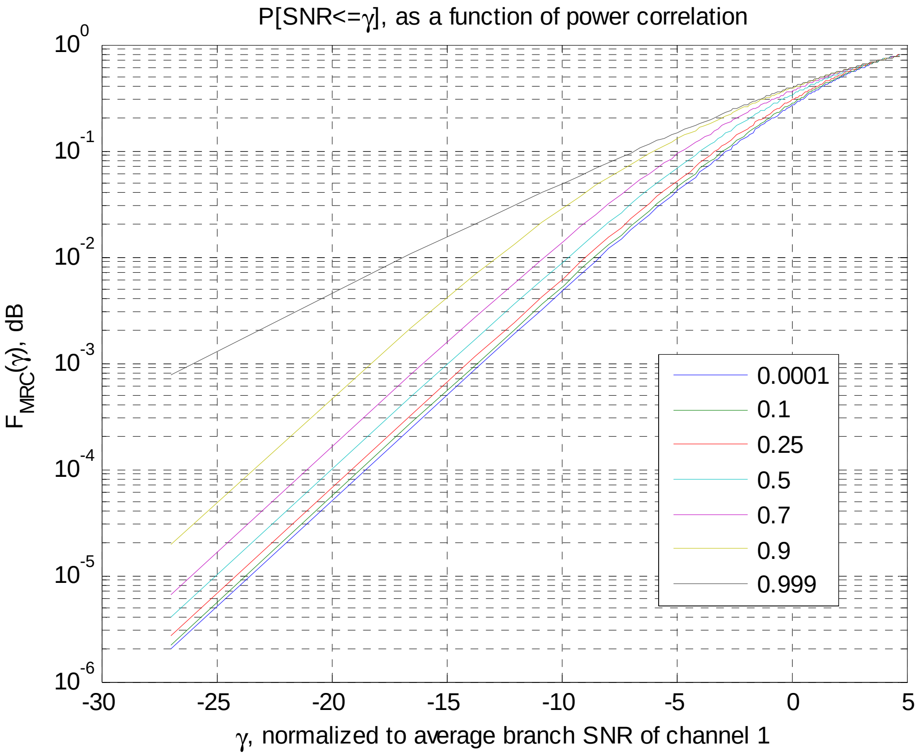

Figure 2.1: CDF for the SNR of MRC combining vs. SNR for different correlation values.

Regardless of which diversity combining technique is used, it is desirable to have the multiple branches in a diversity system as statistically uncorrelated as possible so that if one branch experiences a deep fade, the other branch will not. This means that receiver performance can be improved by spacing the antennas such that spatial correlation between receivers is minimized. To find interelement spacings that provide sufficient amounts of decorrelation, we turn to measurements made in several different environments.

2.5 SIMO Measurements

2.5.1 Transmitter and Receiver Configuration

For characterizing spatial correlation at 2.4 GHz, a dual channel receiver was constructed. A brief overview of the system is presented here, with detailed information on the receiver construction available in the Appendix. Most studies concerned with the 2.4 GHz band have investigated narrowband channel characteristics and have used single frequency channel sounding techniques. With technologies such as 802.11b/g occupying roughly 20 MHz of bandwidth, it would be useful to characterize the ISM band from a more broadband perspective. Thus, the hardware configuration is designed for characterizing the channel using a bandwidth similar to 802.11b/g.

The transmitter equipment consists of a signal generator designed to transmit a comb of CW signals. The CW signals span a total bandwidth of 18 MHz, centered at 2.442 GHz. The tonal signals in the comb are separated by 1 MHz. The transmitter and receiver antennas are vertically polarized omnidirectional antennas. The transmitter antenna was mounted on a wooden mast. The receiver antennas were placed vertically in a wooden holder that allowed for the repeatable adjustment of the interelement separation between the receiver antennas.

The receiver itself consists of a series of evaluation boards interconnected with SMA cables. A block diagram of the receiver can be seen in Figure 2.2. Evaluation boards were used as a convenient and economic approach to test the concept of operations. This approach allows for the ability to easily analyze and verify the system at each stage in the design. The receiver has two channels, each with an omnidirectional 2.4 GHz antenna followed by an 80 MHz wide bandpass filter to attenuate out of band signals. The bandpass signal is then fed into a LNA/mixer board. Down-conversion to an intermediate frequency occurs, followed by an amplification stage. The signal is then sampled and stored. A data capture board interfaces to a computer through a parallel port.

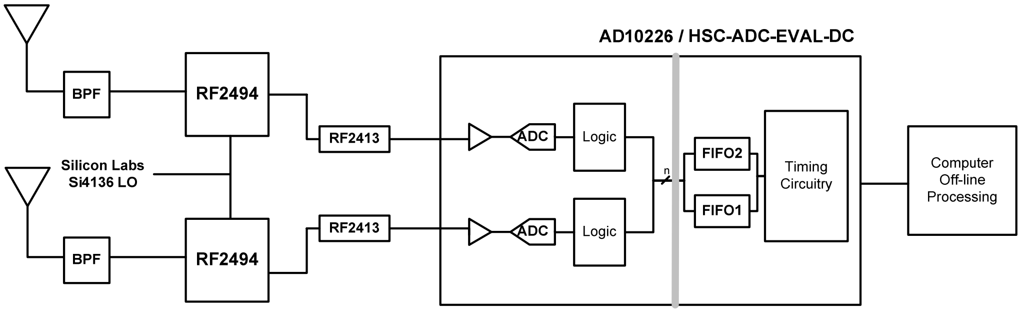

Figure 2.2: Block diagram of the dual channel receiver.

The LNA/mixer board down converts the incoming received signal, centered at 2.442 GHz, to an intermediate frequency centered at 374 MHz. The signal is then bandpass filtered using an on-board filter with approximately 18 MHz of bandwidth. This bandwidth is approximately the same bandwidth required for 802.11b/g transmissions. The signal is further down converted through sub sampling in the A/D board. A sampling rate of 60 MHz was selected to minimize the effects of aliasing on the desired portion of the spectrum. An example of the received spectrum, processed by the ADC Analyzer software from Analog Devices, is shown in Figure 2.3. The center of the received spectrum, 2.442 GHz, is mixed down to 14 MHz. The tonal frequencies separated by 1 MHz can be seen.

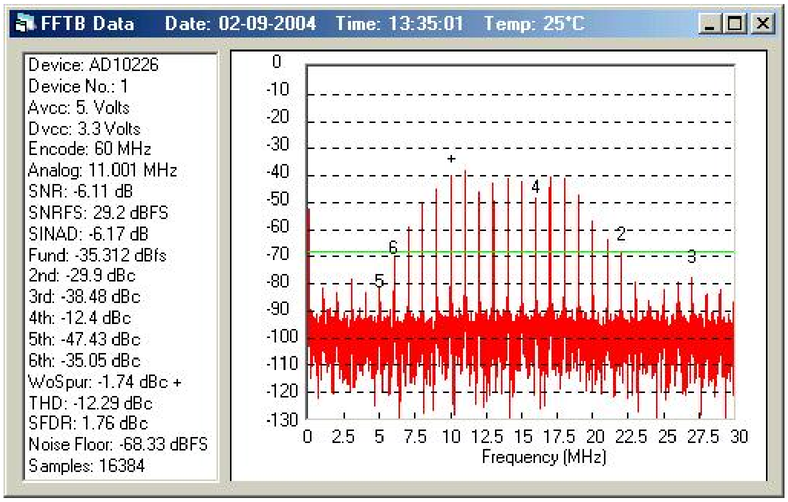

FFTB Data Date: 02-09-2004 Time: 13:35:01 Temp: 25°C

Device: AD10226
Device No.: 1
Avcc: 5. Volts
Dvcc: 3.3 Volts
Encode: 60 MHz
Analog: 11.001 MHz
SNR: -6.11 dB
SNRFS: 29.2 dBFS
SINAD: -6.17 dB
Fund: -35.312 dBfs
2nd: -29.9 dBc
3rd: -38.48 dBc
4th: -12.4 dBc
5th: -47.43 dBc
6th: -35.05 dBc
WoSpur: -1.74 dBc +
THD: -12.29 dBc
SFDR: 1.76 dBc
Noise Floor: -68.33 dBFS
Samples: 16384

Figure 2.3: Received spectrum as viewed on Analog Devices ADC Analyzer software post-sub sampling, with the center frequency of 2.442 GHz mixed down to 14 MHz.

2.5.2 Experimental Setup

2.5.2.1 In Room Configurations

Experiments were conducted on the third floor of EBU2, an engineering building at the University of California, San Diego campus. An illustration of the measurement areas are shown in Figures 2.4 and 2.5. Two measurement scenarios were investigated. In the first scenario, measurements were made with the transmitter and receiver both within a laboratory. For this scenario, a line-of-sight (LOS) path exists between transmitter and receiver. In the second, the receiver remained in the laboratory, and the transmitter was located in a hallway adjoining the room. This transmission scenario is non-line-of-sight (NLOS).

The construction type of the building consists largely of reinforced concrete, with plasterboard on the interior walls. The lab itself contains waist-high lab tables, computer workstations, laboratory equipment, and metal storage lockers.

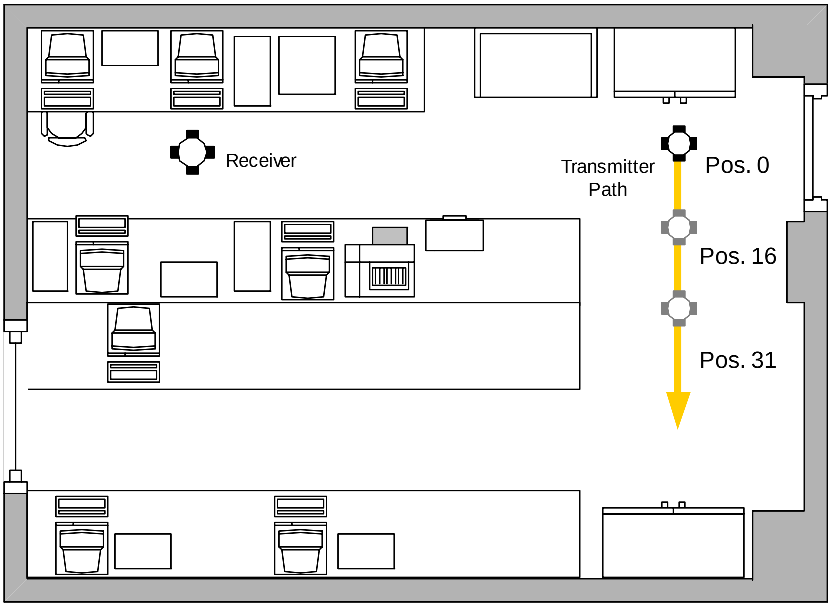

Figure 2.4: Interior layout of EBU2 Room 333B, 30' x 23' and example spatial correlation measurement configuration of receiver and transmitter.

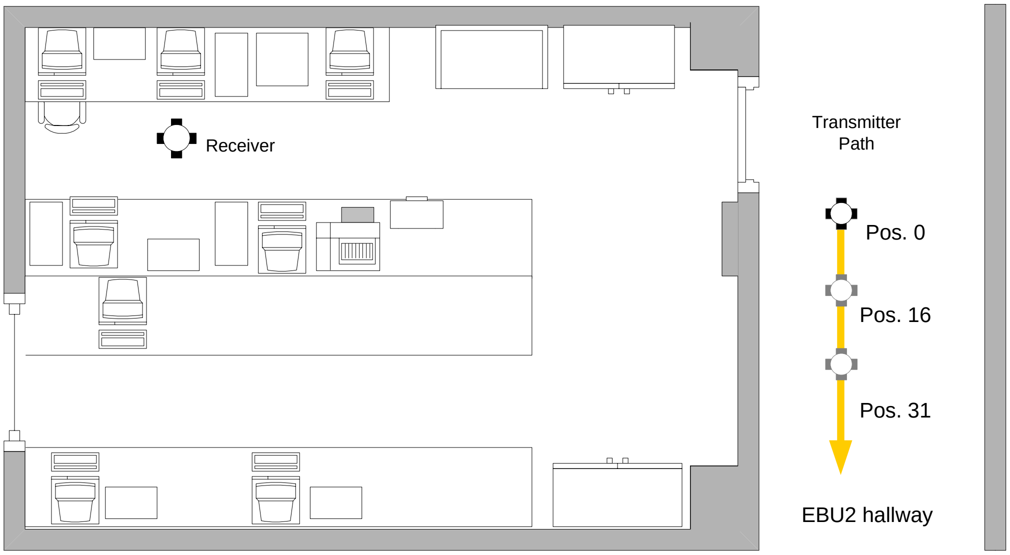

Figure 2.5: Interior layout of EBU2 Room 333B, 30' x 23' and spatial correlation measurement configuration of receiver and transmitter for the Indoor-Hallway scenario.

2.5.2.2 Outdoor Configurations

Outdoor experiments were conducted in areas surrounding the same engineering building. Two outdoor measurement scenarios were investigated. For the first scenario, the transmitter and receiver were placed parallel to an exterior wall of the building. The configuration can be seen in Figure 2.6.

For the second scenario, the transmitter and receiver were placed between two engineering buildings, EBU2 and EBU3B, in an open courtyard area. The configuration can be seen in Figure 2.7. The geometries selected in both outdoor scenarios had a LOS path between the transmitter and receiver.

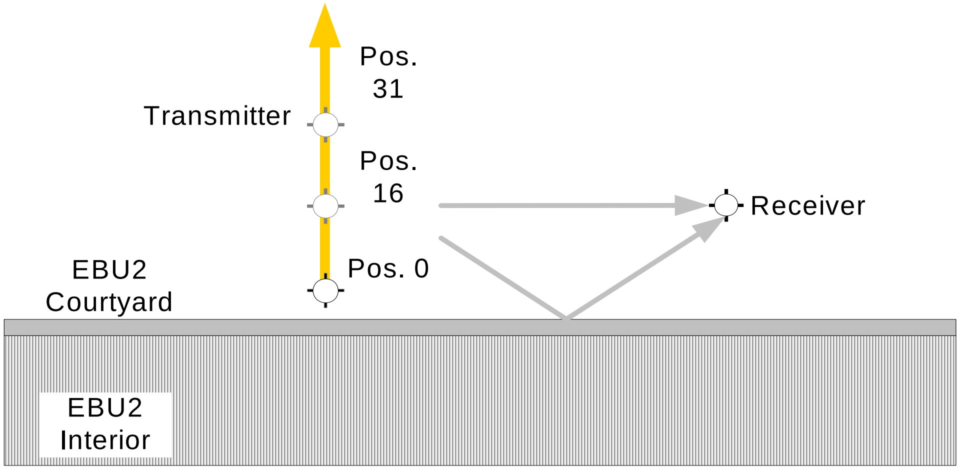

Figure 2.6: Array geometry for the 1st outdoor experiment. The transmitter and receiver are 20.2 feet apart. Position 0 is 11.5 feet from the wall and the receiver is 11.75 feet from the wall.

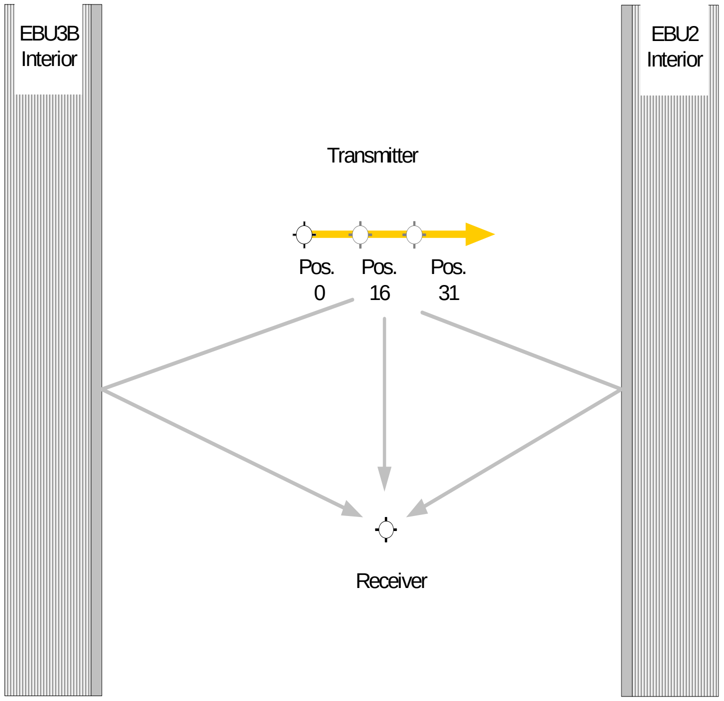

Figure 2.7: Array geometry for the 2nd outdoor experiment. The receiver and transmitter are 20 feet apart and the receiver is 41.4 feet from EBU2 and 42.7 feet from EBU3B/

2.5.3 Correlation results

2.5.3.1 Correlation computation

For determining the correlation coefficient, measurements were taken along a linear track, and 32k samples were taken at f_s = 60 MHz at each of 32 transmitter positions. The transmitter was moved transversely along a linear track relative to the receiver. Data was collected every 8 centimeters along the track.

Correlation of the received power at a particular tonal frequency in the transmitted comb can be investigated by correlating the magnitude squared values of the FFT of the incoming time sequence. Consequently, the time series data was processed, and the magnitude squared of the FFT retained for the central 13 frequencies. The correlation coefficient was calculated from the series of power measurements generated from this process using (2.2).

Spatial correlation versus interelement spacing was determined for each of the frequencies investigated. The correlation coefficient was computed for each of 20 interelement receiver antenna spacings, ranging from 0.25 to 2.5λ in 0.125λ steps, where λ is 12.3 centimeters. The transmitter antenna was moved to different positions, generating different multipath structure at the receiver antennas. From the series of measurements at each position, the correlation coefficient between the powers on the two receive antennas was calculated.

2.5.3.2 Indoor Correlation Results

2.5.3.2.1 In-Room Transmission Results

A typical received power sequence between the two antennas at each transmitter location for a particular data run is shown in Figure 2.8, with receiver antenna interelement spacing of 0.5λ. Clearly, the two antennas experience different environments due to the in-room multipath. Position 4 and Position 22 show two locations where one antenna has substantially larger received signal power than the other

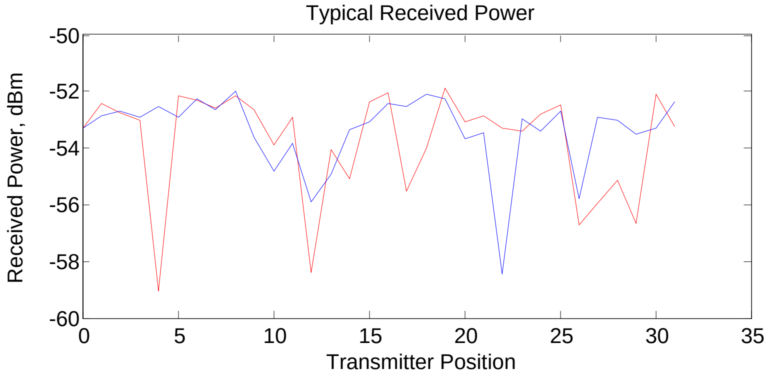

Figure 2.8: Typical received power sequence along the 32 position data track as seen by each of the receiver antennas with the antennas separated by 0.5λ.

antenna. A spatial diversity technique, such as switched diversity, or maximal ratio combining, would be especially useful at these locations for maintaining a high SNR and low outage rate in the communication system.

First, we examine the effects of spatial correlation at a single frequency for different interelement spacings. The correlation was determined for each of 20 interlement receiver antenna spacings, ranging from 0.25 to 2.5λ in 0.125λ steps. The correlation coefficient versus interelement spacing for the center comb frequency, 2.442 GHz, is reported in Figure 2.9. Correlation rapidly decreases between the two receive antennas as the interelement spacing increases, remaining below 0.5 for spacings larger than 0.5λ.

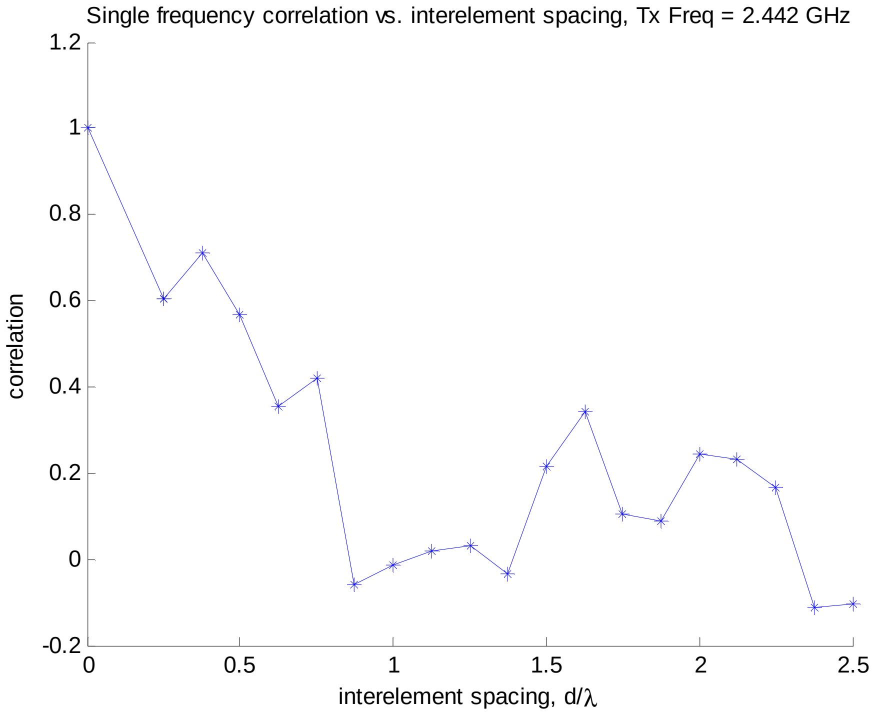

Figure 2.9: Correlation versus interelement receiver antenna spacing for a CW tone transmitted at 2.442 GHz.

The correlation curve has a sinc function-like structure. This structure is not unexpected, and will be investigated more in Section 2.5.3.2.3. Intuitively, as the interelement spacings get larger, the signals are subjected to more dissimilar environments.

Additionally, the in-room correlation was explored across frequency for the interelement spacings. The correlation results for interelement spacings of 0.25, 0.5 and 2λ are shown in Figure 2.10. As expected from both intuition and previous results, the correlation, in general, decreases as the spacing between antenna elements increases. Note that the correlation varies slightly between the different transmit frequencies. This effect shall be addressed later. For interelement spacings exceeding half a wavelength, the correlation coefficient drops to below 0.5. This result indicates that diversity combining techniques would be effective in this environment.

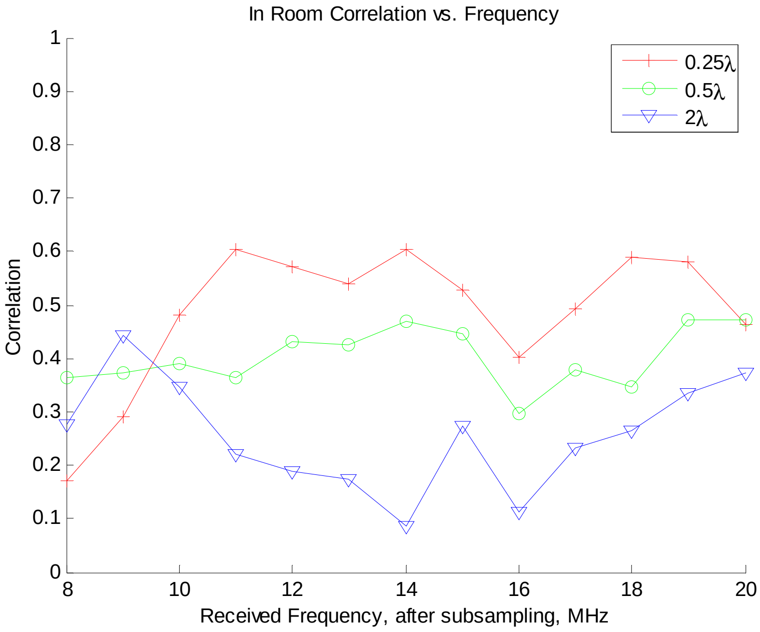

Figure 2.10: In-room correlation results for receiver antenna interelement spacings of 0.25, 0.5, and 2λ.

2.5.3.2.2 Hallway to Room Results

The spatial correlation coefficient was investigated with the receiver in the room and the transmitter placed in an outdoor open-ended hallway. As with the previous measurement scenario, the effect of the interelement spacing on spatial correlation was investigated for a single frequency. The correlation coefficient versus interelement spacing for the center comb frequency, 2.442 GHz, is reported in Figure 2.11.

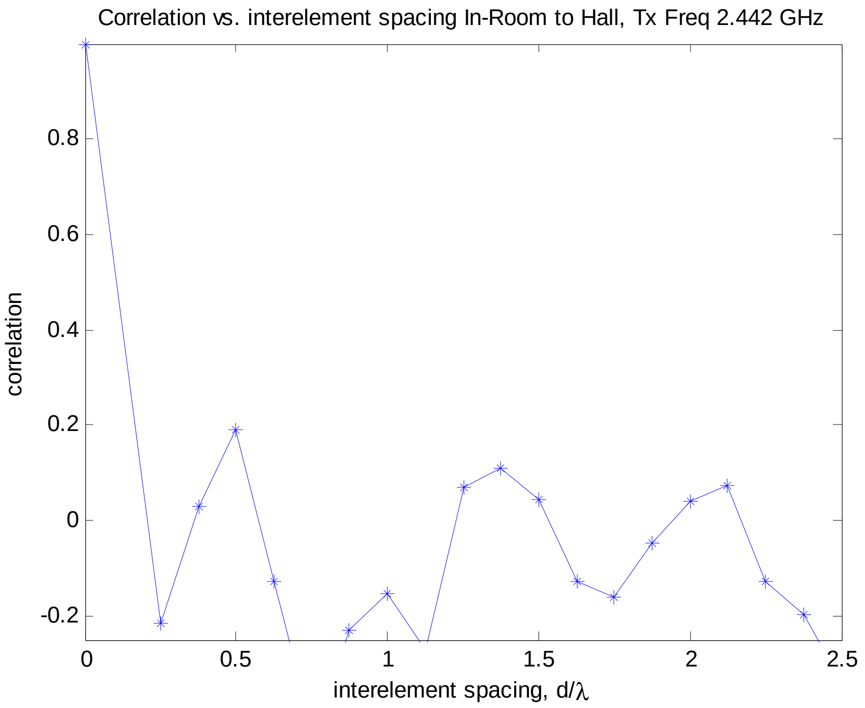

Figure 2.11: Correlation versus interelement receiver antenna spacing for a CW tone transmitted at 2.442 GHz.

The in-room to hallway correlation results for interelement spacings of 0.25, 0.5, and 2λ are shown in Figure 2.12. As with the single frequency case, since there is no direct path between the transmitter and receiver, which are separated by a wall, the correlation coefficient is expected to be lower. This expectation arises as additional scattering will occur, causing the multipath environment to be richer. The reduction in correlation for equivalent interelement antenna spacings is apparent between Figures 2.10 and 2.12. The correlation coefficient is below 0.5, on average, for all interelement spacings investigated, 0.25λ and above.

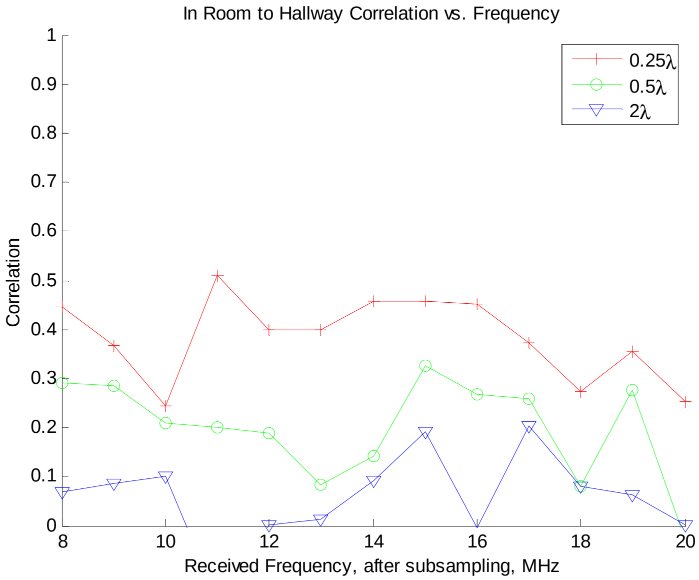

Figure 2.12: Room to hallway correlation results for receiver interelement spacings of 0.25, 0.5, and 2λ.

2.5.3.2.3 Correlation as a Function of Interelement Spacing

To better understand the measured results, consider a plane wave signal arriving from angle θ at a linear array of uniformly-spaced antennas separated by distance, d. If the message sent has unit power, then for two neighboring antennas, the received streams r_1 and r_2 are related according to:

$$E_t\{r_1(t)r_2^*(t)\}=e^{j2\pi\frac{d}{\lambda}\sin\theta} \tag{2.7}$$

If signals arriving at the antenna can be described as a sum of plane waves, and the distribution of the angles of arrival is known, we can determine the correlation function using:

$$\rho(d)=\int \exp\left\{ j2\pi\frac{d}{\lambda}\sin\theta \right\} p_\theta(\theta)d\theta \tag{2.8}$$

A common assumption for the distribution of the angles of arrival is the uniform distribution:

$$p_\theta(\theta)=\frac{1}{2\Delta} \qquad \textit{where} \quad \phi-\Delta\le\theta\le\phi+\Delta \tag{2.9}$$

Subsitituting (2.9) into (2.8), we arrive at:

$$\begin{aligned}\rho(d)&=\frac{1}{2\Delta}\int_{\phi-\Delta}^{\phi+\Delta}\exp\left\{ j2\pi\frac{d}{\lambda}\sin\theta \right\} d\theta\\ &=\frac{1}{2\Delta}\int_{-\Delta}^{\Delta}\exp\left\{ j2\pi\frac{d}{\lambda}\sin(x+\phi) \right\} dx\\ &=\frac{1}{2\Delta}\int_{-\Delta}^{\Delta}\exp\left\{ j2\pi\frac{d}{\lambda}\left(\sin(x)\cos(\phi)+\cos(x)\sin(\phi)\right) \right\} dx\end{aligned} \tag{2.10}$$

For small Δ, the small angle approximations cos(x) = 1, sin(x) = x can be applied:

$$\begin{aligned}\rho(d)&=\frac{1}{2\Delta}\int_{-\Delta}^{\Delta}\exp\left\{ j2\pi\frac{d}{\lambda}\left(x\cos(\phi)+\sin(\phi)\right) \right\} dx\\ &=\frac{1}{2\Delta}\exp\left\{ j2\pi\frac{d}{\lambda}\sin(\phi) \right\}\int_{-\Delta}^{\Delta}\exp\left\{ j2\pi\frac{d}{\lambda}x\cos(\phi) \right\} dx\\ &=\frac{1}{2\Delta}\exp\left\{ j2\pi\frac{d}{\lambda}\sin(\phi) \right\}\mathrm{sinc}\left(2\pi\Delta\frac{d}{\lambda}\cos(\phi) \right)\end{aligned} \tag{2.11}$$

For signals arriving uniformly from a small range of angles, the correlation function has a sinc characteristic, decreasing in magnitude as the interelement spacing, d, increases. Although the general expression in (2.7) has to be altered to describe the power correlation, the result given in (2.11) shows that the envelope correlation function decreases, as a general trend, in magnitude as the interelement spacing increases. Additionally, due to the sinc structure, low correlation values may be found at small wavelengths. Similar behavior was observed in Fig. 2.9 at approximately 1λ and in Fig. 2.11 at 0.25 and at 0.875λ.

2.5.3.2.4 In-Room Power Maps

Power maps were generated to investigate the environment surrounding the receiver. The maps for the two indoor measurement scenarios are shown in Figure 2.13.

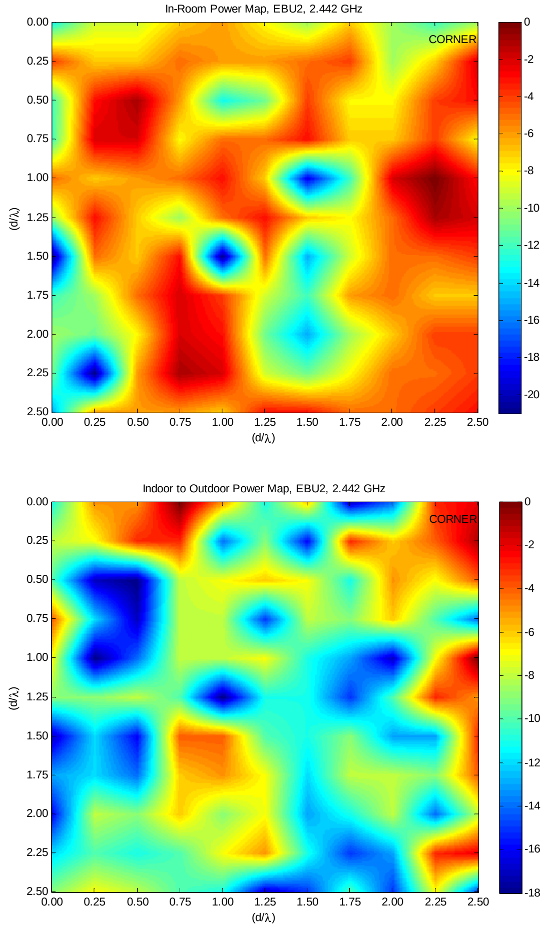

Fig. 2.13 In-Room (Top) and In-Room to Hallway (Bottom) received power maps.

High and low received power levels caused by multipath interference are seen. To orient the maps shown within the room seen in Figure 2.5, the point on the map closest to the corner of the room nearest the receiver has been indicated. These maps highlight the usefulness of spatial diversity, showing how small changes in antenna position can cause an impact upwards of 10 dB in the received signal power. The maps were both generated from data taken at Position 16 on the respective transmitter tracks for the two cases. Note that the NLOS in-room to hallway geometry has a richer multipath structure than the in-room case.

Additionally, power maps at different frequencies were examined. The power maps for three of the frequencies in the transmitted comb are shown in Figure 2.14, taken from the in-room data measured at transmitter antenna position 31. This position corresponds to the end of the track for the correlation measurements. Furthermore, these maps illustrate the potential value of taking advantage of frequency diversity. For the maps of frequencies separated by 1 MHz, it is easy to see that the correlation between frequencies is high by visual inspection of the power maps. However, with 6 MHz of separation between frequencies, a significant amount of decorrelation can be seen. The correlation coefficient between frequencies separated by at least 6 MHz has been shown in a previous set of measurements to be less than 0.5. This data is encouraging as it shows there can be significant gain by employing frequency diversity in ISM transmissions.

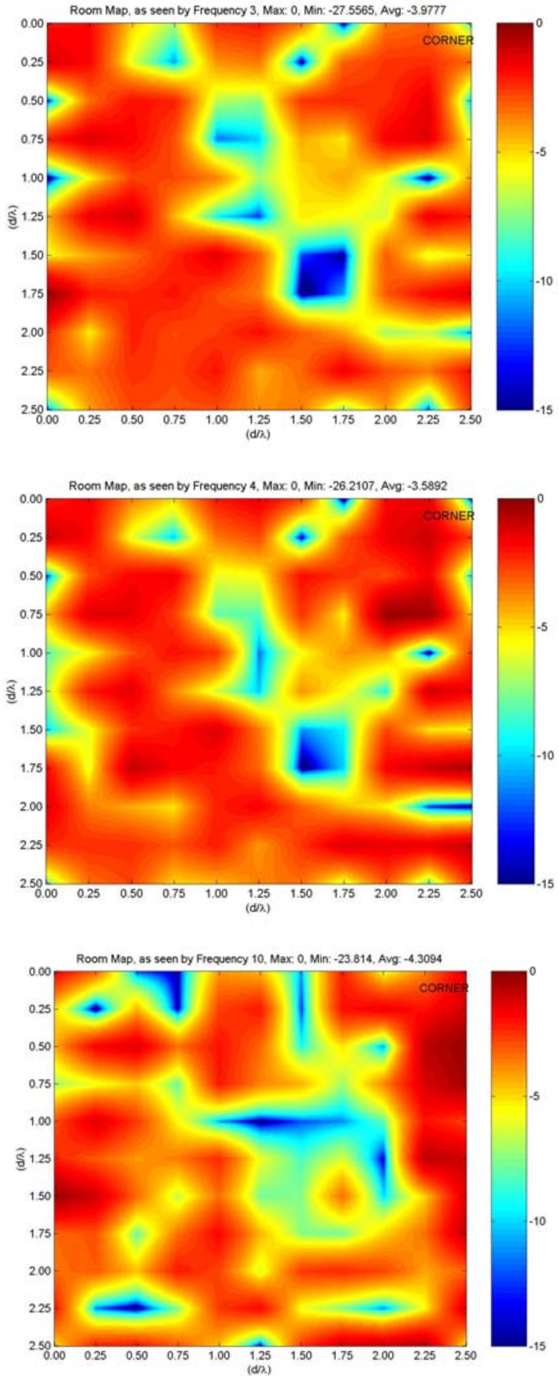
Room Map, as seen by Frequency 3, Max: 0, Min: -27.5565, Avg: -3.9777

Room Map, as seen by Frequency 4, Max: 0, Min: -26.2107, Avg: -3.5892

Room Map, as seen by Frequency 10, Max: 0, Min: -23.814, Avg: -4.3094

Figure 2.14: Two-dimensional received power (dB) maps at transmitter position 31. Top - Received power for one of the comb frequencies, Middle - Received power for the comb frequency 1 MHz away, and Bottom- Received power for the comb frequency 6 MHz further away.

2.5.3.3 Outdoor Correlation Results

2.5.3.3.1 Outdoor Transmission Near Wall Results

The transmitter and receiver were aligned along a wall in the EBU2 courtyard. The correlation coefficient results are shown in Figure 2.15. In this configuration with the close proximity to the wall, all other courtyard walls are a significant distance away, relative to the distance between transmitter and receiver. This results in a strong LOS path and a wall-bounce path of similar strength between the transmitter and receiver. Due to the selection of this geometry, higher correlation values, which exceed 0.5 for some frequencies, were noted at around 1.5λ.

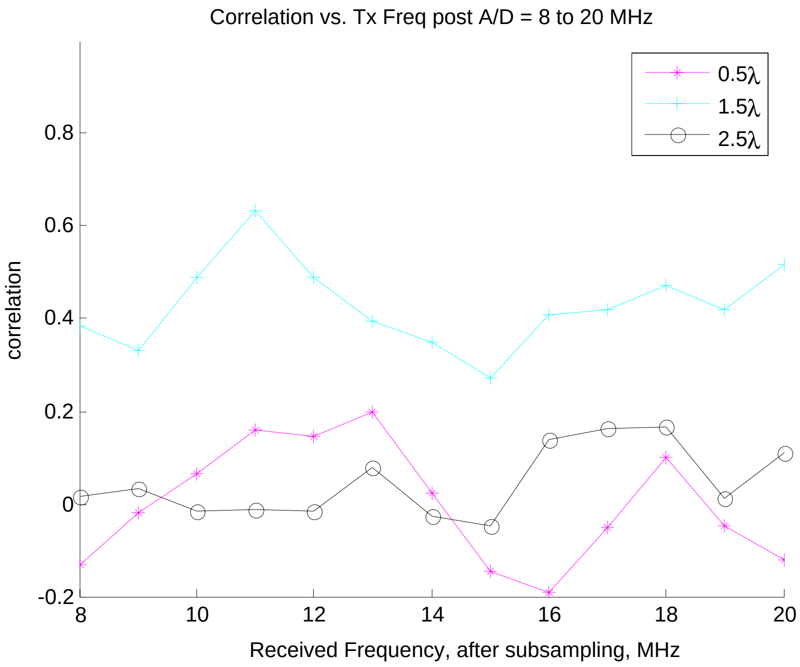

Figure 2.15: Outdoor correlation results with the transmitter and receiver aligned along an exterior wall for interelement spacings of 0.5, 1.5, and 2.5λ.

2.5.3.3.2 Outdoor Transmission In-Between Buildings Results

The transmitter and receiver were placed in an open area, bordered by two engineering buildings on either side. The correlation coefficient results are shown in Figure 2.16. In this configuration, the walls are not in close proximity, relative to the distance between the transmitter and receiver. Due to this geometry, the LOS path dominates the received signal. The correlation results were considerably higher than in either of the previously reported cases. The antennas had to be separated by more than 1.5λ for the correlation coefficient to drop below 0.5 for all frequencies investigated in the transmitted comb.

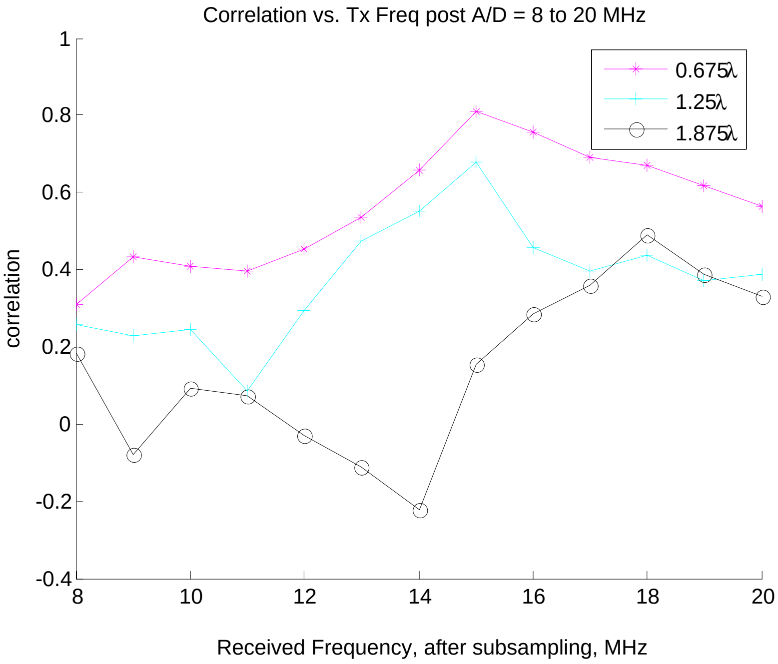

Figure 2.16: Outdoor correlation results with the transmitter and receiver in-between two buildings for interelement spacings of 0.5, 1.5, and 2.5λ.

2.5.3.3.3 Outdoor Power Maps

As with the indoor transmission scenarios, power maps showing the received power in the environment surrounding the receiver were made by stepping a single receive antenna through a repeatable wooden grid. The received power at each grid location was recorded and linearly interpolated between grid points to form a smooth surface.

The resulting power maps for a 2.442 GHz tone are shown in Figure 2.17. In the top figure, the map was taken in the receiver location near the EBU2 wall in the outdoor transmission scenario. Clear bands of high and low received power values caused by multipath interference are seen. This banded structure arises primarily from the interference of the previously mentioned LOS and wall bounce paths. Furthermore, the banded nature emphasizes a lack of multipath richness in this transmission scenario.

In contrast, a power map for the indoor scenario in which both transmitter and receiver were in the same room is shown in the bottom figure. This map highlights the usefulness of spatial diversity. Small changes in position can result in significant changes in the received power and surrounding field. In this case, a few centimeters could result in a 15 dB change in the received power. The structure in this field is richer, due to scatterers (lab equipment, tables, walls, etc.) surrounding the transmitter and receiver.

Bridging these two scenarios is the second outdoor scenario in which the transmitter was placed between two buildings. The power map for this scenario is shown in Figure 2.17, middle. The increase in the number of dominant scattering paths lends to a richer multipath structure than in the other outdoor scenario. However, the difference between the highest and lowest measured received powers is smaller. As mentioned earlier, this occurs as reflection paths from buildings are significantly longer than the LOS path.

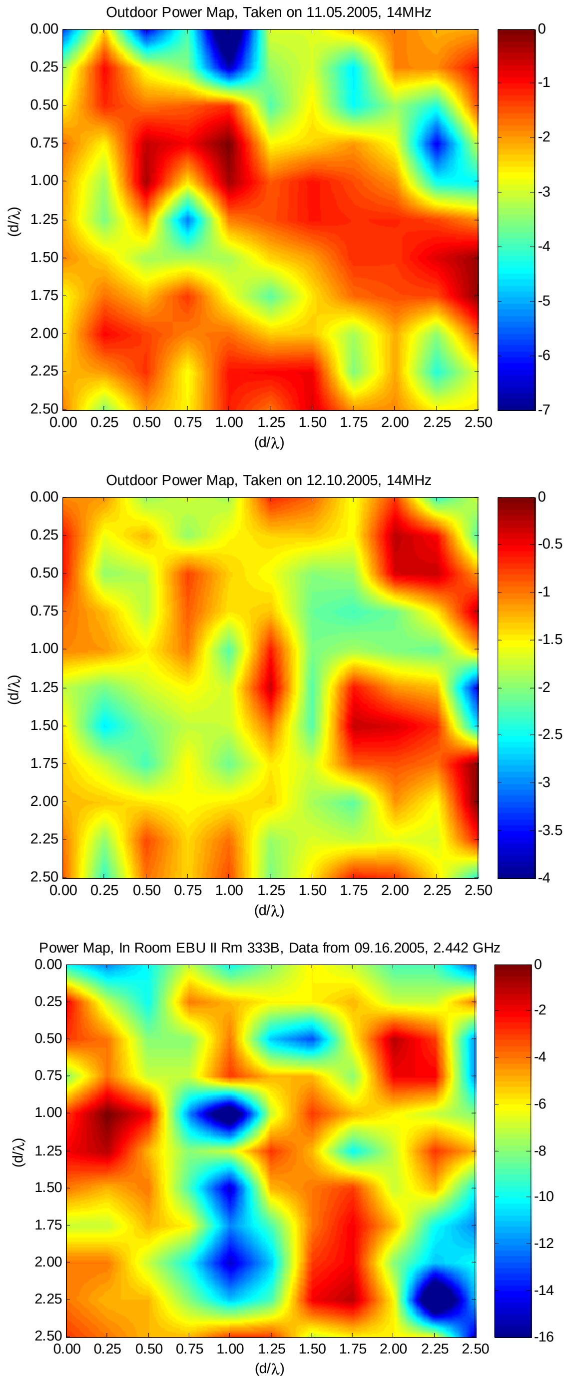

Figure 2.17: Received Power (dB) in the area surrounding the receiver. Top – Outdoor scenario, in which transmitter and receiver are near a wall. Middle – Outdoor scenario in which transmitter and receiver are between buildings. Bottom – Indoor scenario in which both transmitter and receiver are in the same room.

2.5.4 Modeling the Environment

When a signal is transmitted, radiation spreads as the signal propagates away from the source. Although spreading occurs, it is often possible to approximate the signal's trajectory as if it was a straight line, or a ray. By following the rays from the transmitter when the environmental geometry is known, the received signal can be reassembled through superposition at the receiver. This methodology, originating from the field of geometrical optics, provides a means of predicting the signal power at the receiver.

The increasing popularity of indoor wireless communications has increased the need for modeling the wireless channel. Numerous ray tracing algorithms can be found in literature, each with different estimation and prediction capabilities. In [19], a two dimensional ray tracing algorithm is proposed for predicting the received power, and hence coverage, in an indoor environment. In [20], the path loss is modeled using methods to select the most significant rays. A subset of additional ray tracing algorithms with more complex modeling criteria have been explored in [21-23].

By applying basic two dimensional ray-tracing techniques it is possible to predict the power at a receiver. These predictive results are compared with real-life power measurements for two simple outdoor transmission scenarios. In this first scenario, a single wall is considered. In the second, the transmitter and receiver are placed between two buildings to generate a parallel two-wall transmission scenario. Additionally, a directional antenna was used to measure the received power as a function of arrival angle. These directional measurements allow for the determination of potential strong bounce paths, and assist in verifying the usefulness of the ray-tracing methods.

2.5.4.1 Geometrical Optics

Two primary phenomena of concern in geometrical optics are the principles of reflection and refraction. When a transmitted signal encounters a plane surface, part of the signal is reflected, forming a beam that bounces off the incident surface. The other part of the signal is refracted, passing through the medium it encountered, often changing the signal's direction of travel. Let the following notation be defined:

θ_1 = angle of incidence
θ'_1 = angle of reflection
θ_2 = angle of refraction

Note that in geometrical optics, all angles are measured from the normal of the incident plane. It is a well known law of reflection that the angle of incidence is equal to the angle of reflection, $\theta_1 = \theta'_1$. These phenomena are illustrated in Figure 2.18.

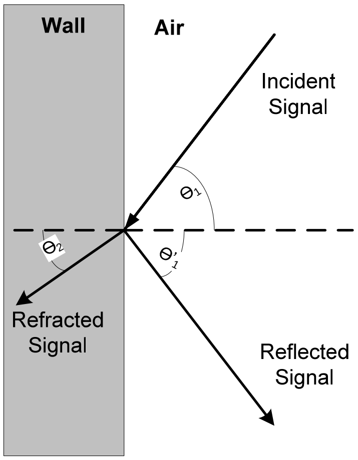

Figure 2.18: Illustration of signal incident on a wall; refracted and reflected rays shown, where $\theta_1 = \theta'_1$.

2.5.4.2 Outdoor Transmitter/Receiver Scenarios

2.5.4.2.1 Single Bounce Path

Several different outdoor transmitter and receiver geometries are explored. For the first scenario of interest, a simple configuration was selected. In this case, a single wall bounce path is considered. A LOS path is present between the transmitter and receiver.

To compute the power of the signal at the receiver, the path lengths of all rays must be determined, which in turn allows for the computation of the phase difference between the paths. Thus, a basic ray-tracing model can easily account for both phase difference at the receiver, as well as path loss. The path loss is computed relative to the LOS path between transmitter and receiver. To find the wall bounce path length, the point where the wall and the incident ray meet can be determined. This computation is performed using the law of reflection by considering similar triangles formed by a single bounce path. Let the following notation be used:

x_t = distance between the transmit antenna and wall
x_r = distance between the receiver antenna and wall
y = distance between transmitter and receiver
y_{rb} = distance between receiver and bounce location
y_{bt} = distance between bounce location and transmitter

The geometry of the arrangement between the transmitter and receiver can be seen in Figure 2.19.

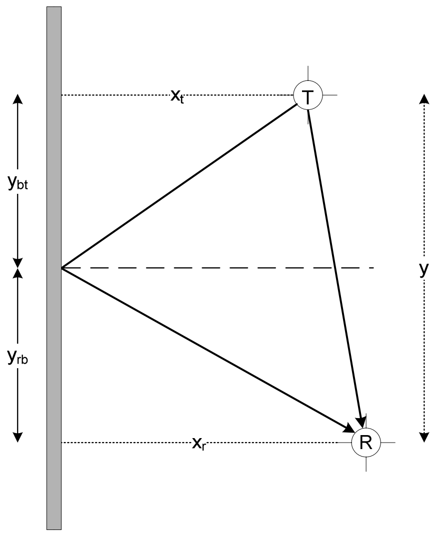

Figure 2.19: Simple one bounce path and LOS path receiver and transmitter geometry, with corresponding notation.

To determine the path length of the bounce path, note that similar right triangles are formed in Figure 2.19 between the wall and the bounce path. Assuming the distances x_t, x_r and y are known, the following relation holds:

$$\frac{x_t}{x_r} = \frac{y_{bt}}{y_{rb}} \tag{2.12}$$

Since $y_{bt} = y - y_{rb}$, by substitution and rearrangement of the equation, we can solve for y_{rb}:

$$y_{rb} = \frac{y x_r}{(x_t + x_r)} \tag{2.13}$$

Indexing from the left bottom corner as the origin, we can now give the coordinates of the bounce point, B_p, the receiver antenna, Rx, and the transmitter antenna, Tx, as $(0, y_{rb})$, $(x_r, 0)$, and (x_t, y) respectively. By determining the bounce point, the LOS and bounce paths can easily be computed using the standard distance formula. Furthermore, with the path lengths determined, the relative path delay between the LOS and bounce paths can be computed. Since amplitude is proportional to the inverse of distance traveled, under a spherical spreading assumption, the path lengths also allow for scaling the amplitude of the arriving time series.

If we further assume reflection occurs perfectly—that is all incident energy is reflected, it is possible to create a two dimensional approximation of the received power in an area with just the information at hand. To do this, the transmitter shall remain fixed, and the receiver position will be stepped in the x and y directions every half a wavelength, where the carrier frequency is assumed to be 2.442 GHz, resulting in 0.5λ = 6.2 centimeters. The direction of stepping will be toward the wall in the x direction, and toward the transmitter in the y direction.

The values used in the theoretical computation are given in Table 2.1.

Table 2.1: Parameters used for the theoretical received power computation

	distance (meters)
x_r	3.56
x_t	3.64
y	6.15

From these values, we can compute the approximate angle of arrival at the receiver from the bounce path by first computing y_{rb} from (2.13) to be 3.04 meters. With two sides of the triangle known, the angle can then be computed to be approximately 50 degrees from the y axis.

To generate a situation with a single, primary bounce path in addition to the LOS path, an outdoor transmission scenario was selected along the wall of a building. For this experiment, a wall along the EBU2 courtyard was selected, as in Figure 2.6. This location was selected mainly due to its proximity to lab, as well as the availability of electrical power.

The EBU2 building is constructed from reinforced concrete blocks. Additionally, there are large windows in the wall, as that portion of the building consists primarily of office space. A planter box exists at the base of the windows, below the transmitter and receiver heights. As such, its presence is ignored for the 2D ray-tracing computations. The transmitter and receiver were oriented along the left wall with the receiver in the foreground, as indicated in Figure 2.19. A photograph of the area used for the experiment is shown in Figure 2.20.

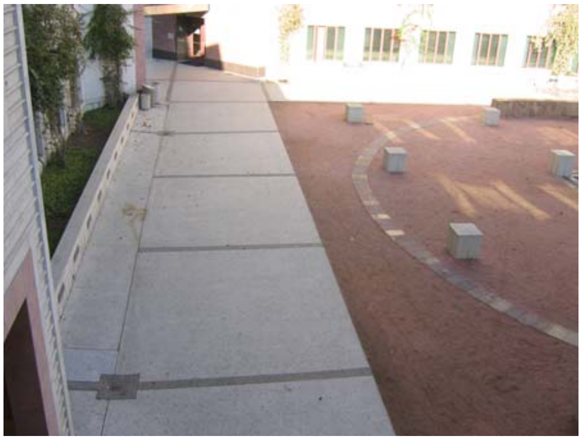

Figure 2.20: EBU2 Courtyard data location; Transmitter/Receiver axis aligned parallel with left wall.

Received power was also measured using a directional antenna in place of the omnidirectional receiving antenna. For this, a Yagi antenna, HG2412Y was used as the receiving antenna and a Wincomm omnidirectional 2.4 GHz antenna was used as the transmitting antenna. The Yagi antenna was rotated on its axis to measure the power received in all directions. A measurement was made every five degrees. This procedure confirms the angle of arrival of strong bounce paths originating from the wall. Power measurements were made using a HP8565 spectrum analyzer, and were normalized to the highest received power.

To make the two dimensional power map, an 11 x 11 grid of measurements were taken with x and y direction interelement spacings of $\lambda/2$ (6.2 centimeters). Interpolation in post-processing generates the smooth surface with a comparable number of points to the theoretical data. A Wincomm omnidirectional antenna was used at both the transmitter and receiver locations. Measurements were made by collecting time series data with a dual channel receiver, and then post-processing the data as described in Section 2.5.1. Power levels are reported normalized to the highest received power. With respect to the receiver setup, the (0, 0) coordinate indicates the southeast corner of the wooden positioner system. Orienting this with respect to the environment, the (0, 0) coordinate is the farthest from the parallel wall and the transmitter.

The results of the theoretical power map computations and the map created from measured data taken in the courtyard are presented in Figure 2.21. Note that transmission through the wall occurs in the real-life case, as well as other bounce paths are present. These factors result in a richer field than the theoretical case can predict with its simplistic assumptions. However, the underlying structure with bands of high and low power due to multipath interference is very similar between the two plots.

Furthermore, the results of the directional power measurements taken with a directional Yagi antenna are shown in Figure 2.22. The y-axis direction indicated in Figure 2.22 is aligned at 0 degrees. The measured data indicates a strong bounce path in the direction of slightly more than 50 degrees from the y-axis. This result is in good agreement with the earlier computations. Note that the measured directional plots are presented in dB above noise floor. Also, note that the antenna pattern for the directional antenna has more than 20 dB of suppression between the mainlobe and sidelobes, giving confidence to the measurements since strong bounce paths a few dB down from the mainlobe will not be unduly influenced by sidelobe leakage [24].

Measured Outdoor Power Map, 2442MHz

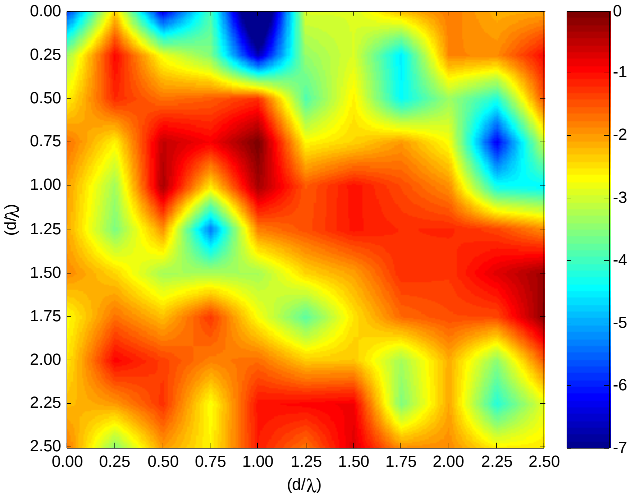

Simulated Outdoor Power Map, 2442MHz

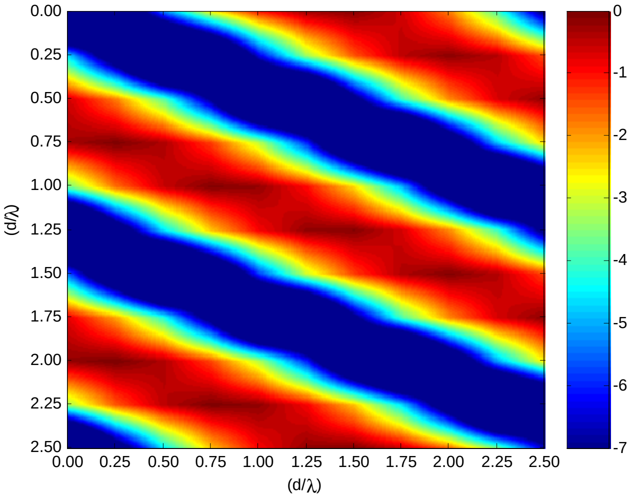

Figure 2.21: Top - Received power, taken in the EBU II courtyard. Bottom - Theoretical received power, considering a single bounce path and LOS path with no attenuation loss due to the wall bounce. Plots are reported in dB, normalized to the highest power value.

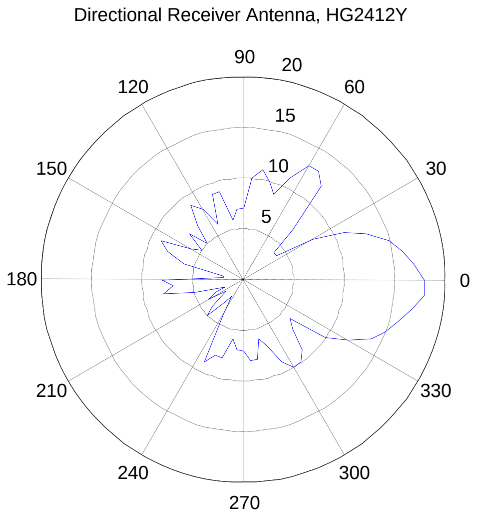

Figure 2.22: Received power, using a directional antenna as the receiving antenna.

2.5.4.2.2 *Two Bounce Paths*

The second case considered is one with two wall bounce paths in addition to the LOS path. That is, we consider a case of transmission, such as between two buildings, where three primary signals will arrive at the receiver with at most one wall bounce per arriving ray. The environment is shown in Figure 2.23.

Figure 2.23: Outdoor environment surrounding the two bounce path scenario. The left building is EBU3B and the right is EBU2.

The location selected is between buildings EBU2 and EBU3B on the University of California, San Diego campus. An outdoor data set was taken over a weekend while students were on break to minimize the foot traffic in the area. As with the previously selected environment, this environment was selected due to the convenience of the location, as well as the convenience of outdoor electrical power. EBU3B is a newer building, consisting of a more open framework with large amounts of windowing. The side of EBU2 closest to the experiment consists primarily of reinforced concrete, with fewer windows.

The configuration of the transmitter and receiver, as well as the locations of the buildings, can be seen in Figure 2.24.

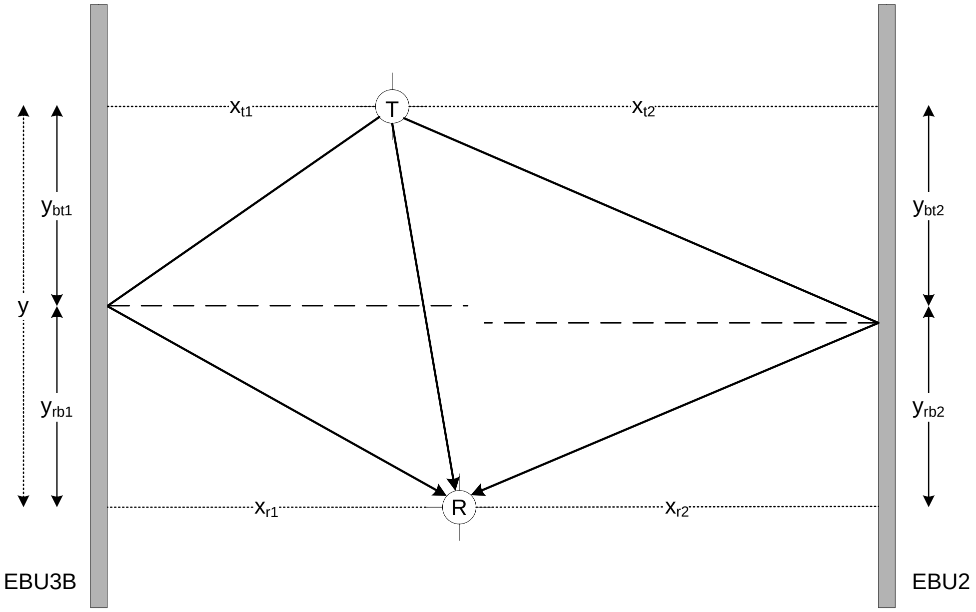

Figure 2.24: Geometry of transmitter, receiver and buildings for the second transmission scenario. A LOS path and a bounce path reflected from each building are considered in the model.

With the HG2412Y Yagi antenna, received power as a function of angle was measured using the same techniques as in the single-bounce scenario. The resulting power measurements are shown in Figure 2.25. Again as before, the y-axis aligns with 0 degrees. The exterior walls of EBU2 and EBU3B are located normal to the y-axis at 270 and 90 degrees, respectively.

By mathematical computation, a bounce path is expected from EBU3B at 77.5 degrees. Another bounce path is expected from the other building at 283.5 degrees. From Figure 2.25, it can be seen that rays are arriving with strong power from the expected directions. However, there are also additional paths with strong power, so it is expected that using only two bounce paths for modeling will not model the environment accurately.

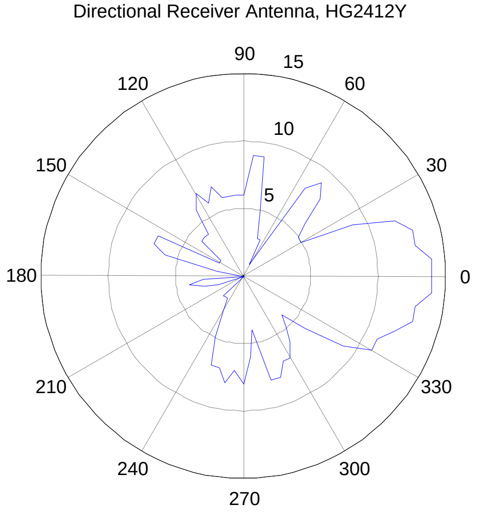

Figure 2.25: Received Power, as viewed by an HG2412Y Yagi antenna spun about its axis.

Using a similar technique as in the single bounce case, the received power map measured between the two buildings can be seen in Figure 2.26, top. This power map has more structure than the single bounce case, which is expected as the experiment location was selected to generate multiple bounce paths. A smaller range of received powers is also noted. This is primarily due to the buildings being farther away from the transmitter and receiver than in the single bounce case. Simulating the received power by ray tracing, and accounting for phase differences and relative path loss, results in the regular checkerboard pattern seen in Figure 2.26, middle.

Instead, if the directional plot is used to retrieve relative path loss and angle of arrival data, the predicted power throughout the two dimensional grid explored can be recomputed. By including a third bounce path at approximately 50 degrees, which can be noted in Figure 2.25, it is possible to more accurately model the area under investigation. This extra bounce path results from a half wall corresponding to an entrance ramp in front of EBU3B. To ensure a useful comparison, the non-LOS paths were constrained in both the two bounce path model and the three bounce path model to the same sum total power. These three bounce path results are presented in Figure 2.26, bottom. Note that the lower two plots in Figure 2.26 have larger dynamic ranges than the measured data. Since the model is simplistic, the discrepancy can arise from a variety of sources, such as from not accounting for transmission loss at the bounce location.

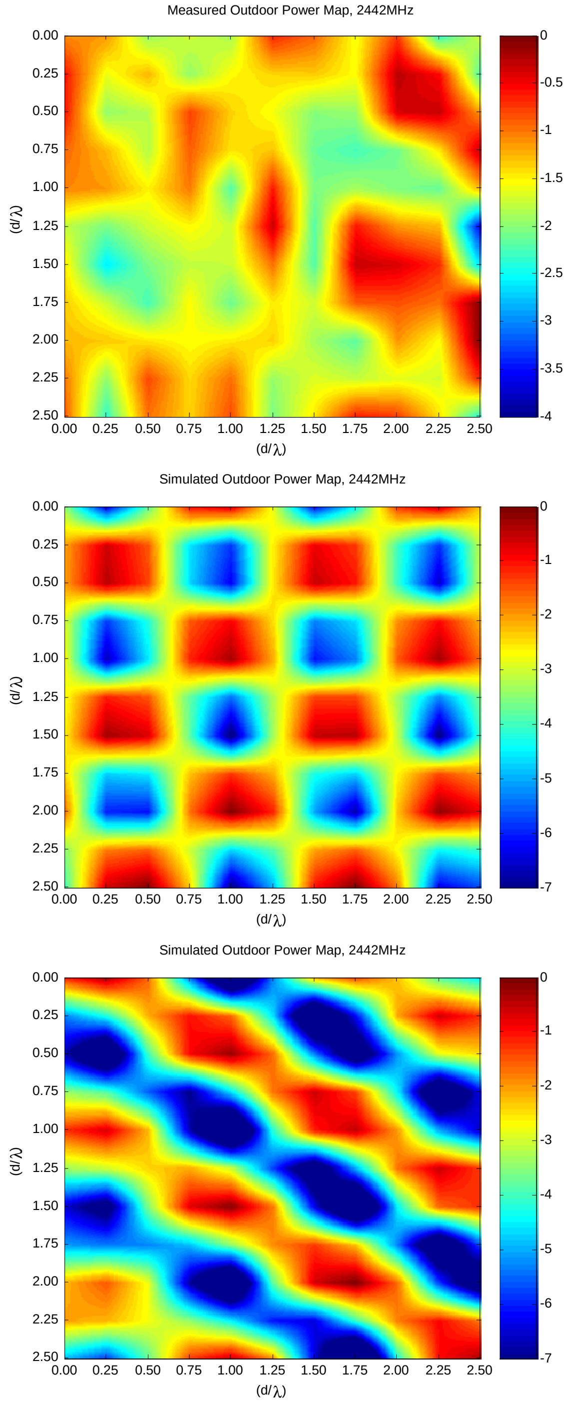

Figure 2.26: Top – Received power, as measured on a 2D grid between EBU2 and EBU3B on the University of California, San Diego campus. Middle – Simulated data through two bounce ray-tracing, middle. Bottom – Improved simulation using a third bounce path.

2.6 Effects of Mutual Coupling

When modeling communication systems at the physical level, a common simplification made is that the antennas do not influence each other. This assumption results in the use of independent pair-wise fading coefficients between transmit and receive antenna elements, which in turn can cause signal subspace techniques to fail [25, 26]. In instances where signal source detection is important, incorrect angles of arrival may be reported [27, 28]. Further, in terms of capacity, mutual coupling can alter the capacity of a MIMO system as it influences the spatial correlation [25, 29-31]. This section explores the effect of mutual coupling on the spatial correlation coefficient, offering insight into the effect of mutual coupling on the measurements made earlier in this chapter.

2.6.1 Mutual Coupling

When an electromagnetic wave arrives at an antenna element, a current is induced in the antenna. This current causes a re-radiation of the received energy. In turn, the re-radiated energy causes a surface current in nearby objects, including other antennas. Thus, the actual signal received in an indoor environment is a combination of the received multipaths and the re-radiated signals. The re-radiation effect is known as mutual coupling. In terms of voltages, this effect can be seen on the voltage induced at an element, V_{ind_i}, as a sum of the directly transmitted voltage, V_{tx}, and the voltage induced in the element from neighboring elements [25]. Denoting Z_{ij} as the mutual impedance between elements i and j, and I_j as the current induced at element j, V_{ind_i} is:

$$V_{ind_i} = V_{tx} - \sum_{j \neq i} I_j Z_{ij} \qquad (2.14)$$

Since there is additional current in the antenna, the received signals are affected. Thus, the statistics of the antenna and incoming signal are both altered. That is, mutual coupling changes antenna gain, beamwidth, pattern, and input impedance. It also changes the received signal distribution and the correlation between antennas.

There are several parameters which influence mutual coupling. The primary parameter that influences the severity of effects from mutual coupling is inter-element separation. To achieve minimal coupling, some studies have shown that half a wavelength of separation between antennas is sufficient, while others suggest that mutual coupling may not be insignificant until a wavelength of separation is achieved [25, 29-31]. In the case of large array systems, the geometry of the array affects the mutual coupling. In rectangular arrays, inner elements will be affected more by mutual coupling than outer elements. This occurs as the inner elements are surrounded by more antennas than the outer elements. Finally, objects in the environment surrounding the antennas affect the mutual coupling.

Although the work presented in [30] does not apply directly to the receiver setup used in the current investigation, as the antennas being used are not chip-based antennas, it is worthwhile to note that mutual coupling can be varied for these sorts of antennas in other ways. The materials for chip-based, or patch, antennas (thickness, type of substrate) also influence the effects of mutual coupling. Also, it is worthy to remark that since the pattern of the antenna is altered, sometimes the phenomenon of mutual coupling is discussed in literature as a form of pattern diversity.

2.6.2 Spatial Correlation and Mutual Coupling

Mutual coupling changes the magnitude of the directly transmitted incoming signals. Because the received signals are modified, so is the correlation between them. The effect of mutual coupling computed from theoretical results depends on the modeling assumptions, with angle of arrival playing a large role. In modeling MIMO systems, the effect is usually introduced into the model through a coupling matrix.

Let **y** denote the received vector, **H** denote the channel matrix, **C** denote the coupling matrix, and **x** the transmitted signal. Then in the presence of noise, **n**, the received vector **y** is given by:

$$\mathbf{y} = \mathbf{CHx} + \mathbf{n} \tag{2.15}$$

For this work, it assumed that **n** is spatially and temporally white additive Gaussian noise with zero mean and unit variance.

In general, the **H**-matrix is of a size determined by the number of received antennas by the number of transmit antennas, n_R x n_T; however, in the experimental data collection system being used, there is a single input and dual output. Thus, the channel matrix is of the form:

$$\mathbf{H} = \begin{pmatrix} h_{1,T} \\ h_{2,T} \end{pmatrix} \tag{2.16}$$

Let there be L scatterers in the field, each with attenuation factor, α_l. Assuming single bounce paths between the transmitter and the receiver, the channel parameter $h_{R,T}$ can be written as:

$$h_{R,T} = \sum_{l=1}^{L} \alpha_l \exp\left(-j \frac{2\pi}{\lambda} \cdot (d_{TS} + d_{SR}) \right) \tag{2.17}$$

where d_{TS} is the distance from the transmitter to scatterer *l* and d_{SR} is the distance from scatterer *l* to the receive element R. The values of α_l can be determined experimentally for a given scatterer. Alternatively, they can be modeled according to a statistical distribution. Commonly, these loss values are modeled as complex Gaussian random variables in simulations.

Note that the coupling matrix can be rewritten as:

$$\mathbf{C} = (\mathbf{Z_A} + \mathbf{Z_T})(\mathbf{Z} + \mathbf{Z_T}\mathbf{I})^{-1} \tag{2.18}$$

where $\mathbf{Z_A}$ is the antenna driving point impedance, $\mathbf{Z_T}$ is the measurement equipment impedance, and $\mathbf{Z}$ characterizes the mutual impedance [26].

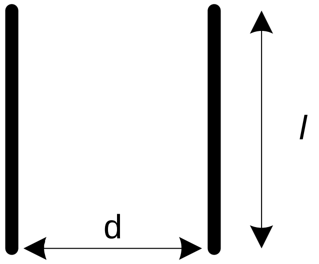

Figure 2.27: Dipole configuration of two identical, side by side elements for mutual impedance computation.

2.6.3 Simulating the Effects of Mutual Coupling for a SIMO system

Typically, it is difficult to obtain a closed form solution for $\mathbf{Z}$. However, in the case of two identical, thin dipoles of finite length, the expression for $\mathbf{Z}$ can be found in nearly any textbook on antennas. For the case of identical side-by-side dipole elements, separated by distance d with lengths *l* that are a multiple of $\lambda/2$, the closed form solution simplifies significantly, with the derivation shown in [25], and the results given in (2.19-2.21). The orientation of the antennas is illustrated in Figure 2.27. The following equations are in terms of the maximum current in antennas 1 and 2 in a SIMO system. Note that for a reciprocal network arrangement, $\mathbf{Z_{21}} = \mathbf{Z_{12}}$. The parameters, $\mathbf{Z_{11}}$ and $\mathbf{Z_{22}}$ are the free-space input impedances of antennas 1 and 2, as if no mutual impedance was present.

$$\mathbf{Z} = \mathbf{R} + j\mathbf{X} \tag{2.19}$$

$$R_{21} = \frac{\eta}{4\pi}\left[2C_i(u_0) - C_i(u_1) - C_i(u_2)\right] \tag{2.20}$$

$$X_{21} = -\frac{\eta}{4\pi}\left[2S_i(u_0) - S_i(u_1) - S_i(u_2)\right] \tag{2.21}$$

$$u_0 = kd$$
$$u_1 = k\left(\sqrt{d^2 + l^2} + l\right)$$
$$u_2 = k\left(\sqrt{d^2 + l^2} - l\right)$$

where $S_i(\mathrm{x})$ and $C_i(\mathrm{x})$ are the sine and cosine integrals defined by:

$$S_i(x) = \int_0^x \frac{\sin(\tau)}{\tau} d\tau$$

$$C_i(x) = -\int_{\mathrm{x}}^{\infty} \frac{\cos(\tau)}{\tau} d\tau$$

Using the above equations, in which Z_T is chosen as the complex conjugate of Z_A to minimize power loss, as noted in [31], the effect of mutual impedance on the correlation between channel coefficients was investigated for a SIMO system. For the simulation, a single transmit element and dual receive antennas, with identical λ/2-length dipole elements, is considered.

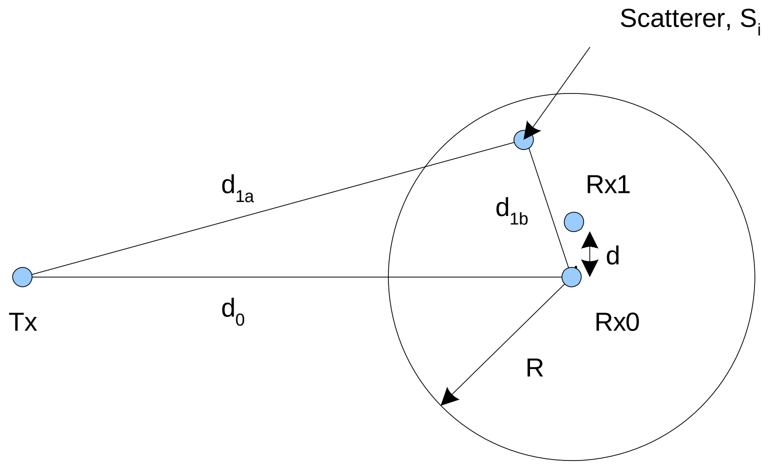

Figure 2.28: SIMO transmission geometry.

A simple channel model is used to generate the geometry of the channel. The model is similar to that found in [31] in which a uniform disc of scatterers is placed around the receiver. For the results shown, the radius of the disc is 200λ and L=100 scatterers are used. The scattering coefficient from scatterer S_i was modeled as a complex Gaussian random variable, with zero mean and unit variance. The geometry of the channel is shown in Figure 2.28.

To generate the statistics required to compute the correlation coefficient between receive antennas for both a mutual coupling and non-coupling case, 1000 channel realizations were created. A typical channel realization is shown in Figure 2.29.

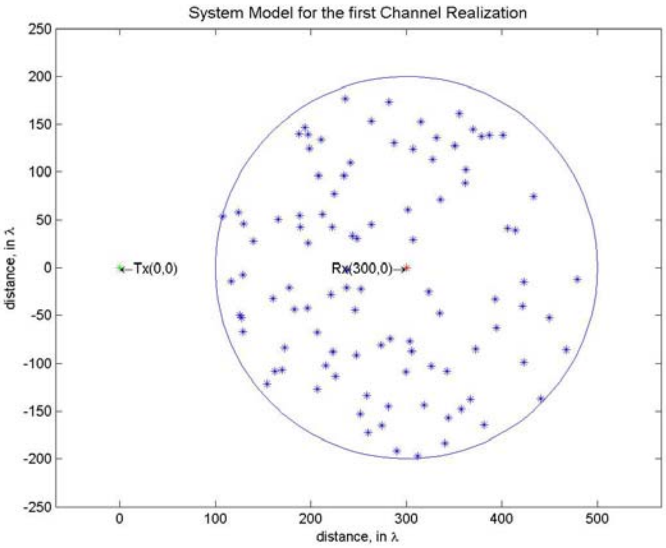

Figure 2.29: Typical channel realization.

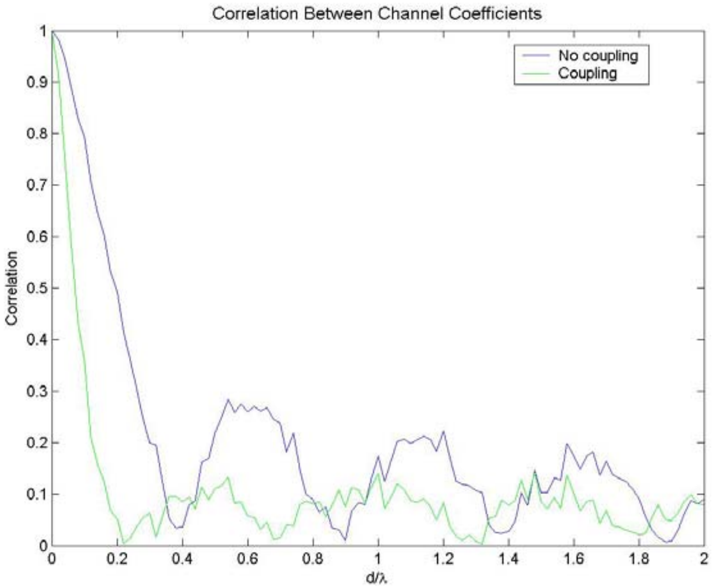

Figure 2.30: The effect of mutual coupling on the correlation, as a function of interelement spacing, between two receive element paths in a SIMO system.

The results of the simulation show that mutual coupling has a larger impact on the correlation between antennas for smaller interelement spacings. As such, when investigating the effects of spatial diversity experimentally, we can see that for smaller spacings, it is difficult to assert claims as to the usefulness of spatial diversity without considering the effects of mutual coupling. It is clear from Figure 2.30 that mutual coupling can reduce the correlation significantly for small interelement spacings, $d < 0.3\lambda$, given the assumed scattering scenario. Indeed, at 0.2λ, the correlation between channels is reduced by more than a factor of 10, which can lead to significant improvements in diversity gain.

2.7 Summary

In this chapter, a SIMO communication system was investigated. Indoor and outdoor correlation measurements were presented. Experimental results show a decorrelation between receiver antennas as interelement spacing increases. For indoor transmission, the correlation between the antennas drops below 0.5 for interelement spacings exceeding half a wavelength, which is roughly 6.14 cm for a transmit frequency of 2.44 GHz. For the two outdoor transmission scenarios investigated, the correlation coefficient dropped to below 0.5 for interelement spacings larger than 1.5 wavelengths. The larger interelement spacing required to decorrelate the received signals in the outdoor scenarios results from insufficient scattering in the environment. Ray tracing models were used to further understand the received power in the region surrounding the receiver.

Additionally, mutual coupling was explored. It was found that the effect of mutual coupling is not necessarily disadvantageous, as the coupling can cause a significant reduction in the correlation of incoming data for closely spaced elements. This is useful as it can increase the amount of diversity gain that can be achieved for small interelement spacings. This capability would be extremely useful to exploit in handheld technology. As technology continues to decrease in size, the amount of electronic real estate available decreases as well, making it difficult to place antennas a wavelength or more apart. By exploiting the ability of mutual coupling to reduce correlation between independent channels, sizeable reductions in correlation can be achieved for considerably smaller interelement spacings. This would allow for good diversity performance in smaller handheld devices where the antennas are placed closer together.

2.8 Acknowledgment

This chapter, in part, is a reprint of the material as it appears in “Indoor Spatial Correlation Measurements at 2.4 GHz,” L. C. Wood and W. S. Hodgkiss, *Conference Record of the Thirty-Ninth Asilomar Conference on Signals, Systems and Computers, 2005*, pp.1588-1592 and “A Comparison of Indoor and Outdoor Spatial Correlation Measurements at 2.4 GHz,” *Fortieth Asilomar Conference on Signals, Systems and Computers, 2006, ACSSC '06,* pp.463-467. The dissertation author was the primary author of these papers.

2.9 References

[1] A. M. D. Turkmani, A. A. Arowojolu, P. A.; Jefford, and C .J. Kellett, "An experimental evaluation of the performance of two-branch space and polarization diversity schemes at 1800 MHz," *IEEE Transactions on Vehicular Technology,* , vol.44, no.2, pp.318-326, May 1995.

[2] C. B. Deitrich Jr., K. Dietze, J. R. Nealy, and W. L. Stutzman, “Spatial Polarization, and Pattern Diversity for Wireless Handheld Terminals,” *IEEE Transactions on Antennas and Propagation*, Vol. 49, No. 9, 2001, pp. 1271-1281.

[3] O. Nørklit, P. D. Teal, and R. G. Vaughn, “Measurement and Evaluation of Multi-Antenna Handsets in Indoor Mobile Communications,” *IEEE Transactions on Antennas and Propagation*, Vol. 49, No. 3, 2001, pp. 429-437.

[4] C. Oestges, D. Vanhoenacker-Janvier, and B. Clerckx, "Wide-band SIMO 1 x 2 measurements and characterization of outdoor wireless channels at 1.9 GHz,"

IEEE Transactions on Vehicular Technology, vol.53, no.4, pp. 1190-1202, July 2004.

[5] S. Y. Seidel and T. S. Rappaport, "Site-specific propagation prediction for wireless in-building personal communication system design," *IEEE Transactions on Vehicular Technology,* vol.43, no.4, pp.879-891, Nov 1994.

[6] J. S. Colburn, Y. Rahmat-Samii, M. A. Jensen, and G. J. Pottie, “Diversity Performance of Dual Antenna Personal Communication Handsets”, *IEEE Antennas and Propagation Society International Symposium*, Vol. 1, 1996, pp. 730-733.

[7] A. F. De Toledo, A. M. D. Turkmani, and J. D. Parsons, "Estimating coverage of radio transmission into and within buildings at 900, 1800, and 2300 MHz," *Personal Communications, IEEE* , vol.5, no.2, pp.40-47, Apr 1998.

[8] K. Giannopoulou, A. Katsareli, D. Dres, D. Vouyioukas, and P. Constantinou, "Measurements for 2.4 GHz spread spectrum system in modern office buildings," *10th Mediterranean Electrotechnical Conference, 2000. MELECON 2000.*, vol.1, no., pp.326-329 vol.1, 2000.

[9] P. Kyritsi, N. Kadri, E. Thang and D. Cox, “Signal correlation in a hallway environment using waveguide mode analysis,” in *Proc. VTC*, Vol 2, 2002, pp. 787–791.

[10] P. Kyritsi, D. Cox, R. Valenzuela, and P. Wolniansky, “Correlation analysis based on MIMO channel measurements in indoor channels,” *IEEE Journal on Selected Areas in Communications.* 21, 2003, pp. 713–720.

[11] H. MacLeod, C. Loadman, Z. Chen, "Experimental studies of the 2.4-GHz ISM wireless indoor channel," *Proceedings of the 3rd Annual Communication Networks and Services Research Conference, 2005*, pp. 63-68, 16-18 May 2005.

[12] B. T. Maharaj, J. W. Wallace, L. P. Linde, M. A. Jensen, "Frequency scaling of spatial correlation from co-located 2.4 and 5.2 GHz wideband indoor MIMO channel measurements," *Electronics Letters*, vol.41, no.6, pp. 336-337, 17 March 2005.

[13] L. C. Wood and W. S. Hodgkiss, "Indoor Spatial Correlation Measurements at 2.4 GHz," *2005 Conference Record of the Thirty-Ninth Asilomar Conference on Signals, Systems and Computers,* pp. 1588- 1592, 2005.

[14] L. C. Wood and W. S. Hodgkiss, "A Comparison of Indoor and Outdoor Spatial Correlation Measurements at 2.4 GHz," *Fortieth Asilomar Conference on Signals, Systems and Computers, 2006. ACSSC '06*, pp.463-467, Oct.-Nov. 2006.

[15] J.D. Parsons. *The Mobile Radio Propagation Channel*. New York: Wiley & Sons, 2000.

[16] R. O. LaMaire and M. Zorzi, “Effect of correlation in diversity systems with Rayleigh fading, shadowing, and power capture,” *IEEE Journal on Select Areas in Commun.*, vol. 14, Apr. 1996, pp. 449–460.

[17] M. Schwartz, W. R. Bennet, and S. Stein, *Communication Systems and Techniques*, New York: McGraw-Hill, 1966.

[18] R. Annavajjala, L. Milstein, "On the capacity of dual diversity combining schemes on correlated Rayleigh fading channels with unequal branch gains," *Wireless Communications and Networking Conference, 2004. WCNC. 2004 IEEE*, vol.1, pp. 300- 305, 21-25 March 2004.

[19] P. M. Rodriguez, L. G. D. R. Guedes, and R. P. Lemos, "On the effectiveness of 2D ray tracing model," *IEEE MTT-S, APS and LEOS SBMO Microwave and Optoelectronics Conference*, 1999. IMOC '99. International , vol.1, pp.312-315, 1999.

[20] Z. Ji; B. Li; H. Wang; H. Chen; Y. Zhau, "A new indoor ray-tracing propagation prediction model," *1999 International Conference on Computational Electromagnetics and Its Applications*, Proceedings. (ICCEA '99), pp. 540- 542, 1999.

[21] C. Ghobadi, P. R. Shepherd, and S. R. Pennock, "A 2D ray tracing model for indoor radio propagation at MM frequencies and the study of diversity techniques," *High Frequency Postgraduate Student Colloquium*, 1997 , vol., no.pp.53-58, 19 Sep 1997.

[22] W. Honcharenko and H. L. Bertoni, "Prediction of wideband RF propagation characteristics in buildings using 2D ray tracing," Vehicular Technology Conference, 1995 IEEE 45th , vol.1, pp.429-433, 25-28 Jul 1995.

[23] V. Degli-Eposti, G. Lombardi, C. Passerini, G. Riva, "Wide-band measurement and ray-tracing simulation of the 1900-MHz indoor propagation channel: comparison criteria and results," *IEEE Transactions on Antennas and Propagation,* vol.49, no.7pp.1101-1110, Jul 2001.

[24] HyperLink Technologies, “HG2412Y Antenna Specification.” http://www.hyperlinktech.com/web/hg2412y.php, 2006

[25] C. Balanis. *Antenna Theory: Analysis and Design*. Harper & Row Publishers, New York. 1982.

[26] B. Clerckx., D. Vanhoenacker-Janvier, C. Oesteges, and L Vandendorpe. “Mutual Coupling Effects on the Channel Capacity and the Space-Time

Processing of MIMO Communication Systems". *IEEE 2003 International Conference on Communications,* 2638-2642. May 2003.

[27] I. J. Gupta and A. K. Ksienski. "Effect of Mutual Coupling on the Performance of Adaptive Arrays". *IEEE Transactions on Antennas and Propagation*, vol. 31, no. 5,:785–791, September 1983.

[28] C. Ludwig, "Mutual Coupling, Gain, and Directivity of an Array of Two Identical Antennas." *IEEE Transactions on Antennas and Propagation*, pp. 837-841. November 1976.

[29] M. K. Özdemir, E. Arvas and H. Arslan. "Dynamics of Spatial Correlation and Implications on MIMO Systems." *IEEE Radio Communications*, S14-S19. June 2004.

[30] T. Svantesson and A. Ranheim. "Mutual coupling effects on the capacity of multielement antenna systems" *IEEE International Conference on Acoustics, Speech, and Signal Processing, 2001*. Proceedings, Vol. 4, pp.: 2485 – 2488. May 2001.

[31] T. Svantesson. "Antennas and Propagation from a Signal Processing Perspective." Ph.D. thesis, Chalmers University of Technology, Sweden. June 2001. Technical report 407.

3 MIMO Communications

Multiple-Input Multiple-Output (MIMO) antenna systems consist of multiple antennas at both the transmitter and receiver. A typical system is seen in Figure 3.1. As with any communication system, the purpose of the system is to reliably convey information across the channel separating the transmitter and receiver. The physical channel that separates the arrays of antennas at either end of the channel is a component of the communication system whose effects must be considered. This channel may have a direct, or line-of-sight (LOS), path between the transmitter and receiver. It may consist of only non-line-of-sight (NLOS) paths, in which radiation arriving at the receiver was reflected from objects between the transmitter in receiver. While these objects may be walls, buildings, vehicles, trees, or other objects, they are collectively known as scatterers in the channel.

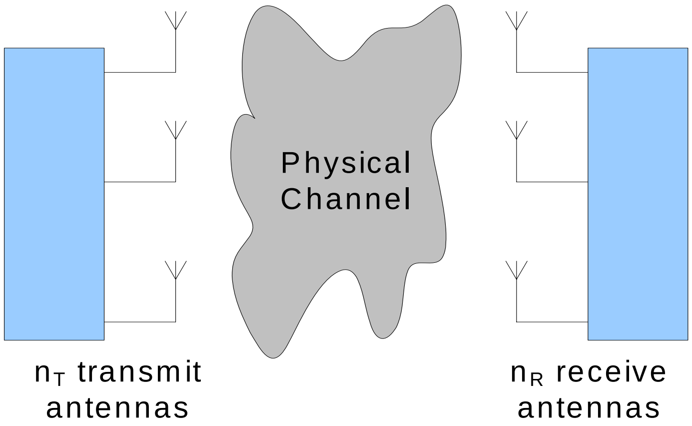

Figure 3.1: Example MIMO wireless channel and link ends.

Propagation through the physical channel that separates the transmitter and receiver is governed by Maxwell's Equations. If we know everything there is to know about a channel and the link ends, including antenna patterns, the location of all scatterers, and the motion of the link ends and scatterers, it would be possible to use Maxwell's equations determine the impulse response of the channel. However, given that it is virtually impossible to know all of this information at every time instance for all frequencies, assumptions must be made about the physical channel in order to reduce the problem to one that is mathematically tractable. As seen in Figure 3.2, the physical channel forms an integral part of the communication system. As such, assumptions made about its behavior will have a significant impact on system design. The optimal solution for designing a communication system based on one set of physical channel assumptions may differ completely from another set. More importantly, the solution derived from a model may differ significantly from the solution needed for real-world transmission.

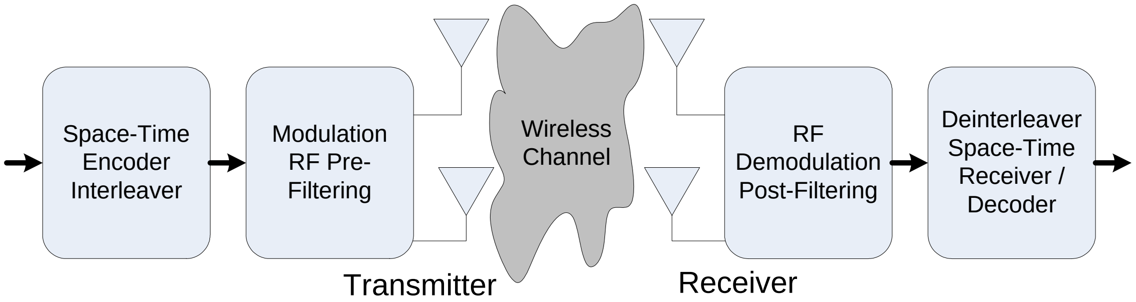

Figure 3.2: Communication system and the wireless channel.

In this section, an overview of different MIMO communication models is given. First, a general overview is given, followed by a more in depth description of three classes of MIMO models: physical, geometric-statistical, and analytical. Additionally, metrics for comparing different MIMO models are described.

3.1 MIMO Communication models

3.1.1 Narrowband MIMO Models

The typical non-time dispersive, narrowband MIMO channel model input-output relationship is given as:

$$\mathbf{y} = \mathbf{H}\mathbf{x} + \mathbf{n} \tag{3.1}$$

where **x** is the n_t dimensional transmit vector, **y** is the n_r dimensional receive vector, **H** is the n_r x n_t channel gain matrix, and the n_r components of the noise vector **n** are assumed to be i.i.d. complex circularly symmetric Gaussian distributed random entries with zero mean and variance σ_n^2. It is common to refer to **H** as the H-matrix. From this notation, it is clear why the MIMO channel is referred to as a matrix channel.

Each element of **H** is the complex gain h_{mn} between the mth receive-antenna element and the nth transmitter element. For a system composed of n_t transmit antennas and n_r receive antennas, the H-matrix can be described as:

$$H = \begin{bmatrix} h_{1,1} & h_{1,2} & \cdots & h_{1,n_t} \\ h_{2,1} & h_{2,2} & \cdots & h_{2,n_t} \\ \vdots & \vdots & \ddots & \vdots \\ h_{n_r,1} & h_{n_r,2} & \ldots & h_{n_r,n_t} \end{bmatrix} \tag{3.2}$$

To give physical context to the H-matrix description, consider the following 2 x 2 MIMO system, in which the transmitter and receiver each have 2 antennas.

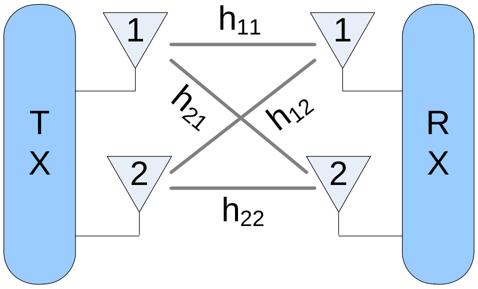

Figure 3.3: A 2 x 2 MIMO System.

Clearly, from Figure 3.3, each element in the H-matrix represents the gain for a particular path from a single transmit antenna to a single receive antenna. These paths are sometimes referred to as parallel paths, or subchannels.

3.1.2 Second Order Statistics

3.1.2.1 Full channel covariance matrix

The full channel covariance matrix, **R**, is a $n_t n_r$ x $n_t n_r$ matrix defined in literature as:

$$\mathbf{R} = E\left\{vec(\mathbf{H})vec(\mathbf{H})^{\mathrm{H}}\right\} \tag{3.3}$$

where vec() is the column stacking operator. For NLOS Gaussian channels, knowledge of **R** will completely specify the statistical behavior of the channel. For these channels, **R** may also be referred to as the correlation matrix. Note that this definition of **R** is from the receiver perspective, and that an equivalent definition from the transmit perspective is also used in literature, where

$$\mathbf{R} = E\left\{vec\left(\mathbf{H}^{T}\right)vec\left(\mathbf{H}^{T}\right)^{\mathrm{H}}\right\} \tag{3.4}$$

For the 2 x 2 MIMO system depicted in Figure 3.3, the covariance, matrix **R** is given as:

$$\mathbf{R} = E\left\{vec(\mathbf{H})vec(\mathbf{H})^{H}\right\} = E\begin{bmatrix} h_{11}h_{11}^{*} & h_{11}h_{21}^{*} & h_{11}h_{12}^{*} & h_{11}h_{22}^{*} \\ h_{21}h_{11}^{*} & h_{21}h_{21}^{*} & h_{21}h_{12}^{*} & h_{21}h_{22}^{*} \\ h_{12}h_{11}^{*} & h_{12}h_{21}^{*} & h_{12}h_{12}^{*} & h_{12}h_{22}^{*} \\ h_{22}h_{11}^{*} & h_{22}h_{21}^{*} & h_{22}h_{12}^{*} & h_{22}h_{22}^{*} \end{bmatrix} \tag{3.5}$$

To fully specify **R**, $n_t n_r$ x $n_t n_r$ parameters are necessary. For large numbers of transmit and receive antennas, the exponential growth in the size of **R** as more antennas are added makes estimation and feedback of this matrix problematic for real-time systems. Thus, for systems in which knowledge of **R** is required, it is attractive to make simplifying assumptions to reduce the amount of parameters needed to fully describe the channel.

3.1.2.2 Link End Covariance Matrices

Alternatively, it is possible to examine the channel statistics from the perspective of the link ends. The link end covariance matrix from the receiver's perspective is defined as:

$$\mathbf{R}_{rx} = E\left\{\mathbf{H}\mathbf{H}^{\mathrm{H}}\right\} \tag{3.6}$$

The corresponding form from the transmitter perspective is given as:

$$\mathbf{R}_{tx} = E\left\{\left(\mathbf{H}^{H}\mathbf{H}\right)^{T}\right\} \tag{3.7}$$

To illustrate why these matrices are considered to be from a link end perspective, consider the receive link end covariance matrix for a 2 x 2 MIMO system:

$$\mathbf{R}_{rx} = E\left\{\mathbf{H}\mathbf{H}^{H}\right\} = E\begin{bmatrix} h_{11}h_{11}^{*} + h_{12}h_{12}^{*} & h_{11}h_{21}^{*} + h_{12}h_{22}^{*} \\ h_{21}h_{11}^{*} + h_{22}h_{12}^{*} & h_{21}h_{21}^{*} + h_{22}h_{22}^{*} \end{bmatrix} \tag{3.8}$$

The off diagonal entries in (3.8) are the sum of two terms. The first term is the correlation between the pair of receive antennas if the signal came from transmit antenna 1. The second is the correlation between the pair if the signal came from transmit antenna 2. Thus, the off diagonal terms contain the total correlation between receive antennas 1 and 2 as a sum of the contributions from all transmit antennas. The same reasoning holds, equivalently, for the link end correlation matrix at the transmitter. The transmit link end covariance matrix for a 2 x 2 system is:

$$\mathbf{R}_{tx} = E\left\{\mathbf{H}^T \mathbf{H}^*\right\} = E\begin{bmatrix} h_{11}h_{11}^* + h_{21}h_{21}^* & h_{11}h_{12}^* + h21h_{22}^* \\ h_{12}h_{11}^* + h_{22}h_{21}^* & h_{12}h_{12}^* + h_{22}h_{22}^* \end{bmatrix} \tag{3.9}$$

3.2 Physical MIMO Models

Numerous physical MIMO models can be found in literature, a subset of which are given in [3-5]. These models attempt to mimic the propagation of waves, rays, or wave fronts from the transmitter to receiver. For modeling these environments accurately, a plethora of physical information must be obtained. The dimensions of the environment and the locations of each of the scatterers are a minimum environmental description. Angles of arrival and departure for each object, transmission coefficients, reflection coefficients, and other characteristics must also be known. Since this information is particular to an environment, it will not port easily from one environment to the next without obtaining all of the numerous model parameters for the new location. Furthermore, the large amount of information that is required in these models would be impractical to use in systems for real-time feedback or operational mode purposes. To overcome this lack of portability, geometrically-based models are often used.

3.3 Geometric-Statistical Models

Geometrical models assume a simplified environmental geometry. Rather than detailing the exact shape and configuration of a room, these models represent an environment as a rectangular shape or as an ellipse. Once the geometry has been determined, a distribution of scatterers in the environment is assumed. The generation of channel gain matrices then becomes a ray tracing problem. Each entry in the channel gain matrix, h_{ij}, is of the form:

$$h_{i,j} = \sum_{l=1}^{L} \alpha_l e^{-jks_{rl}} G_i^*(\theta_{i,l}) G_j(\theta_{j,l}) e^{-jks_{lt}} \tag{3.10}$$

where i and j index the receive and transmit antennas respectively, α is the complex scattering coefficient for each scatterer, k is the wave number, $G_i(\theta)$ and $G_j(\theta)$ are the antenna gains in the direction of scatterer *l*, s_{rl} is the distance from receiver to scatterer, s_{lt} is the distance from scatterer to transmitter, and L is the total number of scatterers. Examples of geometric-statistical models are found in literature in [6-8].

Three common geometric-statistical models will be considered in this work. They include the one-ring model, the combined elliptical-ring model, and the cluster model. A brief overview of these three models will be given in this section, with more details on simulation implementation presented where required.

3.3.1 One Ring Model

The one ring model is one of the simplest geometrical models used to generate channel gain matrices for modeling macrocellular environments. Often, base stations (transmitters) are located at a much higher height relative to the subscriber units (receivers). To model the differences arising from this behavior, a ring of effective scatterers is placed only around the receiver. Generally, the distance between the transmitter and receiver is considered to be large relative to the scatterer ring radius. This assumption allows for closed form expressions for the correlation terms to be determined. All rays from the transmitter may bounce off a scatterer only once before arriving at the receiver. There is no line-of-sight-transmission. A graphical description of the one ring model is given in Figure 3.4. The distance between the arrays is R and the radius of the ring is defined as ρ. The separation between antennas at the transmit and receive link ends are denoted Δ_{tx} and Δ_{rx}, respectively

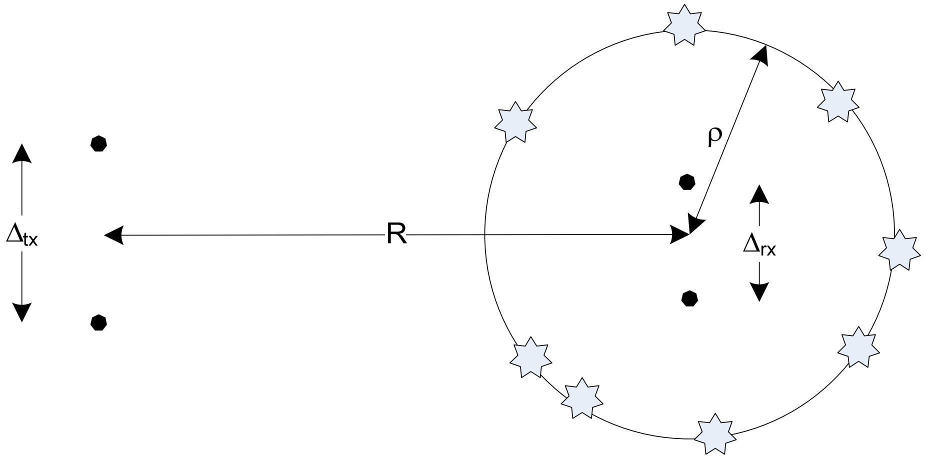

Figure 3.4: Example One Ring Model geometry.

3.3.2 Combined Elliptical Ring Model

A second single-bounce model commonly used is the combined elliptical-ring model. This model is designed for modeling either line-of-sight or non-line-of-sight environments, and is capable of modeling time-dispersive channels. To model the time-dispersive nature, scatterers with identical delays are located on an ellipse, with the transmitter and receiver located at the foci. In positioning the scatterers on an ellipse in such a manner, rays leaving the transmitter that impinge upon any scatterer in the same ellipse before arriving at the transmitter will travel paths of identical lengths. Because of this, the ellipses are referred to as iso-delay ellipses.

To generate a realistic channel, a measured tap-delay profile for a particular environment is used to select the number and size of ellipses. For Rayleigh channels, the number of scatterers associated with each ellipse may be determined by specifying a scatterer density. This is done to place scatterers in the environment in a uniform fashion. If a density is not specified, an alternative methodology is to place a finite number of scatterers per ellipse. This method has increasing density as one moves in a concentric ellipse direction as smaller ellipses will have scatterers placed closer together, on average, than larger ellipses. Additionally, this sort of configuration may not be realistic for the environment under examination. To introduce disparity between the local environments of the transmitter and receiver, a ring of local scatterers is placed around the receiver. Additionally, a disk of exclusion into which no scatterer may fall is placed around the transmitter. The number of scattering ellipses is designated as N. If the environment has a line of sight path, a degenerate ellipse accommodates the modeling of this path. The combined elliptical ring model is depicted in Figure 3.5.

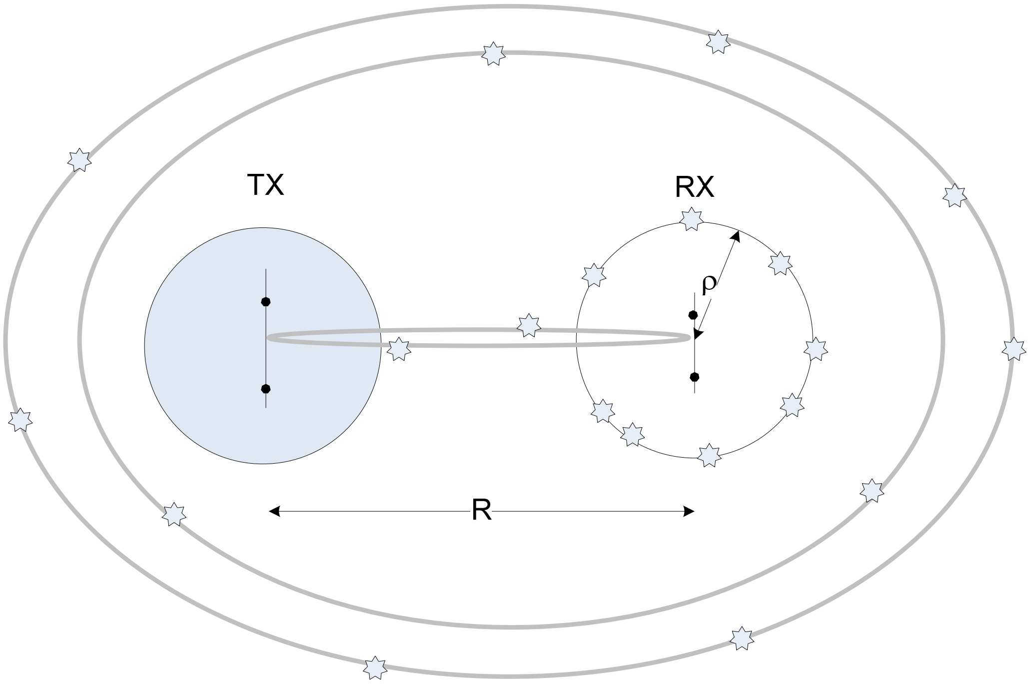

Figure 3.5: Combined elliptical-ring model geometry, with N = 3.

3.3.3 Cluster Model

The one ring model limits the scattering to a ring of effective scatterers around the receiver end of the communication system. Instead, dominant scatterers may be located throughout the environment. The angular resolution of the system may be such that individual scatterers cannot be resolved. Thus, the overall response at the receive array from a particular direction will be a combination of the responses from individual scatterers. To model this behavior, a ring of many individual scatterers is used to form a cluster. Several clusters and their locations relative to the transmitter and receiver are used to represent an environment. Each scatterer has a complex gain associated with it, usually assigned according to a selected distribution, such as a log-normal distribution. A depiction of a cluster model, which uses N = 3 rings of scattering clusters, is given in Figure 3.6.

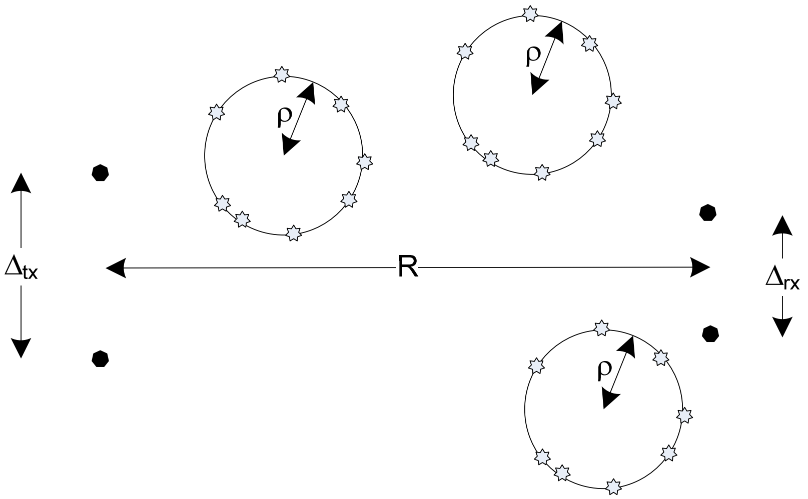

Figure 3.6: Cluster model geometry, with N = 3.

3.4 Analytical Models

The primary drawback to physically-based modeling strategies is a lack of portability between different environments. In the case of parameterized models, the statistical parameters used may not be valid over a large area. Thus, for MIMO system development, where it is desirable to create many different channel gain matrix realizations for a variety of environments, analytical models have become popular.

Analytical channel models are found in literature in a variety of forms, e.g. [9-13]. Some models begin with theoretical assumptions alone. Others fit parameters extracted from measurements into a theoretical model framework. Due to the impact of spatial correlation on the design of MIMO systems, correlation-based analytical channel models are of significant interest to researchers.

3.4.1 Correlation-based models

The general spatial correlation-based model for the MIMO channel may be expressed as

$$vec(\mathbf{H}) = \mathbf{R}^{1/2} vec(\mathbf{H}_{\mathbf{w}}) \tag{3.11}$$

where vec( ) is the operator which stacks the columns of a matrix to form a vector and $\mathbf{H_w}$ is a matrix whose entries are circularly symmetric complex Gaussian distributed random variables with zero mean and unit variance. Recall that the full channel covariance gain matrix, **R**, is a $n_t n_r$ x $n_t n_r$ matrix defined as:

$$\mathbf{R} = E\left\{vec(\mathbf{H}) vec(\mathbf{H})^{\mathrm{H}}\right\}. \tag{3.12}$$

For NLOS Gaussian channels, knowledge of **R** will specify completely the statistical behavior of the channel. For a 2 x 2 MIMO system, where the antenna gains are independent and identically distributed, **R** can be expressed as:

$$\mathbf{R} = \begin{bmatrix} 1 & r & t & s_1 \\ r^* & 1 & s_2 & t \\ t^* & s_2^* & 1 & r \\ s_1^* & t^* & r^* & 1 \end{bmatrix} \tag{3.13}$$

The terms s_1 and s_2 are referred to as diagonal correlation or cross-channel correlation terms. Since the transmitter and receiver antennas are assumed to have the same omni-directional antenna patterns, the terms t and r represent transmit and receive correlations, respectively. For large values of n_t and n_r, the computation of **R** becomes prohibitive. As such, simpler expressions for the full correlation matrix are desirable.

3.4.1.1 Kronecker Model

One of the most commonly used analytical models is the Kronecker model [9-10]. This model approximates the full correlation matrix by a Kronecker tensor product of the two link end correlation matrices, thus giving the model its name. This relationship can be expressed as:

$$\mathbf{R} = \mathbf{R}_{tx} \otimes \mathbf{R}_{rx} \tag{3.14}$$

The simplification of representing the full correlation matrix as a product of the two link end correlation matrices results in the inherent model assumption that the behavior at either link end does not influence the other link end. In other words, the link ends are independent of each other. In turn, this makes the cross channel terms s_1 and s_2 from (3.13) products of the transmit and receive correlations. This assumption can have a significant impact on model performance in predicting measured channel characteristics if this assumption is not well-supported.

The Kronecker model uses the following synthesis equation to generate realizations of the channel matrix, **H** [9-10]:

$$\mathbf{H}_{kron} = \mathbf{R}_{rx}^{1/2}\mathbf{H}_{w}\left(\mathbf{R}_{tx}^{1/2}\right)^{T} \tag{3.15}$$

For modeling environments with an elevated link end, a simplified Kronecker model is often used in which the link end correlation matrix is set to the identity matrix. As a consequence of the Kronecker model's simplicity, it is still used despite significant known performance prediction issues [14-16].

3.4.1.2 Virtual Channel Model

The Virtual Channel model was proposed by A. Sayeed [11]. The Virtual Channel model links "look" directions at link ends together through a coupling matrix, $\mathbf{\Omega}$. The power coupling matrix has entries which specify the average SISO power coupling linking two look directions. The directions at each link end are predetermined, and equally spaced. These predetermined matrices, $\mathbf{A}_{\mathbf{rx}}$ and $\mathbf{A}_{\mathbf{tx}}$ are unitary steering matrices that, equivalently, are collections of vectors of Discrete Fourier Transform (DFT) coefficients. Because of this feature, this model is restricted to modeling only Uniform Linear Array (ULA) geometries.

The angular resolution, or number of virtual angles, is determined by the number of transmit and receive antennas in the system. Thus, the link end bases $\mathbf{A}_{\mathbf{rx}}$ and $\mathbf{A}_{\mathbf{tx}}$ are specified entirely by the number of antennas in the system and do not need to be estimated or recomputed as the environment changes. As such, this model is primarily defined by the power coupling matrix, $\mathbf{\Omega}$. The synthesis equation for this model is given as follows:

$$\mathbf{H}_{virt} = A_{rx}\left(\tilde{\mathbf{\Omega}} \circ \mathbf{H}_w\right)A_{tx}^T \tag{3.16}$$

The (◦) operator indicates an element-wise multiplication, and the (~) operator indicates an element-wise square-root. To generate many realizations, different $\mathbf{H}_{\mathbf{w}}$, whose elements are i.i.d circularly symmetric complex Gaussian, are used. While the prespecified directions may simplify the number of parameters that need to be estimated for this model, they may not provide an optimal representation of the channel's preferred eigenbases. Additionally, the model does not allow for array configurations other than ULA.

3.4.1.3 Weichselberger Model

The structured eigenbasis model proposed by Weichselberger generalizes the Virtual Channel model. Like the Virtual Channel model, Weichselberger's model directly parameterizes a correlation-based model from measurements without making the simplifying assumption of separable link end correlations. This concept is captured in the modeling assumption that the eigenbases of the one-sided correlation matrices are the same as in the Kronecker model, but they are linked together through a coupling matrix. The use of eigenbases in place of DFT directions alleviates issues that the virtual channel model has with small numbers of antennas by allowing the arrays to "look" in the directions with the most power. As such, the Weichselberger model is not restricted to predefined directions. However, this assumption means that unlike the Virtual Channel model, the bases used at the link ends must be estimated, and updated as needed, for different environments.

The model is specified in [12, 13] as:

$$\mathbf{H}_{weich} = \mathbf{U}_{rx}\left(\tilde{\mathbf{\Omega}} \circ \mathbf{H}_{w}\right)\mathbf{U}_{tx}^{T} \tag{3.17}$$

where $\mathbf{U_{rx}}$ and $\mathbf{U_{tx}}$ are the eigenbases arising from the decomposition of $\mathbf{R_{rx}}$ and $\mathbf{R_{tx}}$, and $\mathbf{\Omega}$ is a power coupling matrix. The eigenvectors within $\mathbf{U_{rx}}$ and $\mathbf{U_{tx}}$ form a channel-dependent orthonormal basis. While the full channel eigenmode is n_r x n_t, the Virtual Channel and Weichselberger models approximate the full channel eigenmode with a vector eigenmode. That is, the outer product of a receive eigenvector (or eigenbasis vector) and a transmit eigenvector is used to approximate the full eigenmode. The power coupling matrix $\mathbf{\Omega}$ contains entries that specify the average energy coupled between an eigenvector at the transmit side and an eigenvector at the receive side. Thus, $\mathbf{\Omega}$ is environmentally dependent, reflecting the scattering structure in the environment. It is defined as:

$$\mathbf{\Omega}_{\mathbf{weich}} = E\left\{\left(\mathbf{U}_{\mathbf{rx}}^{\mathbf{H}}\mathbf{H}(k)\mathbf{U}_{\mathbf{tx}}^{*}\right)\circ\left(\mathbf{U}_{\mathbf{rx}}^{\mathbf{T}}\mathbf{H}(k)\mathbf{U}_{\mathbf{tx}}\right)\right\} \tag{3.18}$$

From (3.18) we note that the coupling matrix entries specify the power at the intersection of transmit and receive eigenvector directions.

3.4.2 SIMO vs. MIMO

In Chapter 2, the spatial correlation coefficient between arriving signals at two receiver elements was characterized for several environments. In terms of the above discussion, the SIMO measurement campaign is equivalent to characterizing ‘r’ as given in (3.13). The portion of the MIMO correlation matrix described by our previous SIMO work is depicted in Figure 3.7.

$$\mathbf{R}_{\mathbf{H}} = \begin{bmatrix} \boxed{\begin{matrix} 1 & r \\ r^{*} & 1 \end{matrix}} & \begin{matrix} t & s_1 \\ s_2 & t \end{matrix} \\ \begin{matrix} t^{*} & s_2^{*} \\ s_1^{*} & t^{*} \end{matrix} & \boxed{\begin{matrix} 1 & r \\ r^{*} & 1 \end{matrix}} \end{bmatrix}$$

Figure 3.7: MIMO correlation matrix with SIMO measurements.

Using the measurement hardware currently available, it would be possible to also measure the correlation between two transmit antennas, t. However, the SIMO hardware does not allow for the simultaneous measurement of the cross-correlation terms s_1 and s_2. For the measurement of these terms, a MIMO test bed is required.

3.5 Tools for MIMO Model Comparison

For comparing the performance of MIMO models, it is necessary to define several benchmark metrics. Typically, some form of channel capacity is used as the metric of comparison. Other metrics also considered in this work are eigenvalue spread, two different channel condition numbers, and correlation matrix distance. Additionally, to explore how the underlying physics of the channel are captured, two different beamforming techniques are used.

3.5.1 Channel Metrics

3.5.1.1 Capacity

The uninformed transmitter channel capacity at high SNR is often used as the metric of choice to test the 'goodness' of a model in representing a wireless channel [8, 11, 14-16]. To compute the uninformed transmitter channel capacity metric, we use the following well-known capacity expression:

$$\overline{\mathbf{C}}_{UT} = E_H\left\{\log_2 \det\left(\mathbf{I}_{n_r \times n_r} + \frac{SNR}{n_t}\mathbf{H}\mathbf{H}^H\right)\right\} \tag{3.19}$$

3.5.1.2 Eigenvalue spread

The eigenvalue spread is defined as the ratio of the first eigenvalue to another eigenvalue. Following [17], we specify the eigenvalue spread, ES, as the difference between the average 1st and 3rd eigenvalues, in dB. The term eigenvalue refers here to the square of the respective singular value of **H**. This particular metric gives us an indication of the amount of multipath in the channel, and thus information about the suitability of the channel for different signaling techniques such as beamforming. The eigenvalue spread, ES, is given as:

$$ES = \lambda_1^{dB} - \lambda_3^{dB} \tag{3.20}$$

3.5.1.3 Channel Condition Numbers

Two different condition numbers are considered in this work: the channel condition number and the Demmel condition number. The channel condition number gives a measure of the invertibility of the channel, and is defined as [18]

$$\kappa = \left\| \mathbf{H} \right\|_2 \left\| \mathbf{H}^{-1} \right\|_2 . \tag{3.21}$$

Similarly, the Demmel condition number also can provide information about the invertibility of the channel. However, the Demmel number is scale invariant, separating gain effects from channel invertibility effects. The invertibility of the channel provides knowledge about the 'goodness' of the channel for use in spatial multiplexing or spatial diversity operational modes. Mathematically, the Demmel condition number for a matrix **H** is defined as:

$$\kappa_D = \left\| \mathbf{H} \right\|_F \left\| \mathbf{H}^{-1} \right\|_2 . \tag{3.22}$$

Physically, in [19] it was shown that this metric provides a comparison between the minimum signal constellation distance needed to support spatial multiplexing and spatial diversity modes of operation for a given channel. The notation $\| \cdot \|_F$ refers to the Frobenius norm.

3.5.1.4 Correlation Matrix Distance

For Rayleigh fading channels, the full correlation matrix provides the necessary information for reconstructing the spatial fading statistics. For situations where feedback is available to the transmitter, knowledge of this matrix can be exploited to provide improved system performance. A useful metric in determining the need for updating the knowledge at the transmitter was introduced by the authors of [20]. This metric, called the correlation matrix distance, provides a measure of the similarity between correlation matrices.

The correlation matrix distance metric can provide useful information in a two-fold manner. In the first instance, it can provide a measure of how close a model correlation matrix is to the ideal or measured channel correlation matrix. Secondly, it can be used as a metric to track the variability in the channel. That is, the correlation matrix distance provides a method to characterize a model's ability to represent stationarity in a channel. By comparing how the stationarity of the channel changes with how the models follow the changes in that stationarity, we provide insight into the usefulness of a model for optimal signaling design. For example, this metric could be useful in predicting update rates in feedback systems. When the distance between the true correlation matrix and the matrix being used at the transmitter becomes significant, the matrix at the transmitter must be updated. The correlation metric is defined as [20]:

$$d_{corr} = 1 - \frac{tr(\mathbf{R_1 R_2})}{\|\mathbf{R_1}\|_F \|\mathbf{R_2}\|_F} \tag{3.23}$$

where $0 \leq d_{corr} \leq 1$. This metric provides a measure between the orthogonality of the n-dimensional spaces of $\mathbf{R}_1$ and $\mathbf{R}_2$. The metric is zero for identical matrices. As the subpaces spanned by the two correlation matrices become more orthogonal, the metric increases.

3.5.2 Beamforming

Beamforming is a technique used to identify the arrival angle of a source (or sources) of energy in an environment. In conventional delay-and-sum beamforming, signals at an antenna array are delayed and weighted such that the signal to interference and noise ratio (SINR) is increased. By steering the beamformer to preferentially listen in a particular direction, the beamformer implements a spatial filter, selecting signals arriving from a particular direction over those arriving from another. By coherently adding phased arrivals at different antennas, a narrower response in a desired direction or set of directions is achieved.

Two different beamforming techniques are considered for beamforming on the link end covariance matrices: conventional frequency domain beamforming (CBF) and minimum variance distortionless response (MVDR) beamforming. A detailed decription of these techniques are given in [21].

3.5.2.1 Frequency Domain Beamforming

Frequency domain beamforming is similar to conventional delay-and-sum beamforming, but instead of the processing taking place in the time domain, it occurs in the frequency domain. For frequency domain beamforming on the covariance matrix, the quadratic form of the power at the beamformer output,

$$\mathrm{B}_{\mathrm{conv}} = \mathbf{w}^{\mathbf{H}}\mathbf{R}\mathbf{w} \tag{3.24}$$

is computed, where **R** is a covariance matrix under investigation and **w** is the beamforming weight vector containing both spatial shading information and the phase delay vector, d. The time delay for a plane wave arriving at each sensor will be calculated for each ‘look’ angle of the beamformer, then multiplied by 2πf to find the corresponding phase shift. The phase delay vector, d, is then weighted to form the weighted phase delay vector **w**.

3.5.2.2 MVDR Beamforming

Minimum variance beamforming is a technique that can offer better angular resolution and noise rejection than conventional beamforming. For this technique, we still compute the same quadratic form as given in the CBF covariance processing strategy, but use the adaptive weight vector:

$$\mathbf{w} = \frac{\mathbf{R}^{-1}\mathbf{d}}{\mathbf{d}^{\mathbf{H}}\mathbf{R}^{-1}\mathbf{d}} \tag{3.25}$$

A new weight vector must be computed for each steering direction using MVDR beamforming, making it more computationally expensive than conventional beamforming. Also, unlike the CBF, the MVDR beamformer not only passes the desired signal for the look direction, it also steers nulls in the direction of other strong arriving signals, resulting in its performance improvement. If **R** is not numerically well-posed, the inverse can be unstable, causing the technique to break down. MVDR beamforming may suffer from signal cancellation issues in the presence of correlated arrival signals, such as those arising from correlated multipath.

3.6 References

[1] I. E. Telatar, "Capacity of multi-antenna Gaussian channels," *Eur. Trans.Telecomm.*, ETT, vol. 10, pp. 585-595, Nov./Dec. 1999.

[2] J. Foschini and M. J. Gans, "On the Limits of Wireless Communications in a Fading Environment When Using Multiple Antennas," Wireless Pers. Commun.,vol. 6, pp. 315-335, Mar. 1998.

[3] T. Zwick, C. Fischer, and W. Wiesbeck, *A stochastic multipath channel model including path directions for indoor environments***.** Selected Areas in Communications, IEEE Journal on, Vol.20, Iss.6, Aug 2002. pp. 1178- 1192.

[4] T. Fugen, J. Maurer, W. Sorgel, and W. Wiesbeck, *Characterization of multipath clusters with ray-tracing in urban MIMO propagation environments at 2 GHz.* Antennas and Propagation Society International Symposium, 2005 IEEE, vol.3B, Iss., 3-8 July 2005, pp. 410- 413.

[5] K. H. Ng, E. K. Tameh and A. R. Nix, *Modelling and performance prediction for multiple antenna systems using enhanced ray tracing*. Wireless Communications and Networking Conference, 2005 IEEE, Vol.2, Iss., 13-17 March 2005, pp. 933-937.

[6] W.C.Y. Lee, Mobile *communications engineering, 2nd ed.*, McGraw-Hill, New York, 1997.

[7] A. Saleh and R. Valenzuela, *A Statistical Model for Indoor Multipath Propagation***.** Selected Areas in Communications, IEEE Journal on, Vol.5, Iss.2, Feb 1987, pp. 128- 137.

[8] P. Almers, E. Bonek, A. Burr, et al., “Survey of Channel and Radio Propagation Models for Wireless MIMO Systems,” *EURASIP Journal on Wireless Communications and Networking*, vol. 2007, Article ID 19070, 19 pages, 2007.

[9] J. Kermoal, L. Schumacher, K. Pedersen, P. Mogensen, and F. Frederiksen, *A Stochastic MIMO Radio Channel Model With Experimental Validation*. IEEE J. Select. Areas Commun., vol. 20, no. 6, Aug. 2002, pp. 1211-1226.

[10] K. Yu, M. Bengtsson, B. Ottersten, D. McNamara, P. Karlsson, and M. Beach, *Modeling of wide-band MIMO radio channels based on NLoS indoor measurements*. Vehic Tech, IEEE Trans. on, Vol.53, Iss.3, May 2004, pp. 655-665.

[11] A.M. Sayeed, *Deconstructing multiantenna fading channels*. Signal Processing, IEEE Transactions on, Vol.50, Iss.10, Oct 2002, pp. 2563- 2579.

[12] W. Weichselberger, M. Herdin, H. Özcelik, and E. Bonek, “A Stochastic MIMO Channel Model with Joint Correlation at Both Link Ends,” *IEEE Trans Wireless Communications*, Vol 5, No. 1. Jan 2006, pp. 90-100.

[13] W. Weichselberger, "Spatial structure of multiple antenna radio channels --- a signal processing viewpoint", PhD dissertation, Vienna University of Technology, Vienna, Austria, 2003.

[14] N. Costa and S. Haykin, *A Novel Wideband MIMO Channel Model and McMaster's Wideband MIMO SDR.* Conf. Record of the 40th Asilomar Conf. on Signals, Systems and Computers, , Nov 2006, pp. 956-960.

[15] H. Ozcelik, M. Herdin, W. Weichselberger, J. Wallace and E. Bonek, *Deficiencies of 'Kronecker' MIMO radio channel model.* Electronics Letters, Vol.39, Iss.16, 7 Aug. 2003, pp. 1209- 1210.

[16] L. C. Wood and W. S. Hodgkiss. MIMO Channel Models and Performance Metrics. Global Telecommunications Conference, 2007. GLOBECOM '07. IEEE , pp.3740-3744, 26-30 Nov. 2007.

[17] J.W. Wallace and M. A. Jensen, *Experimental analysis of the time-varying MIMO channel*, Antennas and Propagation Society International Symposium 2006, IEEE, 9-14 July 2006, pp. 321- 324.

[18] D. Gesbert, H. Bolcskei, D. A. Gore, and A. J. Paulraj, *Outdoor MIMO wireless channels: models and performance prediction.* Communications, IEEE Transactions on, vol.50, no.12, Dec 2002, pp: 1926- 1934.

[19] R. W. Heath and A.J. Paulraj, *Switching between diversity and multiplexing in MIMO systems***,** Communications, IEEE Transactions on, Vol.53, Iss.6, June 2005, pp. 962- 968.

[20] M. Herdin, N. Czink, H. Özcelik, and E. Bonek, *Correlation matrix distance, a meaningful measure for evaluation of non-stationary MIMO channels*, Vehicular Technology Conference, 2005. VTC 2005-Spring. 2005 IEEE 61st, Vol.1, Iss., 30 May-1 June 2005, pp. 136- 140.

[21] H. Van Trees, *Optimum Array Processing*. New York, Wiley-Interscience, 2002.

4 MIMO Channels from Experimental Data

4.1 Introduction

Although the structured eigenbasis model proposed by Weichselberger has been shown to provide a closer match than the Kronecker model to the ergodic capacity of measured channels, as shown in [1-3], there has been little comparison between these models using other metrics. Often channel metrics are used as benchmarks for selecting optimal modes of operation in adaptive feedback systems, or are used to optimize systems in the developmental stages. Since the choice of model will influence the accuracy of the results for developing optimal power allocation, spatial multiplexing, and spatial diversity schemes, it would be insightful to have a more comprehensive characterization of the usefulness of these two models [4-5].

In this chapter, we investigate the impact of the choice of the channel model on commonly used channel metrics. This chapter begins with an introduction to the MIMO data sets, measurement environment and measurement equipment. Then, the following metrics are used for comparison: the uninformed transmitter ergodic capacity, eigenvalue spread, the condition number, the Demmel condition number, and the correlation matrix distance. After examining the impact of the environment on the Kronecker and Weichselberger models, we further investigate how the Weichselberger model captures the underlying physics of the channel.

4.2 Data sets

Measured MIMO channel gain matrices used in this work were provided by the Brigham Young University Wireless Research Laboratory. A brief overview of the measurement system and process will be presented. Detailed information can be found in

[6-8] and the references therein. An overview of the three primary environments used in this work will also be given. Other recent measurement campaigns used in characterizing channel and analytical models are reported in [9-10].

4.2.1 Measurement Hardware

The transmitter hardware used by BYU is a custom build radio frequency subsystem that accepts binary sequences from an external digital pattern generator. A local oscillator signal is provided from an external microwave source. The subsystem distributes the pattern and local oscillator signals to individual cards corresponding to each transmit antenna. Each card amplifies the LO signal and multiplies it with one of the binary sequences from the pattern generator, such as a Walsh code, to produce BPSK modulation. The resulting signal is amplified to 0.5 watts and fed to a transmit antenna.

The receive system performs the reverse process, with individual cards on each receive branch performing the operations of amplification, down-conversion, and filtering. The resulting IF signals are sampled using a 1.25 Msample/s A/D converter. This data is then stored and post-processed on a PC.

4.2.2 Channel Estimation Process

To estimate the channel, a three part process is used, consisting of code alignment, carrier recovery, and estimation of the channel. For code alignment, a correlator is used in conjunction with an exhaustive search over all possible codewords to ensure proper synchronization. Following this process, carrier recovery occurs. Finally, the channel is estimated using a channel inversion methodology. The details for this process are given in [6-8].

4.2.3 Data Environments

Three environments are considered in this work. These environments were selected as they provide a range of propagation and scattering conditions. The first environment considered is an outdoor urban setting. The second is a transmission scenario through foliage. The third environment consists of transmitting from inside a building to an outside area. This measurement configuration has significant multipath with a large angular spread.

4.2.3.1 Coal Yard

The Coal Yard environment is an outdoor urban area environment with buildings, a power plant, cars, delivery trucks, and trees. There are two locations of data used from this environment. At each location, four data sets were recorded, for a total of eight data sets. For all data sets, the transmitter was placed in a fixed location in the environment. The odd numbered sets at each location, Sets 1 and 3, were measured with a stationary receiver link end. For these sets, the measured variations in the channel are from environmental changes, such as vehicle or pedestrian movement. These sets are slowly varying and exhibit high temporal correlation from one channel matrix sample to the next. For Sets 2 and 4 from each location, the receiver was moved at 1 ft/s for 30s along a fixed path. The stationary point was at the beginning of the path for all locations. The testbed uses 8 antennas at the transmitter side and 8 antennas at the receiver side. The antennas are arranged in a uniform linear array arrangement, spaced 0.5λ apart. The channel was probed using vertically-polarized monopole antennas. The data is taken using a center frequency of 2.45 GHz, with samples taken every 2.5 ms. For this center frequency, the wavelength corresponds to 12.24 centimeters. An aerial view of the environment and array orientations for Location 1 and Location 2 are given in Figure 4.1 and Figure 4.2 below. While the center of the arrays are at the appropriate location, the array lengths have been exaggerated to show the orientation of the arrays.

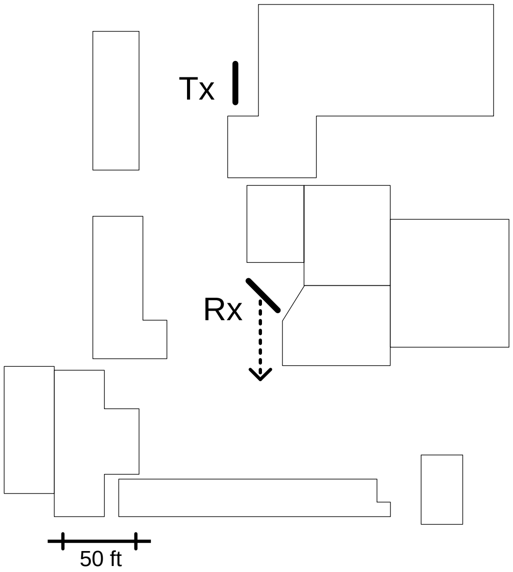

Figure 4.1: Coal Yard, Location 1 environment with relative positioning of transmitter and receiver. For sets in which the receiver is in motion, the path direction is shown by a dashed arrow.

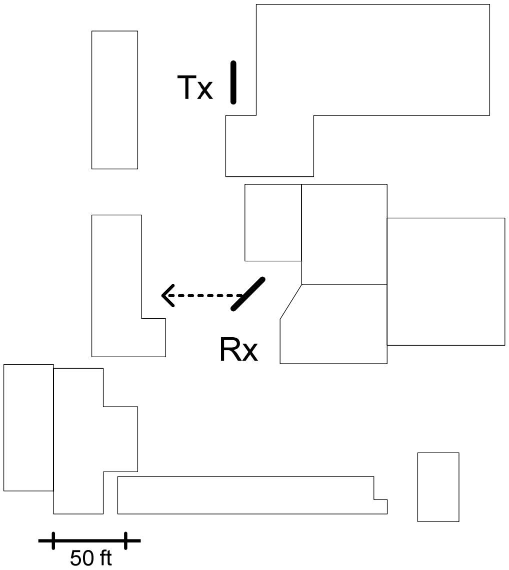

Figure 4.2: Coal Yard, Location 2 environment with relative positioning of transmitter and receiver. For sets in which the receiver is in motion, the path direction is shown by a dashed arrow.

4.2.3.2 Tree Propagation

The tree propagation case was investigated to capture propagation through a distributed scattering environment. The transmitter was placed behind some shrubs and a pine tree. The receiver was then either left stationary for 30 seconds or moved at 1 foot/second for 30 seconds on the other side of the trees from the transmitter. In each measurement, the transmitter was fixed and the receiver was either stationary (Sets 1 and 3) or moving (Sets 2 and 4). As with the Coal Yard measurements, the testbed uses 8 antennas at the transmitter side and 8 antennas at the receiver side and a center frequency of 2.45 GHz, with a system bandwidth of 30 kHz. Measurements are made every 2.5 ms. The vertically polarized antennas are arranged in a uniform linear array arrangement with 0.44λ spacing. An aerial depiction of large building scatterers and ellipsoids representing clusters of vegetation are shown in Figure 4.3.

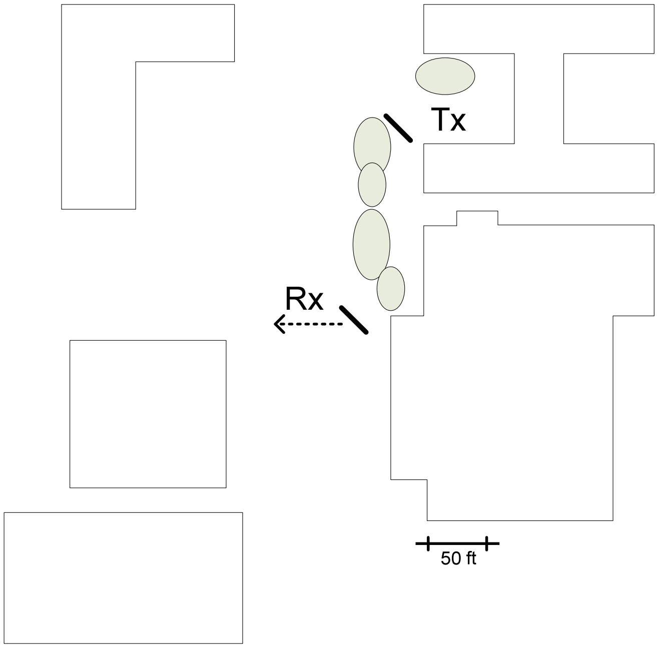

Figure 4.3: Aerial overview of the buildings and vegetation in the Tree Propagation environment with relative positioning of transmitter and receiver, array orientations. For sets in which the receiver is in motion, the path direction is shown by a dashed arrow.

4.2.3.3 Indoor to Outdoor

Indoor to outdoor measurements from a campus pedestrian area to a hallway inside a building were recorded. Measurements were taken with a transmitted signal consisting of 8 tonal frequencies spaced 1 MHz apart, giving the signal 8 MHz of bandwidth. The center frequency of the system was 2.55 GHz. The arrays used at both link ends were 8-element uniform circular arrays of vertically polarized monopole antennas with 0.5λ spacing. In all transmission scenarios investigated for this environment, the transmitter was stationary. Sets designated with an (a) in the title were taken with the receiver stationary to see how much of the channel time-variation was due to the environment itself changing (people, cars, etc.) For sets designated with a (b), the receiver was moved at a rate of 31.75 cm (12.5 in) per second in a straight line with channel samples every 3.2 ms. For this work, we consider primarily single frequency data from records in which the receiver was in motion. The measurement environment was in the same area as the trees propagation environment. An aerial view of the transmitter and receiver locations is shown in Figure 4.4. Note that the transmitter is on the fourth floor inside the building and the vegetation is omitted from the drawing.

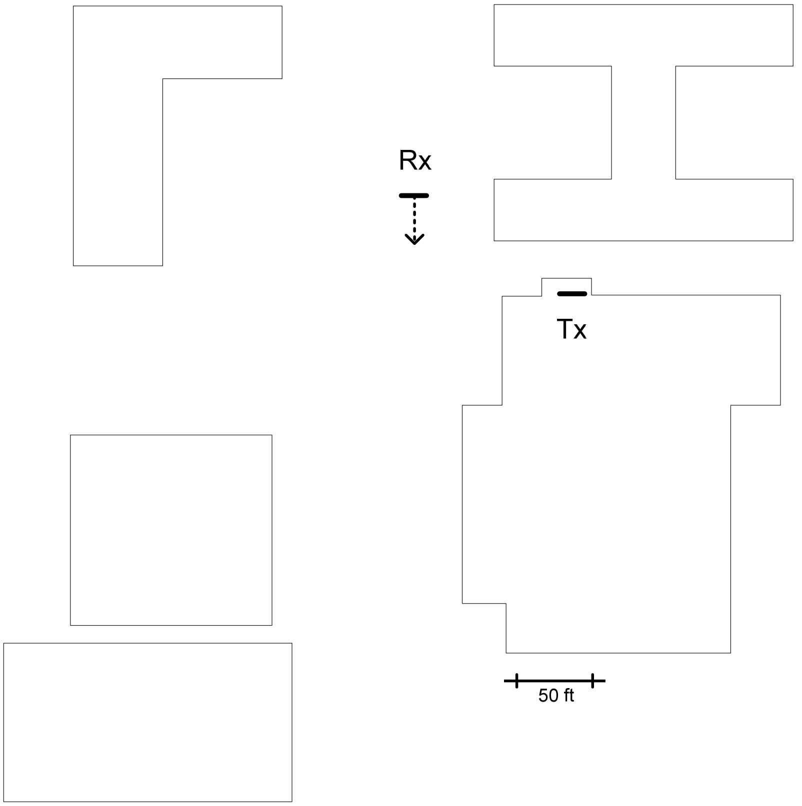

Figure 4.4: Aerial overview of the buildings for the Indoor to Outdoor transmission environment with relative positioning of transmitter and receiver, array orientations. The transmitter was on the fourth floor of a building on the Brigham Young University campus.

4.3 Generating Analytical Models from Measured Channel Matrices

For synthesizing the Kronecker and Weichselberger models from measured channel gain matrices, the model components must first be estimated from the measured channel gain matrix data. Given a sequence of measured H-matrices, the link end correlation matrices can be estimated from the data according to:

$$\hat{\mathbf{R}}_{\mathbf{Rx}} = \frac{1}{M}\sum_{k=1}^{M}\mathbf{H}(k)\mathbf{H}(k)^H \tag{4.1}$$

$$\hat{\mathbf{R}}_{\mathbf{Tx}} = \frac{1}{M}\sum_{k=1}^{M}\left(\mathbf{H}(k)^H\,\mathbf{H}(k)\right)^T \tag{4.2}$$

To determine the link end eigenbases, the eigen-decomposition of the estimated link end correlation matrices was performed. The estimated eigenbases are denoted as $\hat{\mathbf{U}}_{\mathbf{Rx}}$ and $\hat{\mathbf{U}}_{\mathbf{Tx}}$. Finally, the power coupling matrix $\mathbf{\Omega}$ was generated from the measured data and the estimated eigenbases:

$$\hat{\mathbf{\Omega}}_{\mathbf{weich}} = \frac{1}{M}\sum_{k=1}^{M}\left(\hat{\mathbf{U}}_{\mathbf{Rx}}^{\mathbf{H}}\mathbf{H}(k)\hat{\mathbf{U}}_{\mathbf{Tx}}^{*}\right)\circ\left(\hat{\mathbf{U}}_{\mathbf{Rx}}^{\mathbf{T}}\mathbf{H}(k)\hat{\mathbf{U}}_{\mathbf{Tx}}\right) \tag{4.3}$$

In (4.1-4.3) $\mathbf{H}(k)$ refers to the k^{th} measured channel matrix realization from which the estimate is being generated. Using the estimated model components, the Kronecker and eigenbasis model channel matrices can then be synthesized according to (3.15) and (3.17), respectively.

4.4 Channel Metrics: Model Performance Comparison

In this section, the impact of the choice of the channel model on commonly used channel metrics is investigated. To do this, Kronecker and Weichselberger model components are estimated from measured channel data. Many channel realizations are synthesized for each of the models using the estimated model components. The synthesized channels for the Kronecker and Weichselberger models will be then be used to evaluate several channel metrics. The same channel metrics will be evaluated using the measured data. The differences between the measured data channel metrics and the metrics predicted by the two channel models are compared. The results show that the Weichselberger model significantly outperforms the Kronecker model, matching more closely to the true channel metrics.

4.4.1 Experimental Data

Data obtained from two different locations within the Brigham Young University campus Coal Yard were used for comparing the metrics for the two channel models. At each location, four different data sets are available. For the odd-numbered data sets, the transmitter and receiver were stationary. For the even-numbered data sets, the receiver was mounted on a moving platform. The geometry of the Coal Yard sets is given in Figures 4.1 and 4.2. These experimental data sets were recorded using a system with 8 transmit antennas and 8 receive antennas. All antennas were used for the computing the metrics and performing the comparisons. For each metric, the percent error in the prediction between each model and the actual data metric was computed. This error is the magnitude difference between the model metric and the data metric, relative to the data metric, averaged over all data sets.

4.4.2 Results of Metrics Comparisons

4.4.2.1 Uninformed Transmitter Capacity

Using 2000 samples of the **H** matrices from each of the data sets at each location, the average uninformed transmitter capacity was calculated according to (3.19). For this investigation, we hold the SNR fixed at 20 dB unless otherwise noted. The results are summarized in Table 4.1.

For sets 1 and 3 the capacity predicted was in error by 26.7%, on average for the Kronecker model, while the Weichselberger model erred by an average 5.3%. For the even sets, the underlying statistics of the channel gains were better represented in magnitude and phase by a Rayleigh and uniform random distribution respectively. An

Table 4.1: Uninformed Transmitter Capacity, b/s/Hz

Location 1				
	Set 1	***Set 2***	***Set 3***	***Set 4***
Data	16.5	18.4	18.2	18.2
Kron	11.9	17.0	13.3	16.8
Weich	16.0	18.0	17.3	17.7
Location 2				
	Set 1	***Set 2***	***Set 3***	***Set 4***
Data	19.5	18.4	18.9	18.0
Kron	14.3	17.4	14.2	16.6
Weich	18.3	18.1	17.6	18.0

example of the difference in statistics is shown in Figure 4.5, for Sets 1 and 2 taken at Location 1. As the transmitter was not moving for the odd data sets, there was less variability in the environments compared to the even data sets. Thus, the difference in statistics is not surprising. Since the even data sets better fit the underlying assumptions of the statistics for the models under investigation, it is not unexpected that the error for the even sets averages to 7% and 1.6% for the Kronecker and Weichselberger models, respectively.

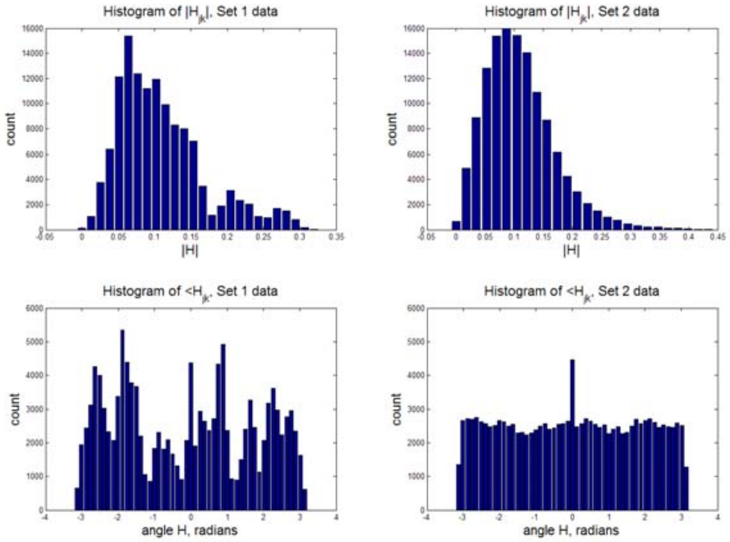

Figure 4.5: Aggregate statistics for the channel gains for sets 1 and 2 in Location 1 within the Coal Yard on the BYU campus.

4.4.2.2 Eigenvalue Spread

The eigenvalue spread gives an indication of how well both channel models represent the environment in terms of modeling the multipath present. The eigenvalue spread was evaluated by computing the squared singular values from the measured and modeled channel matrices. The eigenvalue spread was then determined according to (3.20). In all cases, the Weichselberger model outperformed the Kronecker model in terms of providing a closer match to the actual eigenvalue spread. In general, the Kronecker model consistently overestimated the largest eigenvalue for the data, and underestimated the middle eigenvalues. Since this metric looks at the ratio of the largest eigenvalue to the third largest eigenvalue, this behavior results in the consistent overestimation of the eigenvalue spread. For all data sets, the eigenvalue spread predicted by the Kronecker model differed from the actual eigenvalue spread by 44.2% on average. In contrast, the Weichselberger model averaged just 10.5% error in predicting the actual eigenvalue spread correctly. For both cases, this error was largely driven by the odd data sets, with a larger variability in performance seen by the Kronecker model. The eigenvalue spread results are summarized in Table 4.2.

Table 4.2: Eigenvalue Spread, dB

Location 1				
	Set 1	***Set 2***	***Set 3***	***Set 4***
Data	10.3	8.6	8.3	8.8
Kron	15.9	9.8	13.5	9.8
Weich	9.9	9.3	8.6	9.5
Location 2				
	Set 1	***Set 2***	***Set 3***	***Set 4***
Data	7.1	8.2	5.4	8.3
Kron	12.0	9.0	11.4	10.1
Weich	7.8	8.7	7.6	8.7

4.4.2.3 Condition Numbers

The condition number metrics were evaluated next. Two different forms were examined: the traditional definition, as given in (3.21) and the Demmel condition number, as defined in (3.22). The condition numbers for the measured channel matrices and the synthesized model channel matrices were determined, and the average condition numbers compared.

A significant performance difference was observed between the odd and even data sets for accurate condition number prediction. For the odd data sets, the Kronecker model erred in predicting the channel condition number, on average, by 880%. The Weichselberger model had better performance, but was not a particularly good match for the odd data sets either, with an error of 68.6%. The even data sets provided a closer match in both cases, averaging 61% and 14% error for the Kronecker and Weichselberger models, respectively. It is clear that neither model gives a good representation of the channel condition numbers in environments that are relatively static. Using either model to accurately predict the condition number as a basis for choosing between the operational modes of spatial multiplexing or spatial diversity as in [11, 12] would be difficult for these sorts of environments.

The Demmel condition numbers provided a more accurate match with the channel for the even data sets than the odd. For the even data sets, an average error of 57.5% and 12.8% were observed for the Kronecker and Weichselberger models. To illustrate the difference in the model performance, the histograms of the Demmel condition numbers are shown in Figure 4.6 for Location 1, Sets 1 and 2.

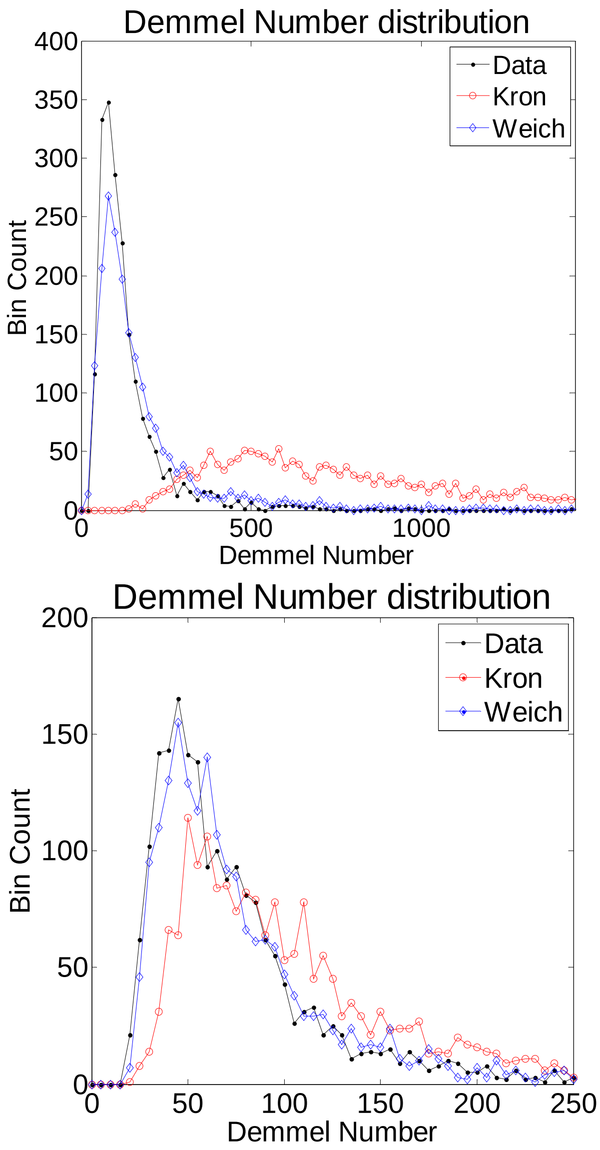

Figure 4.6: Histograms of the Demmel Condition number. *Top* - Location 1, Set 1 (transmitter stationary). *Bottom* – Location 1, Set 2 (transmitter mobile).

4.4.2.4 Correlation Matrix Distance

The correlation matrix distance, as defined in Section 3.5.1.4, is an interesting metric to investigate for a variety of reasons. This metric provides a means for gauging how close the models come to representing the full correlation matrix, **R**. Also, this metric can be thought of as a way to track the stationarity of the channel.

In considering this metric, the length of the average for creating the Weichselberger and Kronecker models must be specified. Specifically, since parts of the model must be estimated from the data, the length of the data used for the estimation will influence the validity of the end model. A short average will lead to high variability in the model representation; a long average will lead to a poor representation of temporally localized changes. Thus, an appropriate average length was selected to generate a good estimate of the channel parameters while not exceeding the time over which the channel is stationary. The average length used for the even sets was 500 samples. For the odd sets 750 samples were used.

First the distance between the correlation matrix for a particular model and the correlation matrix from the data was evaluated to provide a metric for the error between a model's representation and the actual data. Table 4.3 summarizes the performance of the models. While neither model provides a good match for the odd data sets, as with other metrics investigated, the Weichselberger model provides a much closer match. For the even sets, the Weichselberger model erred by 14.9% on average, while the Kronecker erred by19.8%.

Table 4.3: Full Correlation Matrix Distance

Location 1				
	Set 1	***Set 2***	***Set 3***	***Set 4***
Kron	0.31	0.23	0.43	0.23
Weich	0.24	0.19	0.32	0.22
Location 2				
	Set 1	***Set 2***	***Set 3***	***Set 4***
Kron	0.52	0.21	0.53	0.17
Weich	0.36	0.17	0.39	0.11

Secondly, we look at the evolution of the correlation matrix distance over time. Since the correlation matrix distance increases as the channel changes, the metric provides insight into the stationarity of the channel. Typical results for the odd data sets and the even data sets are shown in Figure 4.7. The channel in Location 1, Set 1 is relatively stationary, maintaining the same level of correlation matrix distance as time progresses. The channel in Location 1, Set 2 is less stationary, as seen in Figure 4.7, bottom. In this channel, if the initial estimate at time instance 1 was sent back to the transmitter, the correlation matrix distance provides an estimate of when the channel needs to be updated. In [13], the authors used synthesized data sets to conclude that a reasonable correlation matrix distance threshold was around 0.2. Beyond this threshold, the "old" channel correlation matrix being used at the transmitter differs enough from the actual channel to cause significant performance degradation. In considering the same threshold here, it is clear that around time index 200, an update would have to occur for Set 2. Averaging over Sets 2 and 4 for Location 1, the transmitter would need updates every 193 time units, according to the self-correlation matrix distance on the data. Tracking the difference between the initial data estimate and the Weichselberger model, an update is predicted to be necessary in 198 time units. In comparison, the Kronecker model predicts an update is necessary every 131 time units. For these data sets, time is in units of 2.5 ms.

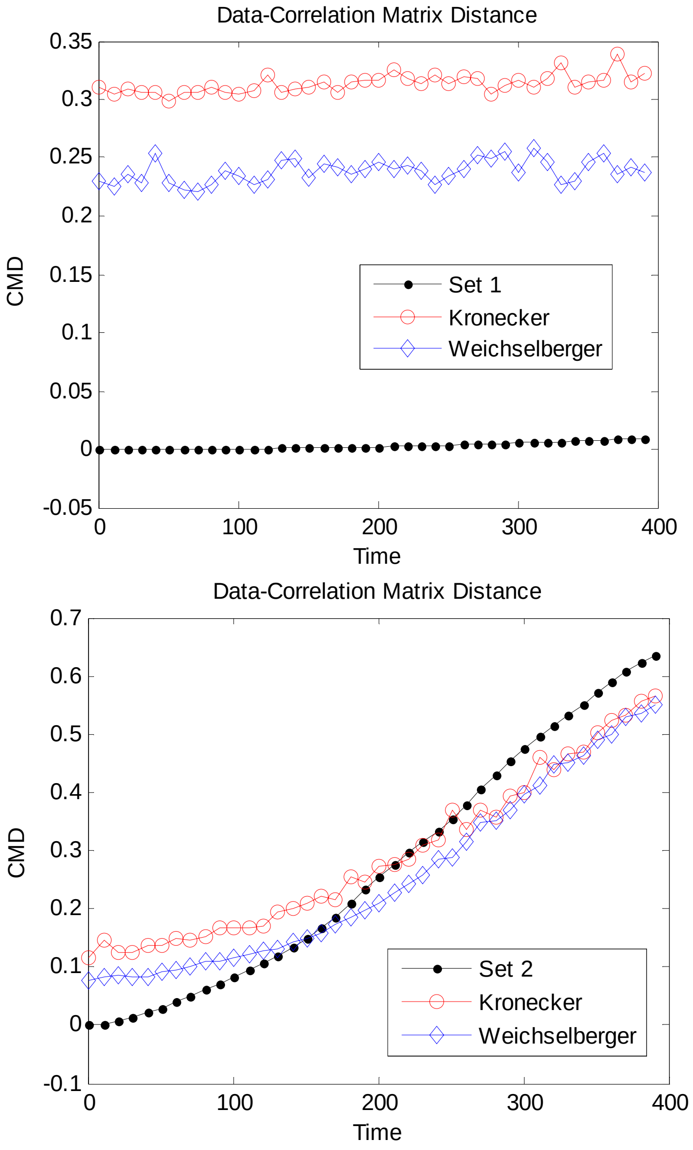

Figure 4.7: Correlation matrix distance as a function of time. Top - Location 1, Set 1 where the transmitter is stationary. Bottom - Location 1, Set 2, where the transmitter is moving. Time is in units of 2.5 ms.

4.5 In-depth Examination of the Weichselberger Model

Now that it has been established that the Weichselberger model is better at providing information about the channel than the Kronecker model, we turn to examining the underpinnings of the model to understand this improvement. This section uses signal processing techniques to better understand how the environment is reflected in the structure of the Weichselberger model generated from measured data. In his doctoral thesis, Weichselberger primarily uses simulated data examples to examine the underpinnings of his model, while using measured data to indicate superior performance in capacity and azimuth power spectrum (APS) representations over two other analytical channel models [14]. Our goal is to tie the model underpinnings to measured data by tying physical environments to the model behavior. Given the environmental and array geometry, we attempt to discern the arrival directions of high power from measured MIMO channel gain data. By comparing the response from the data with the response from the Weichselberger model components, we show how the model represents the environment, tying in the physical components of the channel with the analytical model.

4.5.1 Measurement Environment

To better understand the model, we consider as simple a geometry as the measured data provides. As such, we look at the Coal Yard odd data sets, as the geometries are fixed and all changes are coming from changes in the environment. Since the data acquisition window is short, few environmental changes occur over the window. For these data sets, the channel coupling matrix diagonalizes well. This form of the Weichselberger model indicates that each transmit eigenvector is strongly coupled with only a single receive eigenvector. Three buildings provide excellent candidates for single bounce paths in this non-line of sight environment. They are designated in Figure 4.8. The coupling matrix, $\mathbf{\Omega}$, for this environment is given in Figure 4.9. To examine how the model represents the flow of power within the environment, we turn to beamforming techniques.

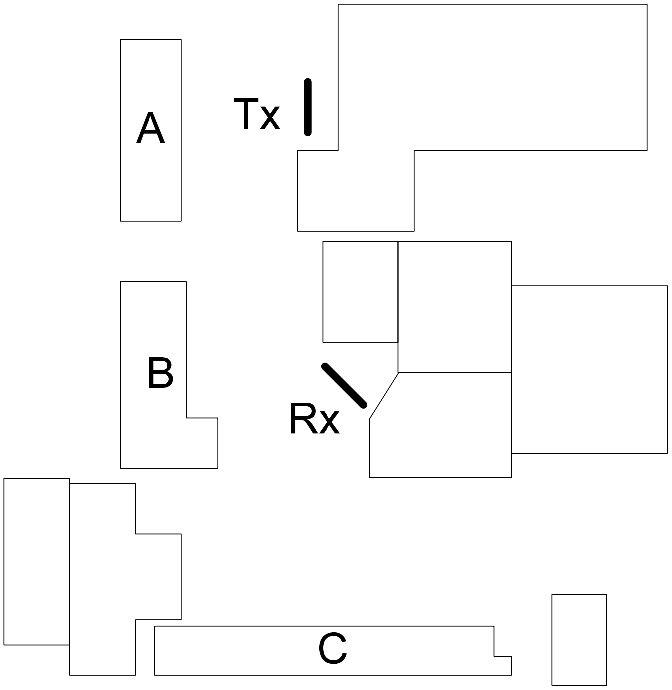

Figure 4.8: Simplified Coal Yard geometry with array orientations, for Location 1, Set 1.

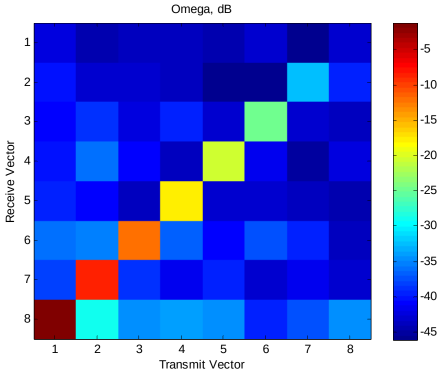

Figure 4.9: Power coupling matrix for Coal Yard, Location 1, Set 1.

4.5.2 Beamforming

To examine the sources of power in an environment from the perspective of the transmitter and receiver, we consider two different beamforming techniques for beamforming on the link end covariance matrices: conventional frequency domain beamforming (CBF) and minimum variance distortionless response (MVDR) beamforming. Both beamforming techniques are used to identify the arrival angle of a source (or sources) of energy in an environment and are outlined in Chapter 3, with more details in [15]. By determining the angles from which high energy sources are arriving, we can determine the likely scatterer for that source within the environment.

While MVDR beamforming has better angular resolution than CBF, a new weight vector must be computed for each steering direction using MVDR beamforming, making it more computationally expensive than conventional beamforming. Also, unlike the CBF, the MVDR BF not only passes the desired signal for the look direction, it also steers nulls in the direction of other strong arriving signals, resulting in its performance improvement. MVDR beamforming may suffer from signal cancellation issues in the presence of correlated arrival signals, such as those arising from correlated multipath. Thus, by using both techniques, we gain confidence in the MVDR results from the CBF techniques, and better resolution from the MVDR results than the CBF ones.

4.5.3 Beamforming Results

4.5.3.1 Coal Yard, Location 1

The link end correlation matrices were processed at the receiver and transmitter using both techniques. A comparison of the two responses is shown in Figure 4.10 and Figure 4.11 for the transmit and receive correlation matrices, respectively. Results are reported for both CBF and MVDR beamforming. If the CBF offers similar but less resolved peaks in the spectrum as the MVDR beamformer, we gain confidence in the output of the MVDR. For the results given, the angular results reported are relative to the orientation of each array, with 0 degrees corresponding to broadside. The output power is plotted in dB vs. θ_m, where θ_m sweeps from -90° to 90°.

For the transmit array, negative angles correspond to looking toward Building C, as seen in Figure 4.8. For the receive array, the negative angles correspond to looking toward Buildings A and B. Strong paths can be seen in the transmitter directions at around -55, -30 and slightly weaker paths at 15, and 75 degrees. For the receiver, strong signals arrive from negative endfire, 5 degrees, and around 40 degrees.

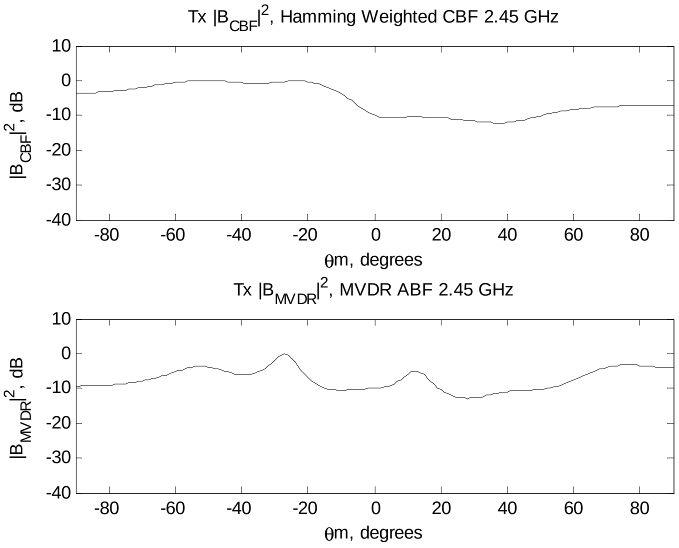

Figure 4.10. Link End Response: Beamforming on the transmit correlation matrix, CBF vs. MVDR

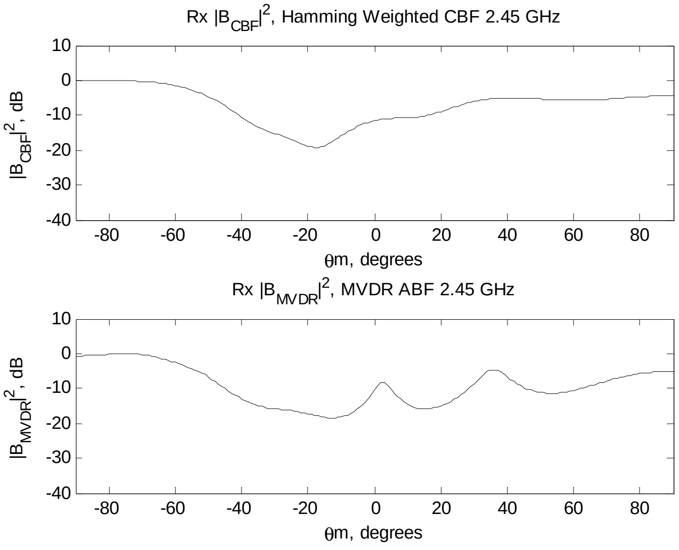

Figure 4.11: Link End Response: Beamforming on the receive correlation matrix, CBF vs. MVDR.

We examine the environment given in Figure 4.8 to see if these arrival and departure directions that align with strong powers make sense. As there are a lot of potential scatterers in the environment, we consider the fact that paths requiring multiple reflections between the transmitter and receiver likely will be attenuated significantly in comparison to single bounce arrivals. Thus, we will examine single bounce paths as our primary sources of the power. Buildings A and B in the environment are the most likely candidates of single bounce, high power contributions between the receiver and transmitter. Relative to the geometries of the transmitter, these buildings could correspond to the -55 and -30 strong transmit directions. On the receiver side, the resolution of the beamformer is not as good in the endfire directions, so it is difficult to distinguish between the arrivals. However, there is a strong contribution arriving at negative endfire that dominates the response of the receive array. Additionally, at the receiver, we expect a strong contribution from Building C that arrives at around 45 degrees. The beamformer indicates strong power arriving from around 40 degrees, which is in reasonable agreement with our expectations, given the environmental geometry.

Now, we consider how the Weichselberger model operates. The model ties the behavior of the link end eigenvectors together through the coupling matrix. From Figure 4.9, we can see that most of the power is contained in the diagonal terms. In fact, for this scenario, 94% of the power is contained in the first 3 diagonal terms. Based on the diagrams, the basis vectors of interest are receive eigenvectors 8, 7, and 6, and transmit eigenvectors 1, 2, and 3. Thus, we now use traditional frequency domain beamforming on the eigenvectors to examine their structure. The results can be seen in Figure 4.12.

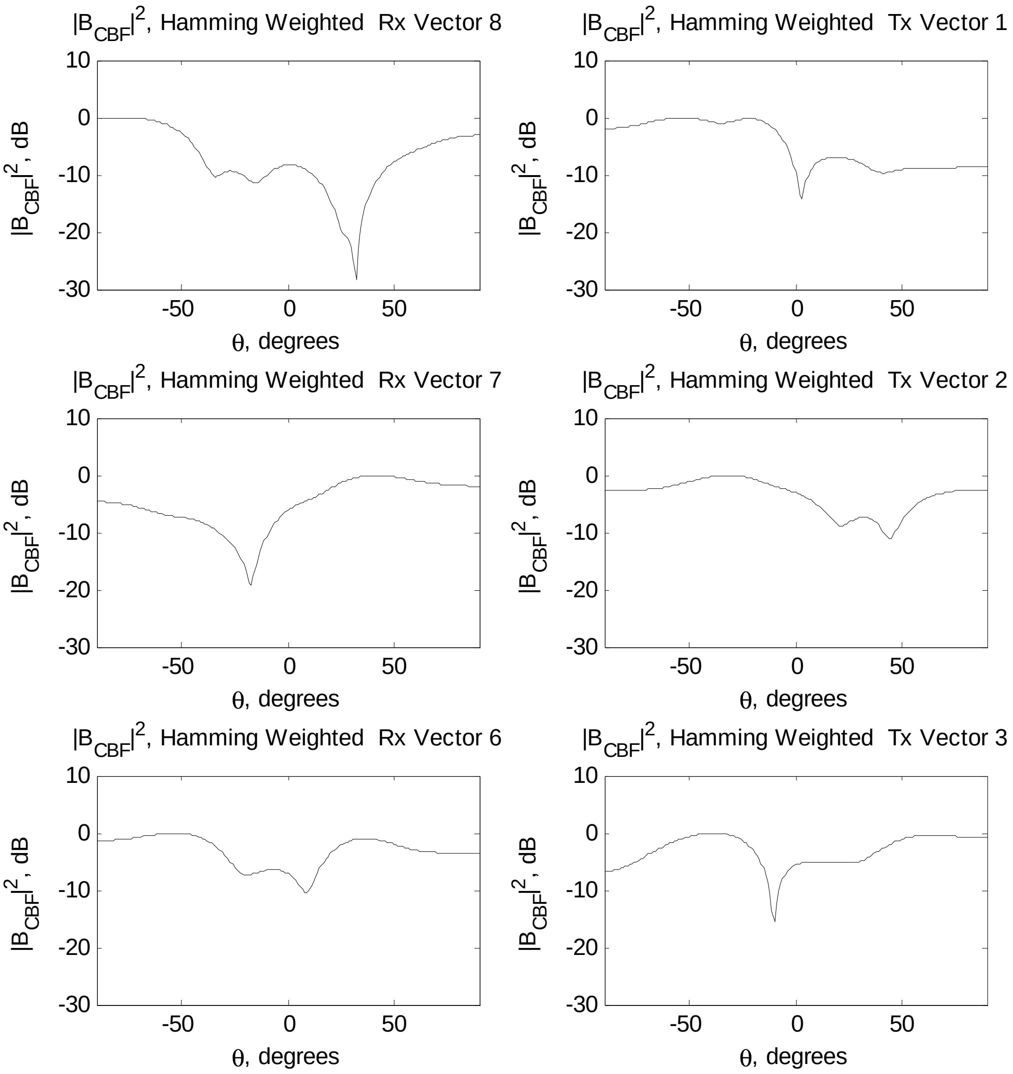

Figure 4.12: Eigenvector Response: Beamforming on the transmit and receive eigenvectors.

Clearly, these eigenvectors dominate the responses seen in Figure 4.10 and Figure 4.11. If we use just the diagonal power values to weight each of these vectors and sum the responses together, we get back a reasonable approximation to the power spectrum from the link end responses, which is seen in Figure 4.13.

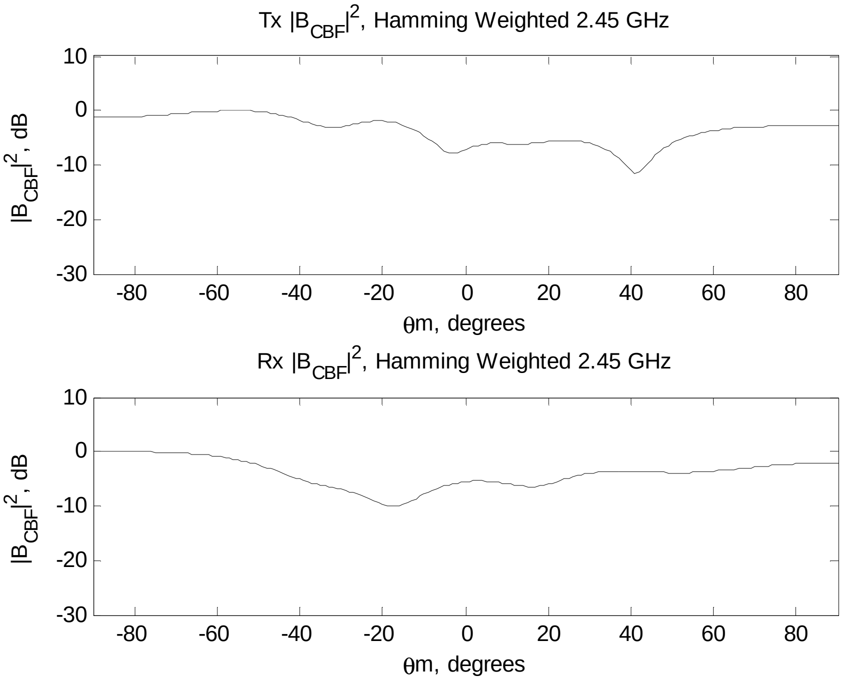

Figure 4.13: Weighted sum response of the highest powered eigenvectors.

4.5.3.2 Coal Yard, Location 2

Given that the primary scatterers in the environment are buildings, it is difficult to move the scatterers to generate a new response. However, if we consider a different receive location, we should see a difference in the response as the multipath has changed. An additional location with the same transmitter orientation and location, but a different receiver geometry is available for investigation. This set will be referred to as Location 2. The receiver is moved to Location 2, and the orientation of the array is a 90 degree rotation from the previous orientation. The movement from location 1 to 2 is small relative to the distance of the scatterers to the arrays. As such, we do not anticipate a significant difference in the transmit array response. However, the receiver axis was rotated, so we now anticipate that the reflections from buildings A and B to be arriving in a broadside direction versus an endfire direction. The new configuration is shown in

Figure 4.14. The coupling matrix is given in Figure 4.15. Note that only approximately 90% of the power is accounted for in the three highest power diagonal terms in this scenario. It would take four diagonal terms in this transmission scenario to account for 95% of the power in the channel.

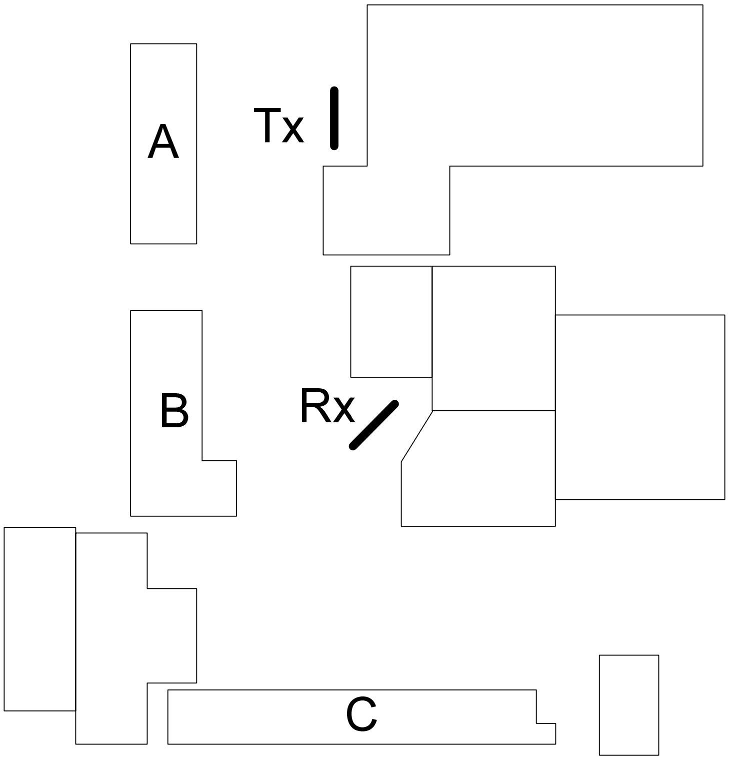

Figure 4.14: Coal Yard geometry, location 2, with array orientations.

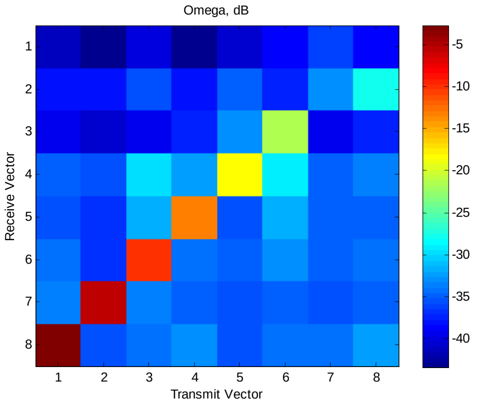

Figure 4.15: Power coupling matrix, location 2.

As with the previous Coal Yard location, we examine the directional responses of the eigenvectors associated with the three highest powers in the diagonal for this new location. The results can be seen in Figure 4.16. As expected, the primary response at the receiver is oriented around the broadside direction. Note, to orient the directions, negative endfire is in the direction of Building B. There is also a contribution

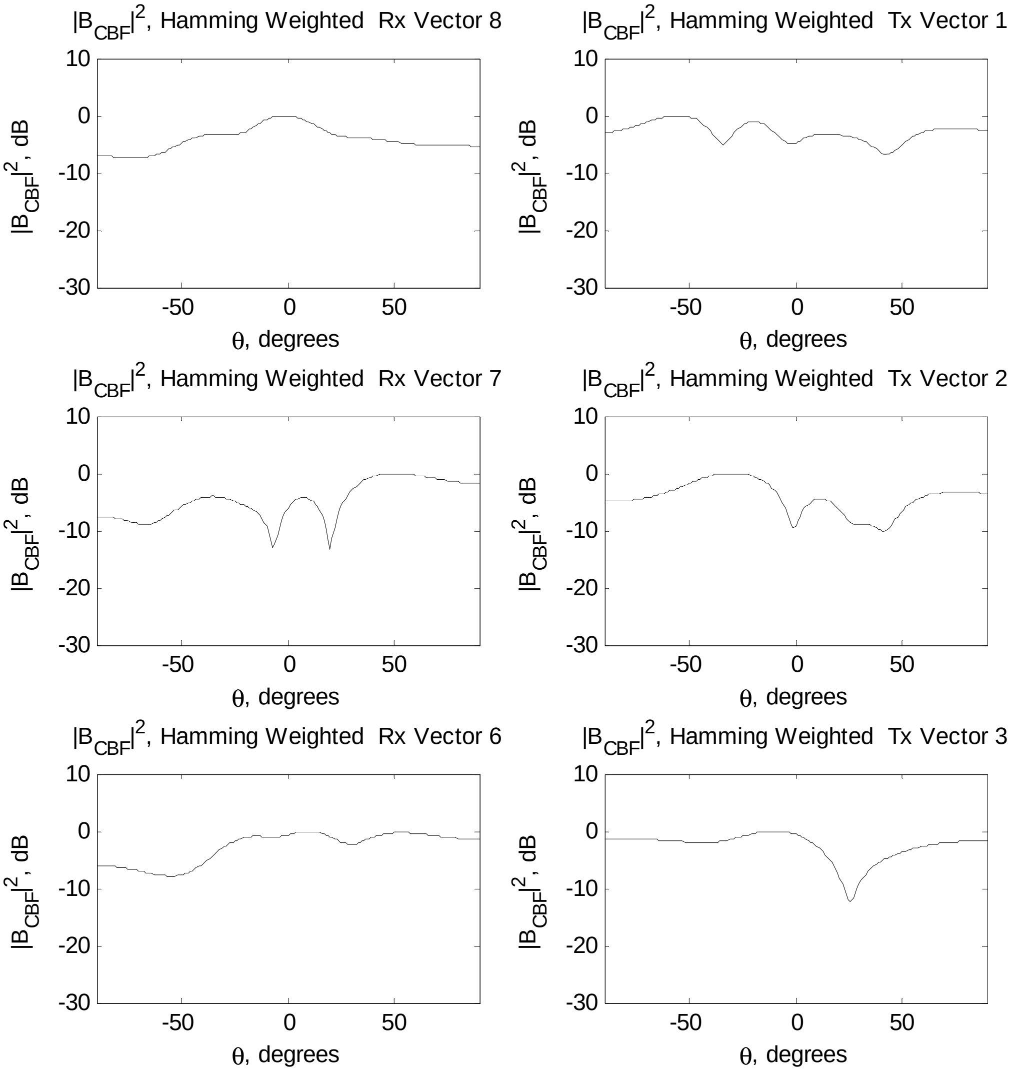

Figure 4.16: Eigenvector Response: Beamforming on the transmit and receive eigenvectors, Location 2.

at approximately 45 degrees, which corresponds to Building C. While the transmitter eigenvectors do not correspond perfectly with the previous example, the two higher powered ones, which contain 90% and 80% of the power in locations 1 and 2 respectively, do show significant similarity. Both have high powered sources in Vector 1 at -60 and -25 degrees. Vector 2 also is similar, in that it indicates high power at around -30 degrees. Vector 3 from Location 2 is also similar, but lacks some of the structure in the positive endfire direction that is found at location 1. Since this vector is at such a low power in comparison to the other two (15 dB down), the lack of correspondence is not surprising.

Clearly, from this example, the eigenvectors capture the antenna configuration, as well as they are dependent on the channel. From the perspective of the transmitter, the channel changed only slightly, with little localized changes, resulting in similar eigenvectors at the link end. At the receiver side, the movement resulted in a change of orientation, corresponding to completely different eigenvectors. From these data sets, we have been able to establish a correspondence with the environment and the model parts. Specifically, we have shown how the eigenvectors represent the antenna array orientation behavior at the link end. We now examine the coupling matrix in more depth.

4.5.4 Structure of Ω: Measured Data

In the previous sections, a strong correspondence between the eigenvectors of Location 1 and Location 2 for the transmit antenna was observed, even though the receive antenna had moved. Due to this similarity, we conjecture that the eigenbases are relatively stable over small changes in position, relative to the scale of the scatterering environment, so long as the geometry of the arrays and their orientations are maintained.

Given this assumption, it is now possible to examine how the structure of $\mathbf{\Omega}$ changes as the environment changes.

For Locations 1 and 2, data sets are available in which the receiver is stationary, as in the previous discussion, and in which the receiver is in motion, moving at a rate of 1 foot/second. If we fix the eigenvectors to be the eigenbases at the starting point, and change the angle at which dominant energy is arriving enough, we ought to see the power in the coupling matrix shift to correspond with the eigenvector that best describes the direction the scatterer is now in.

Since the link end is in motion, we do not expect that the channel will diagonalize as well. Energy will spread out around the diagonal as the channel is changing, so directions will not perfectly align with scatterers, but align with the average response from a direction. This means that some energy will couple into other eigenvectors to best describe the average channel behavior. The eigenvectors, as in the previous cases, are shown for the three eigenvectors that align with most of the power in the channel on both the transmit and receive sides for Location 2, in which the receiver is mobile (see Figure 4.2). They are displayed in Figure 4.17. The coupling matrices for four different sections of the data record are presented in Figure 4.18, labeled with the sample that started the averaging process to estimate the coupling powers. For estimating the coupling matrices, 500 channel matrices were used.

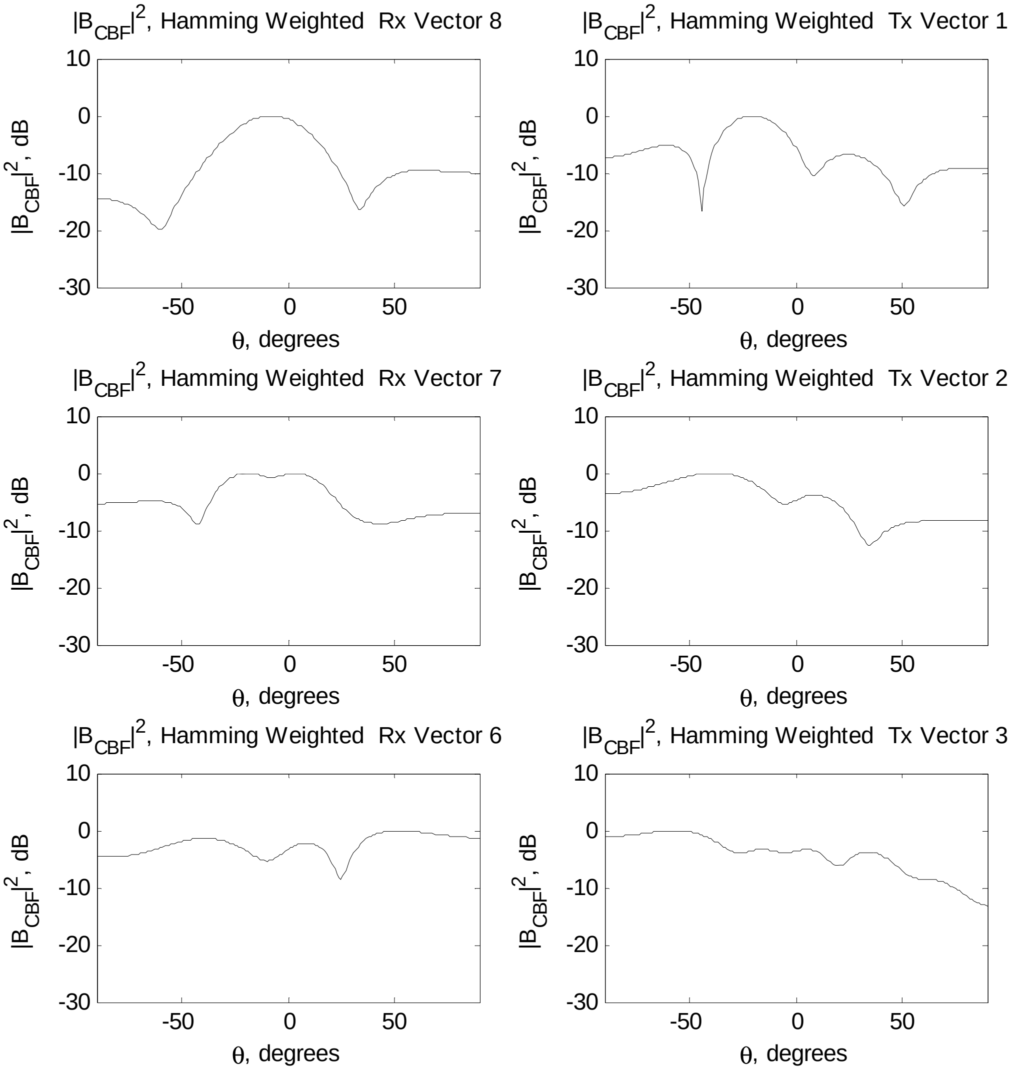

Figure 4.17: Eigenbases Response: Beamforming on the transmit and receive eigenbases, Location 2.

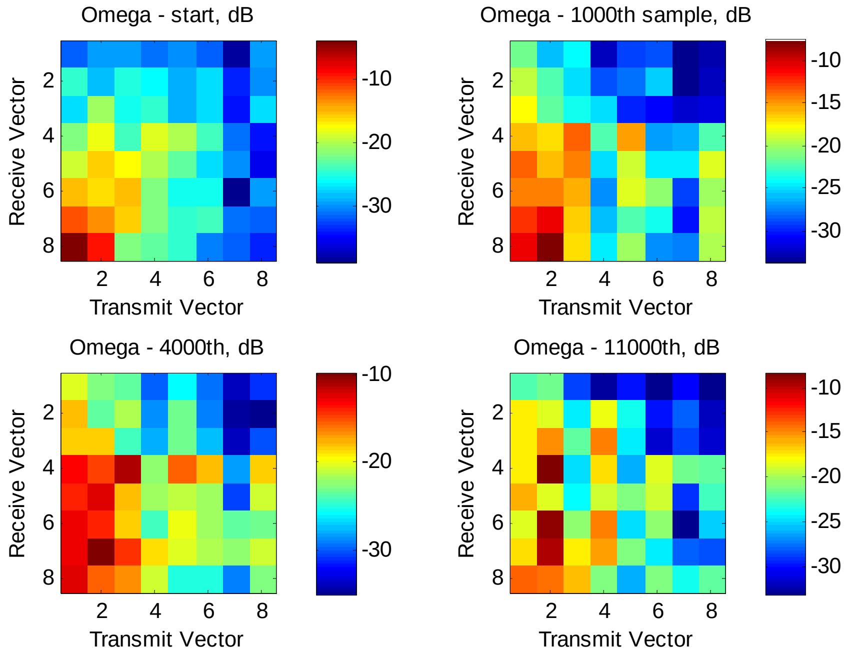

Figure 4.18: Coupling matrices for Location 2 at various times in the data record, generated using the eigenbases associated with the initial **Ω**.

The receiver was moved along a 30 foot path from the initial position on a horizontal track, due left toward Building B. The orientation of the receiver array remained fixed while it was moved. Using principles from geometrical optics, we expect that the angle of incidence and reflection from the scatterer to be equal. At the initial computation of **Ω**, receive eigenvector 8 and transmit eigenector 1 appear to point to building A (see Figures 4.2 and 4.14). As the receiver moves left, we expect that the angle of incidence and reflection to increase, effectively moving the reflection point on Building A in the direction of Building C. This would increase the angle at the transmitter of the high power path from the original -25 degrees toward -30 degrees. As we see in the **Ω** snapshots in Figure 4.18, the highest power value migrates from the first to the second transmit vector. In Figure 4.17, we note that this corresponds to the transmit power aligning more with Vector 2, pointing in the -35 degree direction than in the initial -25 degree direction. By the end of the data sets, the coupling matrix estimated from the data record beginning at the 11000th sample shows that the change in position has now changed the dominant receive positions to eigenvectors that point in directions neighboring the original broadside direction. The receiver power allocation has now adjusted to align with the change of position. Thus, the positioning of the scatterers in the environment, relative to the arrays, determines the distribution of the power in the coupling matrix.

4.5.5 Structure of Ω: Synthesized Data

Since it not possible to move scatterers such as buildings in an environment to examine the impact on the coupling matrix, we turn to geometrically based modeling to create a similar environment. A more detailed overview of using geometrical models to represent the environment is given in Chapter 5. Using a geometrically-based cluster model, similar to [16], the Coal Yard geometry seen in Figure 4.8 was simplified into three single bounce cluster locations, one each at Building A, B, and C. The simplification to just three single bounce locations provided a very close match to the receive environment, with good agreement in the overall power response across the transmit and receive arrays, as well as in the directions of the eigenvectors associated with the strongest powers. The strongest power eigenvectors for both the transmitter and receiver can be seen in Figure 4.19. Compared to Figure 4.17, the transmitter eigenvectors in Figure 4.19 are not as well represented by the model as the receiver eigenvectors are. This mismatch is due to many factors, including model simplification to capture only single bounce energy, as well as due to the use of only three scatterering clusters.

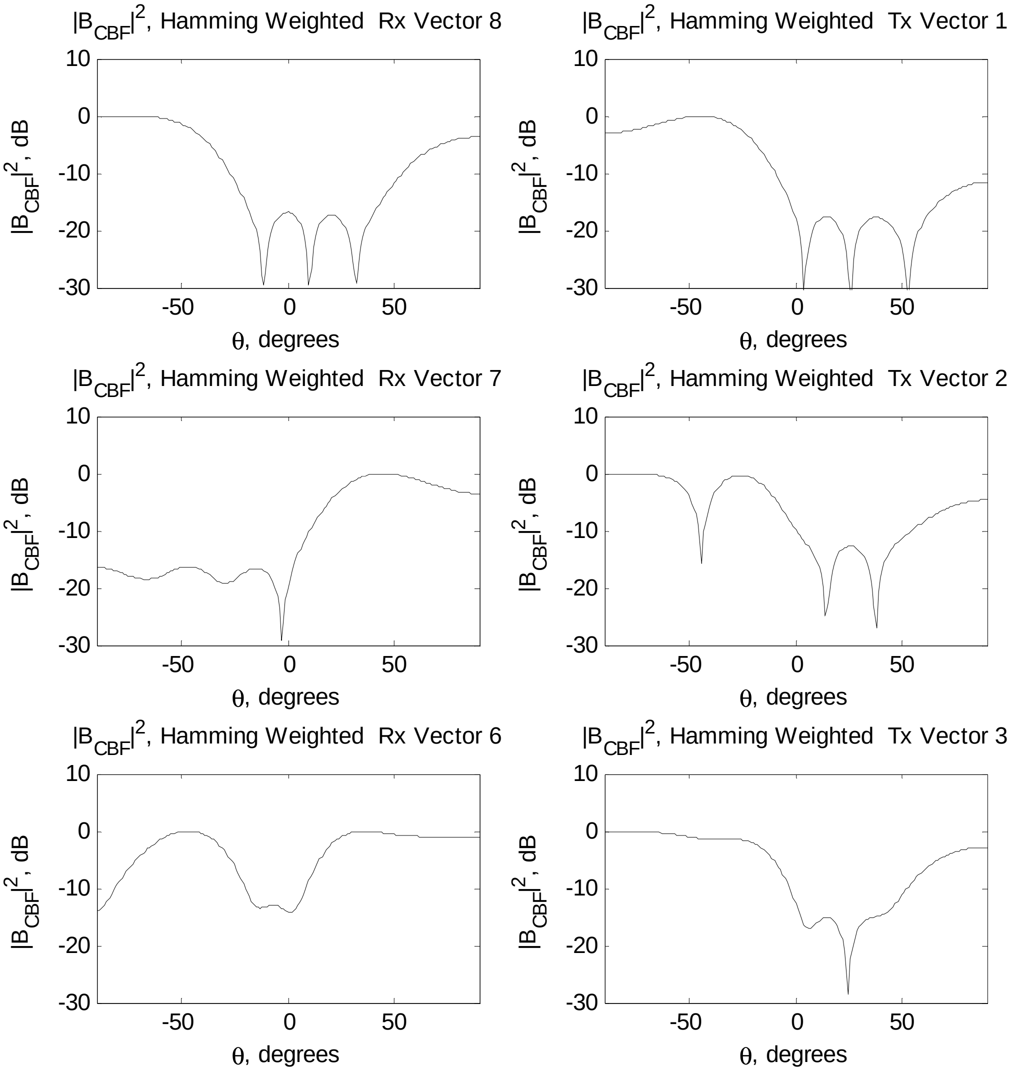

Figure 4.19: Strongest eigenvectors from the geometrical model data.

Using the model as a starting point, we can fix the eigenvectors and recompute the coupling matrix as scatterers move in the environment. In this case, we move the scatterer at building B to the right, as shown in Figure 4.20. In doing so, we expect that there will be a shift in energy on the receiver side from endfire to -45 degrees. Since not all of the scatterers are moving relative to the link ends, as in the previous section, we do not expect all of the energy in the coupling matrix to move. Only the energy associated with the scatter will move to align itself with the best match of the eigenvector. Clearly, since the transmit energy from Building B is now coming in from an angle closer to broadside, it is expected that a shift in energy will occur, moving energy from eigenvector 1 to eigenvectors 2 and 3. Similarly, the energy arriving at the receiver is no longer coming in off endfire from Building B, but is now coming in from roughly -45 degrees, corresponding to eigenvector 6. Thus, the change in energy locations shown in Figure 4.20 within the coupling matrix are as expected.

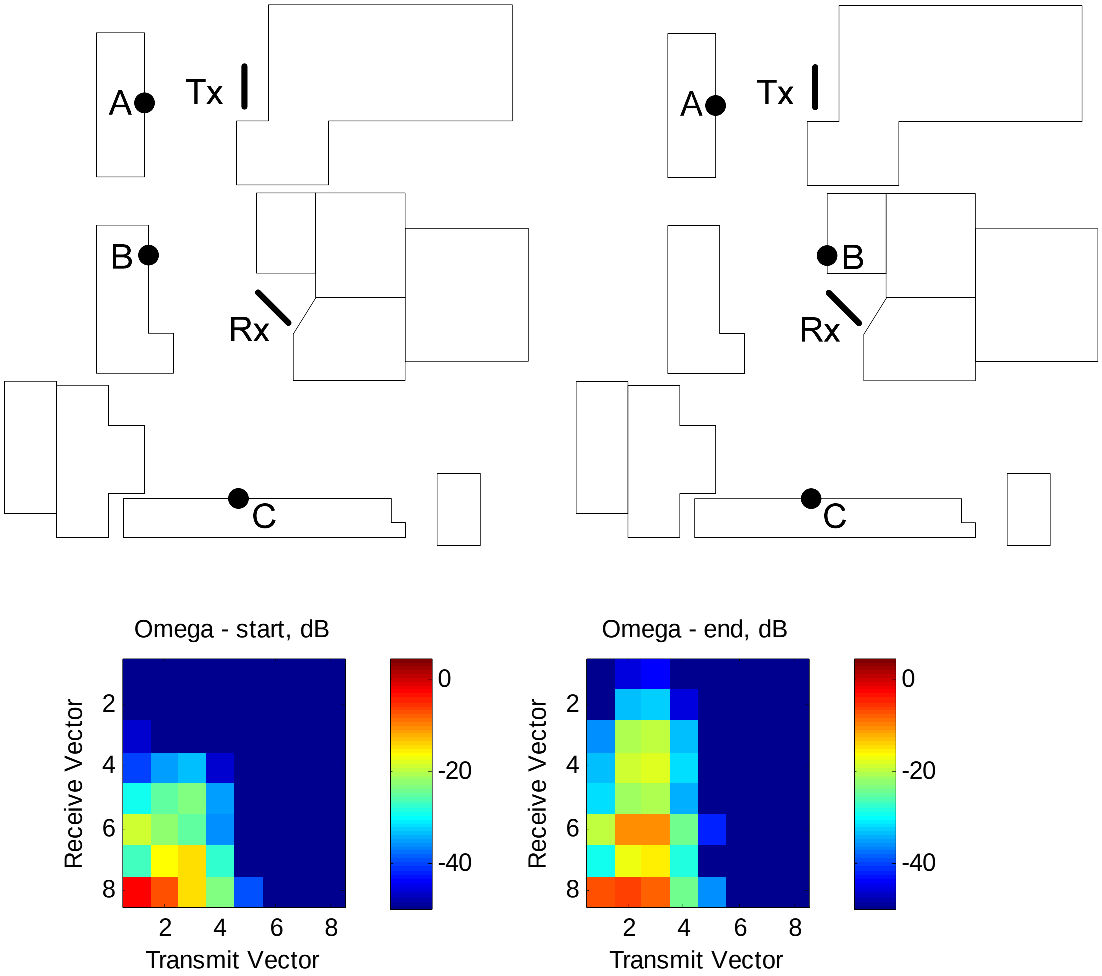

Figure 4.20: **Ω** at the original location within the Coal Yard, left. **Ω** after the scatterer is moved, right.

4.6 Summary

In this chapter, several MIMO data environments with different correlation structures were introduced. The measurements from these environments were used to investigate a variety of metrics used in channel characterization and feedback algorithms for two different analytical channel models. It was shown that the commonly used Kronecker model provides a poor estimate of many channel metrics, whereas the structured model presented by Weichselberger provides a significantly better representation.

Since the Weichselberger model is better suited to predicting the channel metrics investigated, it may have practical applications in the design of adaptive MIMO systems in which a feedback link is present. These applications will receive a more in-depth treatment in a later chapter.

Additionally, we used signal processing techniques to elucidate how the Weichselberger model captures the physical environment. Using measured data from several different data sets, we showed how the dominant scattering directions for an environment and the array orientation were captured by the link end eigenvectors. Furthermore, by fixing the eigenvectors, we showed how the coupling matrix links these directions together, noting the changes in the structure as the multipath in the environment changed due to receiver movement.

This work supports Weichselberger's model as a reasonable approximation to the environment. Although alternate analytical models exist, the simplified assumptions of those models do not render the physical environment with enough accuracy to be useful in a wide variety of transmission scenarios. In the case of the Kronecker model, the lack of a coupling matrix forces all basis vectors to couple into all other basis vectors. For channels, described by coupling matrices like Figure 4.15, severe underestimation of the channel metrics, such as capacity will occur as energy is forced into artificial associations between the transmit and receiver link ends.

4.7 Acknowledgment

This chapter, in part, is a reprint of the material as it appears in "MIMO Channel Models and Performance Metrics," L. C. Wood and W. S. Hodgkiss, *Global Telecommunications Conference, 2007. GLOBECOM '07. IEEE* , pp.3740-3744, 26-30 Nov. 2007 and "Understanding the Weichselberger Model: A Detailed Investigation," L. C. Wood and W. S. Hodgkiss, submitted to MILCOM 2008. The dissertation author was the primary author of these papers.

4.8 References

[1] W. Weichselberger, M. Herdin, H. Özcelik, and E. Bonek, *A Stochastic MIMO Channel Model with Joint Correlation at Both Link Ends*, IEEE Trans Wireless Communications, Vol 5, No. 1. Jan 2006, pp. 90-100.

[2] N. Costa and S. Haykin, “A Novel Wideband MIMO Channel Model and McMaster’s Wideband MIMO SDR,” *Conference Record of the Fortieth Asilomar Conference on Signals, Systems and Computers, 2006*, Nov 2006. pp. 956-960.

[3] M. Ozcelik, N. Czink, E. Bonek, "What makes a good MIMO channel model?," *Vehicular Technology Conference, 2005. VTC 2005-Spring. 2005 IEEE 61st* , vol.1, pp. 156-160, 30 May-1 June 2005

[4] R. B. Ertel, P. Cardieri, K.W. Sowerby, T. S. Rappaport, and J. H. Reed, “Overview of spatial channel models for antenna array communication systems,” *IEEE Personal Commun.*, vol. 5, no. 1, pp. 10–22, Feb. 1998.

[5] P. Almers, E. Bonek, A. Burr, et al., “Survey of Channel and Radio Propagation Models for Wireless MIMO Systems,” *EURASIP Journal on Wireless Communications and Networking*, vol. 2007, Article ID 19070, 19 pages, 2007.

[6] J.W. Wallace and M. A. Jensen, *Experimental analysis of the time-varying MIMO channel*, Antennas and Propagation Society International Symposium 2006, IEEE, 9-14 July 2006, pp. 321- 324.

[7] J.W. Wallace, M. A. Jensen, A. L. Swindlehurst, and B. D. Jeffs, *Experimental characterization of the MIMO wireless channel: Data acquisition and analysis*, IEEE Trans. Wireless Commun., vol. 2, pp. 335–343, Mar. 2003.

[8] J.W. Wallace and M. A. Jensen, "Time-Varying MIMO Channels: Measurement, Analysis, and Modeling,"*IEEE Transactions on Antennas and Propagation*, vol.54, no.11, pp.3265-3273, Nov. 2006.

[9] Y. Cocheril, P. Combeau, M. Berbineau, and Y. Pousset, "MIMO propagation channel characteristics in tunnels," *Telecommunications, 2007. ITST '07. 7th International Conference on ITS* , pp.1-6, 6-8 June 2007.

[10] S. Wyne, A. F. Molisch, P. Almers, G. Eriksson, J. Karedal, F. Tufvesson, "Outdoor-to-Indoor Office MIMO Measurements and Analysis at 5.2 GHz," *Vehicular Technology, IEEE Transactions on* , vol.57, no.3, pp.1374-1386, May 2008.

[11] D. Gesbert, H. Bolcskei, D. A. Gore, and A. J. Paulraj, *Outdoor MIMO wireless channels: models and performance prediction.* Communications, IEEE Transactions on, Vol.50, Iss.12, Dec 2002, pp. 1926- 1934.

[12] R. W. Heath and A.J. Paulraj, *Switching between diversity and multiplexing in MIMO systems*, Communications, IEEE Transactions on, Vol.53, Iss.6, June 2005, pp. 962- 968.

[13] M. Herdin, N. Czink, H. Özcelik, and E. Bonek, *Correlation matrix distance, a meaningful measure for evaluation of non-stationary MIMO channels*, Vehicular Technology Conference, 2005. VTC 2005-Spring. 2005 IEEE 61st, Vol.1, Iss., 30 May-1 June 2005, pp. 136- 140.

[14] W. Weichselberger, "Spatial structure of multiple antenna radio channels --- a signal processing viewpoint", PhD dissertation, Vienna University of Technology, Vienna, Austria, 2003.

[15] H. Van Trees, *Optimum Array Processing*. New York, Wiley-Interscience, 2002.

[16] K. H. Ng, E. K. Tameh and A. R. Nix, “Modelling and performance prediction for multiple antenna systems using enhanced ray tracing.” *2005 IEEE Wireless Comms. and Networking Conf.*, Vol.2, 13-17 March 2005, pp. 933- 937.

5 Using Analytical Models to Represent Geometrical MIMO Channels

5.1 Introduction

This chapter investigates the capabilities of analytical MIMO channel models in correctly capturing the underlying correlation structure of geometrically-based channels. The cross-correlation terms for the Kronecker and Weichselberger models are compared. The differences in the model correlation terms in comparison to the terms derived from the geometrically-based channels are noted, providing additional insight into the limitations of using either model in accurately predicting system performance.

Since the structure of the power coupling matrix drives the performance of the system metrics, it would be insightful to have a more comprehensive understanding of how the underlying physics of the environment influences the structure of the power coupling matrix. System parameters, such as array separation and the number of scatters are investigated for different interelement spacings. To generate the channel matrices, geometrical models are used. The impact on the structure of the correlation matrix is then determined.

5.2 Ability of Analytical Models to Capture Geometrically Modeled Physical Behavior

This section investigates whether analytical MIMO channel models can correctly capture the underlying correlation structure of geometrically-based channels. While the throughput possible in channels with uncorrelated Rayleigh distributed channel gains is well known, in practical transmission scenarios correlation is present. To represent the correlation, a variety of models have been proposed and used in literature to evaluate the channel [1-11]. Many schemes use these models, which may not provide a good representation of the channel or metrics in question.

The limitations and performance differences of two correlation-based analytical models, the Kronecker model and a structured eigenbasis model, are examined and compared. Correlation properties from three geometrically-based statistical models will be used to determine whether either model can adequately represent the correlation behavior of the channel. Additional insight into the limitations of using either model in accurately predicting system performance is provided through an examination of common channel metrics and the impact of modeling mismatch on those metrics.

In [12], the authors showed that the Kronecker model was not able to correctly capture the underlying physics in the channel, where the channel data was generated through a variety of geometrical channel models. This section extends their work to the structured eigenbasis model, which has been shown to better predict a variety of channel metrics, including channel capacity [13-15]. The performance of the analytical channel models in correctly modeling the correlation matrices formed by several geometrical models is examined. The geometrical models under consideration are the one-ring model, the combined elliptical-ring model, and a cluster model. Refer to Section 3.3 for details on these models.

The investigations reveal that while both analytical models tend to under-predict the magnitudes of certain correlation matrix terms for practical transmission scenarios, the Weichselberger model tends to under-predict the terms less severely than the Kronecker model. In fact, in certain transmission scenarios, the Weichselberger model provides a near-perfect match to the correlation values at all interelement spacings investigated. It is then shown how the under-prediction of terms impact common channel metrics. The performance differences between the two analytical models on these metrics are then compared.

5.2.1 Geometrical Model Simulation Parameters

Several different simulation scenarios were investigated, subsets of which are presented in Section 4.5.3. A 2 x 2 MIMO system operating at 2.45 GHz is analyzed. Unless otherwise noted, for all scenarios explored the transmitter and receiver arrays consist of identical linear arrays perpendicular to the transmission axis (broadside configuration). Additional configurations (i.e. broadside to endfire) will also be presented for the one-ring scenario.

For simulating the one ring transmission scenario, a distance of R = 4 kilometers between transmitter and receiver was used. The ring radius was set to ρ = 30 meters. The number of scatterers used was L = 20. Both broadside orientations of the link-end arrays and off broadside geometries were explored. See Figure 3.4 for the model geometry.

For simulating the combined elliptical-ring model, the same R and ρ values were used as in the one ring modeling scenario. The scatterer density was set to 1 km^{-2}, creating a variable number of scatterers per ellipse. The scatterers on the local ring are taken as a subset of scatterers from the first non-degenerate ellipse. The ratio of the scatterers on the local ring to the number on the first ellipse is called the local scattering ratio (LSR). The LSR considered is 0.3. The power-delay profile used for these simulations is consistent with those from the IEEE 802.16 models considered in [12]. An N = 3 ellipse model was considered. See Figure 3.5 for the model geometry.

For the cluster model parameters, a total of N = 5 clusters were considered, with each cluster having L = 20 scatterers. The distance between arrays is still R = 4 kilometers. The ring radius is set to 30 meters. These scattering ring locations were randomly selected, and assigned an average relative power based on the increased path length difference from the line of sight path. See Figure 3.6 for the model geometry.

5.2.2 Correlation Performance

Using the simulation parameters, the one-ring, elliptical, and cluster model channel matrices were generated. Many different realizations were formed for each of the channel models. From these geometrical channel matrices, the parameters required to generate the analytical channel models were estimated. The models were then synthesized according to (3.15) and (3.17).

To explore the differences in the models, a variety of interelement spacings was examined. The transmitter interelement spacing, Δ_{tx}, and the receiver interelement spacing, Δ_{rx}, are set to be multiples of each other. The correlation curves are reported for the one ring model in Figure 5.1 and 5.2, with $\Delta_{rx} = 40\Delta_{tx}$. This gives very different transmit and receive correlation responses. In general, the correlation response is complex, but the real part of the response is plotted. It was noted that the analytical models provided a very close match to the geometrically-based models for the r and t terms (see Equation 3.13), but that the terms s_1 and s_2 differed significantly. Thus, we provide all of the geometrical model correlation terms, but only compare the cross-correlation term s_1 for each of the models. The terms for the Kronecker model and Weichselberger's eigenbasis model are designated s1k and s1w, respectively, in all plots.

In Figure 5.1 under broadside transmission, it is clear that the Kronecker model s_1 term converges toward zero quickly. Due to this behavior, the Kronecker model is often said to ‘average’ the two one ring s_1 and s_2 correlation terms, which oscillate about zero. However, around $d/\lambda = 1.6$, where d refers to the distance between receiver elements, the Kronecker diagonal correlation term is not averaging the s_1 and s_2 terms from the one ring model. Instead, it converges to zero, which is the same average as the interelement spacings get larger. However, it is not the actual average of the response at that particular spacing. In contrast, the eigenbasis model diagonal term does appear to average the two cross terms at a particular interelement spacing. The model still exhibits high correlation values in magnitude, relative to the Kronecker model, at larger interelement spacings when both cross terms have similar high values. This means the Weichselberger model is more likely to provide useful insight into the channel than the Kronecker model since it follows the behavior of the channel.

By examining the underlying mathematics, we gain further insight into the observed behavior of the diagonal correlation terms. Under the Kronecker model assumptions, the term s_1 is a product of the transmit and receive correlations. This occurs as the full correlation matrix is a Kronecker product of the two link end correlation matrices. The same term under the structured eigenbasis model is a little more complex to compute. The full correlation matrix for the structured eigenbasis model can be determined from:

$$\mathbf{R}_{eig} = \sum_{m=1}^{2}\sum_{n=1}^{2} \omega_{m,n} \left(u_{tx,n} \otimes u_{rx,m}\right)\left(u_{tx,n} \otimes u_{rx,m}\right)^{H} \tag{5.1}$$

where $\omega_{m,n}$ is the entry in the power coupling matrix corresponding to the m^{th} receive eigenvector $u_{rx,m}$ and the n^{th} transmit eigenvector $u_{tx,n}$ and $\otimes$ indicates the Kronecker tensor product.

From (5.1) we can see that the correlation terms are weighted sums of the eigenmodes, thus forming a weighted average of the underlying signal space. The power-coupling matrix adapts to the scattering in the environment to change the weighting on the eigenmodes.

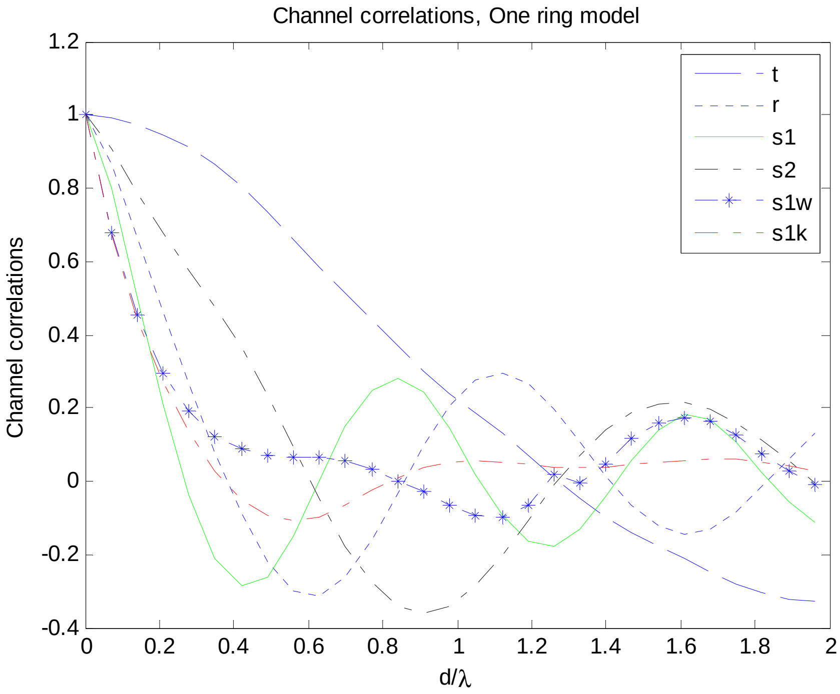

Figure 5.1: Channel correlations as a function of interelement spacing d/λ for the one-ring model, broadside to broadside transmission. The curves t, r, s1, and s2 correspond to the geometrical model correlation terms. The s1w and s1k curves correspond to the equivalent s1 term curves for the Weichselberger and Kronecker models, respectively.

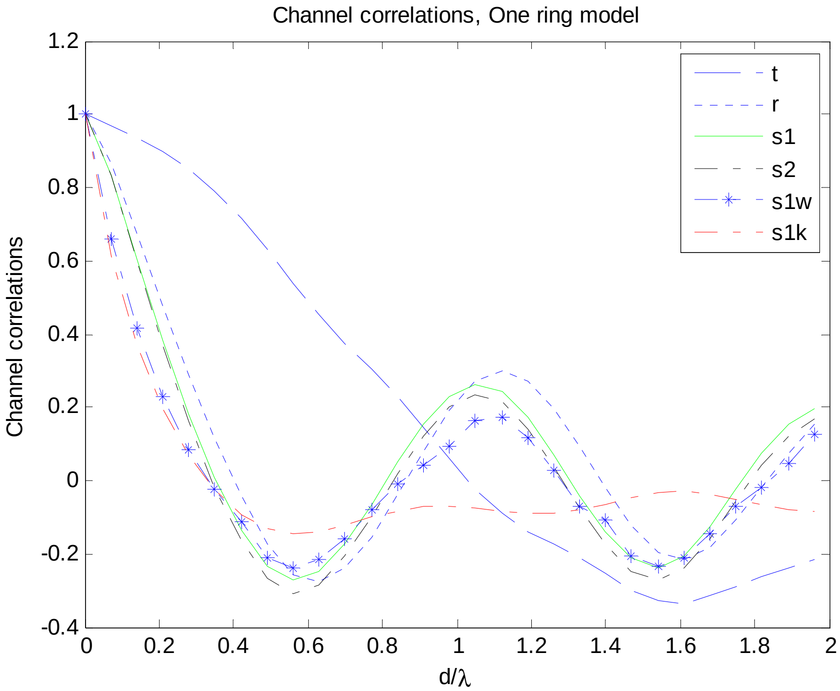

Figure 5.2: Channel correlations as a function of interelement spacing d/λ for the one-ring model, broadside to endfire transmission. The curves t, r, s1, and s2 correspond to the geometrical model correlation terms. The s1w and s1k curves correspond to the equivalent s1 term curves for the Weichselberger and Kronecker models, respectively.

For the broadside to endfire transmission scenario, Figure 5.2, the disparity in the correlations generated by the Kronecker and eigenbasis models is increased. While the Kronecker model s_1 correlation values very quickly tend toward zero, the eigenbasis model provides a close match to the s_1 correlation terms for all interelement spacings. This example further highlights the differences in the averaging behavior of the eigenbasis and Kronecker models.

Similar behavior of the s_1 correlation term was observed in the elliptical model, although the peak correlation values decreased more rapidly due to the increased angle spread from the ellipses. The broadside configuration plot, with an LSR of 0.7, is shown in Figure 5.3. Note that if the LSR is 1, then the model becomes the one ring model, for N = 2.

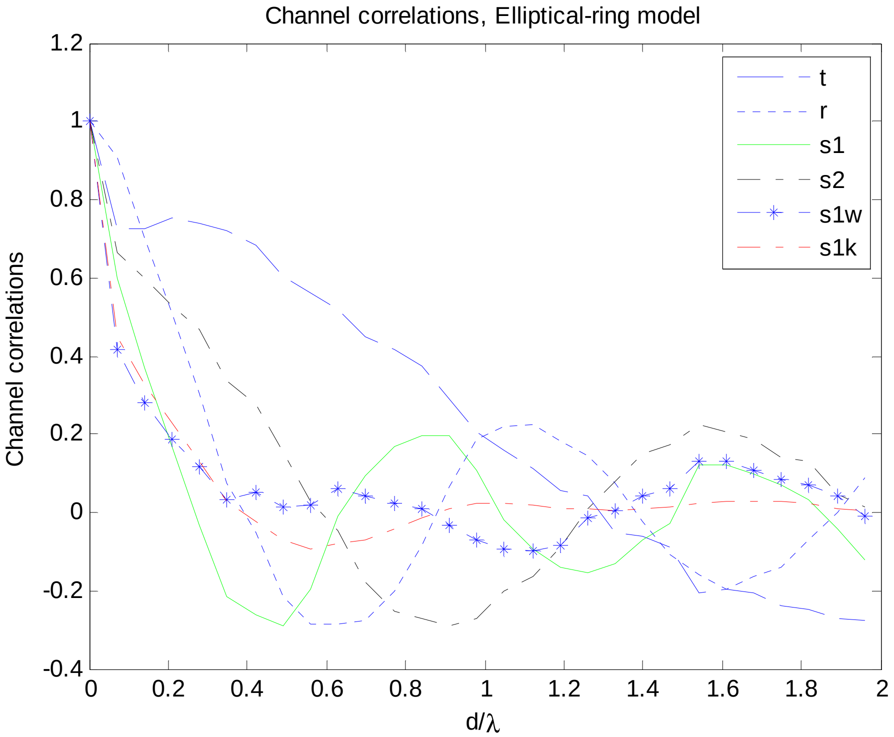

Figure 5.3: Channel correlations as a function of interelement spacing d/λ for the elliptical-ring model, broadside to broadside transmission.

For the cluster model, the centers of the scattering rings were randomly determined, allowing them to fall within a disk of radius R around the midpoint between the transmitter and receiver. For large R, this means that not all clusters fall between the transmitter and receiver. Note that a ring was not placed around the receiver. As such, the correlation values dropped off much more quickly. Also, the transmit and receive correlations exhibit nearly identical behavior, owing to the similar treatment of the link ends. The plot in Figure 5.4 was generated using the same interelement spacings at each link end.

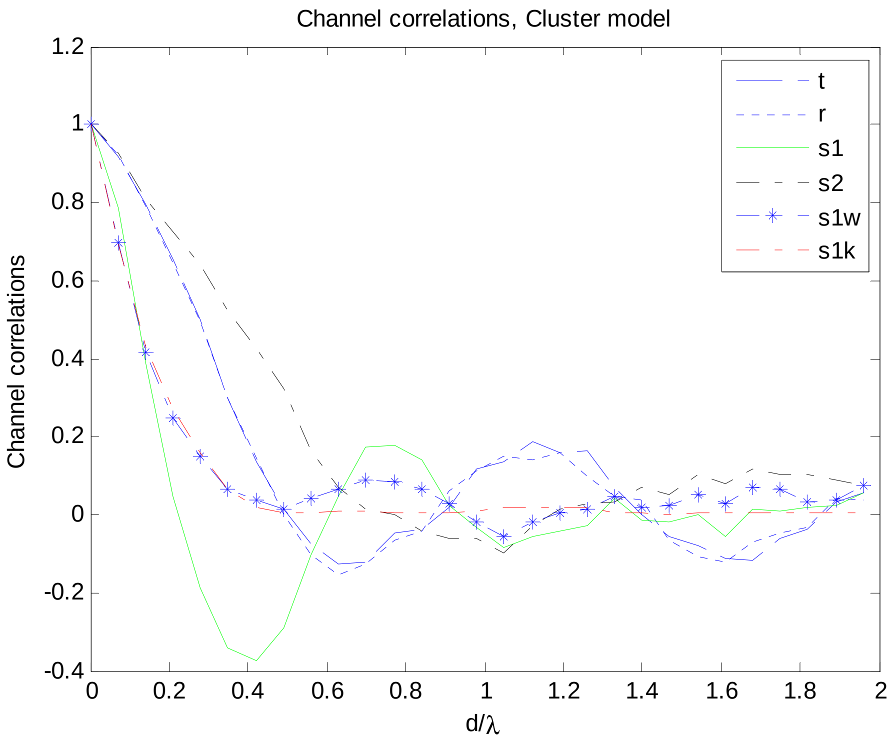

Figure 5.4: Channel correlations as a function of interelement spacing d/λ for the cluster model, broadside to broadside transmission.

5.2.3 System Performance

So far, the correlation mismatch of two analytical models in representing geometrical stochastic-based channel gain matrices has been presented. Now, consider the impact of the mismatch on the predicted system performance. To do this, two different metrics are considered. The first metric is a capacity-like metric. The second metric is a diversity number metric.

In [12], it was noted that at high SNR, the system capacity was proportional to a monotonic function of κ, where κ is equal to:

$$\kappa = E\{\det[\mathbf{HH}^H]\} \tag{5.2}$$

Relative to the i.i.d. fading case, the ratio of κ to κ_{iid} can be expressed for a 2 x 2 MIMO system according to (5.3) [12].

$$\frac{\kappa}{\kappa_{iid}} = 1 - \left(|r|^2 + |t|^2\right) + 0.5\left(|s_1|^2 + |s_2|^2\right) \tag{5.3}$$

The simplified expression in (5.3) facilitates a performance analysis comparison between the two models. Since the cross-term correlations s_1 and s_2 of the Kronecker model are products of the transmit and receive correlations, it is possible to select a geometry in which this product relationship approximately holds. Alternatively, it is possible to select spacings in which the receive and transmit correlation terms, r and t, are close to zero, but the s_1 and s_2 correlation values are high. Thus, the performance of the Kronecker model is very dependent on antenna configuration and system geometry.

On the other hand, the s_1 and s_2 correlation terms of the structured eigenbasis model form an average performance between the actual terms derived from the geometrical models. In a sense, the latter part of (5.3) is re-averaging an average, where some bias is introduced based on the squaring function. For small cross term values, s_1 and s_2, this bias will also tend to be small. Thus, it makes sense why the structured eigenbasis model gives better results than the Kronecker model in consistently predicting system performance in the average capacity sense.

A second important metric that reveals the impact on system performance is the effective amount of diversity in the system. For determining the impact of the models on the diversity measure, consider the definition [16-17]:

$$N_{div} = \frac{n_t^2 n_r^2}{n_t n_r + \sum_{\substack{k,l=1 \\ k \neq l}}^{n_t n_r} |\mathbf{R}(k,l)|^2} \tag{5.4}$$

A nonzero value for any of the correlation terms, r, t, s_1, or s_2, will lower the amount of effective diversity in the system. For the scenarios investigated, the values of r and t were very similar. Thus, the difference in prediction performance of the correct N_{div} will be driven by s_1 and s_2. From the figures in Section 5.3.3, we note that most often, both models tend to underestimate s_1 and s_2 regardless of the interelement spacing selected. However, the Weichselberger model tends to follow the actual cross-term curves better, leading to a significantly smaller mismatch. Thus, we expect the Kronecker model to consistently over-predict the amount of diversity in a system. The over-prediction of diversity influences many metrics for antenna selection. In signaling schemes that involve transmitting on a subset of antennas, a poor representation of the diversity in the system may lead to an overly optimistic algorithm, which in turn can drive up the error rate of the system.

5.3 Impact of Environmental Parameters on the Weichselberger Model

The distribution of power within the Weichselberger model's coupling matrix heavily influences system performance metrics, such as capacity [13-15, 18]. Since the structure of the power coupling matrix drives the performance of the system metrics, it would be insightful to have a more comprehensive understanding of how the underlying physics of the environment influences the structure of the power coupling matrix.

To gain insight into the environmental mechanisms and their effects on the power coupling matrix, a cluster-based geometrical model was created based on measured data. The resulting channel matrices are compared through beamforming techniques to verify similar primary scattering behavior. Once it is determined that a geometrical cluster model can represent a measured environment reasonably well, the cluster model environment is modified to examine the impact of the scattering environment on the structure of the power coupling matrix of the analytical channel model.

5.3.1 Cluster Model From Measured Data

To verify that a cluster model can generate a reasonable environmental approximation, consider measured data from a measurement campaign at the Brigham Young University campus [19-21]. Data obtained from locations within the Brigham Young University campus Coal Yard are used for generating a cluster model. The transmitter was placed in a fixed location and the receiver was mounted on a moving platform.

For generating the cluster model, three scattering locations, one on each of three buildings were used. Only single bounce energy is considered. A total of 25 scatterers per scattering cluster were used. Ray tracing methods were then used to generate the channel matrices, as in outlined in Section 3.4.

To verify that the cluster model is able to generate a reasonable approximation of the environment under consideration, beamforming techniques were used to verify that strong sources of power were arriving at the receiver from similar angles in both the measured and simulated channel gain matrices. This technique was also used in Section 4.5.5, but is examined throughout the data set here. FFT beamforming was used on a single column of the channel gain matrix to examine the response across the receive array. Several time instances were examined. The resulting magnitudes of the beam steering response are shown in Figure 5.5. While the two magnitudes do not align perfectly due to the simplicity of the model, they display a similar character. Thus, a cluster model can be used to provide a reasonable approximation to a measured environment.

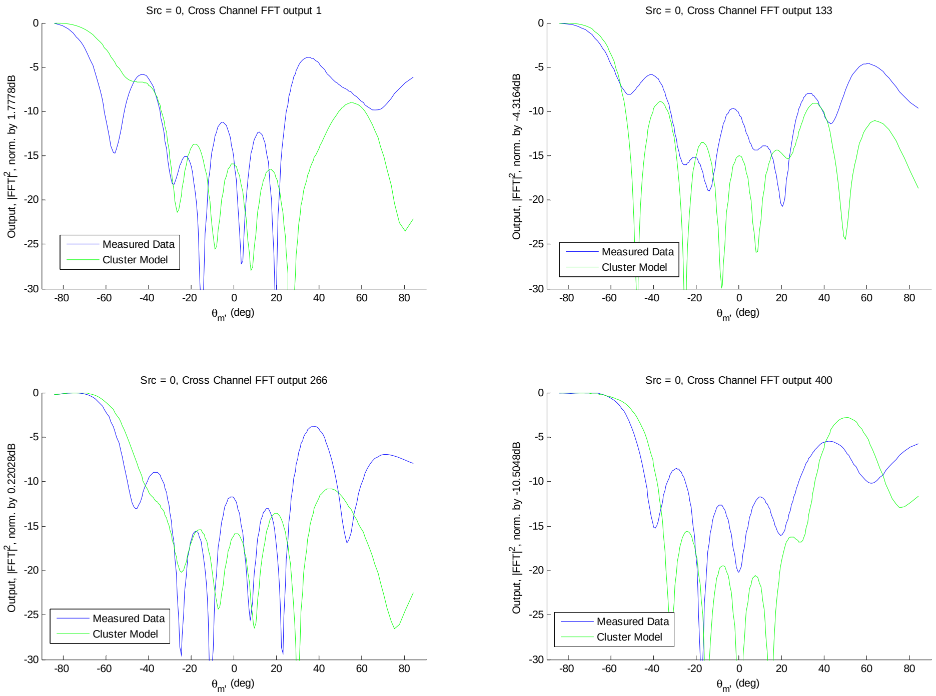

Figure 5.5: Received power vs. angle for measured and simulated data.

5.3.2 Cluster Model Scenarios

Four different environmental scenarios are examined to provide a variety of responses. For each of the scenarios, the same number of cluster rings is used. To place the cluster rings in the environment, scatterers are allowed to uniformly fall in a disk. For each scenario, the location or radius of the disk is changed to vary the environmental response. The arrays are located in a broadside configuration, with the initial separation between them set to R = 400 m.

For the first transmission scenario, clusters are placed randomly in a disk centered between the two arrays, with the disk radius equal to 10R. As such, scatterers will fall both between and around the two link ends. For the second environment under consideration, the disk is still centered at the midpoint between the two arrays. This time, the disk size is set to R/2, forcing all scattering to take place between the transmitter and receiver arrays only. For the third transmission scenario, the disk radius is kept the same, but the disk is moved to the receiver link end. This scenario creates an imbalance in the scattering environment. Finally, the last scenario examines the case when scatterers are located a distance from the arrays. The disk of scatterers is moved a distance d perpendicular to the LOS transmit path between the arrays, and is located equidistant to the link ends. A graphical depiction of the different transmission scenarios are shown in Figure 5.6-5.9 Note that the geometries are not displayed to scale for readability purposes.

For each aspect of the environment explored, three interelement spacings were investigated, with both the receiver and transmitter interelement spacings equal to each other. To generate a breadth of correlation responses between the antennas at the link ends, the spacings selected were 0.25λ, 0.5λ, and 2λ.

5.3.3 Results

For each of the environmental scenarios, 500 cluster model channel matrices are synthesized. These matrices are then used to created the coupling matrices for the Weichselberger eigenbasis model. By investigating several metrics, the impact of the changing environments on how power couples between link ends can be determined.

The first metric examined is the maximum power value in the coupling matrix. The second is the ratio of the power on the main diagonal to the total power in $\mathbf{\Omega}$. By looking at how the maximum value changes, as well as how the power is distributed on and off the main diagonal, we gain insight into the channel characteristics. In [13], it was noted that, in general, the more diagonalized the power coupling matrix, the higher the capacity supported by a channel. This occurs as the capacity expression contains sums of products of the coupling matrix terms. If power is spread throughout the coupling matrix, the products become smaller. If the power is concentrated along the diagonal, the capacity expression becomes larger. Also, if the power is spread out evenly along the diagonal, the capacity is maximized.

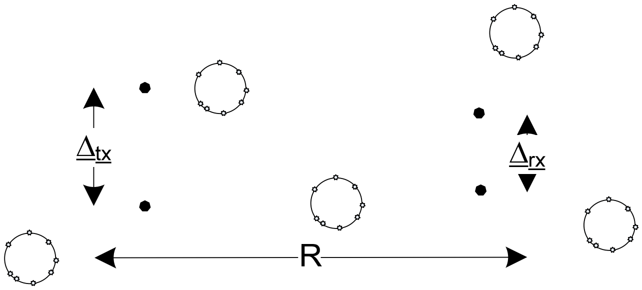

Figure 5.6: Transmission Scenario 1.

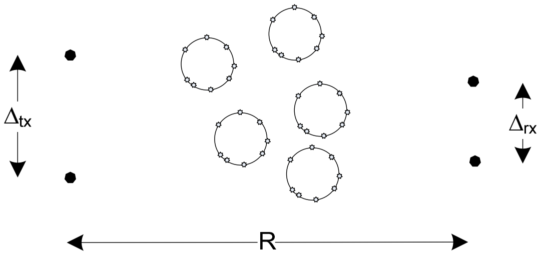

Figure 5.7: Transmission Scenario 2.

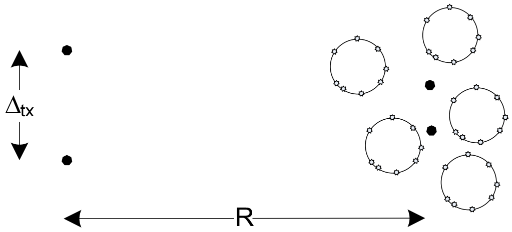

Figure 5.8: Transmission Scenario 3.

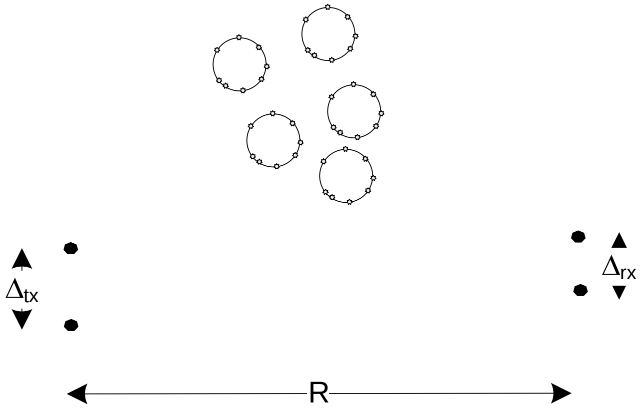

Figure 5.9: Transmission Scenario 4.

5.3.3.1 Number of Clusters

The number of scattering clusters was varied from 1 to 25 and the maximum power value in **Ω** was plotted for each of the three interelement spacings, 0.25λ, 0.5λ, and 2λ, where Δtx = Δrx. All four environmental scenarios were investigated. The maximum **Ω** value for Scenarios 1, 3, and 4 are displayed in Figure 5.10. The response for Scenario 2 was nearly identical to Scenario 3. In all cases, once the environment was described by at least 5 clusters, the response became nearly constant. The smaller interelement spacings resulted in higher power values, whereas the larger interelement spacings resulted in lower power values. This behavior is expected. If the antennas are farther apart, the array aperture is larger. The power in the coupling matrix will be divided into different transmit and receive directions, and the maximum value will be lower. The diagonal power distribution (ratio of the sum of the diagonal power terms to total power) plots followed the same general characteristics as the maximum **Ω** plots.

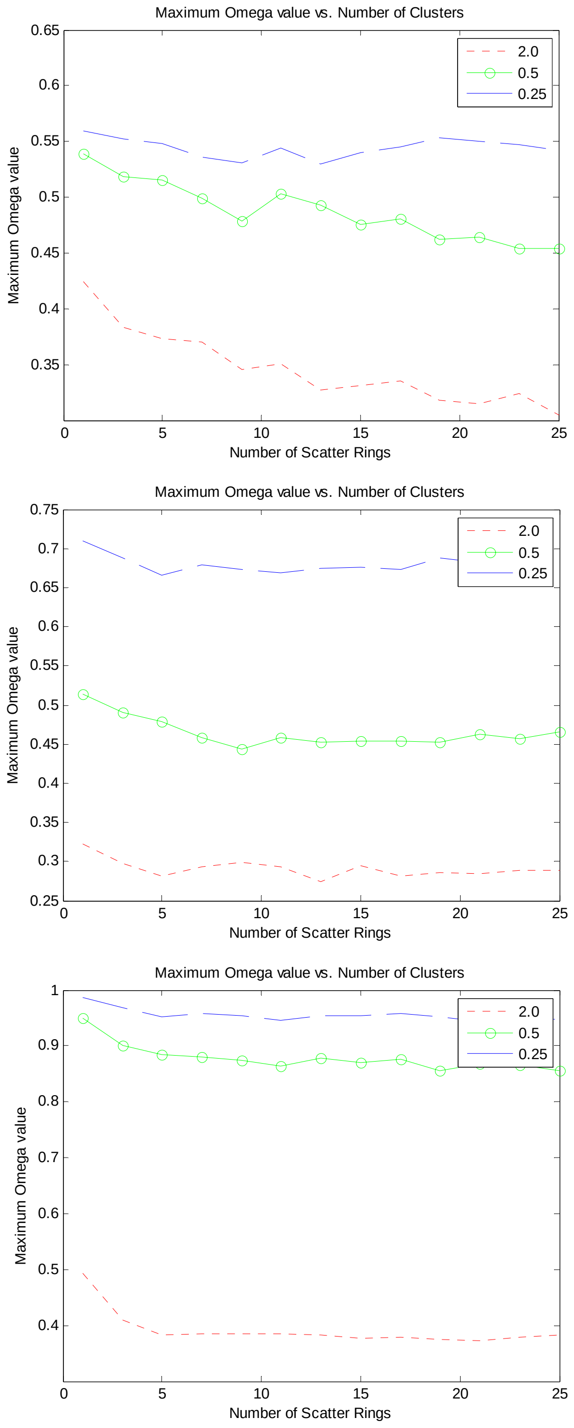

Figure 5.10: Maximum **Ω** value for transmission Scenarios 1, 3, and 4 for interelement spacings of 0.25, 0.5 and 2.0λ.

5.3.3.2 Array Separation

Next, we examine the effect of the distance between the link ends on the power coupling. For examining this particular effect, Scenarios 2 and 3 were examined. Both had similar behavior, except at low N values, where the link end transmission scenario had a more flat response. The initial separation, designated d_0, between arrays was 400 meters and increased to 4000 meters. As before, for larger interelement spacings, the power is spread more evenly in the coupling matrix. As the separation between the arrays grows, the angular spread from which energy is arriving at a link end is effectively reduced. Thus, we expect most of the energy in the coupling matrix to be focused in a particular direction, which means most of the energy will be focused onto the main diagonal, which generally contains the highest power term. The highest term generally appears on the diagonal as the eigenvectors used at the link ends are typically ordered during processing according to the power associated with them. A plot of the ratio of the diagonal term powers to total power as a function of array separation is given in Figure 5.11.

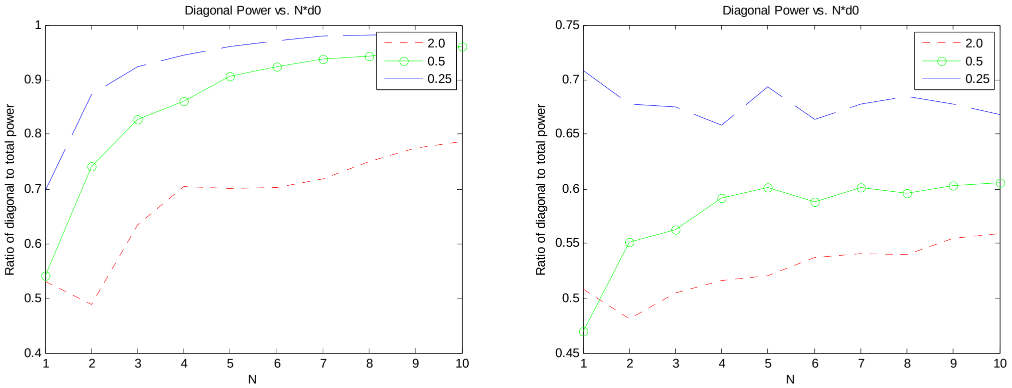

Figure 5.11: Ratio of diagonal to total power vs. increasing array separation for Scenarios 2 and 3 for interelement spacings of 0.25, 0.5 and 2.0λ.

5.3.3.3 Disk Size

The final metric examined is the disk size. By changing the size of the disk, we change the angles from which energy will arrive at the arrays. We examine the effects on the coupling matrix with the distance between the two arrays fixed at d_0 = 400, and the disc size varied between $d_0/4$ to 5* d_0, with 20 scatterer rings. For the smaller spacings, the disk of scatterers is between the arrays. For the larger spacings, the arrays are now contained within the disk of scatterers. When the disk of scatterers is centered between the link ends, there is less angular spread while the disk radius is much smaller than the array separation. In this case, the power is focused on a single path for small interelement spacings, which causes a high coupling matrix value. In turn, this causes a high diagonal power value as the diagonal will contain the high coupling matrix value. For the link end centered disk, the angular spread seen by one of the arrays is significantly larger. This accounts for the lack of high peak values at low interelement spacings seen in Figure 5.12.

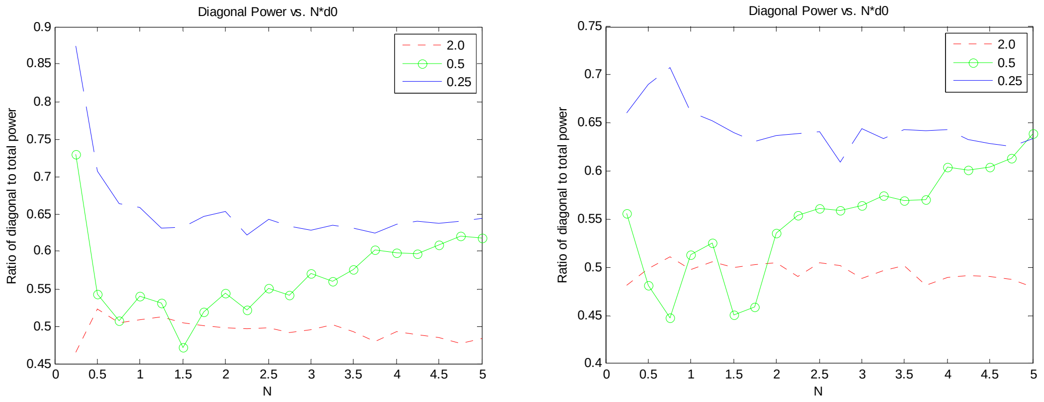

Figure 5.12: Ratio of diagonal to total power vs. increasing scattering disk size for Scenarios 2 (left) and 3 (right) for interelement spacings of 0.25, 0.5 and 2.0λ.

5.4 Summary

In this chapter, the mismatch between the Kronecker and structured eigenbasis models in accurately representing the correlation structures of several geometrical-based stochastic models was examined. Different array orientations and a variety of interelement spacings were explored. It was observed that the Weichselberger model outperforms the Kronecker model, especially at large interelement spacings, in providing a better representation of certain terms in the full channel correlation matrix. By examining the role of the correlation matrix on system parameters, insight is gained into issues that may be caused by the differences in model representation.

The use of geometrically-based stochastic models allows for the ability to control environmental parameters in exploring the fundamental limitations of the analytical models. However, further exploration into the model parameters for measured data is required to validate the observations. Additional work in comparing the coupling structures of the two analytical models may add further insight into the averaging mechanism of the structured eigenbasis model.

By examining how changes in the environment affect the distribution of power in the coupling matrix using geometrical models, we gain insight into the underlying structure observed in measured coupling matrices. The effect of the antenna separation at the link ends on the structure seen in the coupling matrix is also examined.

As the interelement spacings get larger, the power distribution in the coupling matrix becomes more balanced. Furthermore, the angular distribution plays a large role in the distribution, but the number of effective scatterers plays a less significant role. For the environmental parameters investigated here, the metrics for scenarios with large numbers of scatterering clusters were similar to the performance achieved with at least 5 scatterering clusters.

5.5 Acknowledgment

This chapter, in part, is a reprint of the material as it appears in "Impact of Analytical Channel Models on Geometrical Channel Correlation Structures," L. C. Wood and W. S. Hodgkiss, to be appearing in the Proceedings of VTC, Fall 2008. The dissertation author was the primary author of this paper.

5.6 References

[1] A. M. Saleh and R. A. Valenzuela, “A statistical model for indoor multipath propagation,” *IEEE J. Selected Areas Commun.*, vol. 5, no. Feb., pp. 128–137, 1987.

[2] Q. Spencer, M. Rice, B. Jeffs, and M. Jensen, “A statistical model for angle of arrival in indoor multipath propagation,” in *Proc. IEEE Vehic. Tech. Conf.*, vol. 3, 1997, pp. 1415–1419.

[3] J. Blanz and P. Jung, “A flexibly configurable spatial model for mobile radio channels,” *IEEE Trans. Commun.*, vol. 46, no. 3, pp. 367–371, Mar.1998.

[4] D. Gesbert, H. Bolcskei, D. Gore, and A. J. Paulraj, “MIMO wireless channels: Capacity and performance prediction,” in *Proc. IEEE Global Telecommunications Conf. GLOBECOM*, vol. 2, 2000, pp. 1083–1088.

[5] K. I. Pedersen, J. B. Andersen, J. P. Kermoal, and P. Mogensen, “A stochastic multiple-input-multiple-output radio channel for evaluation of space–time coding algorithms,” in *Proc. IEEE Vehicular Technology Conf.*, 2000, pp. 893–897.

[6] J. P. Kermoal, L. Schumacher, K. I. Pedersen, P. Mogensen, and F. Frederiksen, “A stochastic MIMO radio channel model with experimental validation,” *IEEE J. Select. Areas Commun.*, vol. 20, no. 6, pp. 1211–1226, Jun. 2002.

[7] R. B. Ertel, P. Cardieri, K.W. Sowerby, T. S. Rappaport, and J. H. Reed, “Overview of spatial channel models for antenna array communication systems,” *IEEE Personal Commun.*, vol. 5, no. 1, pp. 10–22, Feb. 1998.

[8] P. Almers, E. Bonek, A. Burr, et al., “Survey of Channel and Radio Propagation Models for Wireless MIMO Systems,” *EURASIP Journal on Wireless Communications and Networking*, vol. 2007, Article ID 19070, 19 pages, 2007.

[9] K. Yu, M. Bengtsson, B. Ottersten, D. McNamara, P. Karlsson, and M. Beach, *Modeling of wide-band MIMO radio channels based on NLoS indoor measurements.* Vehic Tech, IEEE Trans. on, Vol.53, Iss.3, May 2004, pp. 655-665.

[10] T. Zwick, C. Fischer, and W. Wiesbeck, *A stochastic multipath channel model including path directions for indoor environments*. Selected Areas in Communications, IEEE Journal on, Vol.20, Iss.6, Aug 2002. pp. 1178- 1192.

[11] T. Fugen, J. Maurer, W. Sorgel, and W. Wiesbeck, *Characterization of multipath clusters with ray-tracing in urban MIMO propagation environments at 2 GHz.* Antennas and Propagation Society International Symposium, 2005 IEEE, vol.3B, 3-8 July 2005, pp. 410- 413.

[12] C. Oestges, B. Clerckx, D. Vanhoenacker-Janvier, and A.J. Paulraj, *Impact of fading correlations on MIMO communication systems in geometry-based statistical channel models*, Wireless Communications, IEEE Transactions on, vol.4, no.3, pp. 1112-1120, May 2005.

[13] W. Weichselberger, M. Herdin, H. Ozcelik, E. Bonek, "A stochastic MIMO channel model with joint correlation of both link ends," *Wireless Communications, IEEE Transactions on* , vol.5, no.1, pp. 90-100, Jan. 2006

[14] N. Costa and S. Haykin, *A Novel Wideband MIMO Channel Model and McMaster’s Wideband MIMO SDR.* Signals, Systems and Computers, 2006, Conference Record of the Fortieth Asilomar Conference on, Nov 2006. pp. 956-960.

[15] L. C. Wood and W. S. Hodgkiss. MIMO Channel Models and Performance Metrics. Global Telecommunications Conference, 2007. GLOBECOM '07. IEEE , pp.3740-3744, 26-30 Nov. 2007.

[16] M.T. Ivrlac, J.A. Nossek, *Quantifying diversity and correlation in Rayleigh fading MIMO communication systems*, Signal Processing and Information Technology, 2003. ISSPIT 2003. Proceedings of the 3rd IEEE Intl Symposium on , pp. 158-161, 14-17 Dec. 2003.

[17] C. Oestges and B. Clerckx. *MIMO Wireless Communications*, Elsevier Ltd, London, 2007

[18] C. Oestges, H. Ozcelik; and E. Bonek, “On the practical use of analytical MIMO channel models,” *2005 IEEE Antennas and Propagation Society International Symposium,* vol. 3B, pp. 406-409, 3-8 July 2005.

[19] J.W. Wallace, M. A. Jensen, A. L. Swindlehurst, and B. D. Jeffs, *Experimental characterization of the MIMO wireless channel: Data acquisition and analysis*, IEEE Trans. Wireless Commun., vol. 2, pp. 335–343, Mar. 2003.

[20] J.W. Wallace and M. A. Jensen, *Experimental analysis of the time-varying MIMO channel*, Antennas and Propagation Society International Symposium 2006, IEEE, 9-14 July 2006, pp. 321- 324.

[21] J.W. Wallace and M. A. Jensen, "Time-Varying MIMO Channels: Measurement, Analysis, and Modeling,"*IEEE Transactions on Antennas and Propagation*, vol.54, no.11, pp.3265-3273, Nov. 2006.

6 Practical MIMO Systems

6.1 Introduction

The structure of the wireless channel gain matrix determines the optimal power allocation, modulation index, data rate, and antenna weights for a MIMO system. Many different MIMO channel gain matrix models have been created for the development of optimal transmission and reception strategies. Channel models vary in complexity, and model different aspects of the channel with varying degrees of accuracy.

Closed loop (CL) adaptive systems in which feedback is provided to the transmitter can yield higher capacities than open loop (OL) schemes. However, the training overhead, processing time, and aging of the channel information has made open loop architectures popular. One such open loop architecture is the Vertical Bell Laboratories Layered Space-Time (V-BLAST) architecture [1, 2].

In this section, we examine OL and CL-MIMO adaptive modulation schemes designed to meet a target bit error rate (BER) constraint. The systems being considered are a modified open loop system which uses V-BLAST and a closed loop system, similar to those examined in [3, 4]. For the open loop system, a V-BLAST strategy where limited feedback of the modulation index and the number of transmit antennas is employed. For the closed loop system, we examine a waterfilling strategy that has been modified from the traditional solution to guarantee that a BER constraint is met.

In the first portion of this chapter, we examine the capabilities of these different systems under M-QAM transmission using simulated data as well as measured data sets for NLOS environments. The difference in the OL-MIMO versus CL-MIMO system performances shows the gains possible for adaptive-rate adaptive-power systems with a limited amount of feedback for measured channels. Unlike other explorations which use only simulated data, this work highlights the performance differences in the models as measured data is used as a performance baseline [6, 7]. Thus, the accuracy of models in representing the channel will be highlighted. Large performance gains between different OL and CL systems have been reported, as in [8], in which 20 dB gains were observed. Other adaptive schemes are summarized in [9] and the references therein.

In the second portion of this chapter, we use the same open and closed loop systems to examine reduced forms of the structured eigenbases model. First, we examine reduced rank possibilities by using the high power quadrant of the coupling matrix in place of the full rank coupling matrix. This can provide a small to significant reduction in the number of parameters that need to be known. Next, we examine using only knowledge of the coupling matrix to determine the system capacity. Both techniques hold promise for reducing the number of required feedback parameters to less than the number required by the Kronecker model, while still providing equivalent or better performance.

6.2 Effect of model choice on M-QAM signaling

In this section the capabilities of different MIMO system architectures are examined. The difference in OL-MIMO versus CL-MIMO system performance shows the gains possible for adaptive-rate adaptive-power systems with a limited amount of feedback for measured channels.

By comparing the performance of the actual environment to the performance predicted by the different channel models, we provide insight into the impact of the choice of model on adaptive communication algorithms. The results show that the

Weichselberger model accurately predicts the average channel behavior for the measured environments explored. However, the Kronecker model under-predicts the throughput as roughly 75% of the total rate possible at an SNR of 25 dB for the CL-MIMO system.

6.2.1 Adaptive M-QAM MIMO

Consider the square M-QAM adaptive modulation scheme with approximate BER as given in [10]:

$$BER \approx 0.2\exp\left[-\frac{3}{2(M-1)}\frac{E_s}{N_o}\right] \tag{6.1}$$

where M is the modulation index, E_s is the symbol energy, and N_o is the noise power. Note that this bound assumes transmission over AWGN channels and is good to within 1 dB for M ≥ 4 and 0 ≤ SNR ≤ 30 dB. For systems implementing rectangular M-QAM, the corresponding approximation for (6.1) is given in [11]. The modulation index for the i^{th} transmit data stream which supports a given BER constraint γ, is given as

$$M_i = floor\left(1-\frac{3}{2}\left(\frac{E_s}{N_o}\right)_i\frac{1}{\ln(5\gamma)}\right) \tag{6.2}$$

where $(E_s/N_o)_i$ denoted the SNR of the i^{th} data stream. Due to the use of the BER approximation in (6.1), we consider only systems whose least possible modulation index is 4-QAM. If the subchannel cannot support 4-QAM while satisfying the BER constraint, the subchannel will not be used. Thus, a threshold SNR must be met. By rearrangement of (6.2) and setting M = 4, the following minimum SNR per data stream in use is determined:

$$\left(\frac{E_s}{N_o}\right)_i \geq -2\ln(5\gamma). \tag{6.3}$$

6.2.2 System Architectures

6.2.2.1 Open-Loop System

In conventional open loop system architectures, no information is fed back between the receiver and transmitter. As such, there is no preference at the transmitter and equal power is allocated to each transmit antenna. Traditional open loop systems such as V-BLAST enable spatial multiplexing transmission without the need for feedback. However, limited feedback of the modulation index and the number of streams can be used in conjunction with the V-BLAST architecture to ensure that a target BER rate is met. Such schemes have been shown to be practical in [12-14].

A V-BLAST architecture that transmits with equal power from all transmitting antennas which uses successive interference cancellation (SIC) and zero-forcing at the receiver is considered, as explained in [1]. Conceptually, in a V-BLAST system each substream in turn is considered to be the desired signal, and the remaining substreams are regarded as interferers. Nulling is performed by linearly weighting the received signals so as to satisfy some performance-related criterion, which in this case is zero-forcing. Superior performance to regular zero-forcing is obtained if nonlinear techniques are additionally used. In this case, symbol cancellation, in addition to the linear nulling, is used to perform detection. The detection process can be summarized as follows: using the nulling vector, form a decision statistic. From the decision statistic, the transmitted vector is estimated. This estimated vector is then cancelled from the received vector, forming a modified decision statistic. The process repeats, until all symbols in the transmitted vector have been detected. Each iteration through the process may be referred to as a layer.

For a given channel realization, the SNR of the first layer is detected by computing the pseudo-inverse of the channel gain matrix and finding the nulling vector **w**. The order used to decode changes the effectiveness of the methodology. For this work, the decoding order of the streams is such that during each iteration of the SIC the stream with maximum SNR is chosen.

The SNR of the first layer is given as

$$\frac{E_s}{N_o} = \frac{P_T}{N_t \|w\|^2} \tag{6.4}$$

where P_T is the noise normalized transmit power and $N_t \leq n_t$. For the first layer, it is assumed that the number of transmit antennas will be n_t. If the SNR of the first layer exceeds the threshold for 4-QAM, then transmission occurs on all antennas. If the SNR does not exceed the 4-QAM threshold, the channel matrix is reduced by one in the transmitter dimension ($N_t = n_t - 1$), and the process is repeated. Since we are feeding back only the number of antennas in use, the transmitter antenna to turn off is selected at random for the channel matrix reduction. Once the proper number of antennas is found, $n_{ts,}$ the modulation index, M, is computed using (6.2). The data rate for the limited feedback system is given by $R = n_{ts} \times \log_2(M)$, where n_{ts} is the number of transmitters transmitting, and $\log_2(M)$ gives the number of bits used per symbol.

6.2.2.2 Closed-Loop Waterfilling MIMO

The waterfilling solution given in [15] is a well-known strategy to optimally allocate power in a maximum capacity fashion for AWGN channels with Gaussian codes. This strategy assumes that the transmitter has full knowledge of the channel (i.e. the channel gain matrix **H**), which can be a significant amount of overhead in comparison to the OL-scheme. While capacity is maximized by allocating power to subchannels with higher SNRs, no BER guarantees are offered in this transmission strategy. As such, an additional constraint must be added to the traditional waterfilling solution to force the weakest eigenmode allocated power to meet the threshold constraint in (6.3).

The waterfilling strategy employed is given by:

$$\alpha_i = \left(\mu - \frac{1}{\lambda_i}\right)^+ \quad s.t. \begin{cases} \sum \alpha_i = P_T \\ \alpha_i \lambda_i > -2\ln(5\gamma) \end{cases} \tag{6.5}$$

where α_i is the power level allocated to transmitted stream *i*, λ_i is the corresponding channel eigenvalue, μ is the waterfilling level, γ is the BER constraint from (6.2), and the notation $(\cdot)^+$ indicates that the quantity must be positive or zero.

Note that since the modulation scheme we are using has discrete steps in SNR that must be satisfied to support a particular modulation index, it may be possible to improve on the waterfilling scheme for M-QAM transmission. Every stream will be allocated some extra power that is not needed to satisfy the modulation index under (6.2). The difference between the SNR needed to meet the modulation index and the actual assigned power can be used to increase the data rate or number of transmitted data streams. Such a rate maximization scheme was given in [3-5], providing only a small improvement in throughput over the waterfilling strategy given in (6.5) for the additional complexity in computation. As such, the rate maximization scheme is not considered in this work.

For the closed loop scheme, if K streams of data, each utilizing M-QAM modulation with modulation index M_i, are transmitted, the throughput per transmission can be computed according to (6.6):

$$R = \sum_{i-1}^{K} \log_2 M_i \tag{6.6}$$

6.2.3 Model Performance Using Adaptive M-QAM

We consider two different sources of data for comparison of model performance. First, we consider simulated data generated from a Rayleigh channel model. Second, we examine the Kronecker and Weichselberger models derived from experimentally observed data measured in the Coal Yard at the Brigham Young University campus. For both sets of channel matrices, we consider systems with 8 transmit and 8 receive antennas. The transmitter is assumed to have perfect knowledge of the exact (or simulated) channel matrix. For each transmit power level investigated, 400 channel matrices are generated from both the Weichselberger and Kronecker models. The average performance is then calculated over these 400 realizations. For each realization, the throughput for the channel is computed for both the OL and CL-MIMO systems.

6.2.3.1 Simulated Channel Matrices

Rayleigh fading channels are of significant interest in communications as they represent multipath environments without a line of sight between the transmitter and receiver. We first consider the case where the antenna elements are uncorrelated. To construct a channel matrix for such a model, the elements h_{ij} are independent, identically distributed symmetric complex Gaussian elements, with zero mean and unit variance. The simulated matrices are then used to compute the OL and CL-MIMO throughput rates for a given SNR, as outlined in Secions 6.2.2.1 and 6.2.2.2.

The throughput results for the OL-MIMO and CL-MIMO scheme can be seen in Figure 6.1 and the number of transmitting antennas can be seen in Figure 6.2, both as a function of SNR. For i.i.d. Rayleigh fading, either channel model performs equally well in predicting the channel response on average. Both channel matrix models under consideration provide good agreement with the simulated data, offering roughly a 23% improvement in throughput between closed loop and open loop transmission strategies. However, in real channels, correlation generally exists between antenna elements. This correlation can be a function of both environmental sources, as well as system sources, such as mutual coupling. The correlation structure results in significantly different performances predicted by the Weichselberger and Kronecker channel models.

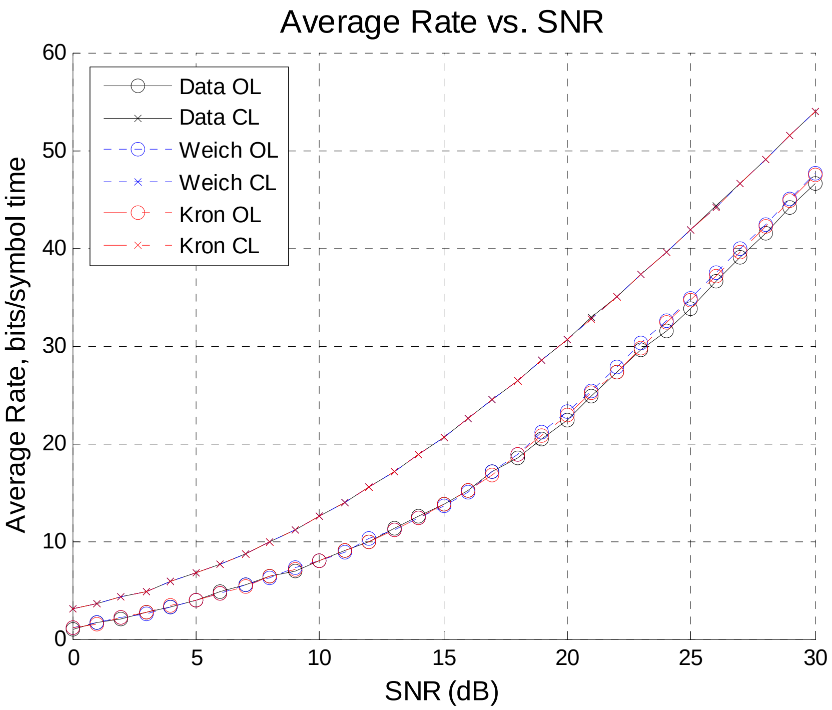

Figure 6.1: Throughput of a simulated Rayleigh channel, BER = 10^{-2}.

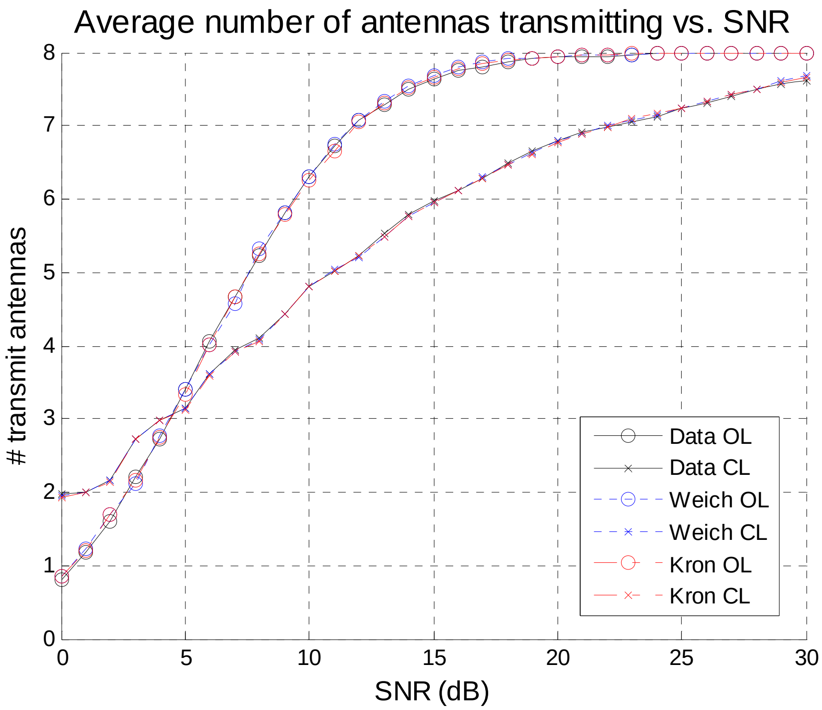

Figure 6.2: Transmitter streams allocated for a simulated Rayleigh channel, BER = 10^{-2}.

6.2.3.2 Coal Yard Channel Matrices

Next, we investigate system performance using channel gain matrices from measured channels. The channel gain matrix data was obtained from two different locations within the Brigham Young University campus Coal Yard (see Section 4.2.3.1). At each location, four different data sets are available. For the odd-numbered data sets, the transmitter and receiver were stationary. Variations in the channel were due to moving scatterers, such as pedestrians. Due to this arrangement, the channel changes very slowly between samples of **H**.

For the even-numbered data sets, the receiver was mounted on a moving platform. This leads to a channel with increased variation between successive estimations of **H**. These experimental sets were recorded using a system with 8 transmit antennas and 8 receive antennas. The antennas used at both link ends were vertically-polarized monopoles. The carrier frequency was centered at 2.45 GHz. For more information on these measurements, and how the channel matrices were subsequently estimated, refer to [16, 17]. The Kronecker and Weichselberger models were derived as discussed in Section 4.2.3.3.

6.2.3.2.1 Stationary Transmitter and Receiver

Results from Location 1, Set 1 are shown in Figures 6.3 and 6.4 for the throughput and antenna streams allocated. We can see the significant performance improvement in using a closed loop system versus an open loop system for a real environment. In comparison to the simulated environment where the antenna elements were assumed to be perfectly uncorrelated, the gains are significant, especially at higher SNRs. At 25 dB, there is a performance gain of 72% of CL-MIMO relative to OL-MIMO for the actual channel matrices. The Weichselberger model predicts the throughput and antenna assignment well at all SNRs considered. The Kronecker model underestimates the throughput of the channel and incorrectly predicts the number of antennas that ought to be transmitting.

Note that since the measured channel is relatively stationary, the data curve for the average numbers of antennas in use has a very stair-step nature. The relatively stationary nature of the channel means that the channel matrices are similar, requiring the same SNRs to trigger transmission on an additional antennas. In contrast, both the Kronecker and the Weichselberger models provide a smoothed estimate for number of antennas in use. Thus, at SNRs slightly lower than the point at which an additional antenna can be supported, it is expected that the Weichselberger model would predict performance slightly optimistically.

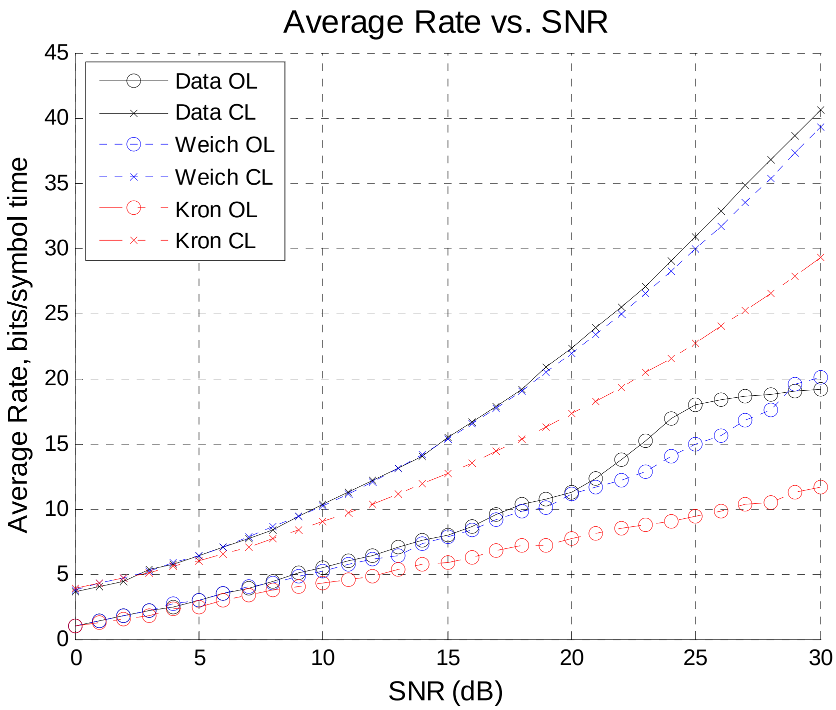

Figure 6.3: Throughput of a measured NLOS channel, stationary transmitter and receiver, BER = 10^{-2}.

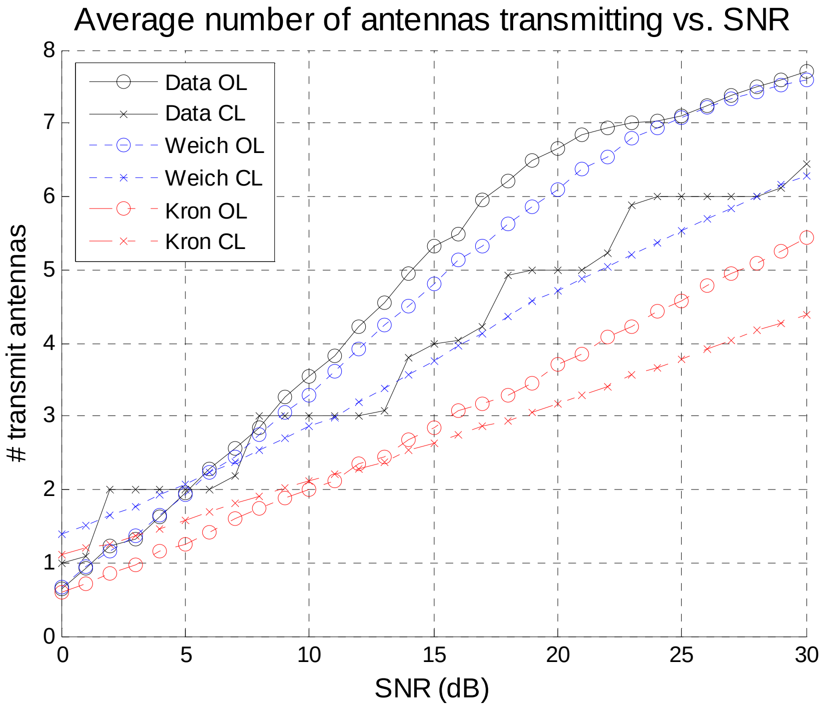

Figure 6.4: Transmitter streams allocated for a measured NLOS channel, stationary transmitter and receiver, BER = 10^{-2}.

6.2.3.2.2 Stationary Transmitter, Moving Receiver

The results from Location 1, Set 2 in which the receiver was in motion are shown in Figures 6.5 and 6.6. The curves are smoother in appearance due to the increased variability in the channel from the receiver being in motion. This also leads to a closer match between the measured channel performance and the performance predicted by the Weichselberger channel model at high SNRs. At 25 dB, there is a similar throughput gain of about 75% of CL-MIMO over OL-MIMO for the actual channel matrices, in comparison to Figure 6.3. Again, the Kronecker model severely underestimates the throughput possible at a given SNR, requiring an additional 6 dB to transmit at an average rate of 10 bits/symbol time using the OL-MIMO system. Similar deficiencies in the Kronecker model were found for the data sets taken at Location 2.

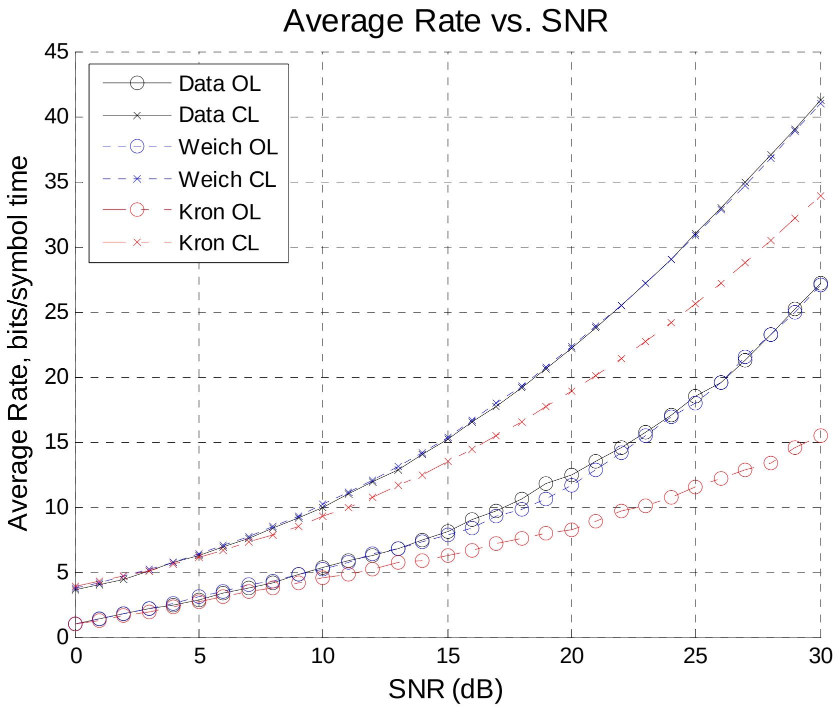

Figure 6.5: Throughput of a measured NLOS channel, mobile receiver, BER = 10^{-2}.

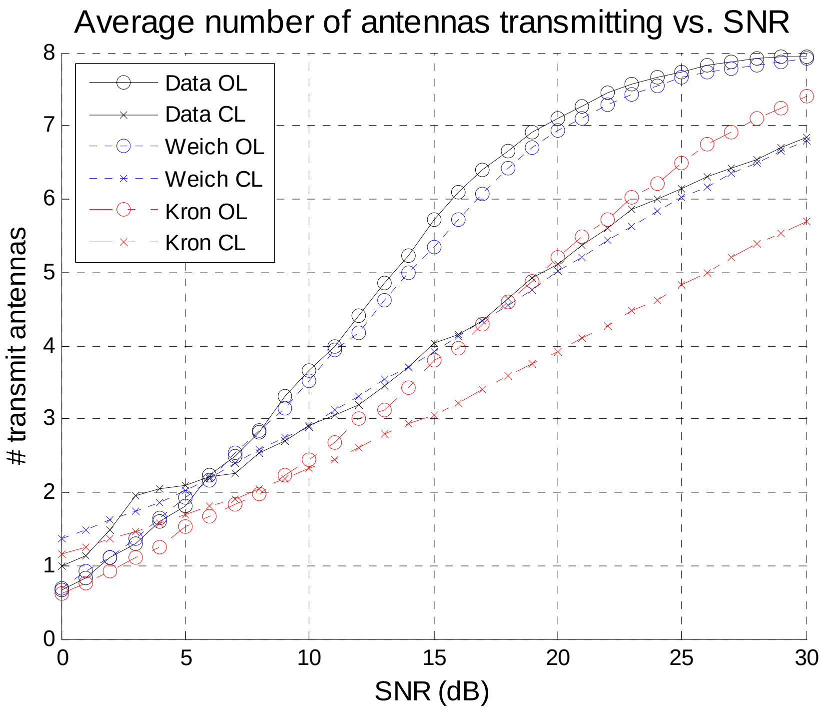

Figure 6.6: Transmitter streams allocated for a measured NLOS channel, mobile receiver, BER = 10^{-2}.

6.3 Reducing the Structured Eigenbasis Model Parameters

While the full coupling matrix and the link end eigenvectors are required to represent a theoretical i.i.d Rayleigh fading channel with no correlation, physical radio environments in which correlation is present may allow for the channel to be represented with reduced knowledge about the coupling matrix. An example environment that may support this reduction in knowledge is an environment with a few dominant scatterers. Although the coupling matrix may be full rank, at low to moderate SNRs, a waterfilling transmission scheme would focus transmission power on the eigenmodes with the dominant scatterers. Such reasoning has facilitated the development of other reduced rank channel representations, such as [18].

In this section, we develop and investigate a reduced form of the Weichselberger model using measured MIMO channel matrices. Several different environments are investigated which vary in multipath richness. We explore the tradeoff between the accuracy in predicting the average channel capacity and the model simplicity as a function of SNR. Additionally, we investigate the structure of the model parts, gaining insight into appropriate strategies by which the information in the Weichselberger model may be compacted.

6.3.1 Reduced Rank Model

An alternate expression for the full Weichselberger model in (3.17) can be given as follows:

$$vec(\mathbf{H_{weich}}) = \sum_{m=1}^{n_r}\sum_{n=1}^{n_t}\sqrt{\omega_{m,n}}\, g_{m,n}\left(\mathbf{u}_{\mathbf{tx},n} \otimes \mathbf{u}_{\mathbf{rx},m}\right) \tag{6.7}$$

where $g_{m,n}$ is an element of $\mathbf{H_w}$, $\mathbf{u}_{\mathbf{tx},n}$ is the n^{th} transmitter steering basis vector, $\mathbf{u}_{\mathbf{rx},m}$ is the m^{th} receive basis steering vector, and $\omega_{m,n}$ is an element in $\mathbf{\Omega}$.

To form the reduced Weichselberger model, we restrict the power coupling matrix to L non-zero values. The selection of which values are non-zero will greatly influence the model's performance. In general, a better match will be obtained by selecting the L largest $\omega_{m,n}$ values as the unaccounted for power will be minimized. However, this methodology may not be practical for use with the Weichselberger model, as acknowledged in [19]. Accounting for the highest power levels in the coupling matrix may not necessarily reduce the complexity of the problem, as columns or rows of $\mathbf{\Omega}$ may not be set to zero. In turn, this means that the rank of the one sided-correlation matrices may not be reduced. Thus, other than obtaining information on how sensitive the low power values are to quantization error, this methodology has little savings in complexity.

Alternatively, rather than selecting the highest powered values, a regularized pattern in $\mathbf{\Omega}$ might be desirable. While including the higher power $\omega_{m,n}$ values, the regularized shaped pattern may also include lower power values, providing a slightly poorer match to the full model in return for savings in complexity. Due to how the power is distributed in the coupling matrix in the measured transmission scenarios investigated, this additional error is often small. If a pattern is selected which reduces the number of rows or columns of the coupling matrix that are nonzero, then the rank of the link end correlation matrices is also reduced. Thus, there will be a complexity impact in this scenario, and a reduction in the number of parameters required for modeling the channel.

6.3.1.1 System Design

For investigating the differences between the models, we will consider two transmission strategies that employ square M-QAM transmission, with $M \geq 4$. For both systems, the rate is maximized such that a target BER constraint is met. The first system is a modified open loop (OL-MIMO) system which feeds back the appropriate number of antennas to use to the transmitter. The second system is a closed loop system that employs a waterfilling strategy. We examine the capacity gain of the open loop vs. closed loop architectures using the measured data matrices. We then compare the performance of the closed loop architecture using channel matrices generated by the Weichselberger and new reduced rank model. By doing so, it is possible to gauge both the performance in how well the models predict the system performance, as well as the benefit of extra feedback versus an open loop strategy. For more details on these strategies, refer to Section 6.1.2 and [1-4].

If the reduced rank model can reasonably capture the environment, it can be used in place of the full model to reduce the feedback parameters. The new reduced model offers a savings in feedback parameters, as not all of the eigenvectors at each link end are required, as well **Ω** has been reduced. Additionally, through the beamforming studies in Chapters 4 and 5, it was found that the link end eigenvectors remain reasonably stable for an environment, but that the coupling matrix required more frequent updates to continue to provide useful information to the transmitter. As such, it would be attractive to compact the information in **Ω**, as the transmitter may not need updated link end eigenbases by the time it needs an updated coupling matrix.

6.3.1.2 Structure of Ω

To evaluate the impact of a reduced eigenbasis model it would be useful to examine several measured channel scenarios. For each environment, measurements were performed using 8 receive and 8 transmit vertically polarized monopole arrays. For Environments 1 and 2, the antennas were in a uniform linear array arrangement. For Environment 3, the antennas were in a uniformly-spaced circular arrangement. Refer to Section 4.2.3 for more information on these environments.

Environment #1: Coal Yard – The transmitter and receiver were located in a Coal Yard to simulate an industrial or suburban type of environment.

Environment #2: Tree Propagation – The transmitter was placed behind shrubs and a tree, with the receiver on the opposite side of the foliage.

Environment #3: Indoor to Outdoor – The transmitter was inside a building in a hallway and the receiver was in a campus walkway area outside the building.

An example **Ω** structure generated from the average of the first 400 measured **H** matrix realizations for each of the environments is shown in Figure 6.7 (see (4.1) to (4.3)). Note that for Environment 3, within the Coal Yard, two different transmission scenarios are investigated. For the first scenario, the transmitter and receiver are stationary and all changes in the channel are due to pedestrians and other environmental changes. In the second scenario, the receiver is moved at a rate of approximately 1ft/sec, causing the channel to be more dynamic. Also, note that the appearance of higher powered coupling matrix elements in the top left corner is a result of the ordering of the receive/transmit eigenvectors from the eigenvalue decomposition used to generate the model parameters.

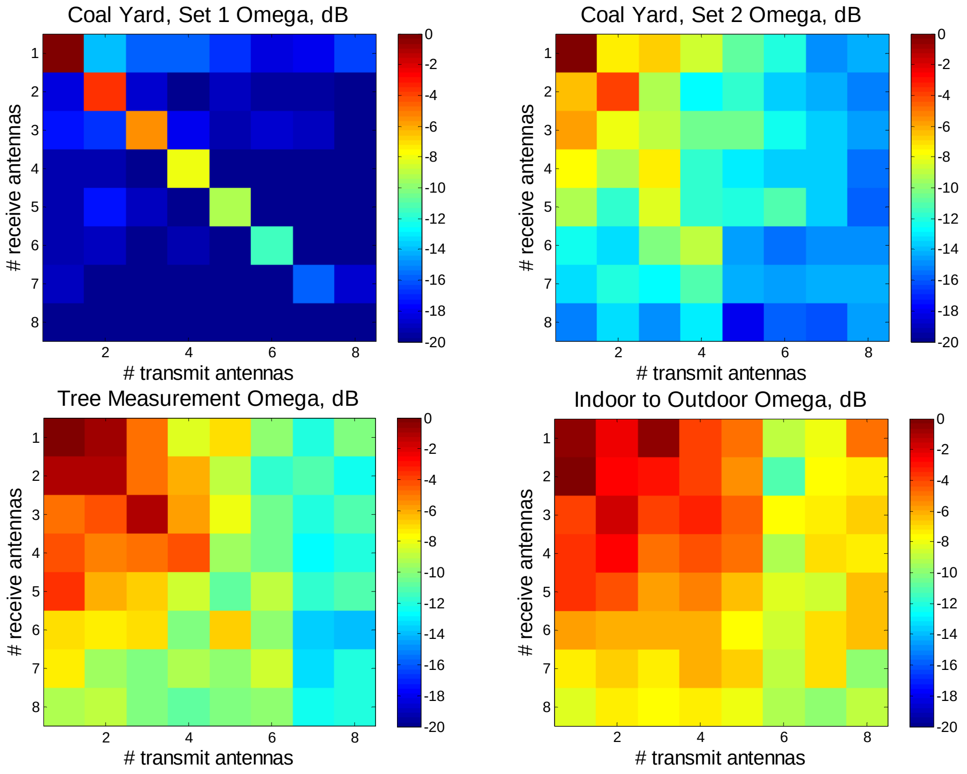

Figure 6.7. Normalized power coupling matrices generated from the first 400 channel realizations in the four environments investigated.

6.3.1.3 System Performance

For each of the environments, the measured channel gain matrices were normalized prior to their use in computing the channel models to ensure a fair comparison of coupling matrix effects. To generate the reduced model, we employ a simplified $\mathbf{\Omega}$ reduction, which accepts the 25 values of $\mathbf{\Omega}$ falling in the 'highpower' quadrant. That is, we generate the model by selecting a 5x5 subset of $\mathbf{\Omega}$ corresponding to the upper left quadrant, as viewed in Figure 6.7. This strategy does not select the highest 25 values in a strictly ordered sense, but may include a few powers that are lower than those found in the remainder of the coupling matrix. Additionally, the number of eigenvectors needed at the transmitter is reduced.

To compare the performance of the reduced Weichselberger model with the full Weichselberger model and the Kronecker model, a CL-MIMO waterfilling strategy was employed using 400 channel realizations of each model. To ascertain the benefit of this additional knowledge over a more simplified strategy, the performance of a modified OL-MIMO M-QAM scheme is also given. The resulting performance curves are plotted in Figures 6.8-6.11.

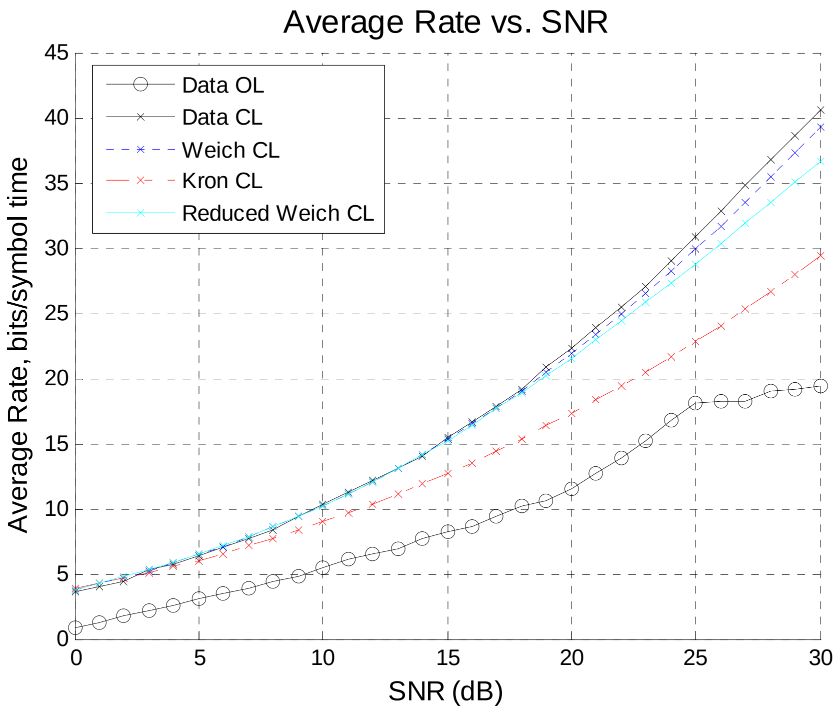

Figure 6.8: Capacity vs. SNR curves for Environment 1: Coal Yard data with a stationary transmitter.

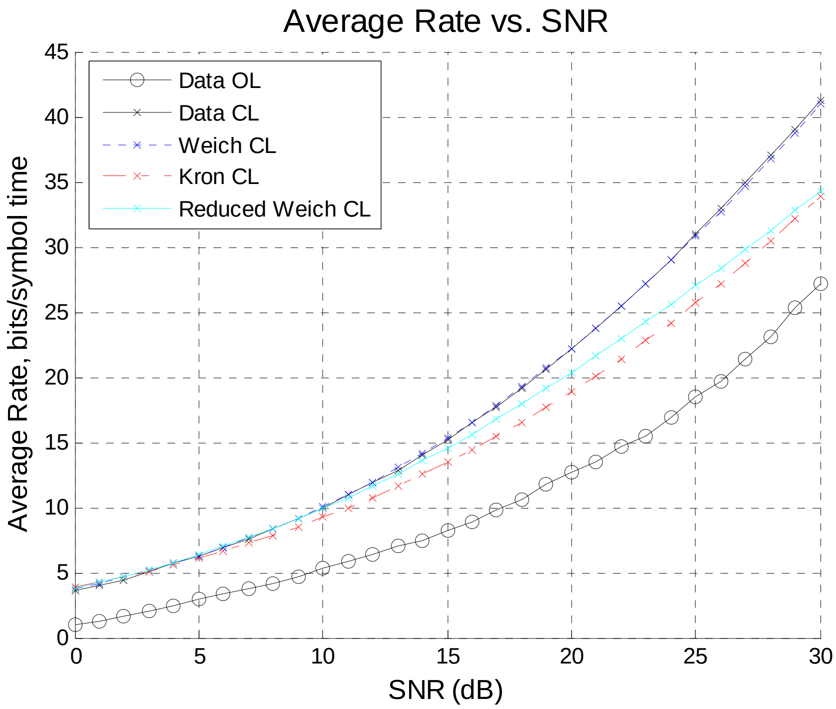

Figure 6.9. Capacity vs. SNR curves for Environment 1: Coal Yard data transmission with a moving transmitter.

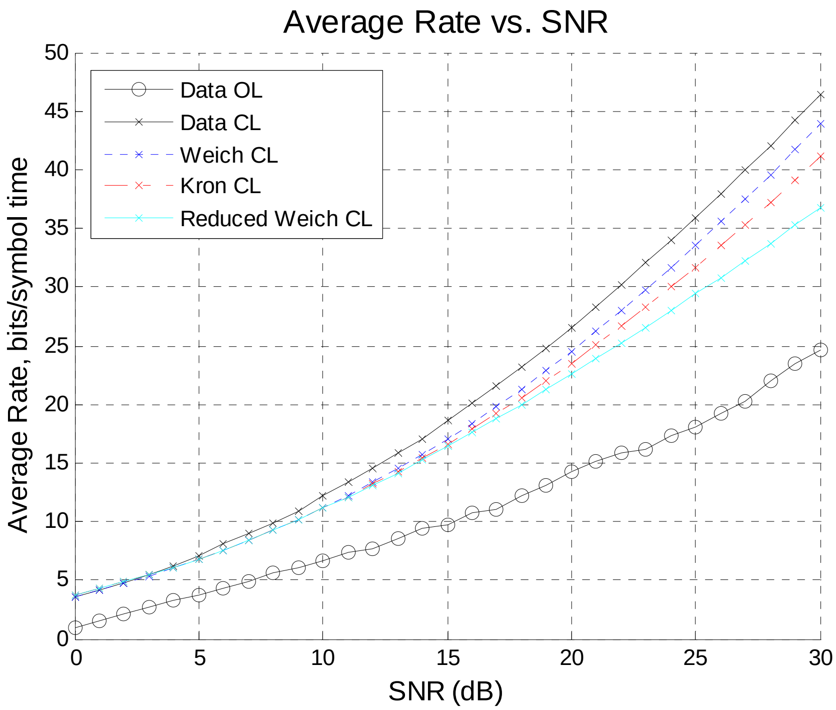

Figure 6.10. Capacity vs. SNR curves for Environment 2: Tree data transmission.

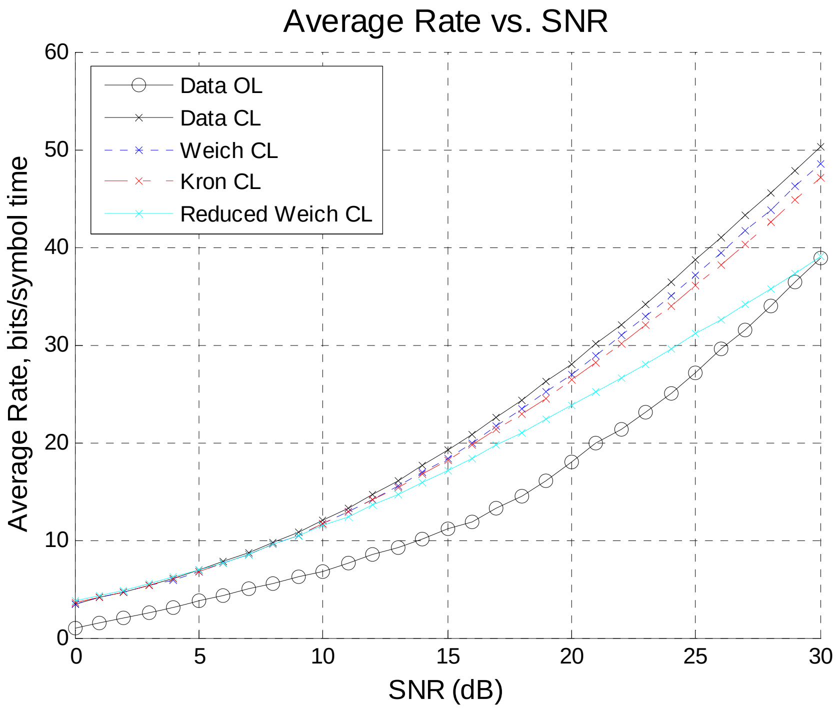

Figure 6.11. Capacity vs. SNR curves for Environment 3: Indoor to Outdoor data transmission.

The performance for the reduced model in the Indoor to Outdoor transmission environment is the worst out of the four scenarios investigated. This is expected, as the signal energy is distributed more equally throughout the $\mathbf{\Omega}$ matrix in this transmission environment. In the second environment with the trees, there are fewer primary scattering directions, and the $\mathbf{\Omega}$ matrix is more diagonalized. However, the reduced model still performs on par with the full model up to an SNR of approximately 13 dB.

Beginning with the Coal Yard environment in which the receiver is in motion, we start to see an improvement with the reduced model over the Kronecker model. This improvement is small, as the performance difference between the Kronecker model and the full Weichselberger model is not significant at low to moderate SNRs. To generate an average rate of 20 bits/symbol time, the Weichselberger model under predicts the SNR required by less than 0.1 dB. In contrast, the reduced model overestimates the SNR required by approximately 1 dB, which is an improvement over the estimate of the Kronecker model, at 2.3 dB. However, in the scenario where the receiver is stationary, the primary scatterer paths remain fairly stable. The channel diagonalizes well. From a spatial multiplexing perspective, if the transmitter sends parallel data streams on the transmit eigenmodes, they will arrive on orthogonal receive eigenmodes with little energy leakage. By selecting the top 5x5 section of the coupling matrix, the largest eigenvalues are captured in the reduced model. Since the closed loop strategy employed uses traditional waterfilling under a BER constraint, power would not be allocated to the remaining 3 parallel channels until high transmit SNRs were reached. Thus, the reduced model performs very well in this environment.

If we assume the Kronecker model to be the 'true' data, and generate a Weichselberger coupling matrix for that model, the underlying difference becomes readily apparent. The Kronecker model artificially spreads energy out into directions it is not naturally found. Similar observations, using angular power spectrum techniques were noted in [19-21]. The original Weichselberger Coal Yard Set 1 coupling matrix is provided again to facilitate a side by side comparison to the Kronecker model coupling matrix in Figure 6.12.

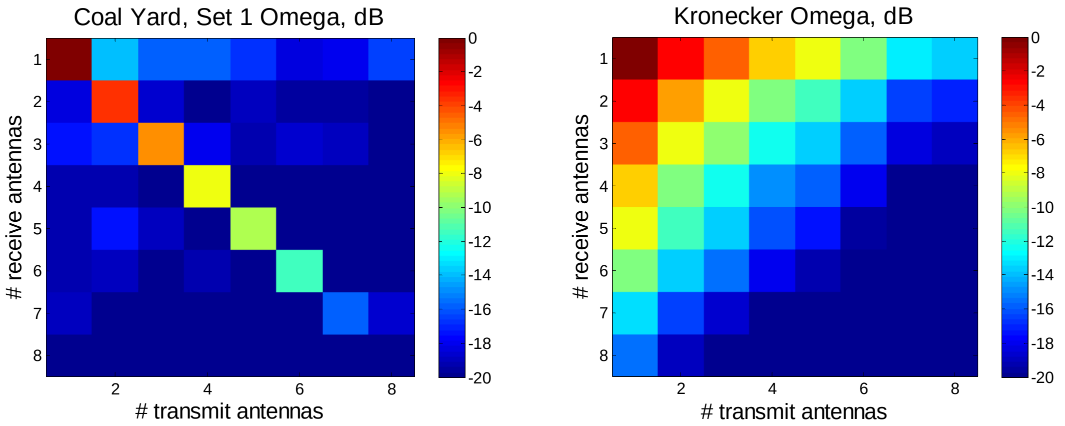

Figure 6.12: Power distribution in the full Weichselberger coupling matrix versus the Kronecker coupling matrix.

Clearly, the reduced model will not perform as well as the full eigenbasis model at high SNRs. As the SNR levels increase, additional subchannels may be excited as more antennas are able to transmit. These additional antennas may cause the full eigenbasis model to have larger rank than the reduced model. When this occurs the reduced model is unable to model the additional capacity available in the channel from the additional antennas. This behavior explains the difference in slope between the full and reduced eigenbasis models at high SNR shown in Figures 6.8-6.11. However, at lower SNRs, the reduced model can predict the capacity of the channel with reasonable accuracy. Thus, for low SNR transmission, knowledge of the high powered section of coupling matrix, **Ω**, may be sufficient for modeling the channel in place of the full expression. When only the coupling matrix needs to be updated, this can provide a savings in feedback overhead.

6.3.2 Knowledge of Ω Only

While the model considered in Section 6.3.1 reduces the rank of the full Weichselberger model to reduce the feedback parameters, consider an alternate methodology to reduce the number of parameters needed to model the channel. If the transmitter only has knowledge of the power coupling matrix, the capacity of the channel can still be computed. Consider the modified uninformed transmitter (UT) capacity expression from (3.17) where the SNR term is absorbed into the channel matrices:

$$\overline{\mathbf{C}}_{UT} = E_H\left\{\log_2 \det\left(\mathbf{I}_{n_r \times n_r} + \mathbf{H}\mathbf{H}^H\right)\right\} \tag{6.8}$$

Substituting the Weichselberger synthesis expression, (3.21), for the channel matrix, **H**, gives

$$\overline{\mathbf{C}}_{UT} = E_H\left\{\log_2 \det\left(\mathbf{I}_{n_r \times n_r} + \mathbf{U}_{rx}\left(\tilde{\mathbf{\Omega}} \circ \mathbf{H}_w\right)\mathbf{U}_{tx}^T\mathbf{U}_{tx}^*\left(\tilde{\mathbf{\Omega}} \circ \mathbf{H}_w\right)^H \mathbf{U}_{rx}^H\right)\right\} \tag{6.9}$$

Since the eigenbasis are unitary matrices, the expression simplifies to:

$$\overline{\mathbf{C}}_{UT} = E_H\left\{\log_2 \det\left(\mathbf{I}_{n_r \times n_r} + \mathbf{U}_{rx}\left(\tilde{\mathbf{\Omega}} \circ \mathbf{H}_w\right)\left(\tilde{\mathbf{\Omega}} \circ \mathbf{H}_w\right)^H \mathbf{U}_{rx}^H\right)\right\} \tag{6.10}$$

Furthermore, the expression can be simplified using the matrix relation, det(**I** + **UAU**$^{\mathrm{H}}$) = det(**I** + **A**).

This results in the simplified expression:

$$\overline{\mathbf{C}}_{UT} = E_H\left\{\log_2 \det\left(\mathbf{I}_{n_r\times n_r} + \left(\tilde{\mathbf{\Omega}}\circ \mathbf{H}_w\right)\left(\tilde{\mathbf{\Omega}}\circ \mathbf{H}_w\right)^H\right)\right\} \tag{6.11}$$

Clearly, from the perspective of capacity, knowledge of the power coupling matrix **Ω** provides all information needed about the channel. If the expression of (6.11) is modified for an informed transmitter, the link end eigenbases are still eliminated from the expression. Thus, we can consider the model performance for the open-loop and closed-loop architectures using just **Ω**.

Modifications of the open-loop and closed-loop system architectures from Section 6.2.2 must be made in order for the algorithms to work using just **Ω**. Note that the waterfilling algorithm requires the eigenvalues of $\mathbf{HH^H}$. Recall E{ $\mathbf{HH^H}$ } is the one-sided receive correlation matrix. For low amounts of averaging, or in relatively stationary environments, the eigenvalues of $\mathbf{HH^H}$ and E{ $\mathbf{HH^H}$ } are approximately equal. For highly variable environments, or equivalently for long averages over a variable environment, this approximation will not hold true. For these environments, the eigenvalues will have to be computed for the channel realizations.

Due to the nature of **Ω**, summing across columns (or rows) gives the eigenvalues of the transmit (or receive) link end correlation matrix. That is [20]:

$$\lambda_{rx,m} = \sum_{n=1}^{n_t} \omega_{m,n} \text{ and } \lambda_{tx,m} = \sum_{n=1}^{n_r} \omega_{m,n} \tag{6.12}$$

Since the eigenvalues can be directly determined from the power coupling matrix, **Ω** can be used directly in waterfilling schemes without generating channel realizations for performance analysis for environments where the eigenvalues of $\mathbf{HH^H}$ and E{ $\mathbf{HH^H}$ } are approximately equal. One such environment is the Coal Yard environment in which both link ends are stationary. The performance curves for this environment are shown in Figures 6.13 and 6.14 below, where the capacity curves generated using knowledge of **Ω** alone are designated “Omega CL”.

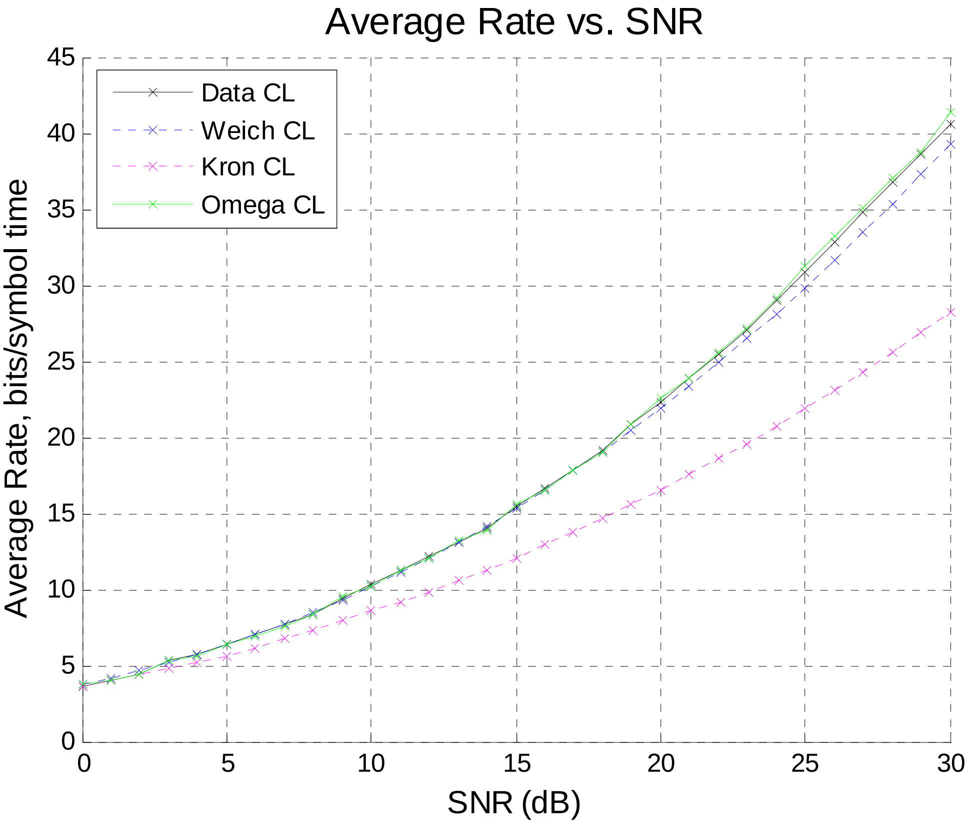

Figure 6.13: Throughput of a measured NLOS channel, stationary transmitter and receiver, BER = 10^{-2}.

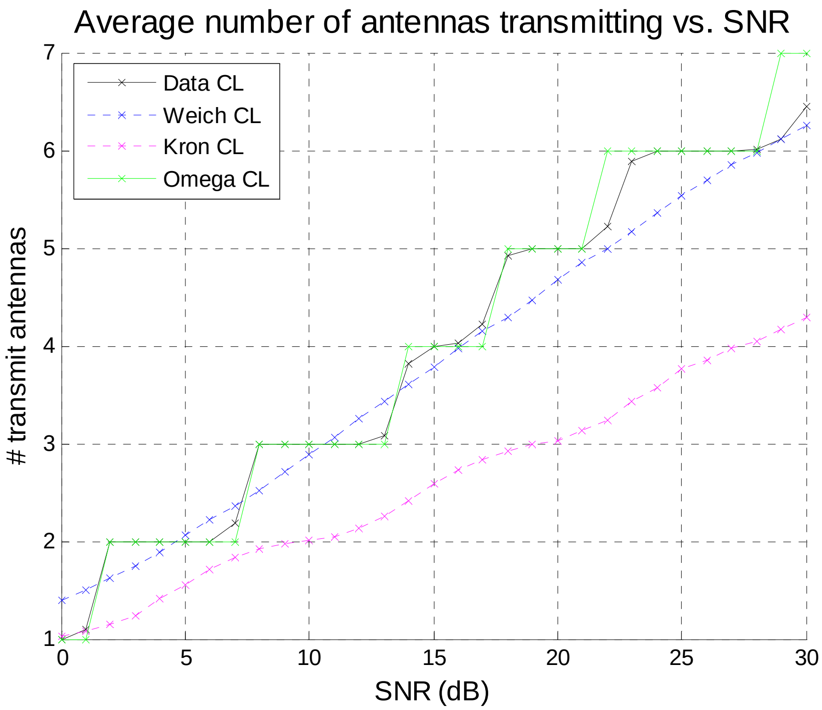

Figure 6.14: Average number of antennas transmitting for a NLOS channel, stationary transmitter and receiver, BER = 10^{-2}.

For the case where the link end receiver is in motion, there is a larger discrepancy between the measured data and the modeled performance. This performance difference is magnified at higher SNR, where the error in estimation of the smaller eigenvalues leads to additional antennas transmitting before the channel can actually support them. The performance at moderate to low SNRs, however, is reasonable. The resulting curves can be seen in Figures 6.15 and 6.16.

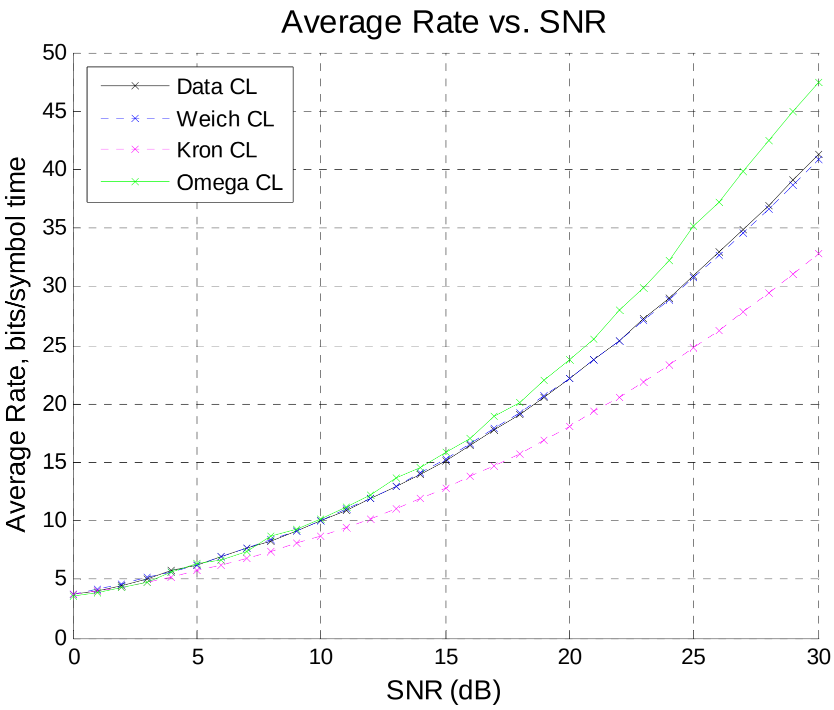

Figure 6.15: Throughput of a measured NLOS channel, stationary transmitter and receiver, BER = 10^{-2}.

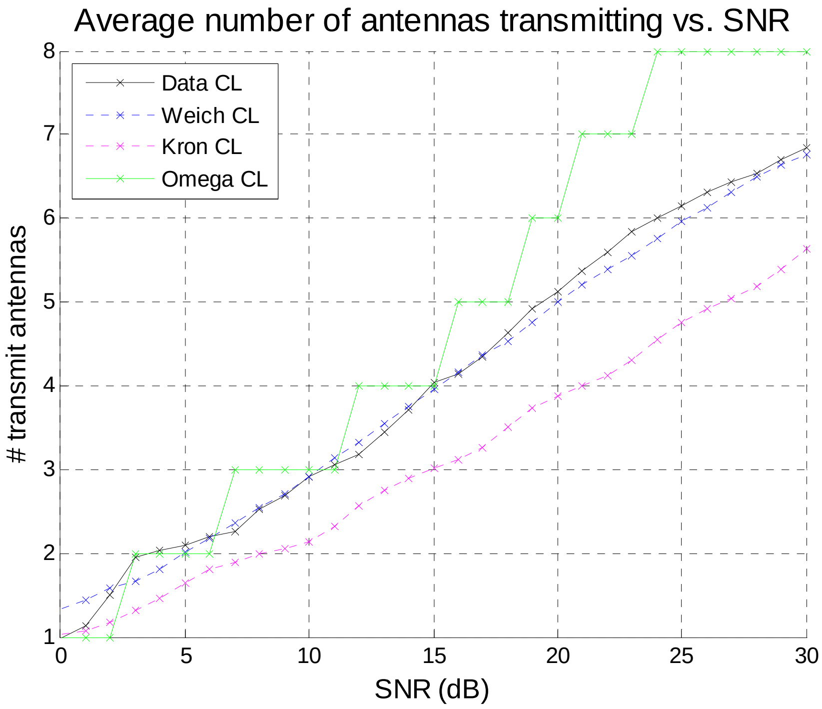

Figure 6.16: Average number of antennas transmitting for a NLOS channel, stationary transmitter and receiver, BER = 10^{-2}.

6.4 Summary

In this chapter, we examined OL-MIMO and CL-MIMO communication systems using simulated data as well as measured data sets for NLOS environments under different channel matrix model assumptions.

The results show a significant difference in adaptive system performance based on the choice of model. The Weichselberger model accurately predicts the average channel behavior for the environments explored. In contrast, use of the Kronecker model results in the incorrect number of active antennas being selected for transmission. It also results in a pessimistic assignment of the modulation index. If the Kronecker model is used for algorithm design, the performance predicted in correlated channels would be inaccurate.

In this section, we have shown that a reduced eigenbasis model can offer a good characterization of channel performance, in terms of capacity, at low to moderate SNRs for a realistic transmission scheme. At higher SNRs, the additional modes of the channel become significant, and the reduced model does not capture the contribution of these modes. Additionally, we have demonstrated that the Kronecker model is significantly outperformed by the reduced rank model in certain transmission scenarios in which the energy is concentrated along the diagonal of the coupling matrix.

Instead of using the whole channel model, knowledge of $\mathbf{\Omega}$ alone may be sufficient for determining the correct system mode of operation. Use of the full coupling matrix reduces the number of feedback parameters without suffering from the high SNR issues seen with the reduced rank modeling. However, knowledge of $\mathbf{\Omega}$ alone does not capture the channel behavior well, in terms of capacity, at SNRs where additional antennas or higher modulation indexes are supported.

For environments such as the Coal Yard, in which the energy is distributed in a diagonalized manner in the coupling matrix, reducing the coupling matrix in a regularized rectangular pattern is not optimal. Clearly, knowledge of the diagonal of the coupling matrix for Set 1 in the Coal Yard would provide nearly all information in the full coupling matrix. An intelligent representation of the diagonal could be used to further compact the Weichselberger representation. This sort of compaction would lend itself to feedback schemes for adaptive MIMO systems where minimizing the feedback overhead is important. Additional investigation would be required to determine the most effective manner in which this compaction should be performed.

6.5 Acknowledgment

This chapter, in part, is a reprint of the material as it appears in "Impact of Channel Models on Adaptive M-QAM Modulation for MIMO Systems," L. C. Wood and W. S. Hodgkiss, *Wireless Communications and Networking Conference, 2008. WCNC 2008. IEEE* , vol., no., pp.1316-1321, March 31 2008-April 3 2008 and "A Reduced-Rank Eigenbasis MIMO Channel Model," L. C. Wood and W. S. Hodgkiss, *Proceedings of IEEE Wireless Telecommunications Symposium*, WTS 2008, pp.78-83, 24-26 April 2008. The dissertation author was the primary author of these papers.

6.6 References

[1] P. W. Wolniansky, G. Foschini, G. Golden, and R. A. Valenzuela, “V-BLAST: an architecture for realizing very high data rates over the rich-scattering wireless channel.” *Proceedings URSI International Symposium on Signals, Systems, and Electronics*, (IEEE, New York, NY, USA), pp. 295--300, 1998.

[2] G. D. Golden, G. J. Foschini, R. A. Valenzuela, and P. W. Wolniansky, "Detection algorithm and initial laboratory results using V-BLAST space-time communication architecture," Electronics Letters, vol. 35, no. 1,Jan. 1999.

[3] R. Gowrishankar, M. F. Demirkol. "Adaptive M-QAM modulation for MIMO systems." *IEEE/ACES International Conference on Wireless Communications and Applied Computational Electromagnetics*, 2005, 3-7 April 2005, pp. 66- 69.

[4] R. Gowrishankar, M. F. Demirkol, and Yun Zhengquing. "Adaptive modulation for MIMO systems and throughput evaluation with realistic channel model." *International Conference on Wireless Networks, Communications and Mobile Computing*, 2005, Vol.2, Iss., 13-16 June 2005, pp. 851- 856 vol.2

[5] L. Ren, Z. Yan, M. Song, J. Song, "An improved water-filling algorithm for mobile MIMO communication systems over time-varying fading channels," Proc. of IEEE Canadian Conference on Electrical and Computer Engineering. May 2004.

[6] G. Lebrun, T. Ying, M. Faulkner, "MIMO transmission over time varying TDD channel with SVD," Electronic Letters, vol. 37, pp. 1363-1364, Oct. 2001.

[7] M. F. Demirkol, M. A. Ingram, Z. Yun, "Feasibility of closed loop operation for MIMO links with MIMO interference," Proc. of the IEEE Int'l Svmp. on Antennas and Prop., Jun. 2004.

[8] A. J. Goldsmith and S. Chua, "Variable-rate variable-power MQAM for fading channels," IEEE Trans. Comm., vol. 45, pp. 1218-1230, Oct. 1997.

[9] S. Catreux, V. Erceg, D. Gesbert, R. W. Heath, Jr., "Adaptive modulation and MIMO coding for broadband data networks," IEEE Comm. Magazine, vol. 40, no. 6, June 2002

[10] S. Chua and A. Goldsmith, "Variable-rate variable-power MQAM for fading channels." *Vehicular Technology Conference*, 1996. 'Mobile Technology for the Human Race'., IEEE 46th, vol. 2, 28 Apr-1 May 1996, pp. 815-819.

[11] S. Zhou and G. B. Giannakis, "Adaptive Modulation for multiantenna transmissions with channel mean feedback," *IEEE Transactions on Wireless Communications*, Vol.3, Iss.5, Sept. 2004, pp. 1626- 1636.

[12] M. F. Demirkol and M. A. Ingram, "Power controlled capacity for interfering MIMO links," *Proc. IEEE Vehicular Technology Conf.,* Oct. 2001.

[13] S. T. Chung, A. Lozano, and H. C. Howard, "Approaching eigenmode BLAST channel capacity using V-BLAST with rate and power feedback," *Proc. IEEE Vehicular Technology Conf*, Oct. 2001.

[14] K. J. Hwang and K. B. Lee, "Transmit power allocation with small feedback overhead for a multiple antenna system," *Proc. IEEE Vehicular Technology Conf*, Sep. 2002.

[15] E. Telatar, Capacity of Multi-antenna Gaussian Channels, Technical Report, AT&T Bell Labs. June 1995.

[16] J.W. Wallace and M. A. Jensen, “Experimental analysis of the time-varying MIMO channel,” *Antennas and Propagation Society International Symposium 2006*, IEEE, 9-14 July 2006, pp. 321- 324.

[17] J.W. Wallace, M. A. Jensen, A. L. Swindlehurst, and B. D. Jeffs, “Experimental characterization of the MIMO wireless channel: Data acquisition and analysis,” *IEEE Trans. Wireless Commun.*, vol. 2, pp. 335–343, Mar. 2003.

[18] G. D. Galdo, M. Haardt, and M. Milojevic, “A subspace-based channel model for frequency selective time variant MIMO channels,” in *Proc. 2004 IEEE 15th Intl. Symp. on Personal, Indoor and Mobile Radio Comm.*, vol. 3, Barcelona, Spain, Sep. 5 2004, pp. 1603–1607.

[19] W. Weichselberger, "Spatial structure of multiple antenna radio channels --- a signal processing viewpoint", PhD dissertation, Vienna University of Technology, Vienna, Austria, 2003.

[20] W. Weichselberger, M. Herdin, H. Özcelik, and E. Bonek, “A Stochastic MIMO Channel Model with Joint Correlation at Both Link Ends,” *IEEE Trans Wireless Communications*, Vol 5, No. 1. Jan 2006, pp. 90-100.

[21] H. Ozcelik, M. Herdin, W. Weichselberger, J. Wallace and E. Bonek, “Deficiencies of 'Kronecker' MIMO radio channel model,” *Electronics Letters*, Vol.39, Iss.16, 7 Aug. 2003, pp. 1209- 1210.

7 On the Preference of Spatial Multiplexing Over Diversity for Correlated MIMO Channels

7.1 Introduction

In designing multiple antenna systems, a fundamental decision that must be addressed is how to best to use the channel resources available. One of the primary tradeoffs in multiple antenna systems is whether to use the channel for spatial multiplexing to increase the throughput, or for spatial diversity to guard against fading.

For spatial diversity systems, multiple antennas are used to combat multipath channel fading. Each link from a transmit to a receive antenna provides a path for the signal to travel. By sending copies of the same information through different paths, multiple copies of the data will arrive at the receive end. If the different paths have independent fading gains, the multiple copies will provide additional reliability by allowing the receiver to choose the highest SNR reception, or to recombine the signals in a smart fashion to achieve even higher gains. A variety of diversity schemes have been explored in literature in [1-4].

In contrast, rather than combating multipath fading, spatial multiplexing exploits the multiple paths formed. For channels in which the channel gains fade independently between pairs of transmit and receive antennas, the channel can be decomposed into parallel channels. To form parallel channels, the transmitted vector is modified with the right singular basis vectors prior to transmission. The received signal is then decomposed using the left basis vectors from the singular value decomposition of the channel. By transmitting different information streams in a smart fashion on the parallel channels, the throughput of the channel can be increased [5-7]. This increase may allow for the ergodic capacity of the channel to be reached, as detailed in [8, 9] for i.i.d Rayleigh fading channels. However, when antennas are all used for increasing the throughput, the spatial diversity gain is not available [10].

The issue of channel resource tradeoffs has been explored in literature [11-16]. In [11], the tradeoff between multiplexing and diversity is discussed for the high-SNR regime for i.i.d. Rayleigh fading channels using outage capacity formulations. In [12], the authors expand upon the work of [11] to examine the finite SNR regime using asymptotic expressions as the number of antennas at both link ends approach infinity. Rician fading channels are examined in [13]. The authors of [14] relax the definition of multiplexing gain in [11] to derive an alternate throughput-reliability tradeoff expression. A non-asymptotic, finite-SNR analysis is explored in [15] for Rayleigh and Rician channels. Also, the analysis includes the special case of Rayleigh fading with Kronecker modeled correlated channels, where correlation occurs at either the transmitter or the receiver, but not both.

Additionally, the question of whether a channel is spatial multiplexing preferred was addressed in [16]. To be spatial multiplexing preferred, the channel must be more suitable for spatial multiplexing transmission. That is, for fixed rate schemes, the worst minimum constellation distance of spatial multiplexing is larger than the best minimum constellation distance for diversity transmission. The larger constellation differences translate into an improvement in the BER of the system. Instead of using an outage probability approach as in [11-15], the authors showed that the channel preference for spatial multiplexing was related to the Demmel condition number. Furthermore, the authors developed intuition for the likelihood of preferring spatial multiplexing for i.i.d. Rayleigh fading channels. However, channels with correlation were not investigated.

In this work, the structured eigenbasis model proposed by Weichselberger is used to examine channels with spatial correlation [17-18]. This model has been shown to more accurately represent the channel in comparison to the more commonly used Kronecker model [18-21]. The structured eigenbasis model directly parameterizes measured channel matrices, linking the behavior at the antenna arrays together through a power coupling matrix. In certain scenarios, the structure of the coupling matrix can offer immediate knowledge about whether diversity is the best mode to use for the channel based on how the power is distributed in the matrix. For full rank power coupling matrices, however, the channel can be used for either spatial multiplexing or spatial diversity, requiring a more detailed investigation. By establishing a relationship between the coupling matrix parameters and the channel usage preference, we establish a useful means for switching between modes in practical wireless systems [22, 23]

In this section, the structured eigenbasis model is used to extend the framework of [16] to channels with correlation, answering the question of when transmitting using spatial multiplexing only is preferred for correlated channels. To generate channels with realistic spatial correlation, the structured eigenbasis model parameters are estimated from four measured data sets. The measurements used in this work are provided from a measurement campaign at Brigham Young University [24, 25]. Several different environments are investigated which vary in multipath richness and correlation.

7.2 Structure of Ω

To evaluate the impact of correlation it would be useful to examine several measured channel scenarios. For each environment, measurements were performed using 8 receive and 8 transmit vertically polarized monopole arrays. For Environments 2 and 3, the antennas were in a uniform linear array arrangement. For Environment 1, the antennas were in a uniformly-spaced circular arrangement.

- *Environment #1: Coal Yard* – The transmitter and receiver were located in a Coal Yard to simulate an industrial or suburban type of environment.
- *Environment #2: Tree Propagation* – The transmitter was placed behind shrubs and a tree, with the receiver on the opposite side of the foliage.
- *Environment #3: Indoor to Outdoor* – The transmitter was inside a building in a hallway and the receiver was in a campus walkway area outside the building.

Refer to Section 4.2.3 for more information on these environments.

For each environment, the distribution of power within the coupling matrix differs. By examining the structure of Ω, we note that certain structures have clear meaning for the channel. If a single column contains the power, the receive array can be excited by a signal from a single source. Since there is only a single source involved, spatial multiplexing is not applicable to this channel. However, this structure indicates that the channel supports receive diversity. Alternatively, if a single row contains all of the power, transmit diversity is supported. If the power is distributed along the diagonal, then the channel decomposes perfectly, in that an eigenvector at the transmitter is uniquely linked to a single receive eigenvector. This would be useful for spatial multiplexing, and would have a power coupling matrix structure as in the Coal Yard, Set

1, as shown in Figure 6.7. However, the channel could still be used for spatial diversity as redundant information could be sent over the parallel subchannels. For the other three coupling matrices given in Figure 6.7, it is even less clear whether spatial diversity or spatial multiplexing transmission will be the preferred mode of transmission for a given rate and SNR as the power is distributed throughout $\mathbf{\Omega}$.

7.3 Spatial Multiplexing vs. Spatial Diversity

It was shown in [16] that the tradeoff between spatial multiplexing and spatial diversity was related to the Demmel condition number. For completeness we summarize their results below.

7.3.1 Spatial Multiplexing

Consider a spatial multiplexing system in which a modulator maps bits to symbols, with R/n_t bits per symbol. The multiplexer then stacks n_t symbols to produce the n_t x 1 vector symbol x(n) for transmission. This configuration results in unique bit streams being transmitted from each transmit antenna. At the receiver, spatial demultiplexing is used to extract an estimate of the original bit stream from the received vector y(n). Maximum-likelihood reception is considered.

For spatial multiplexing transmission, the minimum squared Euclidean distance at the receiver, $d^2_{\min,SM}$, is found by minimizing the distance between the received codeword and the possible codewords at the receiver:

$$d^2_{\min,SM}(\mathbf{H}) = \min_{x,c\in S_{SM},x\neq c} \left\|\mathbf{H}(\mathbf{x}-\mathbf{c})\right\|^2 \tag{7.1}$$

Transmission through the channel modifies the distance properties of the original constellation. Rather than performing an exhaustive search, upper and lower bounds were developed by applying the Rayleigh-Ritz theorem:

$$\lambda_{\min}^{2}(\mathbf{H})\frac{d_{\min,sm}^{2}}{n_t} \le d_{\min,SM}^{2}(\mathbf{H}) \le \lambda_{\max}^{2}(\mathbf{H})\frac{d_{\min,sm}^{2}}{n_t} \tag{7.2}$$

where $\lambda_{\max}^{2}$ is the maximum singular value of the channel and $d_{\min,sm}^{2}$ is the Euclidean distance at the transmitter. Since we are interested in the minimum Euclidean distance, the bound of interest is the lower bound.

7.3.2 Spatial Diversity

For the spatial diversity system, the class of full-rate linear space-time block codes are considered. A modulator maps bits to symbols, with R bits per symbol. A linear block modulation scheme then forms a codeword using N input symbols. For this class of codes, the diversity code distance at the receiver, $d_{\min,MD}^{2}$, can be shown to be bounded according to:

$$d_{\min,MD}^{2}(\mathbf{H}) \le \frac{1}{n_t}\|\mathbf{H}\|_F^2\, d_{\min,md}^{2} \tag{7.3}$$

where $d_{\min,md}^{2}$ is the Euclidean distance at the transmitter and $\| \ \|_F^2$ is the Frobenius norm. Using these bounds, it is possible to determine when the lower bound on the minimum distance for spatial multiplexing will always exceed the upper bound on the minimum distance required for diversity transmission. For channels in which this relationship holds, spatial multiplexing will always outperform spatial diversity, in terms of the union bound on the probability of codeword error.

Comparing the upper and lower bounds, it is found that multiplexing is preferred when:

$$\kappa_D \le \frac{d_{\min,sm}}{d_{\min,md}} \tag{7.4}$$

where κ_D is the Demmel condition number, defined as $\kappa_D = \|\mathbf{H}\|_F \|\mathbf{H}^{-1}\|_2$.

7.4 Statistical characterization of κ_D

To characterize the probability that a system will be in a spatial multiplexing mode for a given rate, it is necessary to determine the cumulative distribution function (CDF) of κ_D. We consider the case where the number of transmit antennas is equal to the number of receive antennas.

7.4.1 Uncorrelated Rayleigh Channels

For square uncorrelated Rayleigh channels, n_t x n_t there exists a closed form solution for the CDF, given as:

$$\Pr(\kappa_D \le \gamma) = (1 - n_t / \gamma^2)^{n_t^2}, \qquad \gamma > \sqrt{n_t} \tag{7.5}$$

When $\gamma = d_{\min,sm}/d_{\min,md}$, the probability that strictly spatial multiplexing is preferred for a given channel can be determined. To compute the theoretical performance as a function of n_t and R, a modulation scheme must first be selected. The same constellation family is selected for both spatial multiplexing and spatial diversity. For a fair comparison of the two schemes, when a constellation is used for spatial diversity scheme, it is a function of R. However, when it is used for spatial multiplexing, it is a function of R/n_t. To be consistent with [16], we examine 2^R-QAM modulation, using the formula $d^2 = 12/(2^R-1)$.

Curves for n_t = 2, 4, 6, 8 are plotted in Figure 7.1 for a simulated uncorrelated Rayleigh channel. The theory curve is plotted using (7.5), and the Rayleigh data curve from simulated channel matrices, is given for comparison.

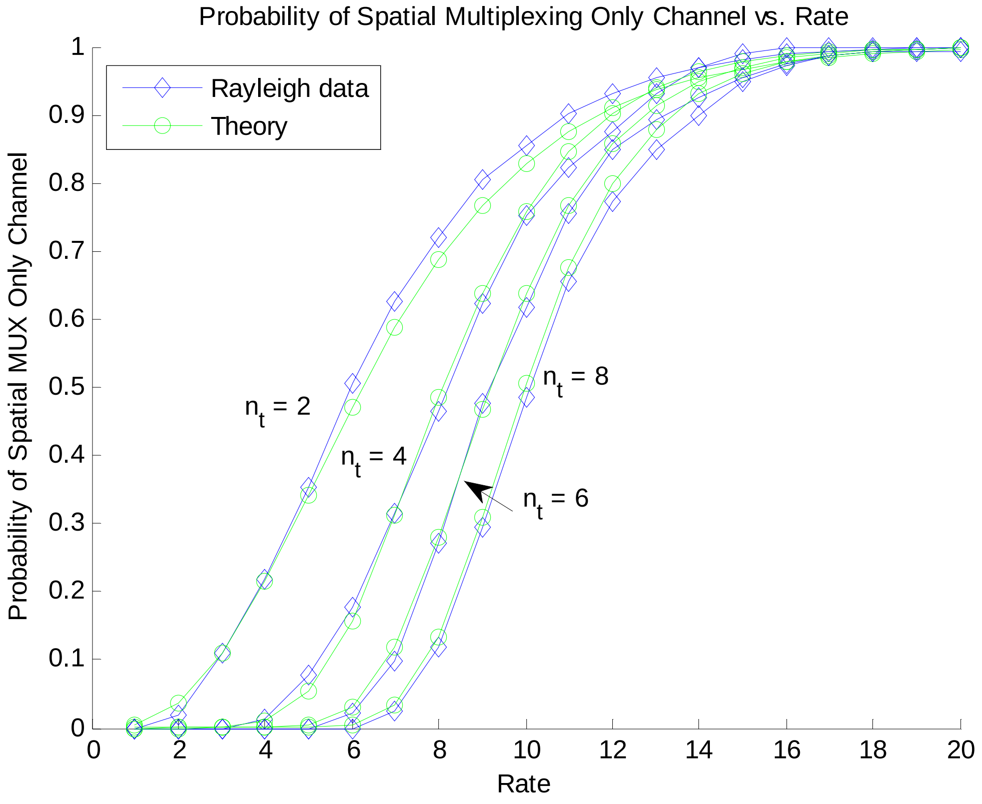

Figure 7.1: Simulated vs. theoretical CDFs for i.i.d Rayleigh fading.

7.4.2 Correlated Channels

Although the uncorrelated Rayleigh fading scenario provides insight into spatial multiplexing preferred channels, it does not address spatial correlation, which can be a significant factor in multi-antenna communication systems. An equivalent closed-form expression to (7.5) for channels with spatial correlation does not exist to the author's knowledge. Instead, to determine the probability that the system will be in a spatial multiplexing preferred mode, CDFs are created from structured eigenbasis channel matrices. These matrices were obtained for each of the four experimental data sets explored. The Demmel condition number was computed for each realization, and the CDFs from the structured eigenbasis model were formed.

The CDF curves for the Rayleigh fading case are roughly similar in shape to those in the correlated channels, except they are shifted toward the right. To achieve the same effect, approximate CDFs were formed by substituting the expression for n_t in (7.5) with αn_t. For each data set, the values of α that best fit the curve were determined. The values of α for each of the data sets for $n_t = 2, 4, 6, 8$ are given in Table 7.1.

It would be useful to be able to determine the α values approximately using the values from the coupling matrix. Such an approximation could allow for rapid feedback of the appropriate transmission mode for the communications system. To estimate α from the power coupling matrix, the largest n_t values in the power coupling matrix are added together. The theoretical CDFs and those formed using the estimated α's are plotted, along with the curves from the structured eigenbasis modeled data in Figure 7.2(a)-(d).

Table 7.1: Values of α

	Coal Yard Set 1	Coal Yard Set 2	Trees	Indoor-Outdoor
$n_t = 2$	1.1	1.05	1.2	1.15
$n_t = 4$	1.35	1.6	1.6	1.45
$n_t = 6$	1.45	2.0	1.85	1.65
$n_t = 8$	1.45	2.0	1.9	1.65

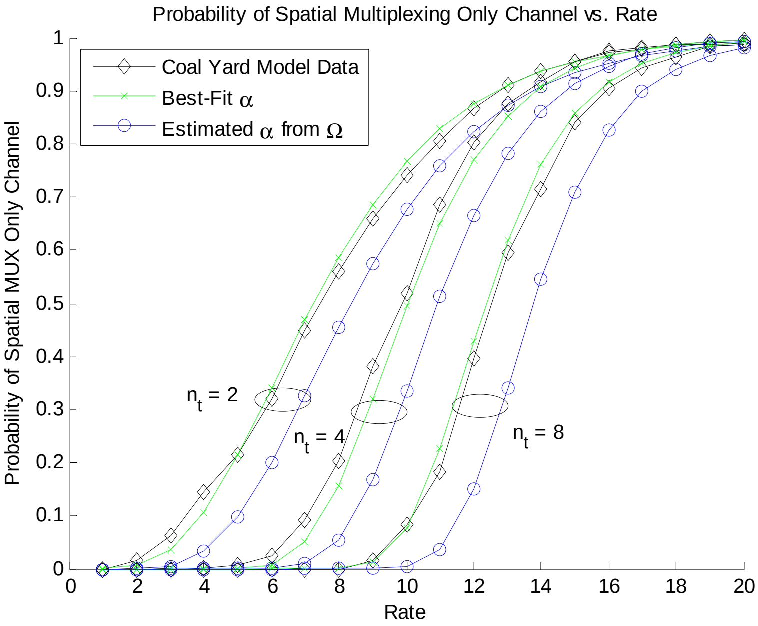

Figure 7.2(a): Probability that spatial multiplexing only is preferred vs. rate for Coal Yard, Set 1 channel.

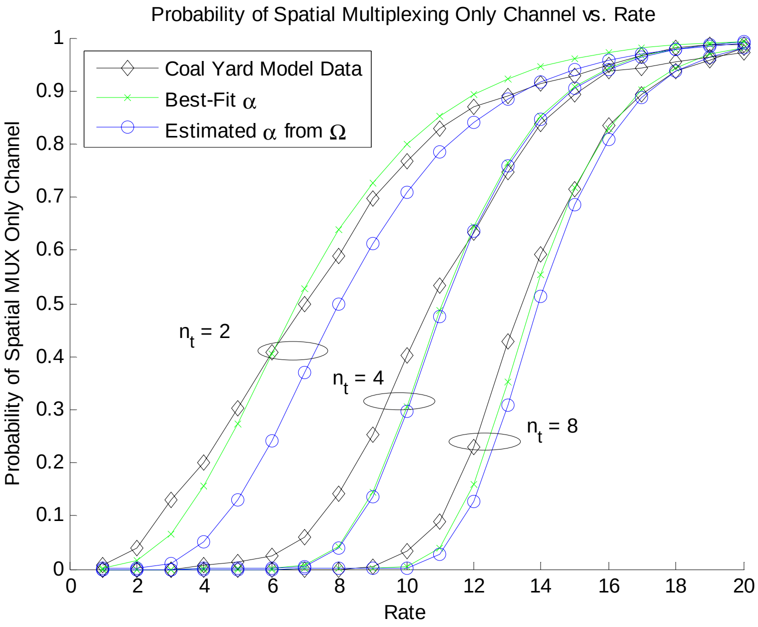

Figure 7.2(b): Probability that spatial multiplexing only is preferred vs. rate for Coal Yard, Set 2 channel.

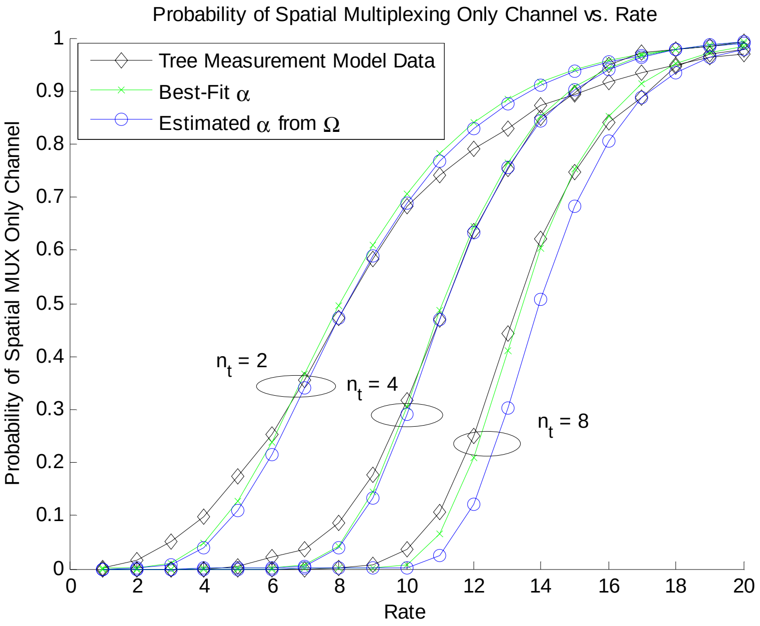

Figure 7.2(c). Probability that spatial multiplexing only is preferred vs. rate for Tree channel.

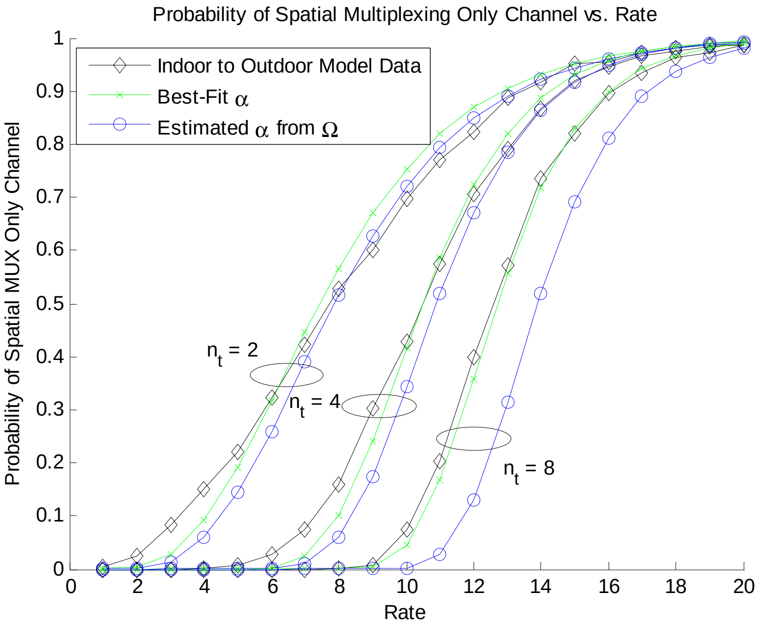

Figure 7.2(d): Probability that spatial multiplexing only is preferred vs. rate for the Indoor to Outdoor channel.

To compare the curves in Figure 7.2 with the i.i.d Rayleigh fading case from Figure 7.1, note that the α parameter for the i.i.d Rayleigh fading scenario is α = 1. The performance of the Rayleigh and correlated data sets are very similar for 2 x 2 systems. However, the difference between the Rayleigh and correlated fading scenarios becomes larger as the number of antennas increases. Thus, for systems with more than 2 antennas at the link ends, the closed form solution of (7.5) does not provide a reasonable estimate. However, by modifying the expression of (7.5) with the parameter α, as estimated from the largest n_t values of the power coupling matrix, a closed form approximation to the true channel CDF can be obtained.

7.5 Summary

In this section, the question of whether a channel is spatial multiplexing preferred was explored for spatially correlated channels. The structured eigenbasis model was used to extend the framework of [16] to channels with correlation. To generate realistic channels with correlation, the structured eigenbasis model parameters were estimated from measured data sets. Empirical CDFs were constructed from many channel realizations. From these curves, the probability that spatial multiplexing only is preferred for a channel was determined.

The spatially correlated CDF curves were compared to the uncorrelated Rayleigh fading case. It was found that the closed form expression for the probability that spatial multiplexing is preferred in uncorrelated Rayleigh fading channels provides a reasonable approximation to the correlated channel explored for 2 x 2 systems. However, for larger numbers of antennas, an alternate expression will be required to accurately predict the probability that a channel will be spatial multiplexing preferred. A closed form approximation to the correlated curves was made by modifying the Rayleigh solution with a parameter that can be determined from the power coupling matrix of the structured eigenbasis model. In practice, the pdf curves assist in the creation of operational mode lookup tables. By restricting the system to a set of operational modes, the transmitter can switch between different transmission modes as the channel changes based on a finite set of parameters. Such a scheme was used in [23] and [26].

7.6 References

[1] A. Wittneben, "Base station modulation diversity for digital simulcast," in *Proc. IEEE Vehicular Technology Conf.*, pp. 848–853, May 1991.

[2] N. Seshadri and J. H. Winters, "Two signaling schemes for improving the error performance of frequency-division-duplex (FDD) transmission systems using transmitter antenna diversity," *Int. J. Wireless Inform. Netw.*, vol. 1, no. 1, pp. 49–60, Jan. 1994.

[3] S. M. Alamouti, "A simple transmit diversity technique for wireless communications," *IEEE J. Sel. Areas Commun.*, vol. 16, no. 8, pp. 1451–1458, Oct. 1998.

[4] V. Tarokh, N. Seshadri, and A. R. Calderbank, "Space-time codes for high data rate wireless communication: Performance criterion and code construction," *IEEE Trans. Inf. Theory*, vol. 44, no. 2, pp. 744–765, Mar. 1998.

[5] G. J. Foschini, "Layered space-time architecture for wireless communication in a fading environment when using multiple antennas," *Bell Labs. Tech. J.*, vol. 1, no. 2, pp. 41–59, 1996.

[6] P. W. Wolniansky, G. Foschini, G. Golden, and R. A. Valenzuela, "V-BLAST: an architecture for realizing very high data rates over the rich-scattering wireless channel." *Proceedings URSI International Symposium on Signals, Systems, and Electronics*, (IEEE, New York, NY, USA), pp. 295--300, 1998.

[7] A. Paulraj and T. Kailath, "Increasing capacity in wireless broadcast systems using distributed transmission/directional reception (DTDR)," U.S. Patent 5,345,599, Sep. 6, 1994.

[8] B. Hassibi and B. M. Hochwald, "High-rate codes that are linear in space and time," *IEEE Trans. Inf. Theory*, vol. 48, no. 7, pp. 1804–1824, Jul. 2002.

[9] S. Sandhu and A. Paulraj, "Space-time block coding: A capacity perspective," *IEEE Commun. Lett.*, vol. 4, no. 12, pp. 384–386, Dec. 2000.

[10] R.W. Heath Jr. and A. Paulraj, “Linear dispersion codes for MIMO systems based on frame theory,” *IEEE Trans. Signal Process.*, vol. 50, no. 10, pp. 2429–2441, Oct. 2002.

[11] L. Zheng and D.N.C Tse, “Diversity and multiplexing: a fundamental tradeoff in multiple-antenna channels,” *IEEE Trans. on Information Theory,* vol.49, no.5, pp. 1073-1096, May 2003.

[12] S. Loyka and G. Levin, “On Finite-SNR Diversity-Multiplexing Tradeoff," *2007 IEEE Global Telecommunications Conference*, pp.1456-1461, 26-30 Nov. 2007.

[13] W.-Y. Shin, S.-Y. Chung, and Y. H. Lee, “Diversity–Multiplexing Tradeoff and Outage Performance for Rician MIMO Channels,” *IEEE Trans. on Information Theory,* vol.54, no.3, pp.1186-1196, March 2008.

[14] K. Azarian, K.; H. El Gamal, “The Throughput–Reliability Tradeoff in Block-Fading MIMO Channels,” *IEEE Trans. on Information Theory,* vol.53, no.2, pp.488-501, Feb. 2007.

[15] R. Narasimhan, ‘Finite-SNR diversity-multiplexing tradeoff for correlated Rayleigh and Rician MIMO channels,” *IEEE Transactions on Information Theory*, vol. 52, no. 9, pp. 3965-3979, Sep. 2006.

[16] R. W. Heath and A.J. Paulraj, “Switching between diversity and multiplexing in MIMO systems,” *IEEE Transactions on Communications*, vol. 53, iss.6, pp. 962-968, June 2005.

[17] W. Weichselberger, M. Herdin, H. Özcelik, and E. Bonek, “A Stochastic MIMO Channel Model with Joint Correlation at Both Link Ends,” *IEEE Trans Wireless Communications*, vol 5, no. 1., pp. 90-100, Jan 2006.

[18] W. Weichselberger, “Spatial structure of multiple antenna radio channels --- a signal processing viewpoint”, PhD dissertation, Vienna University of Technology, Vienna, Austria, 2003.

[19] N. Costa and S. Haykin, “A Novel Wideband MIMO Channel Model and McMaster’s Wideband MIMO SDR,”. *2006 Conference Record of the Fortieth Asilomar Conference on Signals, Systems and Computers*, Nov 2006. pp. 956-960.

[20] H. Ozcelik, M. Herdin, W. Weichselberger, J. Wallace and E. Bonek, “Deficiencies of 'Kronecker' MIMO radio channel model,” *Electronics Letters*, Vol.39, Iss.16, 7 Aug. 2003, pp. 1209-1210.

[21] L. C. Wood and W. S. Hodgkiss. “MIMO Channel Models and Performance Metrics,” *2007 IEEE Global Telecommunications Conference*, pp.3740-3744, Nov. 2007.

[22] H. Sampath, S. Talwar, J. Tellado, V. Erceg, and A. Paulraj, “A fourth generation MIMO-OFDM broad-band wireless system: Design, performance, and field trial results,” *IEEE Commun. Mag.*, vol. 40, no. 9, pp. 143–149, Sep. 2002.

[23] R.W. Heath Jr., S. K. Peroor, and A. J. Paulraj, “Methods of controlling communication parameters of wireless systems,” U.S. Patent 6,298,092, Oct. 2, 2001.

[24] J.W. Wallace, M. A. Jensen, A. L. Swindlehurst, and B. D. Jeffs, “Experimental characterization of the MIMO wireless channel: Data acquisition and analysis,” *IEEE Trans. Wireless Commun.*, vol. 2, pp. 335–343, Mar. 2003.

[25] J.W. Wallace and M. A. Jensen, “Experimental analysis of the time-varying MIMO channel,” *2006 IEEE Antennas and Propagation Society International Symposium*, pp. 321- 324, 9-14 July 2006.

[26] R. W. Heath, D. J. Love, "Multimode antenna selection for spatial multiplexing systems with linear receivers," *IEEE Transactions on Signal Processing*, vol. 53, no. 8, pp. 3042-3056, Aug. 2005.

8 Time Sensitivity of Feedback

8.1 Introduction

The increased throughput possible from using MIMO antenna systems has been well documented in literature [1, 2]. To achieve the high gains possible, adaptive feedback systems make use of channel state information at the transmitter. The gains possible depend on the type of information available and the quality of that information. [3, 4]

The rate of variation within the channel affects the choice of information to feed back. For highly varying channels, the channel may change too rapidly to support the feedback of full channel state information (CSI), but may remain stable enough to use channel distribution information (CDI) to improve the transmission strategy. If the channel is varying slowly enough, the channel information needs to be estimated and sent to the transmitter infrequently, making it is possible to achieve gains with minimal training overhead [5, 6].

The effect of delay, or alternatively, imperfect channel estimates, on capacity has been discussed in literature using a variety of techniques and assumptions about the channel. The effect of CSI delay for measured channels was investigated in [7, 21]. Markov properties were used to determine the impact on system performance in [8]. Temporal effects were also investigated for channel state information at the transmitter (CSIT) using a metric known as the correlation matrix distance in [9]. The effects of delayed channel state information is discussed in [10] and imperfect CSI in [11, 12]. The effects on multi-user systems are considered in [13]. Additional investigations were carried out in [14-17].

Additionally, there is work examining the effects of CSI when the channel is assumed to take the form of a particular spatial correlation based model, the Kronecker model. In [12], the Kronecker model is used to determine the optimal signaling scheme under perfect CSI and CDI conditions. This model has been used in a variety of MIMO feedback schemes and analyses due to its simplified structure. However, this model has been shown to be deficient in its representation of the channel [18, 19]. Instead, a structured eigenbasis model proposed by Weichselberger has been shown to provide a better match in channel representation through a variety of metrics, including capacity [20].

Since these two analytical models are used commonly in the literature, it would be useful to examine the effect of feedback delay on the models' capabilities in predicting the performance degradation in comparison to measured channels.

In this chapter, we examine the effects of CSI and CDI feedback when delays are present using measured data. This measured data was taken at the Brigham Young University campus [21,22]. The framework established in [7] is used for this comparison. The predictive performances of two analytical models are examined, and the coherence distance at which the two models become valid is determined. For all scenarios investigated, the Weichselberger model provides a better estimate of the true channel performance than the Kronecker model. It is shown that if delays exist at both the transmitter and receiver, and if the information cannot be fed back by the time the transmitter has displaced $\lambda/2$, the Weichselberger model can accurately predict the capacity of the channel. However, with perfect channel state information at the receiver (CSIR), the CSIT provides useful information for several wavelengths of displacement or longer for all environments investigated. For these environments, a modified Weichselberger model with temporally correlated innovations would be required for accurate spatio-temporal modeling.

8.2 Capacity with and without CSI at the Transmitter

Consider the narrowband channel relationship in Chapter 3 with channel gain matrix **H**. In practice the channel transfer matrix is estimated through training symbols, resulting in a channel transfer matrix estimate, $\hat{\mathbf{H}}$. This estimate is available to the receiver immediately. However, the estimate must be fed back to the transmitter, resulting in a delay of knowledge at the transmitter. In the case of CSIT, this delay can cause degradation in system performance, as the powers assigned to different channels at the transmitter are based on outdated information. In the case of CSIR, the delay causes additional issues as the channel can no longer be decomposed into orthogonal subchannels.

8.2.1 Delayed CSIT

First, consider the case of delayed CSI at the transmitter. The receiver has perfect CSI, **H**, but the transmitter only has the delayed estimate, $\hat{\mathbf{H}}$. For this work, the estimate $\hat{\mathbf{H}}$ is considered to be error-free. That is, for time delay, $t_d = 0$, $\mathbf{H} = \hat{\mathbf{H}}$. Under these assumptions, we define the capacity for delayed transmit CSI as:

$$C_T = \log_2\left\{\det\left(\mathbf{I} + \frac{\mathbf{H}\mathbf{Q}(\hat{\mathbf{H}})\mathbf{H}^H}{\sigma^2}\right)\right\} \tag{8.1}$$

where **H** is the actual channel at transmission time, σ^2 is the receiver noise variance, and $\mathbf{Q}(\hat{\mathbf{H}})$ is optimal transmit covariance matrix given by the waterfilling solution on the outdated channel information that was fed back to the transmitter. For a channel matrix **H** known to the transmitter, the optimal structure of **Q** has eigenvectors corresponding to the right singular vectors of **H**, and $\mathrm{Tr}\{\mathbf{Q}(\hat{\mathbf{H}})\} \leq P_T$, where P_T is the total allowed transmit power. The above expression at $t_d = 0$ corresponds to the traditional perfect CSI assumption. As the delay between information at the transmitter and receiver increases, the throughput performance will decay. Note that the feedback is no longer helpful at the point where uninformed transmit capacity, defined in (3.19), exceeds the waterfilling capacity resulting from using $\hat{\mathbf{H}}$ as the channel transfer matrix estimate.

Although the effect of delay is in units of time, to be consistent with results presented in [7], we present the results in terms of displacement from the original position when the receiver link end is in motion. This allows for the results to be interpreted for different mobile velocities.

8.2.2 Delayed CDIT

Next we consider the case of delayed distribution information at the transmitter. Often, it may not be practical to feed back channel matrix estimates. However, statistical information about the channel may be available for use. If distribution information is sent back to the transmitter in the form of a channel transmitter-side covariance matrix, $\mathbf{R_{tx}}$ as defined in (3.7), the structure of the optimal input covariance matrix, **Q**, can be determined. The derivation of the optimal structure of **Q** is outlined in [23, 24] and is summarized below for completeness.

Let **H** have the singular value decomposition **H** = **USV$^{\mathbf{H}}$**. Then given the identitiy that det(**I**+**UAU**^{H})= det(**I**+**A**) for unitary matricies, **U**, the ergodic capacity expression can be rewritten as follows:

$$C_T = E\left\{\log_2\left|\mathbf{I} + \mathbf{S}\mathbf{V}^{\mathbf{H}}\mathbf{Q}\left(\hat{\mathbf{R}}_{\mathbf{tx}}\right)\mathbf{V}\mathbf{S}\right|\right\} \tag{8.2}$$

Following the logic of [23] and [24], the optimal directions to use for transmit beamforming are the right side singular vectors of **H**, or equivalently, the eigenvectors of **R$_{\mathbf{T}}$** for the eigenvectors of **Q**. The power constraint, Tr{**Q**(**R$_{\mathbf{tx}}$**)} ≤ P$_{T}$ now applies. The transmit weights now can be determined according to the statistical waterfilling algorithms.

8.3 Capacity with Delayed CSIR

We examine the effect of delayed CSI, when both the transmitter and receiver have outdated channel information. If the communication system attempts to form parallel channels using singular value decomposition techniques, the parallel channels will suffer from self interference. Consider the methodology employed in [21], using the delayed channel estimate, $\hat{\mathbf{H}}$, to form parallel channels. First, the channel is rewritten to explicitly show the difference between the true channel, **H**, and the delayed estimate:

$$\mathbf{y} = \mathbf{H}\mathbf{x} + \mathbf{n} = \hat{\mathbf{H}}\mathbf{x} + (\mathbf{H} - \hat{\mathbf{H}})\mathbf{x} + \mathbf{n} \tag{8.3}$$

Equation (8.3) is modified by inserting an identity matrix in the form of $\hat{\mathbf{V}}\hat{\mathbf{V}}^{H}$ where $\hat{\mathbf{V}}$ is the right singular basis vectors from the decomposition of $\hat{\mathbf{H}}$. Then, at the receiver, parallel channels are attempted by multiplying both sides with the left hand singular basis vectors of the delayed channel estimate matrix:

$$\hat{\mathbf{U}}^{H}\mathbf{y} = \hat{\mathbf{S}}(\hat{\mathbf{V}}^{H}\mathbf{x}) + \hat{\mathbf{U}}^{H}(\mathbf{H} - \hat{\mathbf{H}})\hat{\mathbf{V}}(\hat{\mathbf{V}}^{H}\mathbf{x}) + \hat{\mathbf{U}}^{H}\mathbf{n} \tag{8.4}$$

Equivalently, this can be expressed in simplified notation as:

$$\mathbf{y}' = \hat{\mathbf{S}}(\mathbf{x}') + \mathbf{M}(\mathbf{x}') + \mathbf{n}' \tag{8.5}$$

The subchannels formed are not completely orthogonal to each other. To compute the capacity of this system, the self interference term, **M**, must be taken into account. In general, the statistics of **M** would need to be learned. However, using the simplifications given in [21], the mutual information can be found according to:

$$C_{CSIR}(\mathbf{H}, \hat{\mathbf{H}}) = \sum_i \log_2\left(1 + p_i \, \hat{S}_{ii}^2 \big/ q_i\right) \tag{8.6}$$

$$\mathbf{q}_i = \left\{\mathbf{M}\mathbf{R}_{\mathbf{x}}\mathbf{M}^{\mathbf{H}}\right\}_{ii} + \sigma^2 \tag{8.7}$$

$$\mathbf{M} = \left\{\hat{\mathbf{U}}^H \mathbf{H}\hat{\mathbf{V}}\right\}_{ii} - \mathbf{\Phi}\hat{\mathbf{S}} \tag{8.8}$$

where $\mathbf{\Phi}$ is a diagonal matrix containing the phase information to remove the variation of the individual parallel channels. Equations (8.6-8.8) assume that the interference term has Gaussian statistics, and the receiver knows the level of interference on subchannels, but does not know the level of cross-correlation. The p_i terms are found through waterfilling and are the diagonal terms of $\mathbf{R}_{\mathbf{x}}=\mathrm{E}\{\mathbf{x}'\mathbf{x}'^{\mathrm{H}}\}$

8.4 Results

We first examine the impact of link end motion on the CSI. We consider two different data sets taken within the Coal Yard on the Brigham Young University campus (see Section 4.2.3.1). For the first set, both link ends are stationary. For the second set, the receiver link end is in motion. Since we cannot characterize the effects of delayed CSI for both sets as a function of receiver displacement as the receiver does not move in

Set 1, the results are reported in terms of samples of **H**, where samples are taken every 2.5 ms. The results are shown in Figure 8.1.

To examine the effects of delay, the transmitter is assumed to have the accurate channel estimate at the start. While the channel changes, the outdated channel information is used to precode the data, resulting in a decrease in capacity. For Set 1, information feedback to the receiver will be valid for a long duration, as the capacity remains fairly insensitive to the delay. However, for Set 2, the capacity begins to decrease rapidly. Note that since capacity was generated at an average SNR of 5 dB, the uninformed transmit capacity remains below the capacity of the channel when CSIT is available. For higher SNRs, the uninformed capacity is higher relative to the waterfilling capacity. At some delay, the waterfilling capacity will no longer be useful, as the uninformed capacity will outperform the waterfilling strategy.

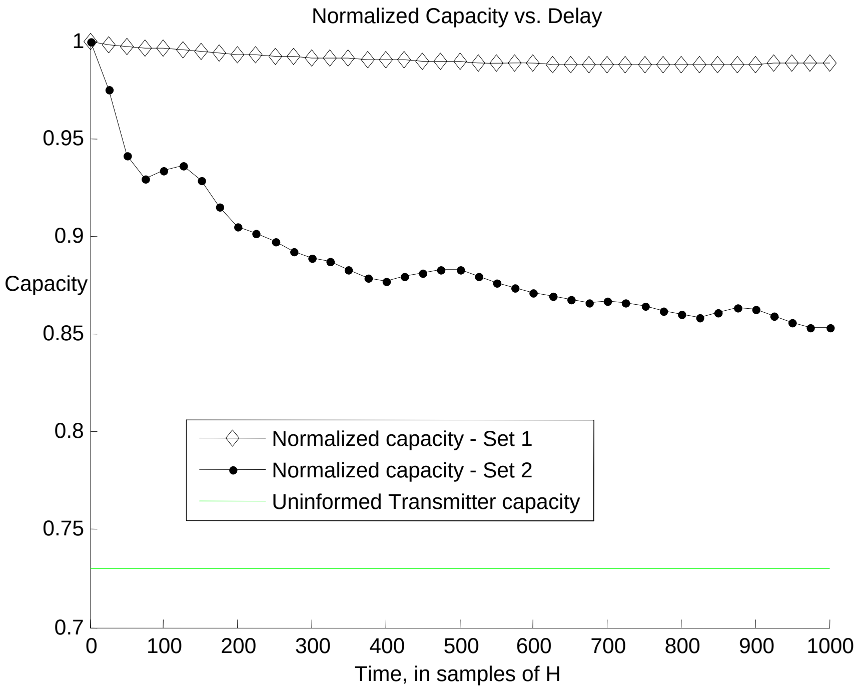

Figure 8.1: Impact of receiver mobility on the CSIT delay.

For the remainder of the investigations, the results are reported at a fixed SNR of 10 dB. We now examine the CSIT and CDIT effects for Set 2 in the Coal Yard, in which the receiver is in motion. We examine how the CSIT and CDIT become outdated for the data and for the two analytical models under consideration. The results for Set 2 in the Coal Yard are shown in Figure 8.2. Although only the first 0.5 meters are shown, the receiver can move more than several meters before becoming out of date. That is, the information fed back to the transmitter provides additional gain over the uninformed transmit capacity for several meters of receiver displacement. These results are consistent with the results presented in [7] for the measured data.

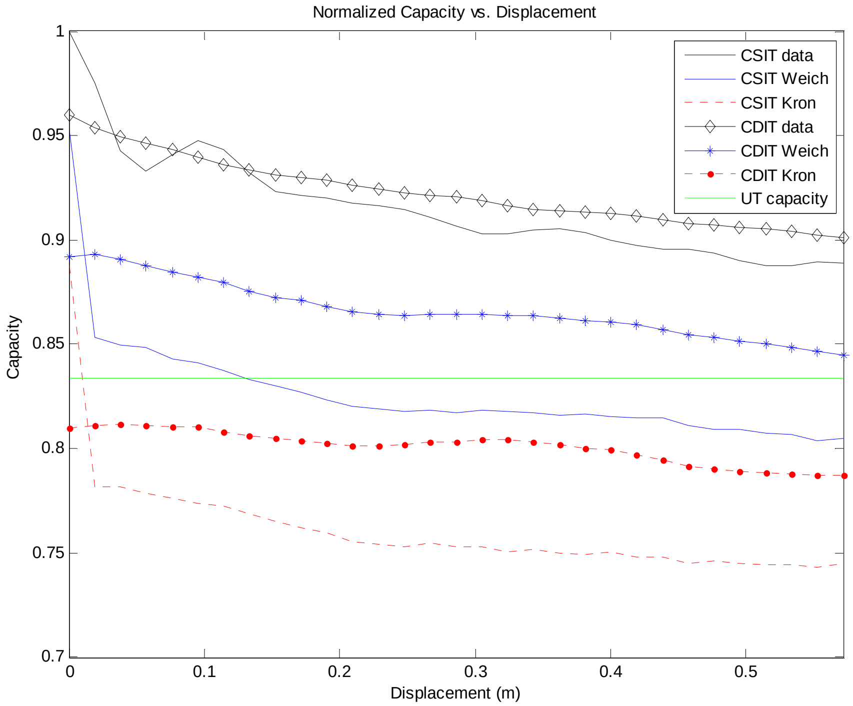

Figure 8.2: Normalized capacity versus delay for a CSIT and CDIT feedback scheme in an urban Coal Yard environment.

Additionally, the results show that the two analytical models, whose component parts are generated from time-varying 400 sample-length averages, offer reasonable performances at displacement = 0, which is the perfect CSIT/CDIT scenario. In this case, both models predict the capacity within 10% of the true value. However, both models under predict the capacity, so as the receiver is displaced even a short distance, the capacity rapidly approaches and crosses the uninformed transmit capacity. Neither model accurately predicts the displacement distance at which the channel information becomes out of date, which is not unexpected as temporal correlation is not built into the models. However, after the initial displacement, the error in prediction is reasonably constant, as seen in Figure 8.3.

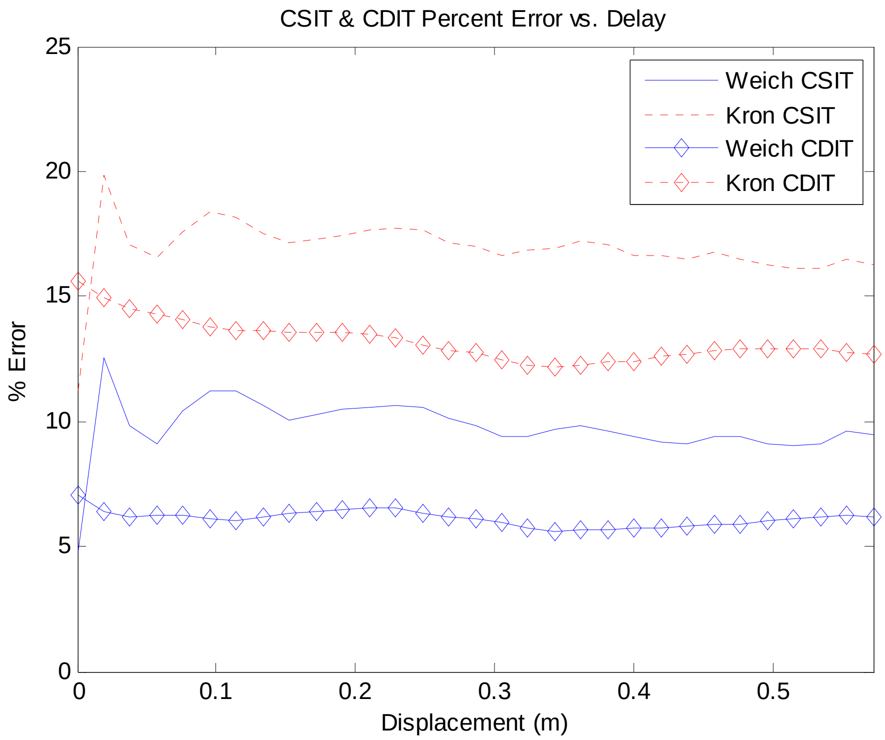

Figure 8.3: Percent error in capacity prediction relative to the measured data capacity versus delay for CSIT and CDIT feedback schemes for the Weichselberger and Kronecker models.

The normalized capacity results for the trees transmission scenario (refer to Section 4.2.3.2) is shown in Figure 8.4. Notice that in this set, the CSIT outperforms the CDIT for nearly 0.5 meters. As with the Coal Yard, it is worthwhile to note that the Kronecker model provides a poor enough channel representation that the uninformed transmit capacity for the channel provides a higher throughput than using the Kronecker model estimates. The error in performance between the measured data and model capacities were similar for this data set and the Coal Yard set.

Finally, we examine an indoor to outdoor transmission scenario (refer to Section 4.2.3.3). The results are seen in Figure 8.5. In this environment, the displacement of a small fraction of a meter is enough to render the CSIT information too outdated to provide useful information. For this scenario, using CDIT may be the only viable option for feedback, depending on the speed of the mobile. The error for this set was a few percentage points less than in the previous two cases. From these results, we note that for feedback algorithms to predict the capacity with delays present at only the transmitter, it will be necessary to modify the Weichselberger model with temporally correlated innovations.

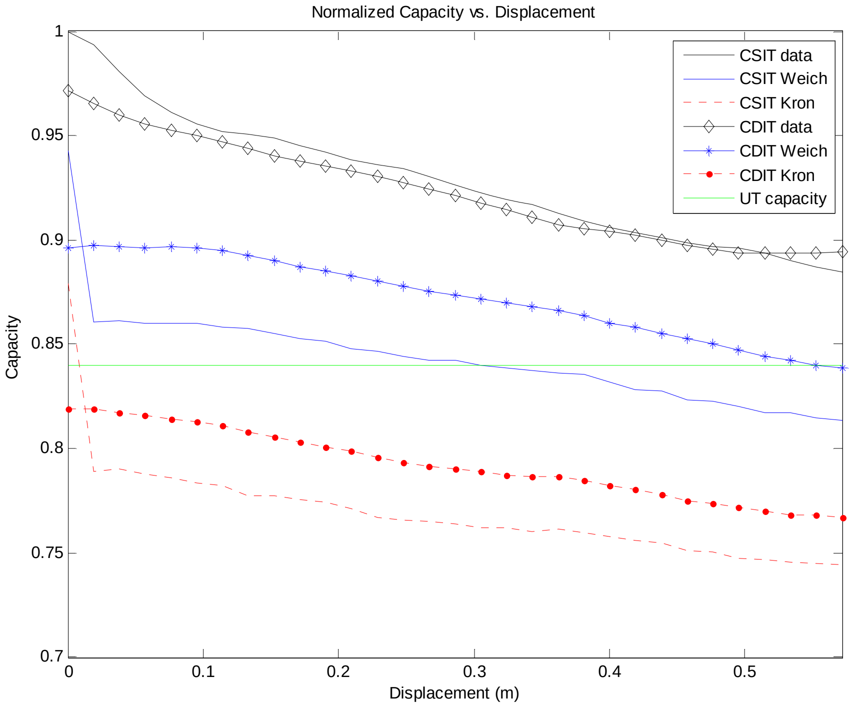

Figure 8.4: Normalized capacity versus delay for a CSIT and CDIT feedback scheme in a tree environment.

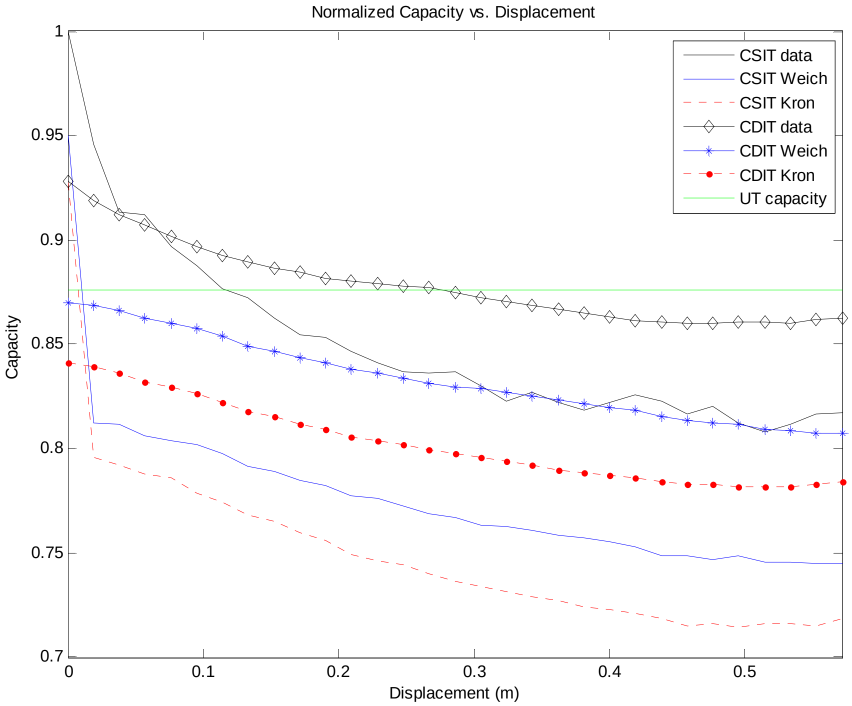

Figure 8.5: Normalized capacity versus delay for a CSIT and CDIT feedback scheme in an indoor to outdoor transmission environment.

Next, we consider the case when both the transmitter and receiver have delayed channel state information. Since the receiver inverts the channel as part of the decoding process, the impact of a delay in information coupounds the temporal effects, causing the channel capacity to drop rapidly with displacement. The resulting curves for the data, Weichselberger model, and the Kronecker model are shown in Figure 8.6 for the Coal Yard data set. Note that while the Weichselberger model and Kronecker models do not account for the exact behavior of the channel, the Weichselberger model provides a more closely matched lower bound to the performance of the true channel over the Kronecker model. The curves for the trees transmission scenario and the indoor to outdoor transmission scenario are shown in Figures 8.7 and 8.8, respectively. For consistency with [7], the curves are reported in terms of wavelength, which is approximately 12.3

centimeters. In the Coal Yard and the indoor to outdoor transmission scenario, the capacity drops rapidly to 50% of the maximum capacity within approximately 0.25 wavelengths. However, the capacity performance for the trees scenario decays more slowly, dropping to 50% of the maximum capacity by 1.4 wavelengths. For this transmission scenario, a lower bound capacity provided by the Weichselberger model becomes valid with a typical displacement of a fraction of a wavelength. For a rapidly moving link end, the model may provide a reasonable estimate without modifying the innovations sequence as the CSI cannot be fed back in a useful time frame.

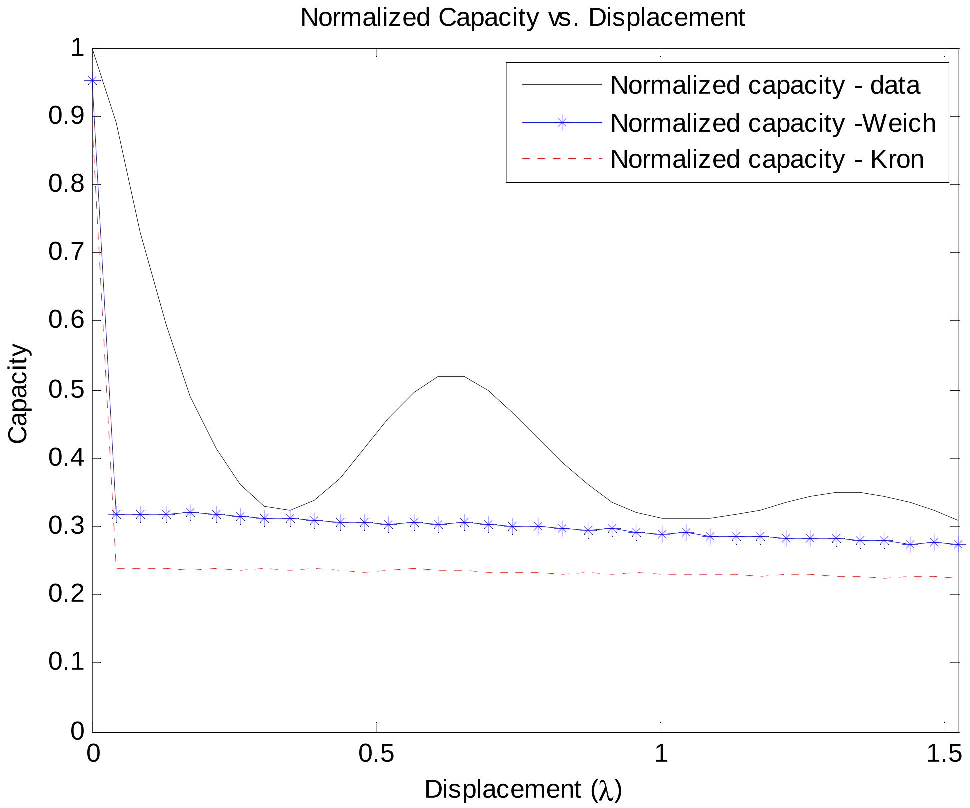

Figure 8.6: Delayed CSIR performance for the data and two models under consideration in the Coal Yard environment.

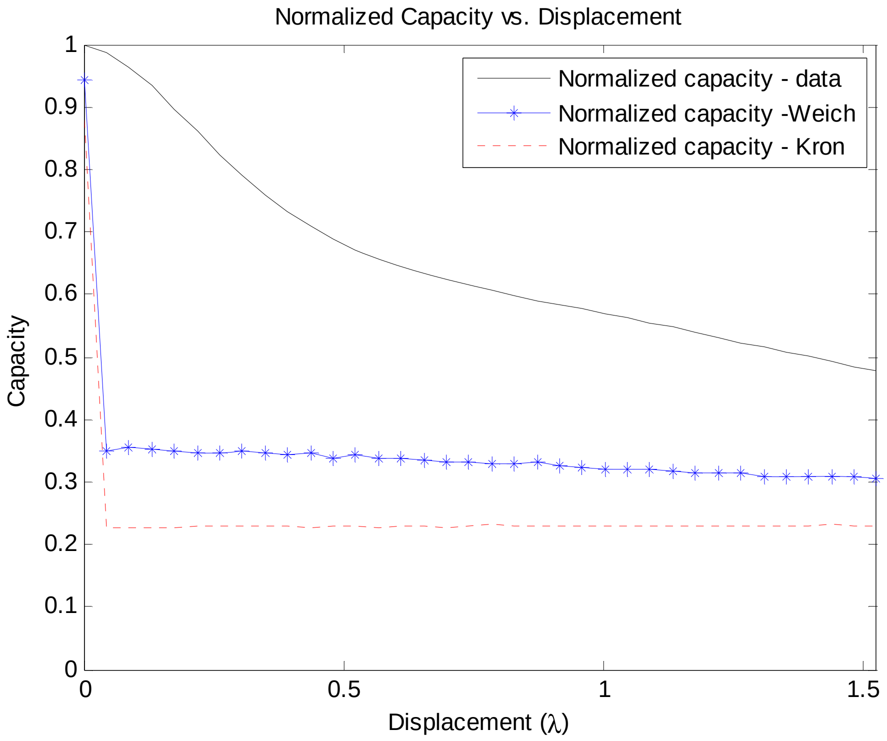

Figure 8.7: Delayed CSIR performance for the data and two models under consideration in the trees environment.

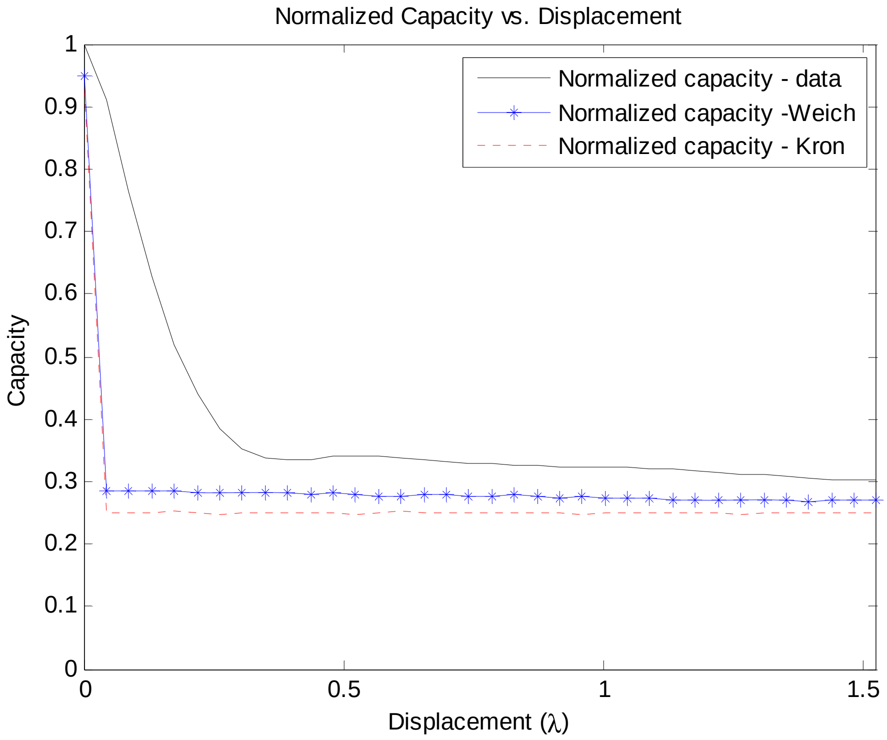

Figure 8.8: Delayed CSIR performance for the data and two models under consideration in the indoor to outdoor environment.

8.5 Summary

We have examined the impact on the throughput when the transmitter or the transmitter and the receiver has an increasingly delayed channel matrix estimate, as well as when delayed channel distribution information is provided to the transmitter for two analytical models. Although these models have been used in the past to discuss the perfect CDIT and CSIT performance, this investigation examines the potential usefulness of the models when delays are present. The overall capacity predictions fall within approximately 10% and 6% for the CSIT and CDIT for the Weichselberger model. Since the coherence of the channel information at the transmitter with perfect CSIR lasts for several wavelengths of displacement, the Weichselberger model needs to be modified to accept temporally correlated innovation sequences. On the other hand, for delayed CSIR, the Weichselberger model provides a good estimate of the lower bound for the true channel performance if the information cannot be fed back within a half wavelength displacement. Further work is required to determine the appropriate methodology for introducing temporal correlation into the Weichselberger model.

8.6 Acknowledgment

This chapter, in part, is a reprint of the material as it appears in “Performance of MIMO Channel Models with Channel State Information at the Transmitter,” L. C. Wood and W. S. Hodgkiss, Globecom 2008, In press. The dissertation author was the primary author of this paper.

8.7 References

[1] E. Telatar, “Capacity of Multi-antenna Gaussian Channels,” Technical Report, AT&T Bell Labs. June 1995.

[2] G. J. Foschini, and M. J. Gans, “On Limits of Wireless Communications in a Fading Environment when Using Multiple Antennas.” *Wireless. Personal. Communications, vol.* 6, no. 3, pp. 311-335, March 1998.

[3] M. A. Jensen and J. W. Wallace, “A review of antennas and propagation for MIMO wireless communications,” *IEEE Trans. Antennas Propag.*,vol. 52, no. 11, pp. 2810–2824, Nov. 2004.

[4] L. Zheng and D. N. C. Tse, “Diversity and multiplexing: A fundamental tradeoff in multiple antenna channels,” *IEEE Trans. Inf. Theory*, vol. 49, no. 5, pp. 1073–1096, May 2003.

[5] B. Hassibi and B. M. Hochwald, “How much training is needed in multiple-antenna wireless links?” *IEEE Trans. Inf. Theory,* vol. 49, no. 4, pp. 951–963, Apr. 2003.

[6] J. Baltersee, G. Fock, and H. Meyr, “Achievable rate of MIMO channels with data-aided channel estimation and perfect interleaving,” *IEEE J. Sel. Areas Commun.*, vol. 19, no. 12, pp. 2358–2368, Dec. 2001.

[7] J. W. Wallace, M. A. Jensen, A. Gummalla, and H. B. Lee, "Experimental Characterization of the Outdoor MIMO Wireless Channel Temporal Variation," *IEEE Transactions on Vehicular Technology,* vol.56, no.3, pp.1041-1049, May 2007.

[8] H. T. Nguyen, J. B. Andersen, and G. F. Pedersen, "Capacity and performance of MIMO systems under the impact of feedback delay," *15th IEEE International Symposium on Personal, Indoor and Mobile Radio Communications, 2004. PIMRC 2004.*, vol.1, no., pp. 53-57, 5-8 Sept. 2004.

[9] M. Herdin, N. Czink, H. Özcelik, and E. Bonek, “Correlation matrix distance, a meaningful measure for evaluation of non-stationary MIMO channels,” *2005 IEEE 61st Vehicular Technology Conference*, 2005. VTC 2005-Spring, vol.1, pp. 136- 140, 30 May-1 June 2005.

[10] K. Kobayashi; T. Ohtsuki; and T. Kaneko, "MIMO Systems in the Presence of Feedback Delay," *IEEE International Conference on Communications, 2006. ICC '06*, vol.9, no., pp.4102-4106, June 2006

[11] T. Yoo and A. Goldsmith, "Capacity and power allocation for fading MIMO channels with channel estimation error," *IEEE Transactions on Information Theory,* vol.52, no.5, pp.2203-2214, May 2006

[12] A. Goldsmith, S. A. Jafar, N. Jindal, and S. Vishwanath, "Capacity limits of MIMO channels," *IEEE Journal on Selected Areas in Communications,* vol.21, no.5, pp. 684-702, June 2003.

[13] A. Anderson, J. R. Zeidler, M. A. Jensen, "Performance of Transmit Precoding in Time-Varying Point-to-Point and Multi-User MIMO Channels," *Fortieth Asilomar Conference on Signals, Systems and Computers, 2006. ACSSC '06,* pp.112-116, Oct.-Nov. 2006.

[14] D. P. McNamara, M. A. Beach, and P. N. Fletcher, “Experimental investigation of the temporal variation of MIMO channels,” in *Proc. IEEE 54th Veh. Technol. Conf.*, Atlantic City, NJ, pp. 1063–1067, Oct. 7–11, 2001.

[15] H. Xu, M. Gans, D. Chizhik, J. Ling, P. Wolniansky, and R. Valenzuela, “Spatial and temporal variations of MIMO channels and impacts on capacity,” in *Proc. IEEE Int. Conf. Commun.*, New York, vol. 1, pp. 262–266, Apr. 28–May 2, 2002.

[16] V. Pohl, P. H. Nguyen, V. Jungnickel, and C. von Helmolt, “How often channel estimation is needed in MIMO systems,” in *Proc. IEEE Global Telecommun. Conf.*, San Francisco, CA, vol. 2, pp. 814–818, Dec. 1–5, 2003.

[17] J. Maurer, C. Waldschmidt, T. Kayser, and W. Wiesbeck, “Characterisation of the time-dependent urban MIMO channel in FDD communicationsystems,” in *Proc. IEEE 57th*

[18] H. Ozcelik, M. Herdin, W. Weichselberger, J. Wallace and E. Bonek, “Deficiencies of 'Kronecker' MIMO radio channel model,” *Electronics Letters*, Vol.39, Iss.16, pp. 1209- 1210, 7 Aug. 2003.

[19] N. Costa and S. Haykin, “A Novel Wideband MIMO Channel Model and McMaster’s Wideband MIMO SDR,” *Conference Record of the Fortieth Asilomar Conference on Signals, Systems and Computers, 2006*, pp. 956-960, Nov 2006.

[20] W. Weichselberger, M. Herdin, H. Özcelik, and E. Bonek, “A Stochastic MIMO Channel Model with Joint Correlation at Both Link Ends,” *IEEE Transactions on Wireless Communications*, vol 5, no. 1., pp. 90-100, Jan 2006.

[21] J.W. Wallace and M. A. Jensen, “Experimental analysis of the time-varying MIMO channel,” *IEEE Antennas and Propagation Society International Symposium 2006*, pp. 321- 324, 9-14 July 2006.

[22] J.W. Wallace, M. A. Jensen, A. L. Swindlehurst, and B. D. Jeffs, “Experimental characterization of the MIMO wireless channel: Data acquisition and analysis,” *IEEE Transactions on Wireless Communications*, vol. 2, pp. 335–343, Mar. 2003.

[23] S. Jafar and A. Goldsmith, “Transmitter optimization and optimality of beamforming for multiple antenna systems,” *IEEE Transactions on Wireless Communications,* vol. 3, pp. 1165–1175, July 2004.

[24] E. A. Jorswieck and H. Boche, "Channel capacity and capacity-range of beamforming in MIMO wireless systems under correlated fading with covariance feedback," *IEEE Transactions on Wireless Communications,* vol.3, no.5, pp. 1543-1553, Sept. 2004.

9 Conclusions & Future Work

In this work, we have focused on characterizing the wireless channel at 2.4 GHz. The key contributions of this dissertation fall into three categories. First, knowledge of the channel was expanded through a SIMO channel measurement campaign. Second, the differences between analytical channel models were explored, with a focus on understanding the usefulness of the structured eigenbasis model. Finally, we explored the effects of model usage on practical system design, understanding how components of the models that capture the physics of the channel can be used in system design, in addition to how accurately the models predict performance.

We began with an exploration of single-input multiple-output systems. A dual channel receiver was built, and the wireless channel was probed. From measurements taken in different environments, the channel correlation was studied. The effect of interelement spacing on the correlation coefficient was explored. Unlike most SIMO studies, the effect of correlation of different frequencies was observed, examining the effects on the ISM band using a bandwidth similar to that required for 802.11 b/g/n technologies. The impact of mutual coupling was also explored.

Next, we turned our focus to characterizing the wireless channel for multiple input multiple output antenna systems. We began with a discussion of MIMO channel models and channel metrics for use in comparing the models. Two models, Weichselberger's structured eigenbasis model and the Kronecker model, were then compared in depth. The structured eigenbasis model was shown to significantly outperform the Kronecker model for all metrics explored. To better understand how the structured eigenbasis model captures the underlying physics of the channel, beamforming was used to verify the capturing of primary propagation paths. Additionally, channel parameters, such as array separation, were explored.

The impact on the structured eigenbasis model parameters were observed. The ability of the model to capture the correlation structure of channels generated using geometrical models was also explored. In this work, the impact of the Kronecker and Weichselberger model simplifications was explored. The magnitudes of the diagonal correlation terms were examined at multiple interelement spacings. It was found that the terms most misrepresented by the models in the correlation matrix are the cross-diagonal terms. While the structured eigenbasis model forms an average representation of the values in these terms, the Kronecker model represents these terms as a product of two other correlations. As such, the Kronecker model severely underestimates these terms at small interelement spacings. Although the structured eigenbasis model misrepresents the terms as well, the averaging found in these terms lends itself to representing average channel parameters, such as channel capacity, well.

The impact of using the models in practical system design and analysis were explored. Open loop and closed loop MIMO system architectures are examined. The ability of either model to accurately predict the system performance was studied. It was found that the Weichselberger model can accurately predict the performance, while the Kronecker model can underestimate the performance by as much as 75% at high SNRs. Since the Kronecker model requires fewer parameters to be estimated and fed back to the transmitter for use in adaptive systems, different strategies for reducing the overhead using the structured eigenbasis model were studied. Two methodologies, reducing the rank of the full model and feeding back just the power coupling matrix were explored.

One of the major fundamental design issues in MIMO systems was studied. The question of how to allocate channel resources between spatial multiplexing and diversity for correlated channels was explored. It was found that the power coupling matrix from the structured eigenbasis model can be used to predict when channels are spatial multiplexing preferred. The Demmel condition number was used to relate the distances of the signal constellations required for equivalent spatial multiplexing and spatial diversity transmissions. By using the largest power values in the coupling matrix, the closed form distribution for the eigenvalues of the i.i.d. Rayleigh channel was modified to provide the ability to predict when correlated channels will be multiplexing preferred. Thus, the model has a direct application to selecting the mode of operation of a MIMO system.

Finally, the impact of the delay of feedback of system parameters was studied for the structured eigenbasis and Kronecker models. The eigenbasis model does a better job at predicting the system performance when there is no delay and in the limit when the delay is large. However, neither model actually predicted the system performance roll-off well since temporal correlation is not built into the model. When delayed information was used at both the transmitter and receiver, the coherence time is short. For rapidly varying channels, the Weichselberger model in its current form may be useful for these channels, as it provides a lower bound on capacity that becomes a close approximate to the measured channel with only a short displacement.

Throughout this dissertation, we have focused attention on characterizing the wireless channel. Correlation was examined in both SIMO and MIMO systems. However, the correlation-based models investigated in this work are not capable of modeling time-varying channels. Further studies involving the temporal correlation aspects of the channel would be useful for forming a spatio-temporal model. Work has already been performed in adding temporal aspects to the Kronecker model in [1]. However, the Weichelberger model has been shown to outperform the Kronecker model in representing the spatial aspects of the channel. As such, it would be useful to expand the Weichselberger model to incorporate temporal effects. Such a temporal model could be formed by modifying the innovations sequence of the Weichselberger model.

Additionally, it would be informative to expand the analysis in this dissertation to wideband MIMO channels. In [2], a wideband version of the Weichselberger model was presented which uses a tensor triple to represent the channel coupling matrix. This triple tensor form makes the model less than intuitive to interpret. The performance was examined using limited data and focused primarily on capacity as the comparison metric. It would be useful to find a more intuitive wideband representation of the Weichselberger model and test its performance using a variety of propagation environments and channel metrics.

The task of improving the modeling of the wireless channel is a continuing challenge, serving a two-fold purpose. First, and foremost, modeling furthers our understanding of the wireless channel. Secondly, model assumptions are often used in the design of systems and algorithms. As modeling becomes more accurate, designs based on those models will perform better in real-world implementation, resulting in more robust wireless communications.

9.1 References

[1] S. Ting, K. Sakaguchi, and K. Araki, "A Markov-Kronecker model for analysis of closed-loop MIMO systems," IEEE Communications Letters, vol.10, no.8, pp. 617-619, Aug. 2006.

[2] N. Costa and S. Haykin, A Novel Wideband MIMO Channel Model and McMaster’s Wideband MIMO SDR. Conf. Record of the 40th Asilomar Conf. on Signals, Systems and Computers, , Nov 2006, pp. 956-960.

Appendix: Receiver Assembly

A.1 Configuration of a 2.4 GHz Dual-Channel Receiver

A 2.4 GHz dual channel diversity receiver was assembled using evaluation boards and discrete components from various manufacturers. The block diagram for the receiver is given below:

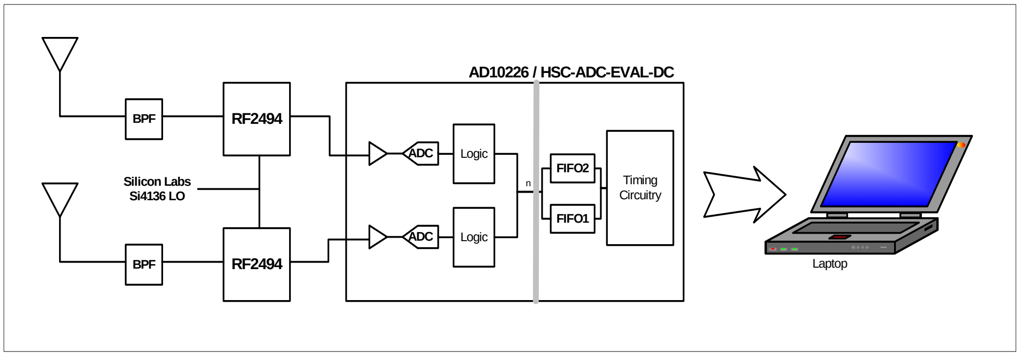

Figure A.1: 2.4 GHz Dual-Channel Receiver

Evaluation boards were used as a convenient and economic approach to test the concept of operations, allowing for the ability to easily analyze the system at each stage in the design.

A.2 Components

A.2.1 Winncom Technologies WLAN Antennas WRO2400-40CM

Each channel has a 2.4 GHz omnidirectional (in the azimuthal plane) antenna attached to the front end of the receiver. Using a wooden frame that essentially is a long groove to hold the antennas upright, the antennas can be moved back and forth, thereby allowing for variable spacing between the two branches.

Antenna Characteristics

Frequency:	2.4 – 2.483 GHz
Gain:	4dBi
Polarization:	Vertical
Dimensions:	7.0” long, 0.63” rad.

A.2.2 Teletronics International Inc. Band-Pass Filter BPF2450

The signal received by the antenna is immediately passed through a bandpass filter with a 2.442 GHz center frequency to suppress out of band interferers. While this is a good thing for the system, the filter also has drawbacks by adding a –3dB insertion loss, which degrades the system performance overall.

Filter Characteristics

Center Frequency:	2.442 GHz
Pass Band:	2.400-2.485 GHz
Insertion Loss:	3dB
Operating Temperature:	-20 C to 70 C

A.2.3 RF Micro Devices RF 2494 LNA/Mixer

The signal from the bandpass filter is fed into the LNA IN port of the RF Micro Devices RF2494 Front End Board. The purpose of the RF2494 board is to mix the signal with an external LO (at 2.068 GHz) in order to get the signal down to an IF of 374 MHz. The RF2494 evaluation board consists of two low noise amplifiers cascaded with two filters. An RF image reject SAW filter, Murata DFC22R44P084LHA centered at 2.442 GHz, precedes the mixing operation. An IF filter, SAWTEK 855898, centered at 374 MHz with a useable bandwidth of 18 MHz is at the output. Note that the RF2494 board adds a gain of +6dB to the system.

A.2.4 Silicon Laboratories Si4136 Frequency Synthesizer

The Si4136 Frequency Synthesizer board provides the 2.068 GHz sinusoid to the LO port of the RF2494 evaluation board. This signal mixes with the 2.442 GHz signal received by the antenna pair to an IF frequency of 374 MHz.

The Si4136 board consists of a VCO with a phase locked loop (PLL), which compares the higher frequency sinusoid with a much more stable lower frequency crystal oscillator through the use of a divider. Software from Silicon Laboratories allows the user to tune to any frequency within specifications.

A.2.5 Analog Devices AD10226 Hi-Speed Dual Channel ADC

The Analog Devices AD10226 125 MSPS 12 bit Hi-Speed Dual Channel analog-to-digital converter accepts the IF signal from the RF2494 board centered at 374 MHz. This signal is still not near baseband, and is downconverted before being handed off to the HSC-ADC-EVAL-DC FIFO board. Instead of adding another mixing stage, which increases the complexity of the system, the signal is downconverted through subsampling. Traditionally, A/D sampling requires that the Nyquist theorem is satisfied; that is, one must sample at a rate that is at least twice that of the highest frequency component of a signal. (In reality, the application may require a much higher sampling rate than twice the highest frequency in order to create a faithful representation of the signal.) The technique of subsampling hinges on the notion that the Nyquist theorem must be satisfied with respect to the bandwidth of the input signal only, and not of the actual signal time series itself. An explanation of how sub-sampling accomplishes the down conversion is as follows.

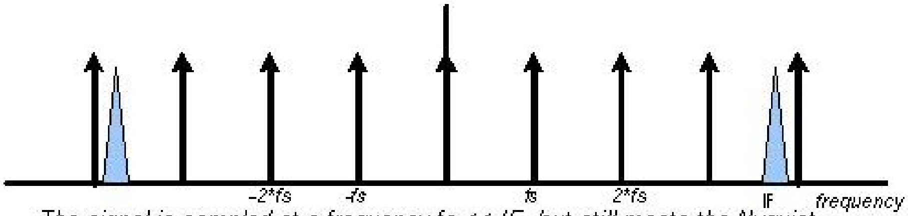

The signal is sampled at a frequency fs << IF, but still meets the Nyquist criteria with respect to the BW of the signal of interest.

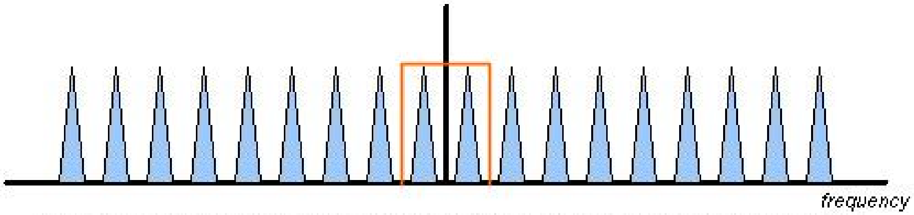

Replicas of the signal appear centered at multiples of the sampling frequency

Figure A.2: Down-conversion using subsampling

In the time domain the IF waveform is multiplied by an impulse train to carry out the operation of sampling. As seen in Figure A.2 above, since multiplication in the time domain is equivalent to a convolution in the frequency domain, the effective result is to place copies of the IF spectrum centered at multiples of the sampling frequency. By setting the sampling frequency to at least twice the bandwidth of the waveform of interest, the replicas will not overlap, and the signal can be recovered by filtering. Note that although subsampling does not require that sampling occurs at twice the highest input frequency, the A/D board still needs to have a bandwidth that will pass the entire signal. For the application presented in this work, the IF frequency of 374 MHz is out of the AD10226 input range of 0-350 MHz, which reduces slightly the level of the sampled signal by 1.0 dB according to specifications.

Since it is required to sample at a rate of at least twice the highest frequency of the baseband signal we are interested in, the clock rate on the AD10226 must be set to comply with the bandwidth of the desired signal. For our purposes, each channel has a 60MHz sampling rate; the IF signal bandwidth is 20 MHz.

A.2.6 Analog Devices HSC-ADC-EVAL-DC FIFO Board

The Analog Devices HSC-ADC-EVAL-DC FIFO Board functions to capture the data following the A/D board. The HSC-ADC-EVAL-DC controller software has the capability to take FFTs of the incoming time series data from the A/D board. The software also has the capability of displaying the time series itself. The amount of data that can be taken at a time by the AD6620 board is limited by the pair of 32k FIFOs on the board. This means that maximally 32k samples of real data can be captured by each chip per data collection command. Note that since the FIFO board can operate with different ADC's, the software must be configured for the particular ADC in use. A *.config file for the AD10226 was generated. To function with the AD10226, the highest 12 bits out of 16 possible, i.e. bits 5-16, must be used. This required configuration is compensated for in the software for on screen display, but not in the data itself. This can be seen by right clicking on the window and exporting the time series data to a *.csv file. The values in the file are offset by a factor of 16, or 2^4, from what they should be to match the on screen display. To use the software, the sampling rate field must be set to match the clock input on the AD10226, and the appropriate computer port selected.

A.3 Receiver Assembly

The evaluation boards, filters, and antennas are connected with SMA cables and appropriate N-type to SMA adapters. Below is a diagram which shows the routing for cables associated with Channel A only, as Channel B has a similar setup. Notice that the output of the oscillator board, Si4136, must be provided to both Channel A and B. To do so, a Mini-Circuits 15542 splitter is used.

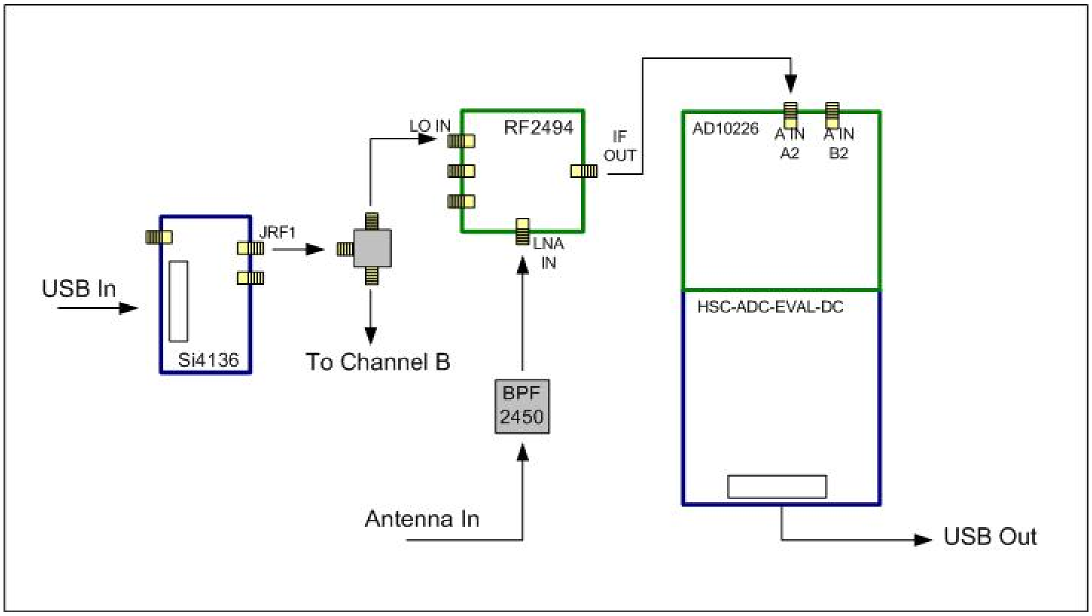

Figure A.3: Cable configuration

Making sure you are properly grounded, power up the boards as follows:

1. Si4136: Connect the +5V input to 5V, and GND to ground. Make sure the USB cable is connected to a computer with the Si4136 controller software installed.
2. RF2494: Connect pins PD, RX EN, GS, and VCC to 3.3V, and ground to the remaining GND pins.
3. AD10226: Connect a 5V input to the two +5V sockets, 3.3V input to the two 3.3V sockets, and ground to GND. Connect a 60 MHz sine wave clock signal (0.8V pk-pk amplitude minimum) to the inputs, ENC A and ENC B. To drive the board using single ended analog inputs, the jumpers JP1 and JP2 must be connected. Also, the following additional settings are used:

On:	JP3, 8, 9, 12, 13, 19, 20, 21, 24, 31
Off:	JP10, 11, 14, 15, 22, 23, 25, 26, 27, 28, 29, 30

Right:	JP18, 32
Left:	JP16, 17
Down:	JP33 (Important: this setting controls clock to channel B)

4. HSC-ADC-EVAL-DC: Connect 3.3V to VCC input and ground to GND. Connect the parallel cable from the board to the parallel port of the computer. Refer to the manual with the evaluation board kit for installation assistance on the software, as well as information on available jumper settings. Note that the timing jumpers may have to be adjusted to level out the noise floor. Refer to the HSC-ADC-EVAL-DC data sheets for the options available. Connect the board to the AD10226 board using the special adaptor board.